



BALLOON-BORNE X-RAY OBSERVATIONS

OF THE SOUTHERN SKY

by

Richard Murison Thomas, B.Sc. (Hons.)

A Thesis presented for the degree of
Doctor of Philosophy in the Department
of Physics, University of Adelaide, January, 1971.

CONTENTS

	<u>Page</u>
SUMMARY	i
PREFACE	iv
ACKNOWLEDGEMENTS	v
CHAPTER 1	INTRODUCTION
1.1.	DISCRETE SOURCES 1
1.1.1.	Known Sources 1
1.1.2.	Source positions and optical identifications. 2
1.1.3.	Time Variations. 7
1.1.4.	Source spectra. 9
1.2.	ASTROPHYSICAL X-RAY PRODUCTION MECHANISMS 10
1.2.1.	Magnetobremstrahlung or synchrotron emission. 10
1.2.2.	Thin source thermal bremsstrahlung 12
1.2.3.	Compton scattering 14
1.3.	THE DIFFUSE X-RAY BACKGROUND. 16
1.3.1.	The soft component, 0.25 KeV 16
1.3.2.	The diffuse background spectrum (> 1 KeV) 17
1.3.3.	Theoretical models 19
1.4.	THE ADELAIDE BALLOON-BORNE EXPERIMENTS 24.

CHAPTER 2	INSTRUMENTATION	
2.1	INTRODUCTION.	28
2.2	THE BALLOON PAYLOAD	28
2.3	THE X-RAY DETECTORS	30
2.3.1.	The Graded Shield Telescope	30
2.3.2.	The Active Telescope	31
2.4.	THE PHOSWICH SYSTEM	33
2.5	PULSE HEIGHT ANALYSIS	35
2.5.1.	Anticoincidence logic	35
2.5.2.	Height-to-time converter.	36
2.6.	IN-FLIGHT ENERGY CALIBRATION	38
2.7	THE MAGNETOMETERS	38
2.7.1.	The Sensors	39
2.7.2.	Digitization and readout	39
2.7.3.	Response of the magnetometers	40
2.7.4.	Instrumental limitations upon measurement accuracy	41
2.7.5.	System Stability	43
2.8.	THE ALPHATRON PRESSURE GAUGE	45
2.9.	HOUSEKEEPING MEASUREMENTS	46
2.10	THE P.C.M. TELEMETRY SYSTEM	47
2.10.1.	Telemetry word format	47
2.10.2.	The data storage unit (D.S.U.)	49
2.10.3.	The data transmission unit (D.T.U.)	50
2.10.4.	The ground station.	51

CHAPTER 3.	LABORATORY X-RAY ASTRONOMY	
3.1.	INTERACTIONS OF X-RAYS WITH MATTER	53
3.1.1.	Photoelectric absorption	53
3.1.2.	The Compton effect	54
3.2.	RESPONSE OF NaI(Tl) TO INCIDENT X-RAYS	55
3.2.1.	Transparency of the crystal to X-rays	55
3.2.2.	The scintillation process in NaI(Tl)	56
3.2.3.	K-escape	57
3.2.4.	Spectral resolution	59
3.2.5.	Summary	61
3.3.	ANALYSIS OF COSMIC X-RAY SPECTRA	61
3.3.1.	Atmospheric and payload absorption	62
3.3.2.	The final response function.	62
3.3.3.	Spectral correction factors	64
3.4.	TELESCOPE CALIBRATION	64
3.4.1.	Background rejection	66
3.4.2.	Energy calibration	68
3.4.3.	Active collimator angular response	69
3.4.4.	Telescope geometric factor	71
3.5.	PRE-FLIGHT ENVIRONMENTAL TESTING	72

CHAPTER 4.	THE MAGNETOMETERS	
4.1.	THE GEOMAGNETIC FIELD	74
4.1.1.	The geomagnetic elements	75
4.1.2.	Variation of smoothed field near Mildura	76
4.1.3.	Geomagnetic anomalies	78
4.1.4.	Time variations.	79
4.2.	ORIENTATION OF THE CROSSED MAGNETOMETERS	80
4.2.1.	Theory.	81
4.2.2.	Numerical computations.	83
4.2.3.	Summary	86
4.3.	CALIBRATION OF THE MAGNETOMETERS	86
4.3.1.	Preflight experimental procedure	87
4.3.2.	Reduction of preflight calibration data	88
4.3.3.	In-flight calibration	89
4.3.4.	Final values of calibration parameters	89
4.4.	FLIGHT PERFORMANCE OF THE MAGNETOMETERS	90
4.4.1.	Anomalous H measurement.	90
4.4.2.	Accuracy of the azimuth measurement	92
4.5.	A ROTATING REFERENCE MAGNETOMETER	92
4.5.1.	Theory	93
4.5.2.	Computations.	95
4.6.	EFFECTS OF CONTAMINANT MAGNETIC	96
4.6.1.	Permanent fields.	97
4.6.2.	Induced fields	98

CHAPTER 5	DISCRETE SOURCE RESULTS, $320^\circ < l < 350^\circ$	
5.1	INTRODUCTION	100
5.2	DATA ANALYSIS	101
5.3	NORMA XR-1 AND ARA XR-1	104
5.3.1.	Spectrum of Nor XR-1	104
5.3.2.	Spectrum of Ara XR-1	106
5.4.	UPPER LIMITS	107
5.5.	SOURCE LOCATIONS	109
CHAPTER 6	ATMOSPHERIC X-RAYS, I	
6.1.	INTRODUCTION	112
6.1.1.	The telescope background	112
6.1.2.	The atmospheric radiation environment	115
6.2.	TRANSITION CURVES, $200 < p < 700 \text{ GM.CM}^{-2}$	117
6.2.1.	Results	117
6.2.2.	Flight-to-flight variations of attenuation length	120
6.2.3.	Differences between the two telescopes	122
6.2.4.	The Gross Transformation	122
6.2.5.	Comparison with other experiments	126
6.2.6.	Other radiations	129
6.3.	THE TRANSITION CURVE MAXIMUM ($p \sim 100 \text{ GM.CM}^{-2}$)	133
6.3.1.	Results.	134
6.3.2.	Discussion	135
6.4.	SUMMARY	136

CHAPTER 7	ATMOSPHERIC X-RAYS, II	
7.1.	INTRODUCTION	138
7.2.	THE HIGHEST ALTITUDES ($p < 100$ GM.CM.^{-2})	138
7.2.1.	Transition curve, $10 < p < 70 \text{ gm.cm}^{-2}$	139
7.2.2.	Extrapolation to balloon float depth	144
7.2.3.	Discussion	146
7.3.	ENERGY LOSS SPECTRA	147
7.3.1.	Pulse height distributions	147
7.3.2.	Spectral colour indices	150
7.3.3.	Spectral structure	151
7.4.	TIME VARIATIONS	153
7.5.	GEOMAGNETIC LATITUDE VARIATIONS	154
7.6.	CONCLUSIONS.	155
CHAPTER 8	THE DIFFUSE X-RAY BACKGROUND, 20-170 KeV	
8.1.	INTRODUCTION	157
8.2.	THE DIFFUSE BACKGROUND SPECTRUM	157
8.2.1.	Extrapolation of transition curve	158
8.2.2.	Spectral results	161
8.3.	GALACTIC DIFFUSE X-RAYS	161
8.3.1.	Galactic plane anisotropy	162
8.3.2.	Galactic line flux	165
APPENDIX:	PUBLICATIONS	A1
BIBLIOGRAPHY		B1

SUMMARY

This thesis presents results from the Southern X-ray sky obtained from flights of the University of Adelaide balloon-borne observatory in the period 1968-69. The altitude dependence of telescope background count rates in the pressure interval ~~3~~⁵700 gm. cm.⁻² is also examined in detail for the ascent phases of the different flights.

Chapter 1 consists of an introduction to the subject of X-ray astronomy and its literature, and also contains a brief summary of the experiments performed by the Adelaide group. The payload and ground-based instrumentation are described in chapter 2, while the physical principles of the X-ray detectors are discussed in the following chapter. The unfolding of an X-ray source spectrum from a measured detector pulse height distribution is described here, as are the laboratory-determined detector characteristics and the pre-flight environmental testing of the payload.

A theoretical discussion of the performance of the azimuth-measurement system, and in particular the effects of geomagnetic field variations and non-horizontal orientation of the magnetometers, follows in chapter 4. It is concluded that the azimuth angle is measured with an uncertainty not exceeding 1.4° . Orientation and field variation effects on a rotating null magnetometer are also predicted.

Chapter 5 reports the observation of significant hard X-ray fluxes from the sources Nor XR-1 and Ara XR-1 and presents upper limits for numerous other sources in the galactic longitude range

$320^\circ < \ell^{\text{II}} < 350^\circ$. Comparison of these data with lower energy rocket results shows that a power law spectrum (in $\text{KeV cm.}^{-2} \text{ sec}^{-1} \text{ KeV}^{-1}$) of exponent 1.5 best fits the Nor XR-1 data for photon energies $> 5 \text{ KeV}$, while Ara XR-1 is best described by an exponential spectrum having $kT = 11 \text{ KeV}$. The Adelaide data for Nor XR-1 makes possible the revision of a previous estimate of $4 \times 10^{21} \text{ cm.}^{-2}$ for the hydrogen atom column density in its direction (Cooke and Pounds 1970), to the new figure of $2 \times 10^{22} \text{ cm.}^{-2}$, which is in better agreement with measurements from other nearby sources. The present status of source positional measurements for $320^\circ < \ell^{\text{II}} < 350^\circ$ is also discussed.

Chapter 6 examines the altitude dependence of various count rates in the atmospheric pressure interval $100 \leq p \leq 700 \text{ gm. cm.}^{-2}$. Radiation attenuation lengths are measured as a function of energy for each flight. Differences are observed between flights. There are also discrepancies between our results and those of other workers. These discrepancies may in part be explained in terms of the dependence of background characteristics on the type of detector employed. On any one flight the numerical relationships between the attenuation lengths of (a) the active telescope energy channels, (b) the active telescope guard rates, and (c) the graded shield telescope energy channel rates, can be well explained using the Gross Transformation. The theoretical difficulties of this interpretation, in view of the expected isotropy at these altitudes of the electron-photon component of secondary cosmic rays, are discussed. Comparisons with the attenuation lengths of other radiation species are found to give no positive clues to the origin of the observed count rates.

In chapter 7, the background count rates are investigated in the pressure range $3 \lesssim p \lesssim 100$ gm. cm.⁻² with particular emphasis on the fitting of functional forms to the altitude dependence. The active telescope pulse height distribution as a function of altitude is also discussed.

The diffuse cosmic X-ray background is measured in chapter 8 and results are consistent with those of other groups. It is found to be isotropic to less than 10% (at the one sigma level) with respect to the galactic plane, between the longitudes $320^\circ \lesssim \ell \lesssim 40^\circ$ and for energies $27 < E < 67$ KeV. This is the only such measurement at these longitudes and energies. A corresponding upper limit at the 3 σ level of 7.26×10^{-4} photons cm.⁻² sec.⁻¹ KeV.⁻¹ rad.⁻¹ was determined for a line source of X-rays in the galactic plane.

PREFACE

To the best of the author's knowledge, this thesis contains no material previously published or written by another person except where due reference is made in the text. It contains no material which has been submitted or accepted for the award of any other degree or diploma in any University.

(R.M. Thomas)

Department of Physics,
University of Adelaide.

January 18, 1971.

ACKNOWLEDGEMENTS

I wish to acknowledge the assistance given me during this work by members of the Cosmic Ray Group of the Department of Physics, University of Adelaide. In particular I am indebted to Prof. K.G. McCracken who gave me the opportunity to enter the field of X-ray astronomy and as my supervisor for the first 3 years provided invaluable guidance and assistance. My thanks are also due to Dr. P.J.N. Davison who assumed Prof. McCracken's supervisory position at the end of 1969. Valuable discussions have also been enjoyed with Prof. W.R. Webber, Dr. J.G. Abley, Dr. P.J. Edwards, Dr. J.R. Harries, Mr. M.C. Clancy and Mr. G. Buselli. Prof. D.M. Boyd of the Department of Economic Geology, University of Adelaide, offered helpful advice concerning the effects at balloon altitudes of known geomagnetic anomalies in the Mildura area.

The initial development of the observatory occurred at the Southwest Centre for Advanced Studies, Dallas, Texas under Prof. McCracken's guidance. For technical support in Adelaide I must thank Messrs. E.F. Hindley and F. Holland. Computing assistance was provided by Mr. E. Williams.

For balloon flight support, the work of Messrs. E. Curwood, J. Hillier, D. Scott and members of the Department of Supply Balloon Launch Facility at Mildura is gratefully acknowledged.

The invaluable offer from Prof. W.H.G. Lewin of the Massachusetts Institute of Technology, of the two balloons used for the flights MIL-1-69 and MIL-2-69 is deeply appreciated.

Financial support was given the research program by N.A.S.A. and A.F.O.S.R. of the United States, and by the Australian Research Grants Committee. I am grateful for the assistance of a Commonwealth Postgraduate Award during the course of this research.

Finally I wish to thank my parents and my wife Sandra for the patience and encouragement they have shown towards me during my studies.

CHAPTER 1.

INTRODUCTION.

Since the initial discovery in June 1962 (Giacconi et al 1962) of cosmic X-radiation, many discrete sources have been discovered and the existence of a diffuse background of X-rays has been confirmed, which is apparently extragalactic in origin. These discoveries have, and will continue to have, important consequences with regard to the evolution of galactic objects, to interstellar and intergalactic matter, cosmic ray physics and cosmology.

This chapter contains a brief review of the current status of the field and concludes with an introduction to the objectives and experiments of the balloon-borne X-ray astronomy group of the University of Adelaide.

1.1. DISCRETE SOURCES.

As of August 1970, about 60 discrete sources have been reported in the literature. However, only about half of these observations have been confirmed by subsequent experiments.

1.1.1. Known Sources.

Various catalogues of discrete X-ray sources have been tabulated in the brief history of X-ray astronomy. In the design phase of the Adelaide programme, the catalogue compiled by the Naval Research Laboratory (N.R.L.) Washington DC (Friedman et al. 1967) was used. This contained 35 sources and was used in determining the scanning patterns in our earliest balloon flights. Subsequent studies have failed to confirm many of the N.R.L. sources.

Webber (1968) in a re-examination of the literature, compiled a catalogue of "confirmed" sources numbering 22, which should perhaps have only been 21 as I have been unable to find any reference in the literature to the confirmation of Cep XR-1. More recently, Dolan (1970a) has published a comprehensive list of 59 sources reported before December 1, 1969, in which no attempt was made to eliminate unconfirmed observations. Of these 59 sources, the 21 of Webber plus 8 others can be regarded as confirmed at the present time (August 1970), and these 29 objects are tabulated in table 1.1 in order of their appearance in Dolan's catalogue. Also listed for each source are galactic longitude and latitude (l^{II} , b^{II}), and right ascension and declination ((α, δ) 1950.0). These co-ordinates are believed to be those of the most precise observations to date. Exhaustive references are cited for each source by Dolan and simplicity dictates that those should not be listed here.

1.1.2. Source positions and optical identifications.

Examination of table 1.1 reveals the long-recognized fact that the majority of confirmed X-ray objects lies within 10° of the galactic equator and so are almost certainly galactic objects. An apparent exception is Vir XR-1 which has been tentatively identified with the optical and radio galaxy known as M87 and Virgo A (Friedman et al 1967a, Bradt et al 1967). Sco XR-1 and the spectacular variable Cen X-4 are both at high galactic latitude but are believed to be galactic. The objects Cet XR-1 (Barnden and Francey 1969) and Cet XR-2 (Shukla and Wilson 1970) are taken to be the same object and the position given is that determined for Cet XR-2 it has not yet been determined whether it is a galactic or extragalactic object.

Table 1.1 Confirmed X-ray Sources (August, 1970)

Dolan's #	Popular Name(s)	l II	b II	α	δ
2	Cet X1-1, 2	159°	-52°	02 ^h 14 ^m	+ 4°13'
4	Tau XR-1	185°	-06°	05 ^h 31 ^m	+21°59'
5	Vel XR-1	263°	+03°	08 ^h 57 ^m	-41°15'
7	Cen XR-3	292°	+02°	11 ^h 23 ^m	-59°
9	Vir XR-1	284°	+75°	12 ^h 32 ^m	12°35'
13	Cen X-2	307°	+00°	13 ^h 24 ^m	-62°
15	Cen X-4	332°	+23°	14 ^h 56 ^m	-32°15'
16	Lup XR-1	323°	+05°	14 ^h 59 ^m	-52°
17	Nor XR-2	324°	-02°	15 ^h 42 ^m	-57°30'
19	Sco XR-1	359°	+24°	16 ^h 11 ^m	-15°31'
20	Nor XR-1	334°	-02°	16 ^h 24 ^m	-51°
24	L5, Sco X-2	344°	+02°	16 ^h 51 ^m	-40°48'
25	L2, Ara XR-1	340°	- 3°	16 ^h 54 ^m	-47°
27	GX 349 + 2, L6, Sco XR-2	349°	+01°	17 ^h 09 ^m	-37°42'
31	GX9 + 9	009°	+09°	17 ^h 30 ^m	-16°36'
34	GX3 + 1, Sgr X-1	003°	+01°	17 ^h 43 ^m	-26°08'
35	L10, GX-2.5	356°	-03°	17 ^h 45 ^m	-33°42'
36	GX 354 - 5, GX-5.6	354°	-05°	17 ^h 47 ^m	-36°
39	GX 5 - 1, GX + 5.2	005°	-01°	17 ^h 59 ^m	-25°00'
40	GX 9 + 1	009°	+01°	18 ^h 00 ^m	-20°32'
43	GX 13 + 1	013°	+01°	18 ^h 10 ^m	-17°08'
45	Ser XR-2, GX 17 + 2	017°	+01°	18 ^h 13 ^m	-13°48'
48	Ser XR-1, GX + 36.3	037°	+02°	18 ^h 45 ^m	+05°18'
51	Cyg X-1	071°	+03°	19 ^h 56 ^m	+35°06'
52	Cyg X-3	080°	+01°	20 ^h 31 ^m	+40°56'
53	Vul XR-1, Cyg X-5	071°	-08°	20 ^h 38 ^m	+29°
54	Cyg X-4	083°	-06°	21 ^h 09 ^m	+38°33'
55	Cyg X-2	087°	-11°	21 ^h 42 ^m	+38°05'
58	Cas XR-1	112°	-02°	23 ^h 21 ^m	+58°30'

Gursky et al (1967) have examined the distribution of sources within the Galaxy and have concluded that there is a correlation with galactic spiral arm structure and that the concentration of sources in the quadrant $290^\circ \leq l^{\text{II}} \leq 20^\circ$ (which is of interest to southern hemisphere observers) can be conveniently located within the Sagittarius spiral arm (as defined by Sharpless 1965) at a distance of ~ 2 kpc. The Cygnus sources may be placed about 4 kpc. distant, beyond the Orion arm and in an arm revealed by 21 cm. observations.

The most accurate position determination of an X-ray source has been that of Sco XR-1, using the modulation collimator technique (Oda 1965, Gursky et al 1966). Its location in either of two rectangles of dimension $1' \times 2'$ arc has led to its optical identification with a 13th magnitude, flickering blue star (Sandage et al 1966). Its high galactic latitude ($b^{\text{II}} = +24^\circ$) appears to be the result of its nearness, of the order of a few hundred parsecs (Manley 1970). It has also been tentatively identified with a radio source (Andrew and Purton 1968), and accurate position measurements at 6 cm. wavelength (Ables 1969) have shown that the radio emission is centred on the optical object to within $\sim 15''$ arc. Intensity measurements have revealed it to be an irregular variable over its entire observed spectral range, from X-rays (Hill et al 1968, Lewin et al. 1968, 1970b, Overbeck et al 1968, Evans et al, 1970b) through optical (Westphal et al 1968) to radio (Ables 1969). Non-periodic variations are observed on time scales of minutes for the optical flicker and of minutes, hours and days for the X-ray, radio and longer term optical variations.

Another optical identification, in fact the first of an X-ray source, was that of Tau XR-1 with NGC 1952 or the Crab Nebula, a supernova remnant and synchrotron radio source, Taurus A. Bowyer et al (1964) conducted a rocket experiment during a lunar occultation of the Crab. It was established that the Xradiation originated from an extended source which coincided with the optical nebulosity but had only about half its angular extent. The physical nature of the Crab was complicated even further when Staelin et al (1968) found that it contained a member of the recently discovered class of objects, the pulsars (for brief reviews of the nature of pulsars see Radhakrishnan 1969, and Chiu 1970). Designated NP 0532, the pulsar was also found to pulse optically (Cocke et al 1969) and in the X-ray region as well, in which about 10% of the total flux was found to be pulsed at the same period ($\sim 33\text{ms}$) as the radio pulsations (Fritz et al 1969, Bradt et al 1969, Fishman et al 1969, Floyd et al 1969). The pulsation rate has been found to be slowing down by about 1 part in 2400 per year (Richards 1968).

The optical pulsar has no discernible diameter and current speculation is that this is a neutron star with an inclined dipole magnetic field which emits beamed radiation and whose rapid rotation produces pulsations in the received flux of period equal to that of the rotation (Woltjer 1968). An attractive consequence of the energetics of this model (Goldreich 1969, Gunn et al 1969), reveals that the observed slowing down of the rotation rate can provide sufficient energy for the acceleration of particles to ultrarelativistic energies with the consequent emission of synchrotron or magnetobremstrahlung X-rays.

The sources Sco XR-1, Cyg XR-1 and Cyg XR-2 have been subjected to a preliminary examination for X-ray pulsar characteristics but with null results (Friedman et al. 1969). Comparing the radio pulsar catalogue and the X-ray object catalogue reveals that at this time, Tau XR-1 provides the only instance of a one-to-one correspondence.

Other identifications of optical objects with known X-ray sources are still in the tentative stage, owing mainly to the poor angular resolution with which X-ray observations can currently be made. Identifications using the method which was successful for Sco X-1, viz, extrapolating the X-ray spectrum back to optical wavelengths and deducing the apparent magnitude and colours of the optical object, have been claimed for Cyg X-2 (Giacconi et al. 1967, Kraft 1967), Cen X-2 (Eggen et al. 1968), and Cen X-4 (Eggen et al. 1969). However, for various reasons, among them being lack of agreement of the actual properties of the chosen optical object with the extrapolation (Cyg X-2), the large number of stars within the X-ray error circles (Cyg X-2, Cen X-2) and lack of any correlation in the temporal behaviour of the optical and X-ray emission (Cen X-2), these claims are still in doubt. Recent work by Schnopper et al. (1970) using a rotating modulation collimator has resulted in the elimination (Kunkel et al. 1970) from consideration of suggested optical candidates for the galactic centre source GX 3 + 1 (Freeman et al. 1968, Blanco et al. 1968, Johnson et al. 1968).

In addition to Sco XR-1, Tau XR-1 and Vir XR-1 which have already been mentioned, some known optical and radio objects have been tentatively reported to emit low energy X-rays.

These have been;

- (a) an L.R.L. (Lawrence Radiation Laboratory) observation of a strong soft source (0.2 to 2 KeV), Cyg X-5 which can be identified with both Vul XR-1 (Friedman et al 1967) and the supernova remnant, the Cygnus Loop (Grader et al 1970); Schklovsky (1968) has in fact predicted that the Cygnus Loop should be an intense source of soft X-rays due to lines of ionized oxygen;
- (b) the supernova remnant Cas A, and,
- (c) Tycho's supernova, SN 1572 (both Gorenstein et al 1970); both of these sources were examined for pulsar characteristics but with inconclusive results owing to poor counting statistics; and finally,
- (d), the Large Magellanic Cloud (Mark et al 1969).

1.1.3 Time Variations:

Time variations of intensity have been mentioned above for Sco XR-1 and Tau XR-1. In addition there is evidence for time variability of Cyg X-1 (Overbeck et al 1968, Dolan 1970 b), at energies above 20 KeV. Variability has also been suggested to explain inconsistencies between various other results where perhaps systematic errors may have been more responsible.

Two spectacular and undisputed instances of source variability have been recorded. Cen X-2 was not observed during a 1965 observation of Grader et al (1966), but suddenly blazed out to become comparable in intensity to Sco XR-1 shortly before April 4, 1967 when it was observed by Harries et al (1967) in the energy

range 2 to 8 KeV. Its behaviour prior to this date can perhaps be inferred from records of VLF radio reception which acts as a measure of X-ray source activity by virtue of the resultant D region electron density variations (Edwards et al 1969). After the initial observation its intensity declined and its spectral form changed and on May 17 it was seen for the last time at low energies (Francey et al 1967, Cooke et al 1967, Chodil et al 1967). L.R.L observations on September 18, 1967 and Nov. 3, 1968, failed to detect it (Chodil et al 1968, McGregor et al 1969), in spite of the report of a positive flux by Rao et al (1969) on November 3 and 7, 1968. These observations have been interpreted by McGregor et al as the effect of other nearby sources. Cooke and Pounds (1970) are of the same opinion with respect to the result of Rao et al but report a significant flux from Cen X-2 on April 1, 1969, at a very low level consistent with the other null results reported.

Significant hard fluxes were observed from balloon experiments on October 15 and 24, 1967 by Lewin et al (1968a,c) and perhaps on Feb 29 1968 by Buselli (1968). These three balloon measurements were all made after May 17 following the decline of Cen X-2 at lower energies, and there is evidence that this harder spectral component may have developed some time after the initial low energy outburst. The 2 measurements of Lewin et al indicated that the hard flux was experiencing a decline in intensity, and had diminished by about 30% between Oct. 15 and 24. By March 20, 1969 it was no longer detectable at high energies (Lewin et al 1970a)

The second spectacularly variable source, Cen X-4, was observed in the energy range 3 to 12 KeV from two Vela satellites (Conner et al 1969). This source appeared abruptly between July 6 and 9, 1969 at an intensity level comparable to that of Sco XR-1. It faded and by the end of September 1969 was $\lesssim \frac{1}{2}$ % of its maximum intensity (Evans et al 1970a). Meanwhile it had been observed by rocket, between 2 and 25 KeV, on Aug. 7 (Kitamura et al 1969). A search for a hard spectral component analogous to that of Cen-X-2 was conducted by the Adelaide group on August 25, 1969 (Thomas et al 1969, 1970) employing the smaller of the two payloads mentioned later in this thesis (section 1.4). No such component was found but this did not necessarily exclude the possibility that Cen X-2 and Cen X-4 were similar objects, since no high energy observation of Cen X-2 was made until 6 months after its low energy discovery. An abortive attempt was made to test this hypothesis in March 1970 by the Adelaide group. No other observations are known which permit exclusion of this possibility.

1.1.4. Source Spectra

This brief review of the present observational knowledge of discrete sources is now concluded with a discussion of their observed spectral characteristics. The observed differential energy spectra $E \cdot N(E) \cdot dE$, where $N(E)dE$ is the number of photons in the energy interval E to $E + dE$, fall into two basic classes as follows:-

(a) The power law spectrum, $E \cdot N(E) \cdot dE = \text{constant} \cdot E^{-\lambda} dE \dots \dots \dots 1.1$
where the exponent λ is a positive constant, and

(b) The exponential spectrum, $E \cdot N(E) \cdot dE = \text{constant} \cdot \exp\left(\frac{-E}{E_0}\right) dE \dots \dots 1.2$
where the e-folding energy E_0 is characteristic of the source.

The two classic illustrations of these different spectra are provided by Tau XR-1 (power law), and Sco XR-1 (exponential), although these now appear to be more complex than earlier thought. Tau XR-1 appears to suffer a spectral steepening at 100 KeV and over the observed range of energies cannot be described by a power law with a unique exponent, while the spectrum of Sco XR-1 seems to flatten beyond 20 KeV, the degree of which is possibly time-dependent, with the result that it cannot be described by a unique E_0 . This is discussed with reference to source models and emission mechanisms in the next section.

1.2 ASTROPHYSICAL X-RAY PRODUCTION MECHANISMS:

The basic physical processes which produce the bulk of the observed cosmic X-ray photons are well understood and in general depend on the presence of cosmic electrons. However, despite this understanding it is not possible to uniquely relate an observed spectrum to a particular physical mechanism, since theoretical work has shown that an emitted spectrum can be strongly dependent on the source model used and not so dependent on the basic physical process operating within the model. The physics of the most favoured production mechanisms is now briefly outlined.

1.2.1. Magnetobremstrahlung or synchrotron emission.

This radiation is characterized by strong polarization and results from the orbital motion of extremely energetic electrons in magnetic fields. Less energetic electrons and/or weaker magnetic fields are believed to be responsible for strong radio sources so that a synchrotron X-ray source might be expected to be a synchrotron radio source (e.g. Tau XR-1)

An electron of energy $\epsilon = \gamma m_0 c^2$ (eV) in a magnetic field with component B_{\perp} (gauss) perpendicular to the instantaneous electron velocity will radiate a photon spectrum whose emitted energy (eV) peaks at $h\nu_{\max} = 5.8 \times 10^9 B_{\perp} \gamma^2$ (Morrison 1967.) For $h\nu_{\max} = 100$ KeV and $B_{\perp} = 100 \mu\text{G}$ the corresponding electron energy $\epsilon = \gamma m_0 c^2 \sim 2 \times 10^{14}$ eV. The electron half-life against this radiation loss is given by $\tau_{\frac{1}{2}} = 3.9 \times 10^4 B_{\perp}^{-3/2} (h\nu_{\max})^{-1/2} \sim 1.3 \times 10^8$ sec., or 4 years. The observed time stability of the hard X-ray emission from Tau XR-1 means that continuous electron acceleration is required to maintain the supply of energetic electrons against radiative loss.

The emitted synchrotron photon spectrum is determined by the electron spectrum, which is given by a power law $n(\gamma)d\gamma = n_0 \gamma^{-m} d\gamma$ ($m > 0$), will produce a power law photon spectrum,

$E \cdot N(E) dE = \text{constant } E^{-\lambda} dE$, $\lambda = \frac{1}{2} (m-1)$. However, Manley (1966) has shown that an exponential photon spectrum will result from synchrotron emission by an approximately flat electron spectrum with a high energy cut-off. Webber (1968) has also pointed out that theoretical spectra presented by Stein and Ney (1963) to explain solar flare continuum radiation by synchrotron emission from an exponential electron distribution, bear a striking resemblance to the spectrum of Sco XR-1 as measured over the 10 energy decades from X-rays to radio. It is thus possible for either an exponential or power law spectrum to result from magnetobremstrahlung.

1.2.2 Thin Source Thermal Bremsstrahlung.

If a source contains a near-Maxwellian electron distribution at characteristic temperature T , electron-ion collisions will produce thermal bremsstrahlung or free-free emission. The energy radiated per unit solid angle, per unit volume, per unit frequency interval ($\text{erg. cm.}^{-3} \text{ sec.}^{-1} \text{ ster.}^{-1}$) is given by (Allen 1963, Morrison 1967)

$$j_{\nu} = 5.443 \times 10^{-39} \left[T^{-\frac{1}{2}} g(\nu, T) \sum n_0 n_{\pm} Z^2 \right] \exp\left(\frac{-h\nu}{kT}\right)^{-1.3}$$

where k is Boltzmann's constant, n_0 and n_{\pm} are the number densities of electrons and ions of charge $\pm e$ respectively, the Gaunt Factor $g(\nu, T)$ is approximately equal to unity, and varies only slowly as a function of $h\nu$. Thus free-free emission produces an exponential spectrum with e-folding energy $E_0 = kT$ (c.f. equations 1.2).

Tucker and Gould (1966) have found that in addition to the bremsstrahlung continuum there should also be recombination edges and emission lines associated with such a source. For a gas at 5×10^7 °K they predict the most easily observable non-continuum features to be the O^{+8} and Ne^{+10} recombination edges. In contrast to magnetobremsstrahlung, free-free emission is unpolarized.

Thermal mechanisms have also been advanced to explain power law spectra (Hayakawa et al 1966). More recently, Sartori and Morrison (1967) have argued that superposition of the thermal spectra from a number of distinct temperature regions in a source provides a good fit to a single power law spectrum. They have suggested that this might be the case in Tau XR-1. The observed spectrum of ScoX-1 from about 1 to 100 KeV is consistent with either a two-temperature (about 4 and 15 KeV) exponential description, or more roughly a single exponential ($\lambda = 2.8$) power law (Buselli et al 1968, Holt et al 1969).

Thus it is not possible to uniquely identify exponential or power law spectra with either the thermal or synchrotron production mechanisms. Additional data from more definitive experiments are required. For example, the detection of polarized X-rays would favour a magnetobremstrahlung origin, while the detection of spectral lines or edges would indicate a thermal source.

Attempts have been made to detect the polarization of X-rays from Sco XR-1 and Tau XR-1 (Angel et al 1969, Wolff et al 1970). The measurements have been severely limited by counting rate statistics and no conclusive results have been obtained. However, the preliminary results are $(4.9 \pm 5.2)\%$ for Sco XR-1 which is essentially a null result and $\leq 20\%$ for Tau XR-1 which is consistent with either zero or the observed optical and radio polarization. No radio or optical polarization has been observed in Sco XR-1.

Line emission from Fe^{+24} and Fe^{+25} at ~ 7 KeV was tentatively claimed for Sco XR-1 by Holt et al (1969) and has been confirmed by Acton et al (1970). This almost certainly provides decisive evidence for thermal emission. Thus far, only null results have been obtained for iron line emission from the Crab (Boldt et al 1969).

1.2.3 Compton scattering:

Another important non-thermal X-ray production mechanism is Compton scattering (Felten and Morrison 1963, 1966) in which X-radiation results from the transfer of energy from relativistic electrons to photons in electron-photon interactions. It is sometimes referred to as "inverse" Compton scattering since the photon gains energy rather than loses it as in the more familiar type of Compton interaction. No magnetic field is necessary so there will be no radio emission directly related to the X-ray emission.

An electron of energy $\epsilon = \gamma m_0 c^2$, $\gamma \gg 1$, upon undergoing an "inverse" Compton interaction with a low energy (E_0) photon imparts a small fraction of its energy to the photon. The photon energy is increased to $E \sim \gamma^2 E_0$, provided $\gamma E \ll m_0 c^2$. Thus electrons of energy $\sim 10^{10}$ eV interacting with photons of energy $E_0 \sim 0.1$ eV, will produce ~ 10 MeV photons. The electrons required are of lower energy than those required for synchrotron emission of X-ray and γ -ray photons of the same energy. Since all collision angles are possible, a spectrum of scattered photon energies results and this can be calculated using the equations of classical Thomson scattering for the condition $\gamma E \ll m_0 c^2$. For a power law electron spectrum given by $n(\gamma) d\gamma = n_0 \gamma^{-m} d\gamma$, the Compton photon spectrum observable at the Earth is also given

by a power law:-

$$I_{h\nu} = 10^3 (56.9)^{3-m} n_0 R \rho T^{\frac{m-3}{2}} (h\nu)^{\frac{1-m}{2}} \dots\dots\dots 1.4$$

Here $I_{h\nu}$ is in $\text{eV cm}^{-2} \text{sec}^{-1} \text{sr}^{-1} \text{eV}^{-1}$, n_0 is in electrons cm^{-3} , R is the line of sight extent of the emission region in light years, T is the characteristic blackbody temperature of the photon distribution in $^{\circ}\text{K}$, $h\nu$ is the scattered photon energy in eV and ρ is the energy density of the low energy photon distribution in eV cm^{-3} .

Values of photon energy densities are given in table 1.2.

Table 1.2 Cosmic photon energy densities * (eV cm^{-3})

Isotropic X-ray	5×10^{-4}
Microwave 2.7°K	2.5×10^{-1}
Galactic starlight	5×10^{-1}
Extragalactic starlight	10^{-2}
Galactic Infra red (0.4 to 1.33mm.)	6

*Morrison (1966), Ipavich and Lenchek (1970)

The electron lifetime is given by $\tau_c(\gamma\rho) = \frac{2 \times 10^{19}}{\gamma\rho}$ seconds, so that

10^{10} eV electrons interacting with galactic starlight having $\rho \sim 0.5 \text{ eV cm}^{-3}$ will survive for $\sim 10^8$ years. The Compton effect

is not thought to be a significant process in discrete sources (except perhaps in X-ray galaxies) because of the high electron and photon densities required for objects of such small extent.

It has been suggested by Demoulin and Burbidge (1968) as a possible origin for X-rays from the M87 jet but Burbidge himself has expressed doubts and favours synchrotron emission as an explanation (Burbidge 1969).

However, it is highly regarded as the process operating in intergalactic space to produce the diffuse background flux of X-rays

from interactions of cosmic ray electrons with the 2.7°K blackbody radiation (Felten and Morrison 1966., Brecher and Morrison 1969) and the following section discusses this possibility in more detail.

1.3 THE DIFFUSE X-RAY BACKGROUND:

The existence of a diffuse flux of background X-radiation of apparently extragalactic origin has raised important questions concerning cosmology, interstellar and intergalactic matter and cosmic ray physics. The diffuse X-ray background appears to have at least two components, one at high energies, ≥ 1 KeV, and a low energy flux which has been observed at ~ 0.25 KeV.

1.3.1. The Soft Component, 0.25 KeV.

The low energy (~ 0.25 KeV) background flux (Bowyer et al 1968, Henry et al 1968, Baxter et al 1969, Bunner et al 1969), has been observed to be above the simple power law extrapolation of the hard spectrum (see section 1.3.2.) and a different origin seems likely. This has become a matter of great interest because closed universe cosmologies require the universe to have a mean density of 10 hydrogen atoms m^{-3} . Galactic matter cannot meet this requirement and if the "lost" matter exists, it must be found in the intergalactic medium and must have a temperature of $\sim 0.1 \times 10^6$ $^{\circ}\text{K}$ (Gould, 1968). Thermal emission of soft X-rays provides the only means of detecting such a gas, and Henry et al (1968) suggest their results are consistent with such intergalactic emission.

If this is so, the transparency of intergalactic space to the radiation places constraints on heavy element abundances in the intergalactic medium. In particular C and N must be present at $\lesssim 2\%$ of their cosmic abundances and this in turn places limits on the cumulative "pollution" of intergalactic space by galaxies and exploding objects during cosmological time (Sciama 1969).

Attenuation of this low energy radiation is observed in the direction of the galactic plane, but Bowyer et al and Bunner et al. have noted that the amount of galactic absorption is inconsistent with the amount of galactic neutral hydrogen as indicated by 21 cm. measurements. They suggest that a random, clumpy, cloud-like distribution of interstellar HI may resolve the question.

The questions raised by the low energy background will not be further pursued in this thesis. I now turn to a summary of the higher energy background, for which some experimental results obtained by the Adelaide Group will be presented in Chapter 8.

1.3.2 The diffuse background spectrum (≥ 1 KeV)

The diffuse X-ray background intensity above 1 KeV has been found to be isotropic with respect to the galactic plane to within about 10% (see section 8.2) and this fact suggests an extragalactic origin. Many models have been offered to explain the existence of this radiation (see section 1.3.3), and these models must satisfy not only the constraint of isotropy, but also the observed spectral characteristics of the radiation.

Early observations revealed that the diffuse background spectrum could be described by a power law with exponent $\lambda \sim 1$ (see equation 1.1).

However, more recent measurements point to the existence of a break in the spectral exponent in the energy interval between 10 and 100 KeV. The magnitude of the exponent change and the energy range over which it occurs are currently under discussion. Bleeker and Deerenberg (1970a) have tabulated some recent results concerning the exponent $\lambda + 1$ of the differential number spectrum $N(E)dE = N_0 E^{-(\lambda+1)} dE$, and table 1.3 contains these and in addition some others.

Table 1.3: Diffuse background spectra

Experiment	Energy Range (KeV)	Spectral Index ($\lambda + 1$)
Seward et al. (1967)	4-40	1.6
Matsuoka et al. (1968)	4-8	nearly flat
Boldt et al. (1968)	2-20	1.3 ± 0.1
		+0.07
Boldt et al. (1969)	2-20	1.35 ± 0.10
Gorenstein et al. (1968)	1-13	1.7 ± 0.2
Henry et al. (1968)	1.5-8	1.4 ± 0.1
Ducros et al. (1969)	2.5-12	1.34 and 1.29
Bleeker et al. (1968)	20-180	2.40 ± 0.20
Bleeker et al. (1970a)	20-220	2.45 ± 0.10
		+1.7
Hudson et al (1966)	20-70	2.7
		-0.6
Kasturi Rangan et al. (1969)	20-130	2.4 ± 0.4
Rothenflug et al. (1965)	20-50	2.6 ± 0.5
Rothenflug et al. (1968)	15-100	2.43 ± 0.05
Rocchia et al. (1967)	20-1000	2.5 ± 0.2
Cunningham et al. (1970)	2.6-19	1.86

The exponent thus has an average value of ~ 1.5 below ~ 20 KeV and ~ 2.5 above 20 KeV. However, exact values for the exponents and for the break energy are difficult to ascertain. Boldt et al. (1969) suggest a change in spectral index of about unity between 20 and 80 KeV. Gorenstein et al. (1968) believe that a single power law exponent of ~ 1.7 is applicable up to 60 KeV, above which there is a change of about one half power.

Bleeker and Deerenberg (1970a) maintain that a sharp break lies between 10 and 20 KeV from a comparison of their balloon results between 20 and 220 KeV with rocket results for $E < 10$ KeV. Wilson (1968) maintains that a sudden change of index can have little physical significance and favours a gradual variation of exponent from ~ 1.6 to ~ 2.4 over the 10 to 100 KeV energy interval.

The characteristics of the spectral index change are presently of high observational priority since they impose strong constraints on any diffuse background source model.

1.3.3 Theoretical Models

There are basically two types of theoretical model which have been constructed to satisfy the spatial and spectral characteristics of the diffuse background at the energies being considered here. One, first suggested by Gould and Burbidge (1963) considers the background flux to result from the superposition of distant, usually cosmologically-evolving, X-ray-emitting galaxies, while the other (Felten and Morrison 1963, 1966) proposes that the X-radiation is produced in metagalactic space by the inverse Compton interaction of cosmic ray electrons and low energy photons. A number of variations exist upon these two basic model categories.

Gould and Burbidge (1963) first suggested that the superposition of unresolved normal galaxies, each of which emits X-rays at an intensity comparable to our own galaxy, may explain the diffuse background. However, the predicted background intensity falls about two orders of magnitude below that observed.

Silk (1968) brought cosmological factors into consideration and assumed that the X-ray intensity of normal galaxies evolves with time in a manner analogous to radio emission as indicated by radio source counts. In this way he was able to obtain good agreement with observation if galactic sources such as Sco XR-1 and Tau XR-1 were typically present in other galaxies. However, his assumptions concerning normal galaxy evolution have no observational basis.

Compton scattering in radio galaxies of 3° K. blackbody photons by the radio-emitting electrons was suggested as a source mechanism independently by Bergamini et al. (1967) and Brecher and Morrison (1967). An attempt was made to account for the cosmological evolution of both the radio sources and the 3° K. primordial radiation, and it was found that the X-ray background intensity could be explained if such galaxies were located at red-shifts $z \sim 5$. More detailed developments of this model have appeared by Rees and Setti (1968) and Felten and Rees (1969). However, its weakness lies in the fact that the assumptions with regard to radio-galaxy evolution are based on data whose interpretation still contains ambiguities (Brecher and Burbidge 1970). Also the observed X-ray spectral break is not easily explained.

Another Compton scattering superposition model is that of Longair and Sunyaev (1969a) in which relativistic cosmic ray electrons and infra-red photons are involved. Both the electrons and the photons are assumed to be produced in the nuclei of galaxies which are weak radio emitters but very strong in the infra-red.

Examples may be Seyfert galaxies and radio-quiet quasi-stellar objects (Q.S.O's). The model can give rise to a break in the X-ray spectrum of a single object due to electron energy losses. However, superposition of such spectra, which may not all have identical intrinsic properties and which originate at many different red-shifts, would be expected to "smear out" the break in the observed spectrum. This objection is of course applicable to all superposition models.

The final significant superposition model is due independently to Apparao (1969) and Tucker (1970) who consider that the integrated effects of new-born pulsars in distant galaxies may account for the observed X-ray background. The assumption is made that pulsars emit X-rays far more copiously in their very early life as supernovae than at a later age, and by assuming a pulsar evolutionary model, taking NPO532 as a guide, it is possible to account for the observed background intensity. No spectral predictions are made. However, there is a lack of direct evidence in support of the assumption that new pulsars are powerful X-ray emitters. In addition the usual difficulties arise when one tries to account for the X-ray spectral break using a superposition of many such sources.

Felten and Morrison (1963, 1966) first investigated the possibility that Compton interactions (a) between galactic halo electrons and galactic starlight photons, and (b) between metagalactic cosmic ray electrons and 2.7° K. photons, might produce background X-rays. However, the expected intensity in each case was inadequate by at least 2 orders of magnitude. Brecher and Morrison (1969) re-examined the question of electron escape from normal galaxies and

assumed that the observed break in the local galactic electron spectrum and the inferred break in the radio spectra of normal galaxies (at about 3 GeV) was intrinsic to the electron source mechanisms in say supernovae, pulsars or galactic nuclei. Good agreement was then obtained with observation and also the 40 KeV X-ray break could be related to the proposed 3 GeV break in the intergalactic electron spectrum. However, the assumptions with regard to electron escape from normal galaxies and the intergalactic electron spectrum have no direct observational support.

Wilson (1968) has developed a variation of the Felten-Morrison model by using the work of Kellermann (1966) in which the spread of observed radio source spectral indices was explained by proposing the injection of relativistic electrons with a single power law exponent (~ 1.5) into radio source magnetic fields in series of bursts. Energy losses due to (a) ionization, independent of electron energy E_e , (b) adiabatic expansion and bremsstrahlung, proportional to E_e , and (c) synchrotron and Compton interactions, proportional to E_e^2 , result in a 3-component power law electron spectrum with exponents about 1.5, 2.5 and 3.5

These electrons escape into the metagalactic medium and upon interaction with the 3°K . radiation produce a 3-component X-ray spectrum with exponents about 1.7, 2.3 and 2.7 with increasing photon energy, the spectral breaks occurring between 10 and 100 KeV and at ~ 1.5 MeV.

The X-ray results appear to be consistent with this model. However, the prediction of the 1.5 MeV break appears inconsistent with the gamma-ray observations of Vette et al. (1970) which indicate a flattening, rather than a steepening of the spectrum above about 1 MeV. However, these results can be attributed to red-shifted ($z \sim 100$) π^0 decay photons (Stecker 1969 a,b) whose flux exceeds the predicted Compton flux at these energies and thus makes unobservable the 1.5 MeV Compton spectral break.

Silk and McCray (1969) are able to predict the observed X-ray spectrum between 10 KeV and 1 MeV by postulating non-thermal bremsstrahlung of sub-cosmic ray electrons, with energies $E_e \sim 1$ KeV to 10 MeV which at present are unobservable, with a low-density (10^{-7} cm^{-3}) thermal, ionized intergalactic plasma which itself has been heated by the electrons, in an expanding universe. Good agreement with observation is obtained but unfortunately the required sub-cosmic ray electron flux cannot be independently verified.

Hayakawa (1969b) and Boldt and Serlemitsos (1969a) have independently calculated that the inner bremsstrahlung of intergalactic suprathermal protons with ambient electrons is also able to produce an X-ray intensity comparable to that observed.

There is thus a wealth of theoretical models from which to choose, none of which is completely satisfactory. The superposition models encounter difficulties in reproducing the observed spectral break and also rely on speculation concerning the evolution of normal galaxies, radio galaxies and pulsars and concerning the properties of Seyfert galaxies and radio-quiet Q.S.O's.

The metagalactic models depend on assumptions with regard to largely unknown intergalactic particle fluxes, the intergalactic gas density and also on assumptions with respect to cosmological evolution.

It therefore seems that with so many theoretical alternatives, it is now up to the experimental astrophysicist to provide observations which will lead to the elimination of many of these models. This can be achieved by more precisely determining the directional properties of the X-ray background using instruments of finer angular resolution, in an effort to resolve the superposed contributions from discrete X-ray galaxies. Also necessary are measurements of improved spectral resolution to determine the exact quantitative nature of the spectral break in the 10 to 100 KeV region.

1.4 THE ADELAIDE BALLOON-BORNE EXPERIMENTS

The X-ray telescopes of the University of Adelaide payload consist of alkali halide scintillators which have been given directional properties with respect to the incident radiation, by appropriate shielding and collimation techniques (see chapter 2). In contrast to conventional astronomical observations however, severe atmospheric attenuation at X-ray wavelengths necessitates the operation of X-ray astronomy observatories above the bulk of the earth's atmosphere. Figure 1.1 illustrates this attenuation as a function of photon energy at different atmospheric depths. One optical depth for 30 KeV photons corresponds to an atmospheric pressure of 3 gm. cm.^{-2} and to an altitude of $\sim 40 \text{ km}$ or 130,000 feet.

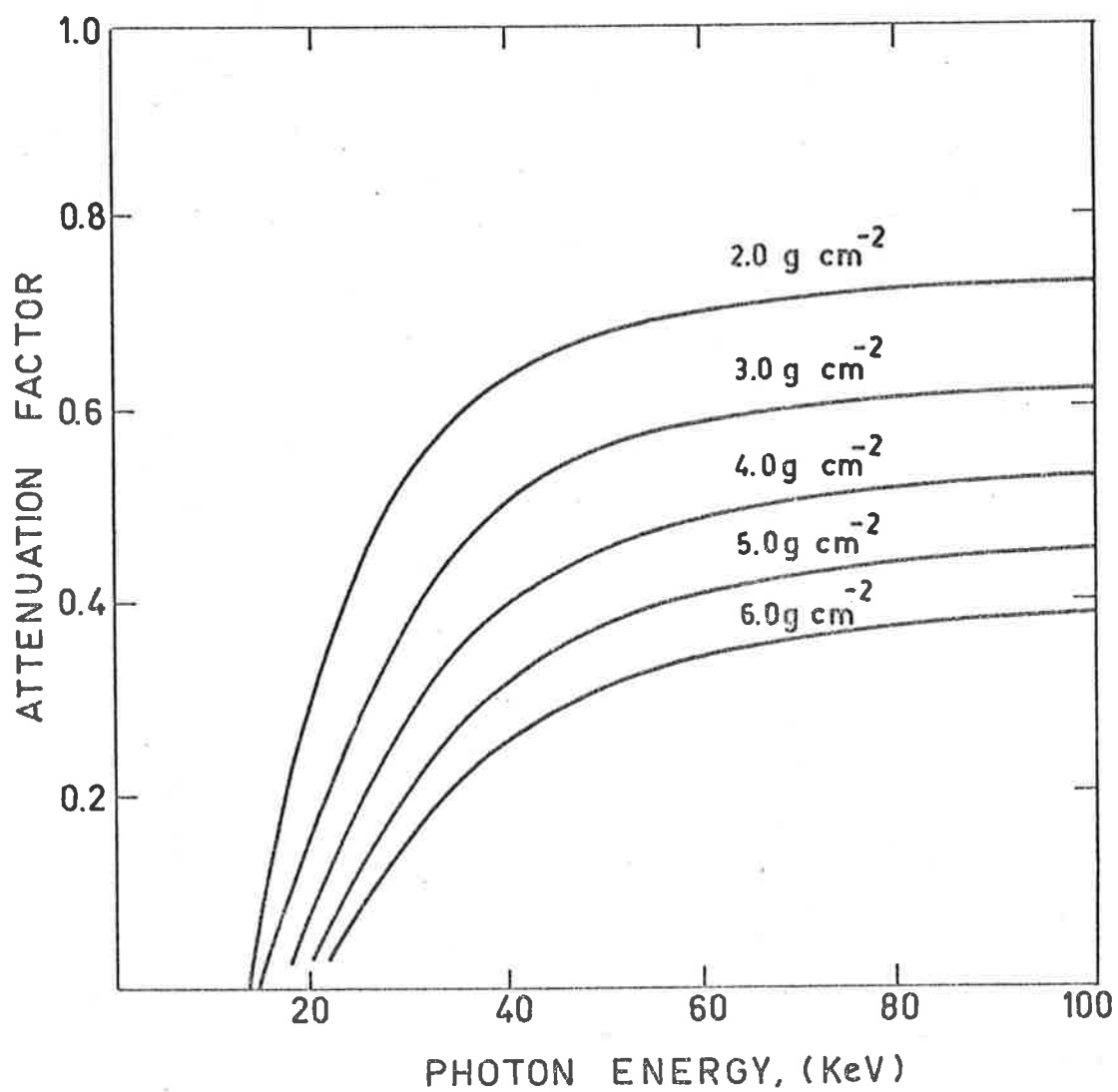


Fig: 1.1 Atmospheric attenuation of Xradiation as a function of energy for different atmospheric depths.

This altitude is accessible to large modern balloons carrying typical X-ray astronomy payloads of ~ 300 kg. weight, and is sufficient to permit useful work down to photon energies of ~ 15 KeV. At energies lower than ~ 15 KeV, observations are best made using rockets or satellites, since for example, at 3 KeV, unit optical depth is $0.005 \text{ gm. cm.}^{-2}$. The usefulness of rockets declines at higher energies due to the loss of counting statistics resulting from the short observing time available (~ 5 minutes) and the decrease in intensity of cosmic X-ray spectra with increasing energy. Longer observing times (~ 5 hours) are possible using balloons and statistically significant results can consequently be obtained up to energies of ~ 200 KeV in spite of the increased attenuation of the primary X-radiation and the increased cosmic ray induced background originating in the residual atmosphere. Of course, the ideal observing vehicles are satellites (and eventually the Moon) which are capable of combining all the good features of balloons and rockets without their disadvantages. To date, only relatively small X-ray telescopes have been flown on spacecraft, and the area-time products for their exposure to any region of the sky have been only comparable, and often less, than that attained with pointed balloon-borne observatories. The planned launching of several satellites in 1970-74 should alter this situation. Meanwhile, balloon-borne observatories provide the best means of making high energy cosmic X-ray observations.

Balloon experiments flown from Southern Hemisphere locations, for example Australia, are especially valuable. This is a consequence of the southern location of the galactic centre region and the adjacent galactic longitudes l^{II} between $\sim 300^\circ$ and 10° , in which many discrete X-ray sources with hard spectra are to be found (Buselli et al. 1968, Thomas 1968, Lewin et al. 1968a, 1969, Riegler et al. 1968). The two most spectacular X-ray variables observed, Cen X-2 and Cen X-4 (see section 1.1.3), as well as the Magellanic Clouds, have southern locations also. In fact, reference to table 1.1 (section 1.1.1) shows that 19 of the 29 listed confirmed sources have southern celestial declinations.

In the University of Adelaide experiments, two altazimuth mounted X-ray telescopes were usually employed. These were an actively collimated and shielded telescope (the "active telescope") and a graded shield, passive collimator telescope (the "graded shield (GS) telescope"), which will be described in chapter 2. Details of flights launched from Mildura, Victoria (except where indicated) are listed in tables 1.4 (a) and (b). Both telescopes were flown on the flights MIL-1-68, MIL-2-68, MIL-1-69 and MIL-2-69, while for the other flights only the active telescope, pointing vertically, was employed upon a payload of reduced weight. The bulk of the X-ray results presented in this thesis were obtained from the active telescope.

Table 1.4 (a) Flight details, University of Adelaide

Flight Designation	Launch Date and Time U.T.*	Float (U.T.)	Cutdown (U.T.)	Altitude gm. cm ⁻²	Active telescope Pulse Height Analyser	
					Ch#o bounds (KeV)	Channel increments (KeV)
MIL-1-68	1968, Feb 28 18 ^h 36 ^m	21 ^h 31 ^m	01 ^h 32 ^m	2.7	7.0,17.0	10.0
MIL-2-68	1968, Nov 26 18 ^h 01 ^m	Not Reached	20 ^h 19 ^m	Premature Cut-down		
** MIL-1-69	1969, April 26 14 ^h 28 ^m	16 ^h 55 ^m	20 ^h 31 ^m	3.2-3.7	12.7,22.7	10.0
** MIL-2-69	1969, May 1 21 ^h 42 ^m	00 ^h 06 ^m	07 ^h 16 ^m	3.2-3.8	12.7,22.7	10.0
MIL-3-69	1969, Aug 25 03 ^h 09 ^m	05 ^h 30 ^m	08 ^h 18 ^m	4.5	10.8,19.7	9.7
MIL-1-70	1970, Mar 25	Abortive Flight				

* To obtain Eastern Australian Standard Time (EAST), add 10^h00^m
To Universal time.

**launched from Waikerie, South Australia.

Table 1.1 (b) Flight Environmental Conditions (from ESSA reports)

Flight	3 hourly Kp indices	Solar flares \geq importance 1
MIL-1-68	5-,50,50,5-	Nil
MIL-2-68	2 ⁻	In (1754 to 1810 hrs.)
MIL-1-69	10,20,20	Nil
MIL-2-69	20,2 ⁻ ,3 ⁻ ,20	Nil
MIL-3-69	1+,0+	Nil

CHAPTER 2INSTRUMENTATION2.1 INTRODUCTION

In this chapter a description of the experiment payload will be given with the bias towards engineering aspects. The physical principles involved in the X-ray telescopes will be discussed more fully in chapter 3, and those involved in the use of the magnetometers, in chapter 4.

It will be commented now that the Adelaide observatory is a moderately complex instrument, whose correct operation depended greatly on a number of subsystems which required a great deal of technical development. Since these subsystems were crucial to the successful performance of the flight objectives, and since they also exercised a control on the type of data that could be obtained, they will be reviewed now in conceptual detail.

2.2 THE BALLOON PAYLOAD

The flights MIL-1-68, MIL-2-68, MIL-1-69 and MIL-2-69 (see table 1.4) used almost identical payloads which comprised the two X-ray telescopes briefly mentioned in section 1.4. The payload was attached to balloon rigging lines through a central vertical shaft which was driven in either direction on command by an electric motor. The moment of inertia of the balloon resulted in the payload being rotated in azimuth. Care was taken to minimize torsional oscillations by using spreaded ribbon suspension. A pair of horizontal, orthogonal flux-gate magnetometers provided a measurement of the telescope azimuth with respect to the horizontal intensity component of the local geomagnetic field.

The zenith angle of the active telescope was fixed at 32° for MIL-1-68 but could be varied by ground command in subsequent flights. Its value was measured using a vertical plumbob and a shaft encoder. The zenith angle of the graded shield telescope was fixed before each flight and was not variable.

Separate electronics packages were carried containing the active telescope 16 channel pulse height analyser (P.H.A.), and the G.S. telescope P.H.A. The Data Storage Unit (D.S.U.) contained mainly binary registers for the accumulation of energy channel counts, while the Data Transmission Unit (D.T.U.) contained the telemetry circuitry which converted the physical data into a bit rate and then a mixed audio signal which was used to modulate two one watt FM transmitters having carriers of slightly different frequency near 70 MHz. A block diagram of the total system's essentials is shown in figure 2.1.

To the active telescope was attached the in-flight energy calibrator which moved an X-ray line-emitting isotope (Gd^{153} or Am^{241}) into the field of view for about one minute in seventeen in order to check on the stability of the detector energy calibration.

Control equipment of the Australian Department of Supply balloon launch facility was included in the payload which was wrapped in a 10 cm. thick poly-urethane-foam thermal shield (~ 5 cm. thick over telescope fields of view) which ensured temperature stability to within about $5^{\circ}C$. for the duration of a flight. Protective "crush-pad" was tied to the bottom and sides of the payload to minimize the shock suffered by the payload upon landing.

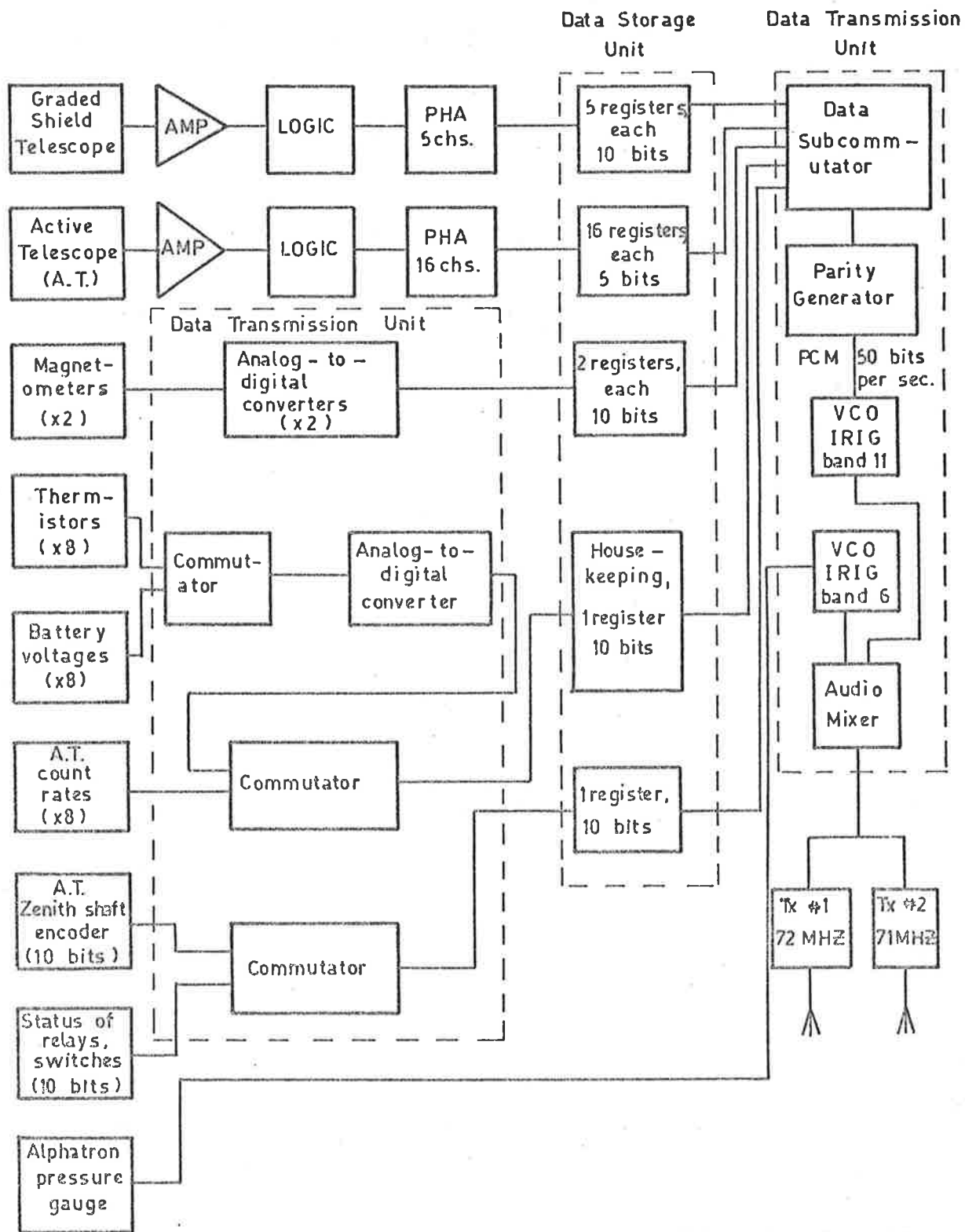


Fig: 2.1 Total system block diagram of the University of Adelaide balloon-borne X-ray astronomy experiment.

The complete payload weighed about 300 kg. and float altitudes of the order of 40 km. (residual air pressure 3 to 4 gm. cm.⁻²) were typically attained. The experiment floated at ceiling altitude for between 3 and 8 hours, depending on the wind vector and Department of Civil Aviation air space regulations.

The flights MIL-3-69 and MIL-1-70 differed from the 4 previous flights in that only the active telescope was flown, pointing vertically upwards and making the use of magnetometers unnecessary. The decrease in payload weight was considerable and allowed the use of smaller balloons.

2.3 THE X-RAY DETECTORS

Since the active telescope provided the bulk of the data used in this thesis, it will be described more fully than the graded shield telescopes. However, I shall describe the latter first.

2.3.1 The Graded Shield Telescope

The graded shield telescope is shown diagrammatically in fig.2.2 and is basically similar to the pioneering design of Boldt et al.(1966). It consists of a graded shield well of lead on the outside, then a silver-tin alloy whose major constituent is silver, and innermost a cylindrical sheet of conetic shielding which is a cobalt-nickel alloy and which also provides magnetic shielding for a photomultiplier tube. The graded shield makes use of the X-ray edges of the materials involved to progressively degrade high energy photons to energies below the lower boundary of the energy range being analysed.

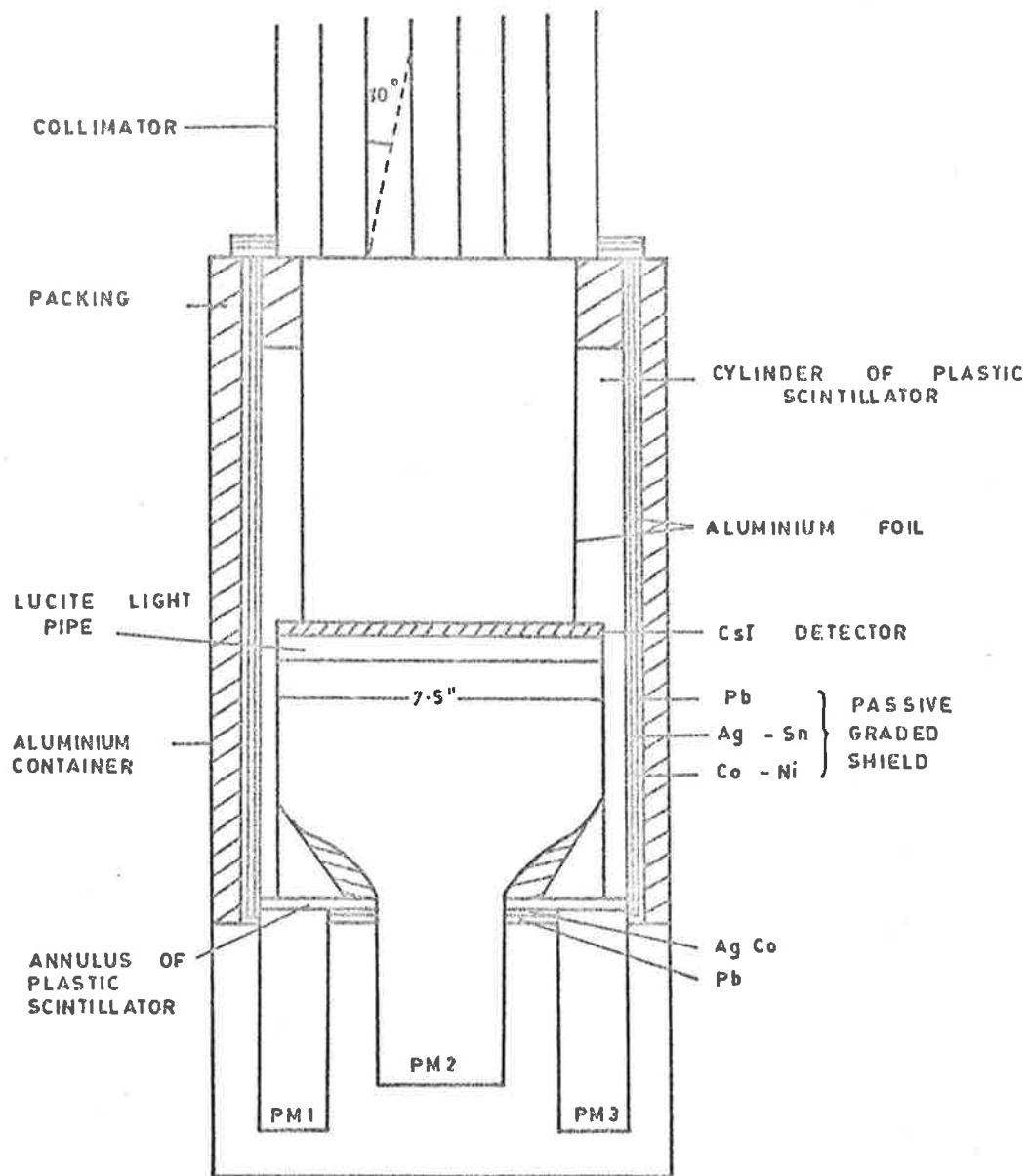


Fig: 2.2 The Graded Shield Telescope

In this way incident high energy photons are excluded from the detector except when coming from a large forward-looking solid angle defined by the crystal-shield geometry.

The viewing angle can be further reduced by placing a passive copper collimator at the open end of the telescope. Inside the outer passive graded shield is an inner anticoincidence shield of polytoluene scintillator which is viewed by 4 photomultipliers and which minimizes the charged particle contribution to the main detector counting rate.

The central detector is a 19 cm. diameter, 3 mm. thick CsI(Tl) crystal of sensitive area 220 cm^2 and is viewed through a lucite light pipe (to improve uniformity of light collection) by a single 22 cm. diameter photomultiplier (PM) tube. Light pulses from this crystal which satisfy the anticoincidence requirement are pulse height analysed (4 channels from 30 to 80 KeV for MIL-1-68, 5 channels from 30 to 125 KeV for later flights) and the resulting spectrum, together with the guard count rate, telemetered to ground every 4 seconds. The zenith angle of the graded shield telescope is not variable and is fixed before a flight at a value in accord with the observing plan of the experiment.

2.3.2 The Active Telescope

The active telescope is shown diagrammatically in fig. 2.3 and is similar in principle to the design of Petersen et al. (1967). It comprises a 2 mm. thick NaI(Tl) scintillating crystal viewed by three RCA6199 photomultipliers in parallel and shielded by at least 16 mean free paths (at 100 KeV.) of scintillator in all directions other than those within a conical viewing angle of 3.9° FWHM (full width at half-maximum response).

UAX-001

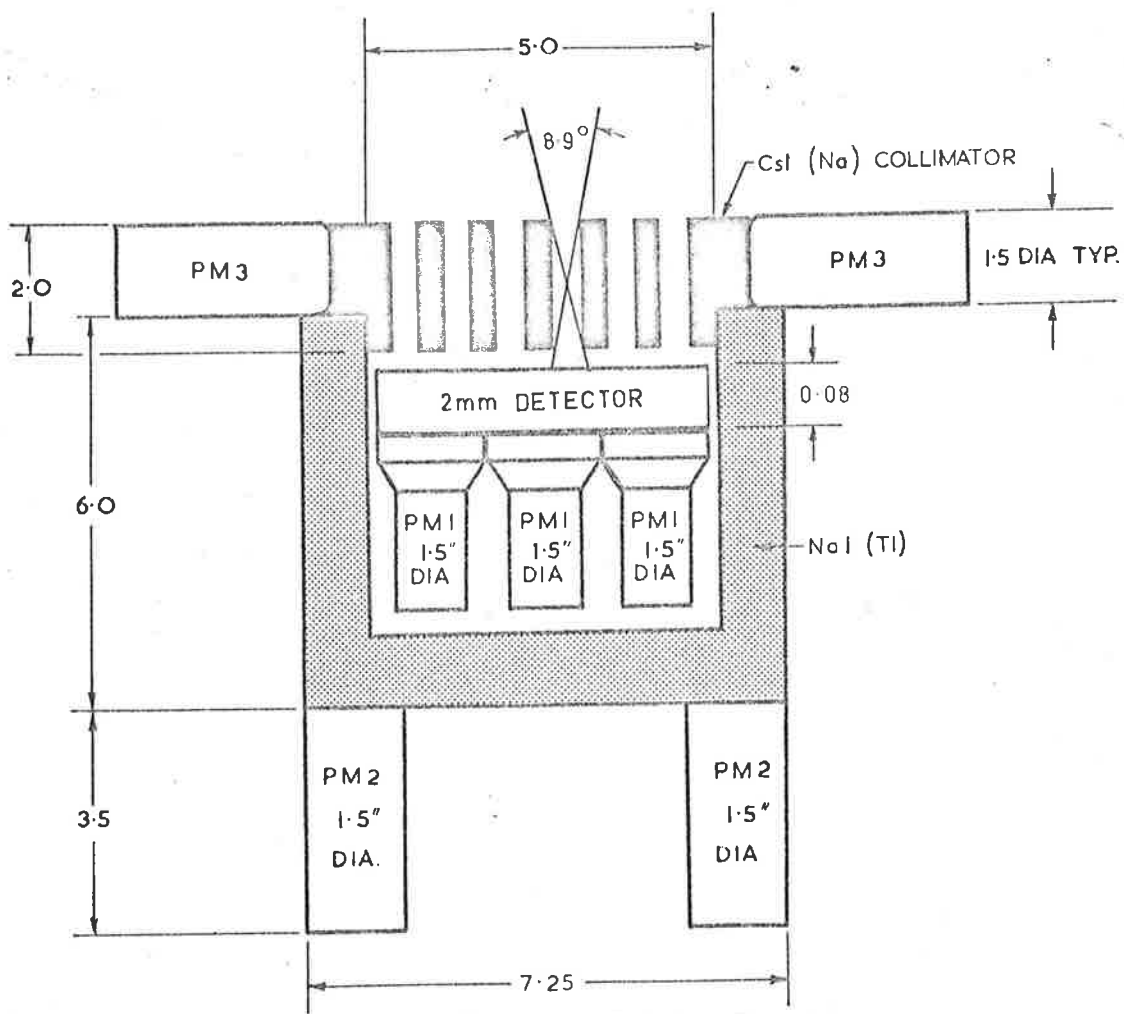


Fig: 2.3 The Active Telescope

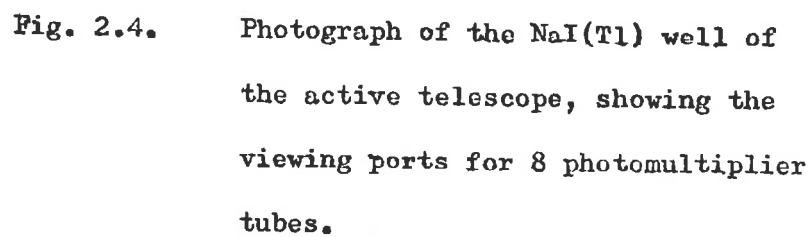
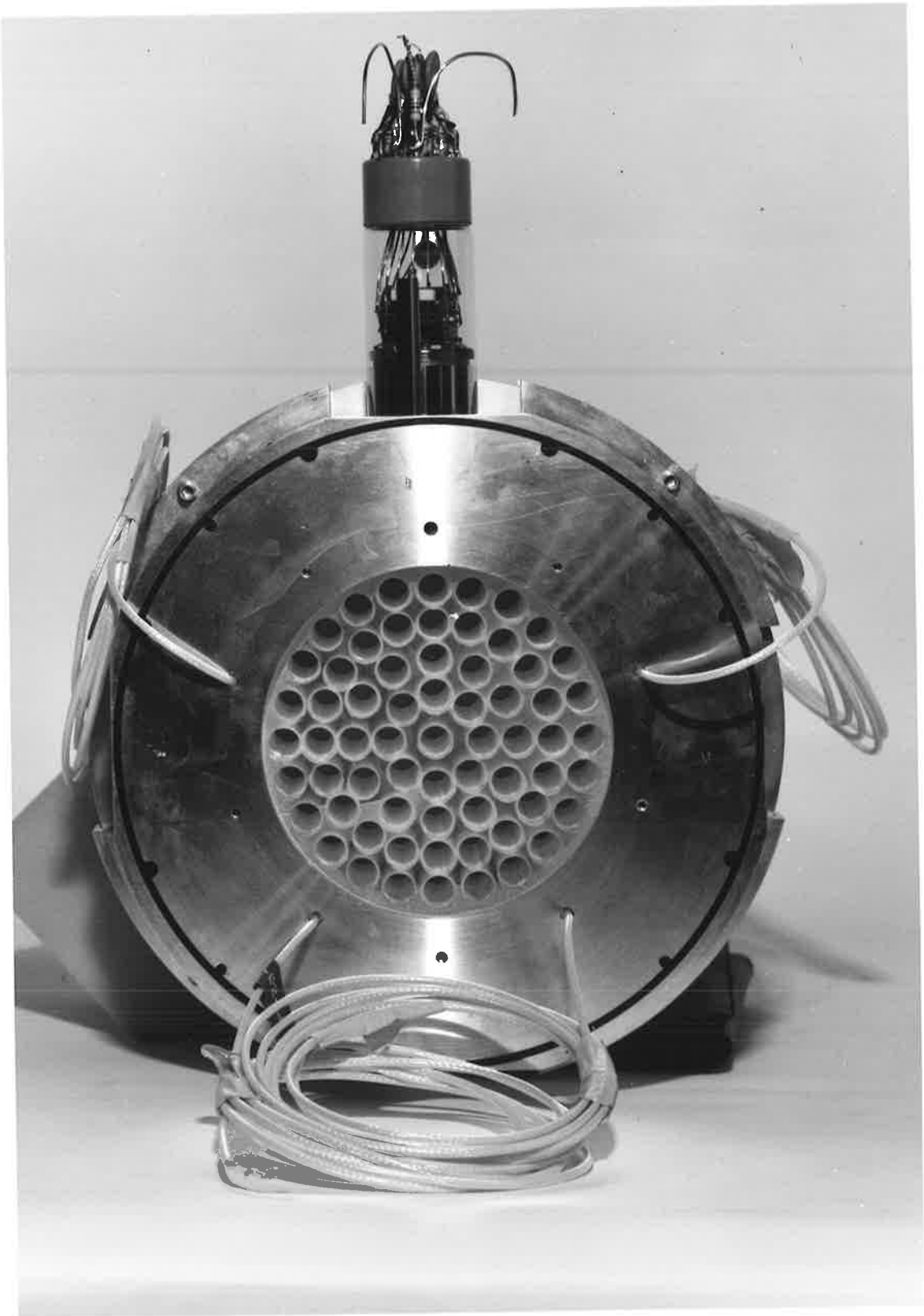


Fig. 2.4. Photograph of the NaI(Tl) well of the active telescope, showing the viewing ports for 8 photomultiplier tubes.



Fig. 2.5. Photograph of the CsI(Na) collimator
of the active telescope, together
with one of four photomultiplier tubes.



This shielding is achieved by placing the central detecting crystal within a cylindrical "well" scintillator made of 2.5 cm. thick NaI(Tl) (see fig. 2.4) and viewed by eight RCA6199 photomultiplier tubes.

Collimation is achieved by a 5.9 cm. thick crystal of CsI(Na) scintillator through which are drilled, parallel to the telescope axis, 65 holes of 1 cm. diameter (see fig. 2.5). This scintillator is viewed by 4 photomultipliers, once again RCA6199's. The sensitive area of the detector is 54.3 cm^2 and the geometry factor for an isotropic flux is $1.36 \text{ cm}^2 \text{ sterad}$.

This telescope differs from the graded shield telescope in that its shielding and collimation are achieved entirely by active means, thereby reducing the effects of radiation which scatters from the guard and collimator materials into the central detector and produces unwanted background.

The major practical problem confronting experimentalists in this field is that of suppressing detector backgrounds to a level which will allow point sources to become evident. Components of the background counting rate are (a) an inherent cosmic ray induced background or guard leakage background caused by interactions of charged cosmic rays and high energy photons with the telescope's collimator, guard and general surroundings, producing daughter products which then escape detection by the guard system, (b) diffuse atmospheric X-radiation entering through the telescope aperture, which is secondary radiation originating from cosmic ray interactions with the overlying atmosphere, and (c) a diffuse X-ray background of cosmic origin which enters the telescope aperture after attenuation by the overlying atmosphere.

These components will be discussed more fully in chapters 6 and 7. Here I will just point out that whereas components (b) and (c) will contribute according to the solid angle of the telescope concerned, irrespective of its structural configuration, component (a) is very much determined by the methods of collimation and shielding used.

Component (a) contributes significantly less to the background rate of an actively collimated detector, since any energetic daughter products of high energy cosmic ray interactions within the collimator material will generate an anticoincidence signal to prevent the pulse height analysis of any secondary radiation which might reach the central crystal. No such safeguard exists for a passively collimated telescope, although the presence of the plastic scintillator as part of the graded shield guard provides protection against such phenomena in the well guard. The background rate of the active telescope at float altitude is estimated to be about 10^{-2} that of an unshielded 2 mm. crystal (Peterson et al. 1967).

2.4 THE PHOSWICH SYSTEM

The phoswich system is designed to minimize the spurious response of the active telescope which originates from Compton interactions in the central detector or in the light pipe which provides the optical coupling between the central crystal and the PM tubes. Good optical coupling is necessary to ensure uniform light collection over the face of the crystal and hence linearity of detector response with photon energy. A lucite light pipe is generally employed. However, Compton recoils which occur either in the crystal of lucite and which simultaneously deposit a recoil electron in the lucite and a scattered photon in the crystal, will contribute to the spurious counting rate.

In order to eliminate this source of background it was decided to replace the lucite light pipe with polytoluene plastic scintillator in which Compton recoil electrons would be detected. Both the NaI(Tl) and the plastic are viewed by the same PM tubes. However, since the light decay times for polytoluene and NaI(Tl) are 10nsec. and 250nsec. respectively pulse shape sensitive circuits can discriminate between the pulses from each scintillator. The plastic pulses due to the Compton recoil electrons are then used in anticoincidence with the NaI(Tl) pulses to reject central crystal events associated with the Compton electrons.

Figures 2.6 (a) and (b) illustrate schematically the operational details of the phoswich. The input signal to the PHA is taken from the PM tube anode which is held at a potential of +1000 volts. An identical signal, but of smaller amplitude and inverted, is taken from the PM tube 10th dynode and is used separately to generate the phoswich anticoincidence signal. Pulse shape discrimination is achieved by means of a delay line clipping cable comprising $2\frac{1}{2}$ metres (delay ~ 10 nS) of RG-58U coaxial cable of characteristic impedance 50Ω and terminated with a resistance of 5Ω .

This choice of clipping cable parameters has been found to be optimal for effective pulse shape discrimination which is achieved by means of the reflection, with inverted polarity, of any signal appearing at the open end of the cable. The plastic pulses of very short duration decay to zero before the return of the reflection from the 5Ω termination which adds a large negative backswing to the original positive pulse.

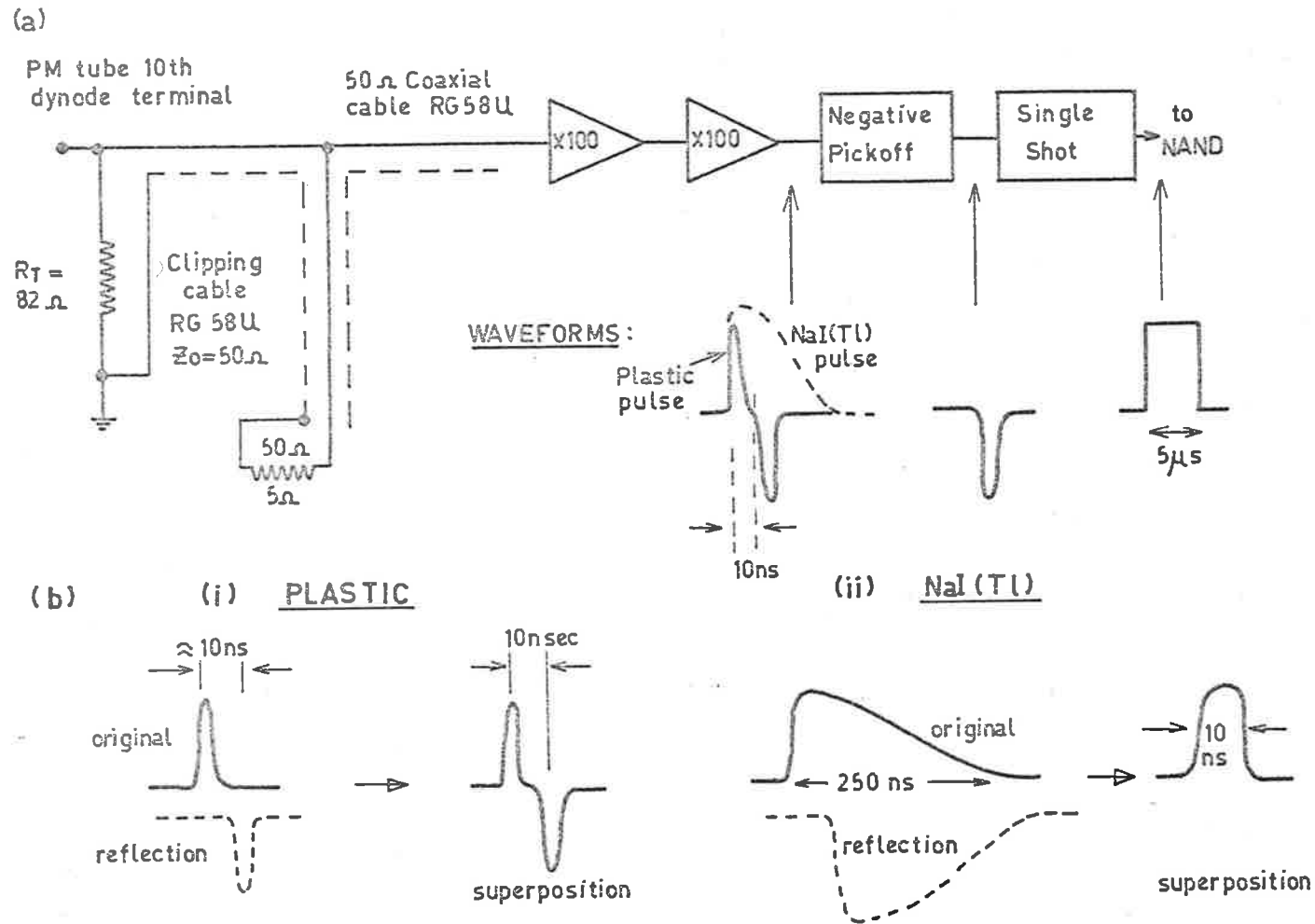


Fig: 2.6 (a) Generation of the phoswich anticoincidence signal.

(b) Effect of delay line clipping cable on (i) plastic pulses and (ii) NaI(Tl) pulses.

However, a NaI(Tl) pulse of longer decay time is still very nearly at its maximum amplitude as the reflection returns. Superposition of the opposite polarity original and reflected components results in abrupt cancellation of the pulse with very little negative backswing. Circuitry designed to recognise a negative backswing numerically greater than a preset discrimination value is then employed to "pick off" each plastic pulse. "Picked off" pulses activate a single shot multivibrator, thereby generating the phoswich input signal to the anticoincidence gate.

The effectiveness of the phoswich and the other guard rates with regard to background rejection is discussed with quantitative results in chapter 3.

2.5. PULSE HEIGHT ANALYSIS

The active telescope 16 channel pulse height analyser is shown schematically in fig. 2.7. Pulses from the central crystal are first amplified by a charge-sensitive preamplifier in order to minimize the pulse attenuation caused by coaxial cable capacitance. A standard voltage amplifier then follows. The output of the voltage amplifier then goes to two parallel sections of the system, the height-to-time converter, and the anticoincidence circuitry.

2.5.1 Anticoincidence logic

Two discriminators are used to define the upper and lower levels of the energy range to be analysed. A pulse whose height exceeds either reference level triggers the respective single-shot multivibrator. The resulting outputs are both "ones" (+5 volts) only for a pulse whose height is within the analysis range.

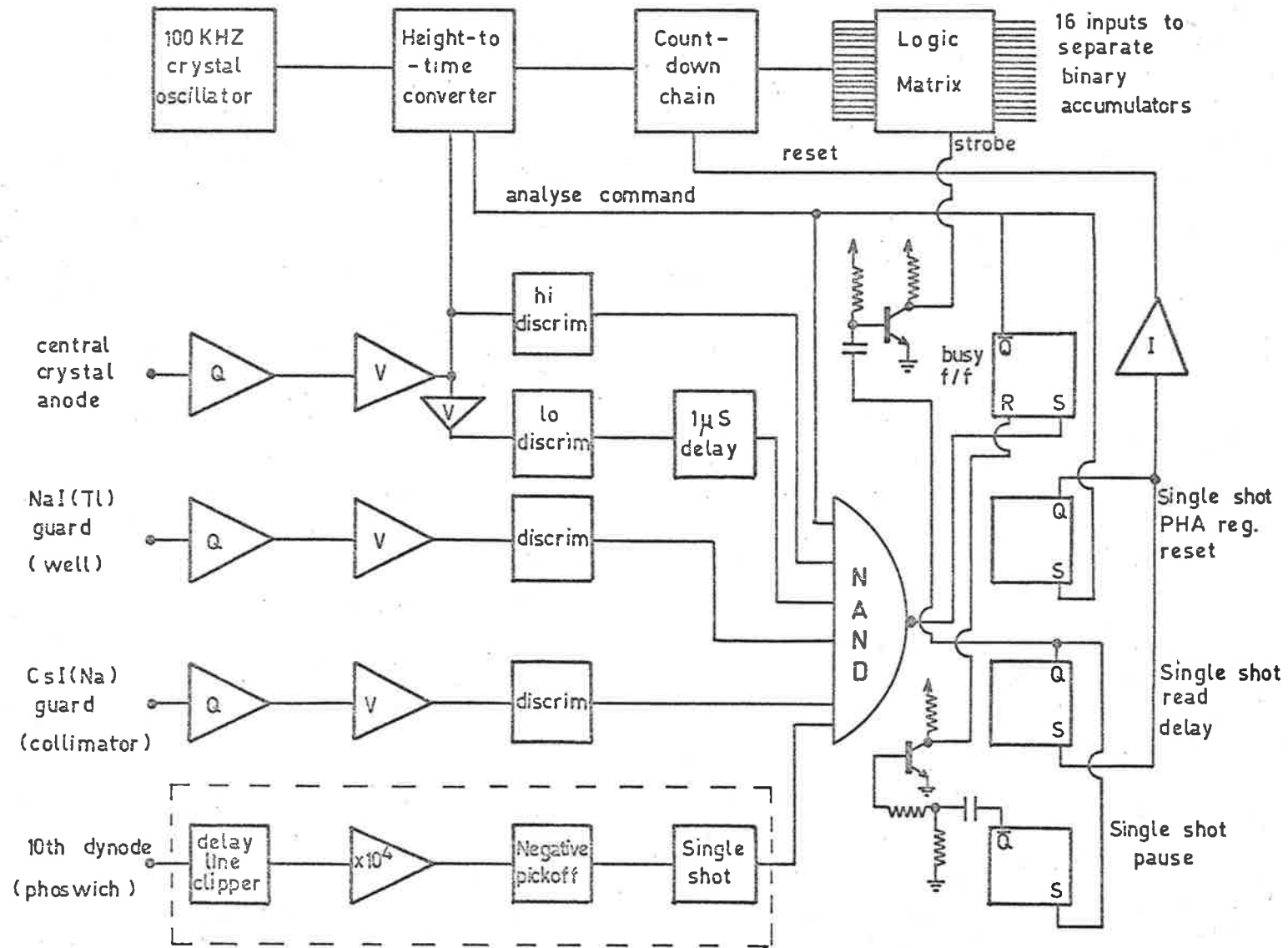


Fig: 2.7 Block schematic of the active telescope 16-channel pulse height analyser.

Three other discriminator signals at the NAND gate input come from the collimator, well and phoswich scintillators respectively and are "ones" in the quiescent or non-vetoing state. Should a veto pulse arrive, the appropriate input drops to "zero" level to indicate its presence. All discriminator pulse lengths are $5\mu\text{sec}$. The remaining NAND input is from a single-shot which indicates whether the circuitry is "busy" analysing a previous input pulse. It is a "one" in the quiescent state and zero during the busy state.

The NAND gate into which all these signals are fed obeys the logic that its output will be a "zero" if all inputs are "ones" and will be a "one" if at least one input is a "one". Consequently the NAND output will be quiescent, in the "one" state, except for a central detector pulse which satisfies the anticoincidence requirements, i.e. a pulse whose amplitude falls within the desired energy range, which is not coincident with any event in either the collimator, well or light pipe, and which does not arrive during the analysis of the previous pulse.

Such a pulse is indicated at the NAND output by a zero and this signals the pulse height analyser to begin analysing.

2.5.2 Height-to-time Converter

This crucial unit of the PHA digitizes pulse heights, thereby facilitating their measurement and sorting into channels. A block diagram appears in fig. 2.8.

All central detector pulses appear at the input but only those satisfying all anticoincidence criteria pass beyond the linear AND gate. This is opened when the NAND output signals a valid event, fires a single-shot and generates a $2\mu\text{sec}$. strobe signal.

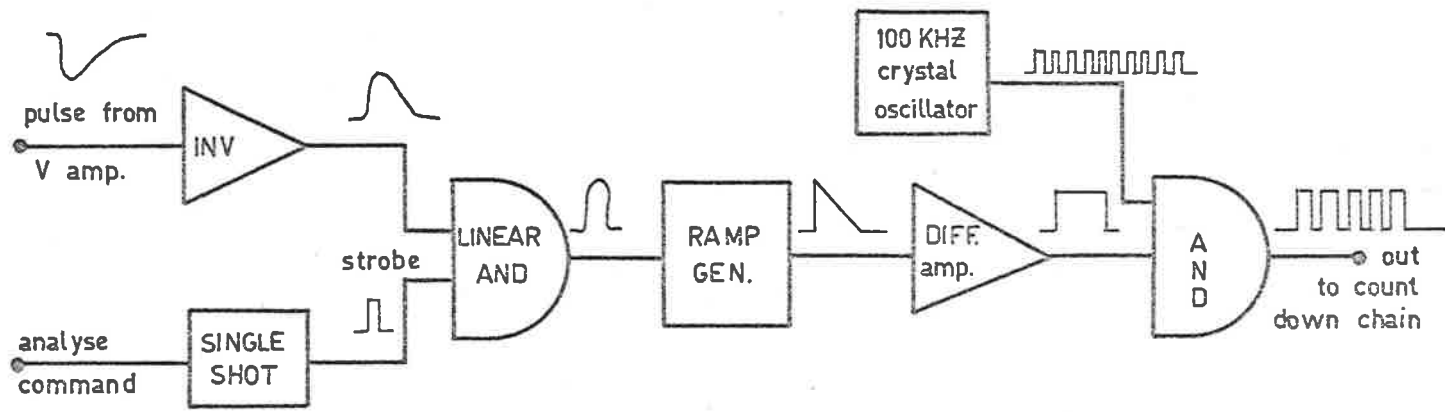


Fig: 2.8 Block schematic of the height-to-time converter of the 16-channel pulse height analyser.

Strobed pulses pass on to the ramp generator, in which a mica capacitor (C farad) is charged to the pulse height (V volts) and is immediately allowed to discharge through a constant current (i_c amp) circuit. In this way a linear voltage ramp is generated, of duration Δt seconds, where $\Delta t = CV/i_c$. The discharge rate is about 3 volts per millisecond and linearity with the original pulse height is conserved for pulses not exceeding ~ 7 volts in amplitude. Temperature stability has been established to within 6% over the range -20°C . to $+50^\circ\text{C}$. by use of a thermistor bias control in the constant current discharge circuit.

A difference amplifier detects the instant at which the ramp voltage reaches earth potential and produces a rectangular output pulse, also of duration Δt seconds. This signal is used to gate the output from a 100KHZ crystal oscillator to produce a pulse train containing $10^5 \cdot \Delta t$ pulses ($\ll V$). The pulse train is scaled down by a factor of 16 such that for the energy range analysed, the number ($\ll V$) of output pulses lies between 1 and 16 inclusive, corresponding to the 16 energy channels. The use of a high frequency pulse train, followed by a scaler, minimizes any error introduced into the energy calibration as a result of the digitization operation.

Logic operations then follow which recognize the number of output pulses and generate a pulse which is assigned to a 5 bit binary register in the DSU corresponding to the appropriate energy channel. The contents of each energy channel are accumulated for 4 seconds before being read out into the telemetry stream and the register reset. The channel reading operation is described more fully in section 2.10.

A more complete description of the pulse height analyser and of the laboratory performance tests on the active telescope system are to be found elsewhere (Clancy 1971).

2.6 IN-FLIGHT ENERGY CALIBRATION

In order to verify the stability of the active telescope energy calibration under the peculiar environmental conditions pertaining to a balloon flight, it was necessary to use a system of in-flight energy calibration. This was accomplished by driving a gamma source into the telescope field of view for 64 seconds every 1024 seconds. The timing signals to achieve this were derived from the countdown chain of the 100 KHz crystal oscillator located in the DTU.

For MIL-1-68 the source used was Gd.¹⁵³ (see table 3.3) which has a peak at 41 KeV and two peaks of almost equal intensity at 97 and 103 KeV. which in view of the detector's energy resolution could be regarded as a single line at 100 KeV. This source provided two calibration points thereby allowing a check on the system linearity also. However, its short half-life of 236 days rendered it ineffective within about a year. Consequently, for flights MIL-1-69 etc., an Am²⁴¹ source was used, with a line energy of 60 KeV and a half-life of 460 years.

Analysis of in-flight calibration data verified that no significant energy calibration changes occurred on any flight of the payload.

2.7 THE MAGNETOMETERS

The azimuthal orientation of the payload is measured by a pair of nominally orthogonal and horizontal flux-gate magnetometers, each of which measures the geomagnetic field component in the axial direction of the sensor.

2.7.1 The Sensors

Each sensor consists of a high permeability magnetic core which is driven into saturation by an alternating magnetic field generated in a surrounding coil by a 5 KHz excitation current. Even harmonics are generated whose amplitude (Δ) is proportional to the directed ambient field component (H_{11}) parallel to the core axis. This amplitude is then translated into a DC level (V) proportional to Δ and hence to H_{11} . V may be either positive or negative according to the direction of H_{11} . However, the final output DC level (V_o) is always positive and equal to $V + V_B$ where V_B is a positive bias voltage. Hence

$$V_o = V_B + \text{constant} \cdot H_{11} \quad \dots\dots\dots 2.1a$$

The geomagnetic field is of sufficient intensity to induce a magnetization field which is a significant fraction of the total saturation of the high permeability core, and is measurable with ease. The instruments employed were manufactured by the Schonstedt Instrument Co. (Heliflux Magnetic Aspect Sensor, type RAM-3).

2.7.2 Digitization and read-out

Figure 2.9 shows the azimuth measuring system schematically. The two Schonstedt units are supplied by a stabilized 6.3 volt DC supply and the analogue outputs are sampled for 800 mS at intervals of 4 seconds. The two sampled DC levels are then digitized by analogue-to-digital (A-D) converters and the resulting pulse trains are counted by two 10-bit registers which are cleared and read out into the telemetry format (see section 2.10) every 4 seconds. The system characteristics are calibrated during flight by replacing the magnetometer analogue signals with a stabilized reference voltage $\sim V_B$ at the same time as the in-flight energy calibration is performed (see section 2.6)

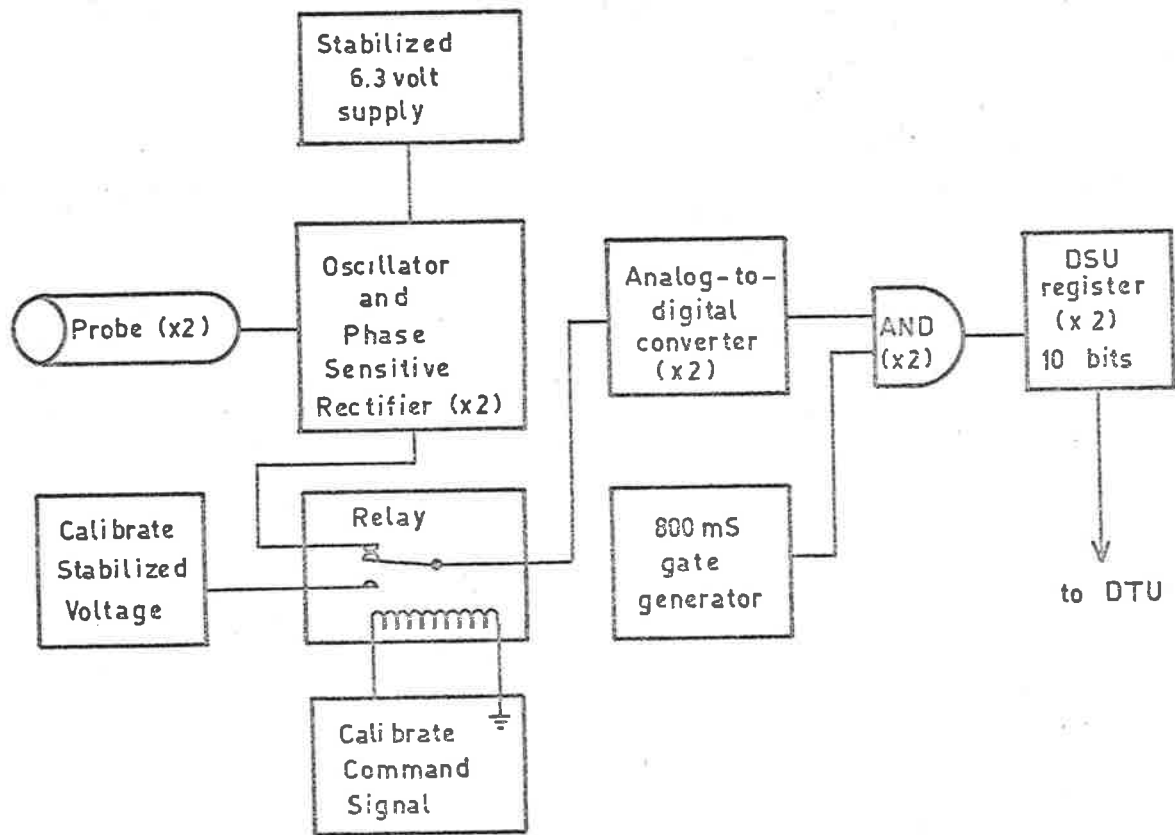


Fig: 2.9 The magnetometers and the azimuth measuring system.

The knowledge is essential of the time relationship of the magnetometer sample intervals and read-out times to the accumulation intervals and read-out times of individual energy channels in order to determine channel count rate profiles as a function of azimuth. These time relationships are shown diagrammatically in fig. 2.10. The mean azimuth during a data acquisition period must be separately calculated for each channel by assuming a linear azimuth variation with time and interpolating between consecutive azimuth angle read-outs.

2.7.3 The Response of the Magnetometers

The idealized response $M_i(\phi)$ of the i^{th} horizontally oriented magnetometer as a function of true azimuth ϕ is sinusoidal, thus:

$$M_i(\phi) = M_{i,0} + \frac{H}{K_i} \cos(\phi + \phi_{i,0} - D); \quad i = 1, 2 \quad \text{---} \quad 2.1$$

$M_{i,0}$ is the sinusoid mean value which is related to the DC bias V_B in the analogue output (see equation 2.1a), H is the geomagnetic horizontal intensity component, K_i is the magnetometer sensitivity, $\phi_{i,0}$ is the azimuthal displacement of the sensor axis from the telescope axis and D is the geomagnetic declination or the angle between magnetic and true north.

The quantities $M_i(\phi)$ and $M_{i,0}$ are in units of "counts" (frequency multiplied by sample time) from the A-D converters. If H is in gammas (1 gamma (γ) $\equiv 10^{-5}$ oersted of intensity or 10^{-5} gauss of induction in regions of zero susceptibility), then K_i is in units of gammas per count. Values of K_i were obtained by combining the measured amplitudes of the calibration curves $M_i(\phi)$, $i = 1, 2$, with measurements of H obtained at Mildura by the Geophysical Branch, Australian Bureau of Mineral Resources (BMR, see table 4.2), and were typically between 100 and 200 γ per count (see table 4.6).

Time Relationships in Data Acquisition and Read-out Operations

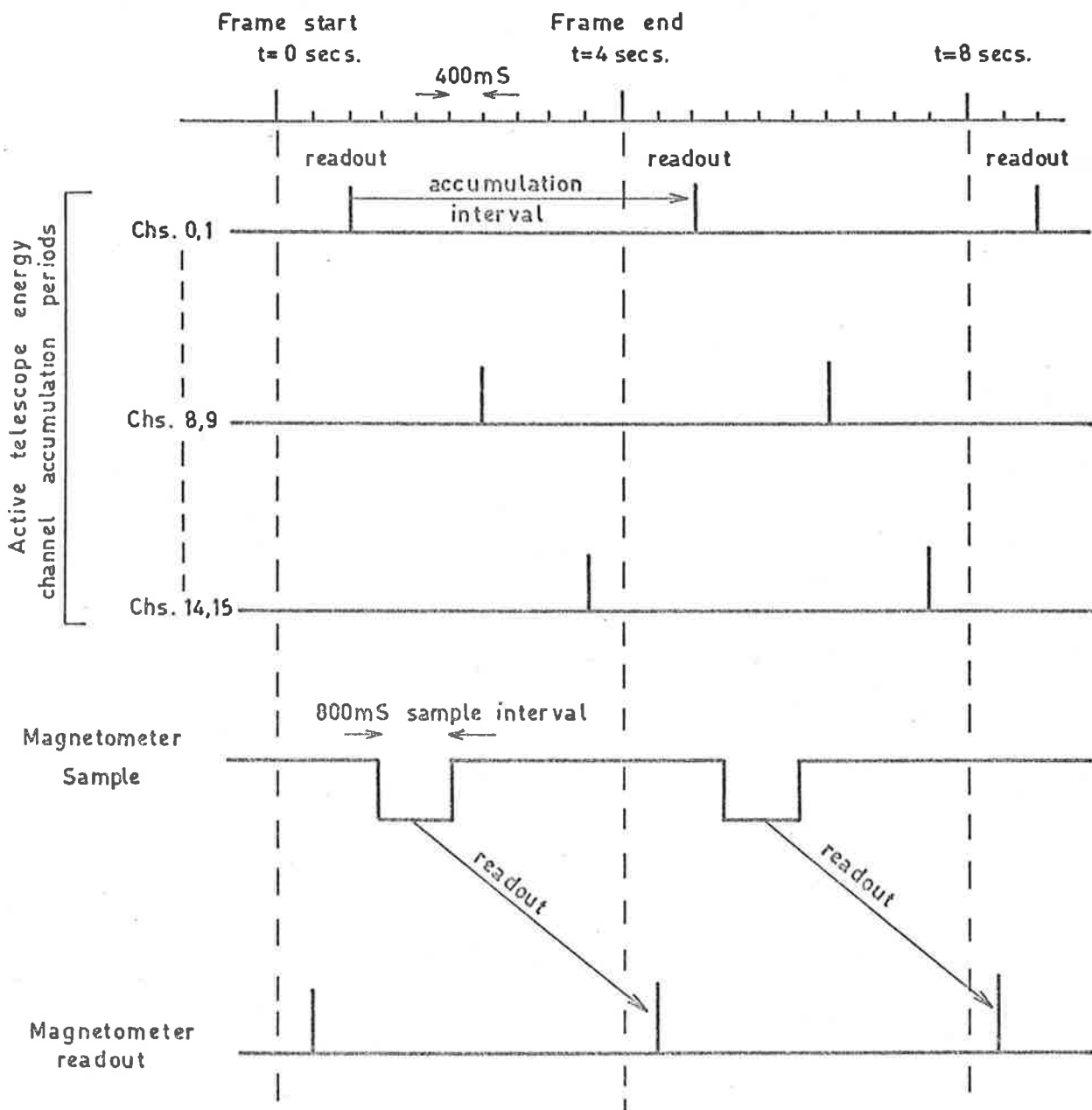


Fig: 2.10 The sampling and read-out sequences for the PHA energy channels and the magnetometers.

The quantities $M_{i,0}$, $\phi_{i,0}$ ($i = 1, 2$) must also be determined by calibration, while D is known over an entire balloon flight path from BMR measurements.

Solution of the two simultaneous equations 2.1 yields for ϕ :

$$\tan(\phi + \phi_{1,0} - D) = \cot(\phi_{2,0} - \phi_{1,0}) - \frac{K_2}{K_1} \cdot \frac{M_2 - M_{2,0}}{M_1 - M_{1,0}} .$$

$$\operatorname{cosec}(\phi_{2,0} - \phi_{1,0}) \left[M_1 \neq M_{1,0} \right] \text{--- 2.2 ,}$$

from which two possible numerical solutions for ϕ are obtained. The quadrant of the correct solution is obtained by using either of equations 2.1. This value of ϕ is independent of any variations in H . Also a measurement of the value of H may be made by substituting the solution ϕ back into equation 2.1 and solving for H . This measurement provides a check on the correct operation of the magnetometer system.

Equations 2.1 and 2.2, their use, and the determination of the calibration parameters involved will be fully discussed in chapter 4.

2.7.4 Instrumental Limitations Upon Measurement Accuracy

The digitization of magnetometer outputs sets a limit to the attainable angular resolution of an azimuth measurement. Equation 2.2 shows that the change in azimuth per unit change in output count is given by

$$\frac{\partial \phi}{\partial M_i} \approx \frac{-K_i}{H} \cos(\phi + \phi_{j,0} - D); \quad i \neq j; \quad i, j = 1, 2 \text{ --- 2.3}$$

Tables 4.2 and 4.6 give values of H and K_i respectively, with the result $\left| \frac{\partial \phi}{\partial M_i} \right| \leq \frac{1}{3}$ per count for the angular resolution. Similarly the error in an absolute azimuth measurement per unit error in a sinusoid mean value is given by

$$\frac{\partial \phi}{\partial M_{i,0}} \approx \frac{K_i}{H} \cos(\phi + \phi_{j,0} - D); \quad i \neq j, \quad i, j = 1, 2 \text{ --- 2.4}$$

Typically, $M_{i,0} = 250$ counts (see table 4.6) and a one count error ($= 0.4\%$) may result in a possible azimuth error of $\frac{1}{3}^\circ$.

Another small instrumental effect, which for precisely horizontal magnetometers will not influence the azimuth measurement but will affect any determination of H , is a result of the finite magnetometer sample time (800 mS) and the rotation of the payload. For a rotating payload, A-D converter counts are accumulated not at a single azimuth but over a range of azimuths $\delta\phi = \int_{t_0 - \delta t}^{t_0 + \delta t} \frac{\partial\phi}{\partial t} dt$, where $\frac{\partial\phi}{\partial t}$ is the time rate of change of azimuth and $(t_0 - \delta t, t_0 + \delta t)$ is the sample period.

If $\nu_i(\phi(t))$ is the A-D converter output frequency for the i^{th} magnetometer at azimuth $\phi(t)$, then

$$\nu_i(\phi(t)) = \nu_{i,0} + \lambda_i \cos(\phi(t) + \phi_{i,0} - D), \quad i = 1, 2 \dots 2.5$$

If $\phi(t) = \text{constant}$ and $\delta t = 0.4$ seconds, integration over the sample period yields equation 2.1 with $M_i = 0.8\nu_i$, $M_{i,0} = 0.8\nu_{i,0}$ and $\frac{H}{K_i} = 0.8\lambda_i$.

However, if $\phi(t)$ is linear within the sample interval i.e. $\phi(t) = \phi_0 + \alpha(t - t_0)$, where ϕ_0 and α are constants, integration of 2.5 gives

$$M_i = M_{i,0} + \frac{H}{K_i} \cdot \frac{\sin 0.4\alpha}{0.4\alpha} \cdot \cos(\phi_0 + \phi_{i,0} - D) \quad \text{--- 2.6}$$

Comparison with equation 2.1 shows that the mean and phase of the response sinusoid are unaffected but that the amplitude is reduced.

For an extremely rapid payload rotation rate, $\alpha = 25^\circ$ per sec., the magnitude of the effective relative H change is $\left| \frac{\Delta H}{H} \right| = 1 - \frac{\sin 0.4\alpha}{0.4\alpha} \approx 0.005$, and the absolute variation is $\Delta H \sim -125\gamma$, for $H = 25,000\gamma$.

This is only just comparable with the instrumental sensitivity. More typical payload rotation rates of 1° per sec. result in a negligible effect.

Because the change is effectively in the measured value of H and is identical for both magnetometers, the accuracy of the azimuth measurement will not be impaired (see equation 2.2).

2.7.5 System stability

The stability of a Schonstedt unit as a function of time has been checked in a 30 hour laboratory test. No A-D converter was employed and the analogue output of an arbitrarily oriented magnetometer, powered by a stabilized bench supply, was sampled by a digital voltmeter at 5 minute intervals. Negligible drift was observed.

However, the flight system consists of one A-D converter per magnetometer and a battery power supply whose discharge during flight results in a small variation in the nominally stabilized 6.3 volt magnetometer supply. This produces a small change in the system output characteristics which can be monitored by means of the periodic in-flight calibration already described.

Figure 2.11 shows the time behaviour of the battery pack and the regulated 6.3 volt supply during a 14 hour laboratory rundown of the payload batteries. Also shown are the magnetometer outputs M_i (arbitrary azimuth) and the magnetometer calibration outputs $M_{i,cal}$. An independent measurement (not plotted) of the reference voltage used for calibration showed that it decreased by 10 mV over the 14 hours. From the known A-D converter frequency vs. input voltage characteristics, a corresponding 2 to 3 count decrease in $M_{i,cal}$ would be expected. This was in fact observed (see Fig. 2.11) and demonstrated that the A-D converter characteristics remained constant for the 14 hours, a period comparable to the maximum expected duration of a balloon flight.

BATTERY RUNDOWN
MARCH 12, 1969

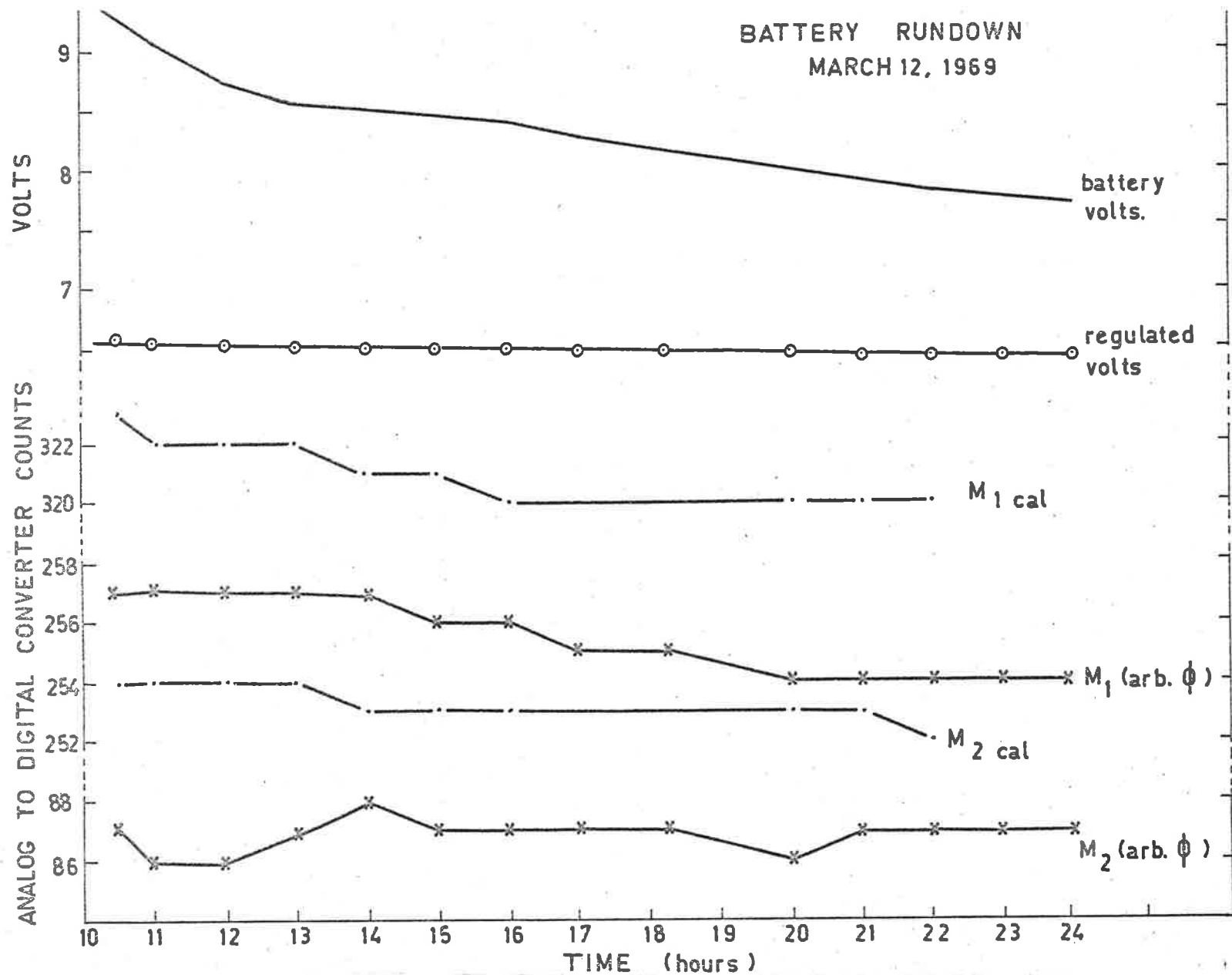


Fig: 2.11 Effects of battery rundown on the magnetometer system.

Since both the $M_{i,cal}$ and $M_{i,o}$ are derived from the Schonstedt bias voltage V_B (see equation (2.1a)), variations in $M_{i,cal}$ imply variations in $M_{i,o}$ which will have an effect on the accuracy of the azimuth measurement. However, the $M_{i,o}$ should be independently monitored for changes since they are determined by other factors besides V_B and cannot be simply adjusted using the observed variations in the $M_{i,cal}$. In-flight checking procedures for the $M_{i,o}$ are described in chapter 4. Sinusoid amplitude changes due to the effects of rundown on the values of K_i may be regarded in terms of an equivalent horizontal intensity variation, since both the magnetometers have a common stabilized supply and identical relative changes in amplitude will occur. As a result the only effect on the azimuth measurement due to battery rundown will be in the values of the $M_{i,o}$ ($i = 1,2$) and these should be closely monitored during a flight. The time variations of M_1 and M_2 (arbitrary azimuth) shown in fig. 2.11 result from the combination of variations in the sinusoid means $M_{i,o}$ and the amplitudes $\frac{M}{K_i}$ ($i = 1,2$).

Temperature effects are not significant under flight conditions. The thermal insulation surrounding the payload ensures that internal temperatures remain within about 5°C . of those at launch ($\sim 20^\circ\text{C}$). The Schonstedt units have been temperature-tested between $\pm 20^\circ\text{C}$. and reveal a negligible temperature co-efficient. The A-D converters have a negligible co-efficient above 0°C ., but below 0°C ., their output frequencies change by about $+1\%/^\circ\text{C}$. drop in temperature. However, the electronics package containing the A-D converters has never dropped below $+15^\circ\text{C}$., during a flight.

Consequently temperature effects should be insignificant with regard to the reliable operation of the magnetometer system.

2.8 THE ALPHATRON PRESSURE GAUGE

The corrections which must be applied to cosmic X-ray fluxes due to absorption in the overlying atmosphere are strongly dependent on the air thickness, especially at low energies (see fig. 1.1). It is therefore necessary to know at all times the depth at which the balloon is floating. The Department of Supply balloon launch facility at Mildura provides three means of determining this parameter. The aneroid bellows-type barotransmitters become inadequate above about 100 K ft. ($\sim 10 \text{ gm. cm.}^{-2}$), and their alphasatron gauges contribute significantly to the telescope background rates. Tracking-radar measurements, used in conjunction with the US Extension to the ICAO Standard Atmosphere, 1962, provide an accurate means of determining the residual pressure. However, the possibility of radar malfunction or signal loss is ever present and it is **therefore** desirable to have an independent measurement.

The alphasatron employed by us consists of a sensitive electrometer which measures the ionization current from a weak ($< 1 \mu\text{Ci}$) alpha particle source (Howard et al. 1968). Am^{241} is used and unlike Po^{210} , its long half-life of 460 years obviates any necessity for regular replacement and frequent instrument recalibration. Its output is a rectangular waveform, the repetition rate of which is a measure of the atmospheric density. This is put on an analogue telemetry subcarrier for data transmission, and upon reception at the telemetry ground station is demodulated and recorded on magnetic tape and on a strip chart recorder.

The alphasatron contributes negligibly to the telescope background count rates. The pressure is determined to an accuracy of about 0.1mb, in the interval between 1 and 10 mb (1mb \cong 1.019716 gm. cm.⁻²).

2.9 HOUSEKEEPING MEASUREMENTS

It was deemed desirable to monitor certain parameters of an engineering nature to check the overall system operation. Examples are the active telescope guard rates, the upper and lower level discriminator rates, the PHA busy flip-flop rate, battery voltage levels and temperatures in various parts of the payload.

These quantities were sequentially sampled by a 32-position subcommutator over the housekeeping cycle of period 128 seconds. The counting rates were sampled twice per cycle and the slowly varying analogue quantities once only. The rates, when sampled, were scaled and fed into a 10-bit register in the DSU, while each analogue quantity was switched by activation of one of 16 reed relays and digitized by an A-D converter. The stability and linearity of the A-D converter was checked once per cycle by inclusion of three reference voltages in eight voltages monitored.

Temperatures at eight places in the payload were monitored by thermistors. The potential drop across each resistor was amplified and switched into the A-D converter when the appropriate sub-commutation signal activated one of the eight reed relays assigned to the thermistors. The temperatures of the following were monitored: the batteries; the active telescope central crystal, the top and bottom of the active well crystal, the graded shield telescope crystal, the PHA, the telemetry electronics packages (DSU and DTU), and the alphasatron.

The payload was thermally shielded with sheets of styrofoam insulation and temperatures rarely varied by more than about 5°C. from the pre-launch temperature.

2.10 THE PCM TELEMETRY SYSTEM

An X-ray astronomy balloon flight lasting for approximately 10 hours will produce a considerable quantity of data which must be recorded for future analysis. The digital PCM telemetry (Pulse Code Modulation) was chosen for the X-ray observatory to guarantee computer compatibility and also to permit the incorporation of data validation codes. The NRZ (non-return to zero) PCM system used is a digital system in which the presence or absence of a pulse is used to transmit information.

2.10.1 The Telemetry Word Format

The telemetry format comprises 10 pulse widths or bit widths per word with 20 words constituting a complete telemetry frame of duration 4 seconds. The frame format is set out in table 2.1 just as it is printed following real time decoding. The first 10 bit word is the Barker frame-synchronization word which aids in the ground decoding of the data. Next in turn are the housekeeping word and the two magnetometer words. The remainder of the left hand side (i.e. words 2 to 9) is occupied by the 16 channel PHA, each channel of which uses 5 bits, or half of the telemetry word.

Word 2 on the right hand side is the time word or frame counter which is the output of a 10 bit register whose accumulated count advances by one unit per frame. It recycles every 2048 seconds (~34 minutes) so it does not characterize each frame unambiguously, but this is never a practical problem.

Table 2.1 Telemetry Word Format

Word	Left hand side 10 bits, 200mS		Right hand side 10 bits, 200mS
9	Ch.14	Ch.15	STATUS
8	Ch.12	Ch.13	GRADED SHIELD GUARD
7	Ch.10	Ch.11	GRADED SHIELD CHANNEL 5
6	Ch.8	Ch.9	GRADED SHIELD CHANNEL 4
5	Ch.6	Ch.7	GRADED SHIELD CHANNEL 3
4	Ch.4	Ch.5	GRADED SHIELD CHANNEL 2
3	Ch.2	Ch.3	GRADED SHIELD CHANNEL 1
2	Ch.0	Ch.1	TIME
1	MAGNETOMETER 1		MAGNETOMETER 2
0	BARKER		HOUSEKEEPING

Words 3 to 8 on the right hand side are 5 graded shield PHA channels plus the guard count rate, and word 9 is a "status" word which permits the monitoring of the status of quantities which have a "yes/no" character and whose state can be indicated by either of 2 levels, 0 or + 5 volts. Calibration source positions (i.e. "in" or "out"), rotation relay positions, etc., are telemetered in this fashion.

The least significant (2^0) of the 10 bits is lost upon insertion of the parity bit, which is either a zero or a one depending on what is required to give the word the necessary odd parity, i.e. an odd number of ones. The requirement of odd parity for a valid data word assists in data analysis by enabling the recognition of errors in the demodulated bit stream owing to poor telemetry reception or a decoding malfunction. An error in one bit changes the word parity from odd to incorrect even parity which is easily recognised. Such data is omitted from analysis. Error rates are normally very low and the case of two errors in one word giving odd parity incorrectly may be ignored.

2.10.2 The Data Storage Unit (DSU)

The DSU contains a 10-bit accumulation register for each type of data to be measured and a 10-bit shift register for each side of the word format. Sequentially applied "word read" pulses instantaneously transfer the data word in each accumulation register into the shift register. The accumulation registers are also reset by the word read pulse. This occurs every 4 seconds for any given word and the word read pulses to consecutive words are separated by an interval of 400 milliseconds. After a word has been read into the shift register, application of "bit shift" pulses (50 bits per second) shifts the word out one bit at a time, thereby generating a bit stream which after parity insertion becomes the transmitted digital data.

The data are read from the accumulators at times which differ by 400 mS. from one word to the next. This means that the 4-second periods over which the various data words are accumulated are not concurrent, with the result that the spectrum derived from a single telemetry frame does not correspond to a single azimuth (unless the payload is constant in azimuth).

The relationship of the PMA data acquisition periods to the times of azimuth measurement and read-out is shown in fig. 2.10. The mean azimuth during the data acquisition period of each channel must be calculated for that channel by linear interpolation of the azimuths read out in consecutive frames, using the known time relationship between the various operations.

2.10.3 The Data Transmission Unit (DTU)

The DTU controls the extraction of data from the DSU, inserts parity, subcommutates the housekeeping data, generates the IRIG subcarrier signals and mixes them to produce the composite video signal which modulates the transmitter. A crystal-controlled 100KHz oscillator supplies timing and gating pulses after scaling and the use of logic circuitry.

IRIG Subcarrier bands which have been used are band 11 (7.35 KHz) for the PCM data, while bands 6 (1.7 KHz), 9 (3.9 KHz), 12 (10.5 KHz) and 14 (22 KHz) have been used for various analogue purposes. Examples are the alphasatron signal, the PMA busy flip-flop (with a view to pulsar observations) and a magnetometer error signal when azimuth servo-control was attempted.

These frequencies are mixed and the resulting video signal modulates two 1 watt FM transmitters operating between 71 and 73 MHz. Coaxial sleeve antennas are employed and the power output from each is theoretically sufficient to obtain usable signals up to a distance of 750 Km., which is the maximum line of sight range for a balloon at 40 Km. altitude.

2.10.4 The Ground Station

A block schematic of the ground station appears in fig. 2.12. The system has two parallel sections to accommodate the two carrier frequencies transmitted from the payload.

One section is used solely to demodulate and record the digital signal and print it out after decoding in three-digit octal form plus parity. The composite video signal, the PCM signal and a reference signal comprising voice annotation, a standard time signal broadcast by the radio station VNG, Victoria, and an 8 KHz synchronization tone for tape playback, are each recorded on one track of a three channel Ampex ER-300 tape recorder. The magnetometer words are extracted by the decoder, the original output levels are recovered and applied to the X and Y inputs of an oscilloscope to provide a real-time azimuth indication. The time word and the status bits are also extracted and displayed on the control panel to provide operator guidance.

In the other section of the ground station, the total video signal is also recorded on one track of an Akai M-7 tape recorder to provide redundancy. This signal is also demodulated in real time and the resulting data are displayed on a multi-channel strip chart.

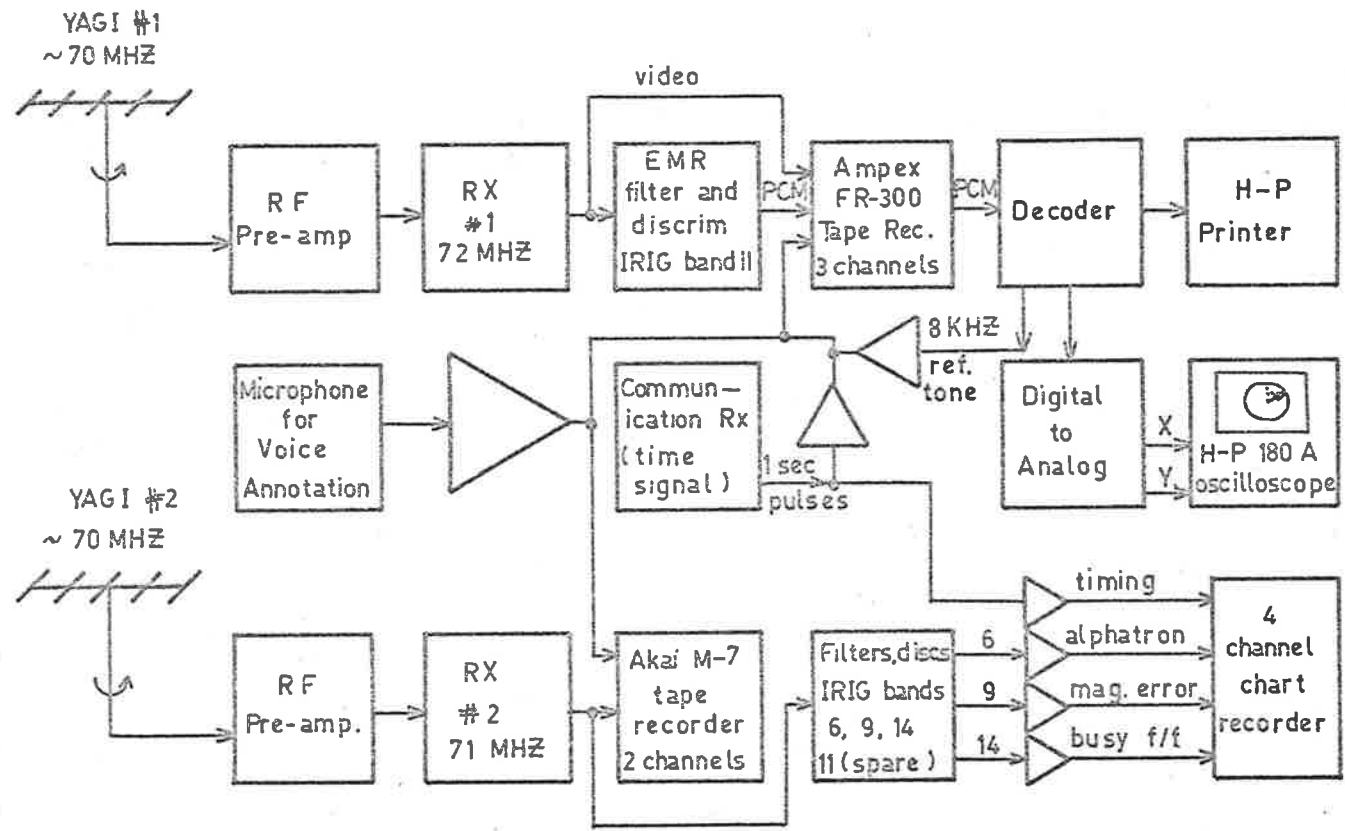


Fig: 2.12 Block schematic of the telemetry ground station.

The reference signal mentioned above is recorded using the other channel of the M-7 and the time signal is put on one of the strip recorder channels.

This system offers excellent real-time data inspection facilities and achieves the proper recording of all data for subsequent analysis, thereby providing a suitable degree of redundancy for safeguard purposes.

Upon return to the laboratory, the telemetry tapes are replayed and the recorded PCM signal is fed into the Data Acquisition System in order to generate a Fortran-compatible magnetic tape of the entire flight. This tape can be used on the CDC 6400 computer at the University of Adelaide to analyse data by employing special purpose data analysis programmes.

CHAPTER 3LABORATORY X-RAY ASTRONOMY3.1 INTERACTIONS OF X-RAYS WITH MATTER

The detection and study of X-ray spectra requires that the photons interact in some way with the detection apparatus. In the energy range of interest here, 10 to 200 KeV the most important interactions are photoabsorption and the Compton effect. Pair production becomes important only above 1.02 MeV and will not be considered here.

3.1.1 Photoelectric absorption

This occurs when an incident photon of energy E is totally absorbed by an atom and is accompanied by the ejection of a photoelectron usually from the K. or L shell, with an energy $T = E - E_B$ where E_B is the electron binding energy. When the vacant shell is later filled, fluorescent X-rays and Auger electrons are emitted with energy E_B and usually reabsorbed yielding further photoelectrons, so that in general there is complete deposition of the incident photon energy by ionization loss of electrons. In practice some fluorescent radiation does escape the detector volume, resulting in incomplete energy deposition and requiring an escape-correction to be made in any spectral analysis (see section 3.2.3).

The probability that a photon of energy E will penetrate a thickness x gm. cm.⁻² of matter of atomic number Z without suffering photoabsorption is given by

$$p_p(E) = \exp[-\mu_p(E) x] \quad \text{--- 3.1}$$

where $\mu_p(E)$ is the mass absorption coefficient (cm.² gm.⁻¹), which increased roughly as $Z^4 E^{-3}$ at energies greater than the K absorption edge.

Between 10 and 100 KeV its exact energy dependence is complex owing to the presence of K and L shell absorption edges at which $\mu_p(E)$ increases sharply. Detailed measurements and tables are available however (Victoreen, 1943).

3.1.2 The Compton Effect

This involves the elastic collision of the incident photon ($E = h\nu = \alpha m_0 c^2$) with an atomic electron of rest mass $m_0 c^2$ which although strictly bound, may be regarded as free if its binding energy $E_B \ll E$. If the photon is scattered through an angle Θ , its energy after scattering is given by $E' = \frac{E}{1 + \alpha(1 - \cos \Theta)}$. The energy of the recoil Compton electron is given by $T_c = E - E'$, which has a maximum value (the Compton "edge") of $T_{cm} = \frac{2\alpha E}{1 + 2\alpha}$, corresponding to a head-on collision with $\Theta = 180^\circ$.

An important difference between the Compton and photoelectric interactions is that the photon energy is not **completely** absorbed in a single Compton interaction. As a result the total Compton attenuation co-efficient $\mu_c(E)$ has two terms, a scattering co-efficient for removal of photons from the beam and the absorption co-efficient to account for the transfer of energy from photon to recoil electron. At constant photon energy these co-efficients go as Z/A , which is 0.45 ± 0.05 for all elements except hydrogen, so that they are nearly independent of the absorber material.

Since full energy deposition (per photon) in a detector is desirable for an unambiguous spectral determination, it is important that photoabsorption should dominate over the Compton effect, and this requires that a detector of high Z material should be used.

Figure 3.1 shows the individual co-efficients and the total mass absorption co-efficient $\mu(E)$ for NaI(Tl) scintillator material in which Iodine ($Z = 53$) is primarily responsible for absorption. Note that for $E \lesssim 100$ KeV, $\mu(E) \sim \mu_p(E)$ and that $\mu_c(E)$ only becomes significant at higher energies.

3.2 RESPONSE OF NaI(Tl) TO INCIDENT X-RAYS

The basic interactions of X-rays with NaI(Tl) have been described and now attention is turned to the manner in which these interactions are detected and converted into voltage pulses for the purpose of electronic processing. Particular attention is given to the factors involved in the transformation of the original differential X-ray photon spectrum $N(E)dE$ photons $\text{cm}^{-2} \text{sec}^{-1}$ in the energy interval $(E, E + dE)$, into the differential pulse height distribution $F(H)dH$ observed from the photomultiplier (PM) tubes which view the scintillator. An understanding of these factors is essential to the correct interpretation of observed pulse height spectra as will be described in section 3.3.

3.2.1 Transparency of the Crystal to X-rays

The energy dependence of $\mu(E)$ in NaI(Tl) is given in fig. 3.1 and shows that for a 2 mm. thick (0.74 gm. cm^{-2}) crystal, the probability of absorption is $\gtrsim 99\%$ for $E \lesssim 60$ KeV but has decreased to $\sim 60\%$ at 100 KeV. Thus if the differential photon spectrum incident normally at the crystal surface is $N'(E)dE$, the energy distribution of absorption events is given by $N'(E) \{1 - \exp(-\mu(E)x)\} dE$, where $x \text{ gm. cm}^{-2}$, is the crystal thickness. This is usually taken to be the energy distribution of detected events also, and this is what will be assumed in this thesis.

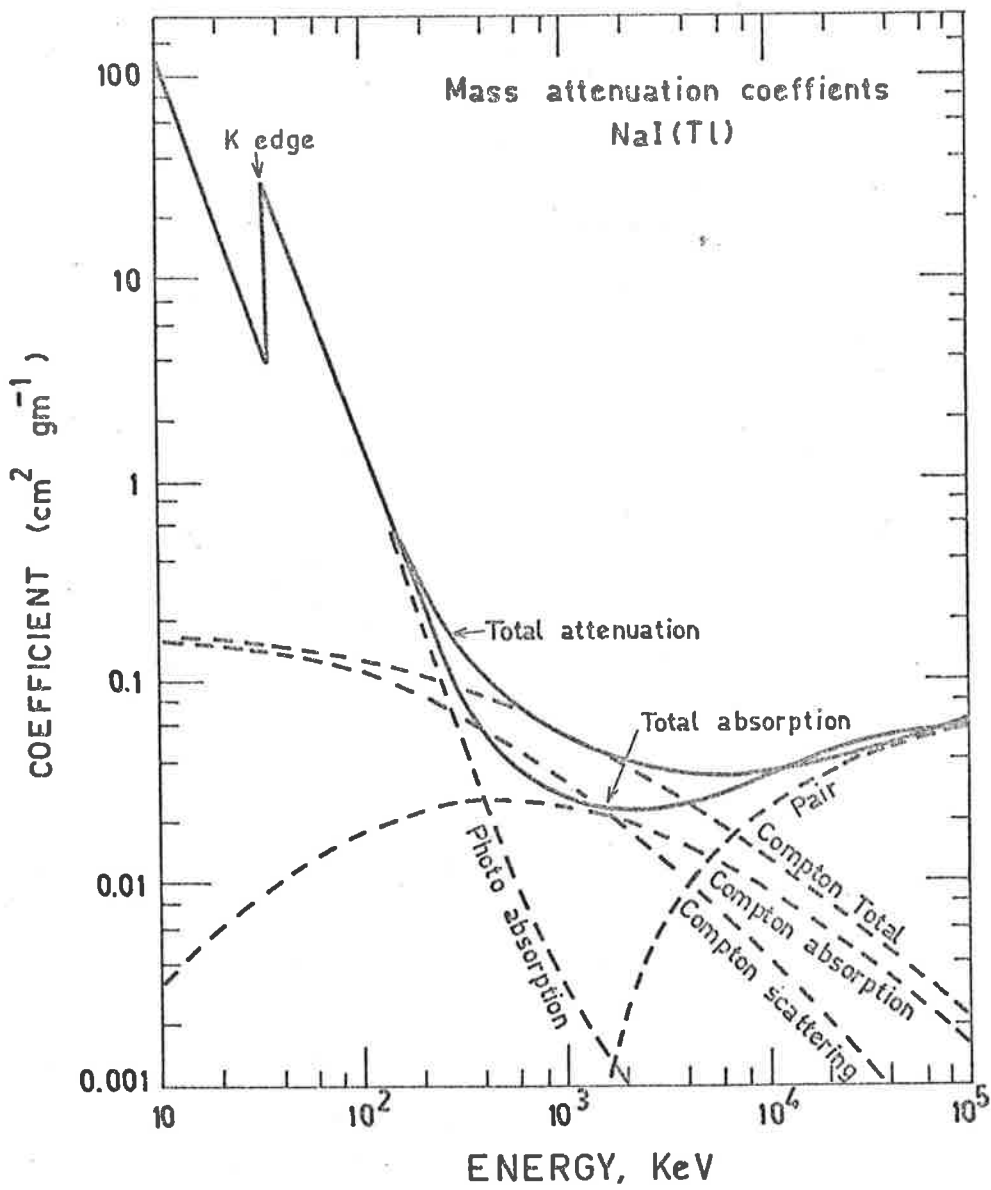


Fig: 3.1 Photon attenuation co-efficients in NaI(Tl) as a function of energy.

However, it must be recognized that this is only an approximation to the truth. Patla and Kiss (1965) have shown that measured and theoretical values of detection efficiency do not always agree as a result of the apparent failure of some absorption events to produce detectable scintillations. Further the crystal will deviate from its nominal thickness, further affecting the energy dependence of the efficiency. In view of both these affects, it is recognized that an actual measurement of the detection efficiency, i.e. the fraction of absorbed photons which give detectable PM tube pulses is desirable where possible.

3.2.2. The Scintillation Process in NaI(Tl).

This subject has been thoroughly treated by Mott and Sutton (1958) Birks (1964) Price (1964) and Aitken (1968(a)) and only a superficial review is attempted here.

The energy of an absorbed photon is converted into visible light by first exciting electrons from the NaI(Tl) valence band into its conduction band. Part of this excitation energy is then transferred to the Tl^{+} luminescence centres which emit visible photons upon deexcitation. Approximately 30 photons per KeV of incident energy are emitted in a wavelength band centred on 0.42 microns, and the light pulse has a decay time constant of about 250 nanoseconds. There is a temperature variation of +0.3% per $^{\circ}C$. in light output but this effect is minimized by ensuring the effective thermal insulation of the telescope during flight. Table 3.1. lists some properties of NaI(Tl) in comparison with the two other inorganic scintillators employed upon the Adelaide payload.

Table 3.1 Scintillator properties, $20 \lesssim h\nu \lesssim 200$ KeV

Property	NaI(Tl)	CsI(Tl)	CsI(Na)
Light o/p (L) relative to NaI(Tl)	1.0	0.30	0.80
Temperature co-eff $\frac{dL}{dT}$ ($T < 100^\circ\text{C.}$)	+0.3	+0.6	+0.5
Decay time constant (nS)	250	800	650
Density gm. cm. ⁻³	3.67	4.51	4.51
Max. emission wavelength (micron)	0.42	0.55	0.42

The linearity of light output with X-ray energy is good but there exists a smooth deviation of $\sim 5\%$ in the proportionality constant over the range 20 to 100 KeV and there is a sudden change also of about 5% near the iodine K edge (Aitken et al. 1967). Variations of this small magnitude are not significant at the present state of development of X-ray astronomy and no attempt at correction has been made in the present data analysis. To the author's knowledge no other workers in the field have included any such corrections. However, as techniques improve and observations of higher statistical precision are obtained it will become necessary to fold the non-linearity effect into NaI(Tl) telescope spectral response functions, since corrections for the escape of iodine K X-ray photons are only slightly larger and are currently applied by most workers.

3.2.3 K-escape

Not all photoelectric interactions of photons in NaI(Tl) result in complete energy deposition since in a small fraction of these the fluorescent X-ray photons produced by de-excitation of the I^{127} atoms escape from the crystal without re-absorption.

Between 10 and 200 KeV Kshell absorption predominates in the primary interaction. Each daughter photon takes away a mean energy of 29.2 KeV, a value obtained by weighting the K_{α} and K_{β} line energies with their intensities. Hence each photon that results in a K-escape photon only deposits $(E-29.2)$ KeV in the scintillator (provided that the incident photon energy exceeds the K-electron binding energy of 32.3 KeV.)

For a collimated photon beam normally incident on a crystal of thickness t gm. cm.^{-2} whose front surface has linear dimensions large compared with the mean free path of the K x-rays, Mott and Sutton (1958) show that the probability per incident detected photon of escape from the front surface is given by

$$p(E) = \frac{1}{2} w_k \delta_k \mu(E) \int_0^t \int_0^{\pi/2} \exp \left[\left(-\tau(E) + \frac{\tau_k}{\cos\theta} \right) x \right] \sin\theta d\theta dx \quad 3.2$$

where w_k is the iodine K fluorescence yield, δ_k is the fraction of photoelectric events occurring in the K shell, $\mu(E)$ and $\tau(E)$ are the photoelectric and total mass attenuation co-efficients respectively, τ_k is $\tau(29.2 \text{ KeV.})$, θ is the angle between the normal to the surface and the K X-ray escape direction and x gm. cm.^{-2} is the depth of penetration of the incident photon in the crystal. Because τ_k is large for NaI(Tl), escape from crystals thicker than 2 mm. is small and t may be regarded as being infinitely large. Equation 3.2 then becomes

$$p(E) = \frac{1}{2} w_k \delta_k \frac{\mu(E)}{\tau(E)} \left[1 - \frac{\tau_k}{\tau(E)} \cdot \ln \left(1 + \frac{\tau(E)}{\tau_k} \right) \right] \quad 3.3$$

A useful experimental parameter is the ratio $P(E)$ of the number of counts in the escape peak (with energy $(E - 29.2)$ KeV.) to the number in the full absorption photopeak for mono-energetic (E) radiation. This is given by $P(E) = \frac{p(E)}{1-p(E)}$. The results of detailed calculations of $P(E)$ have been published by Axel (1954) and their significance to balloon X-ray astronomy emphasized by Stein and Lewin (1967).

The value of $P(E)$ for a 2mm. thick crystal of NaI(Tl) is $\sim 12.5\%$ for $E \geq 60$ KeV., increases to $\sim 27.5\%$ at $E = 32.2$ KeV and is zero for $E < 32.2$ KeV. These probabilities are used in what follows to make allowance for K-escape in the unfolding of source spectra from measured pulse height distributions.

3.2.4 Spectral resolution

As a result of statistical fluctuations in the processes involved in the conversion of X-ray energy into a voltage pulse from the PM tubes, monoenergetic X-radiation undergoing photoabsorption produces a photopeak with an approximately normal distribution of output pulse heights rather than the delta function distribution applicable to a detection system with perfect energy resolution. Energy resolution is experimentally best characterized by either ΔE (KeV) the full width of the distribution at half the maximum intensity (FWHM) or the relative FWHM given by $\eta(E) = \frac{\Delta E}{E}$, whose energy dependence is described below. The standard deviation $\sigma(E)$ of the normal distribution is related to ΔE and $\eta(E)$ through $\Delta E = 2.354\sigma$ and $\sigma(E) = \frac{E}{2.354} \eta(E)$, respectively (Evans 1963).

The width $\eta(E)$ has three components, η_I , η_P and η_M which are related through $\eta^2 = \eta_I^2 + \eta_P^2 + \eta_M^2$ (Birks 1964). The partial width η_I is attributable to intrinsic properties of the scintillator such as statistical fluctuations in the number of photons produced per scintillation, spatial non-uniformities in the crystal luminescence efficiency, the statistics of multiple absorption events, both photoelectric and Compton, which contribute to the photopeak and the effects of the non-linear energy response of the crystal.

The width η_p is determined by variations in light collection efficiency over the crystal surface, by statistical fluctuations in the passage of scintillation photons to the PM tube photocathode and the subsequent emission of photoelectrons. For example, the system optical geometry is different for each individual scintillation, for a large crystal especially, and so the photon collection efficiency of the photocathode will also be different, even for an otherwise perfect phosphor. Also, self-absorption, reflection losses, light trapping by total internal reflections at the crystal boundaries, and inefficient light piping will cause variations in the fraction of photons collected. The photocathode adds to the variance of the pulse height distribution through the usual statistical fluctuations in the number of emitted photoelectrons, through surface non-uniformities and random thermal emission.

The statistics of electron multiplication through the PM tube dynode chain is responsible for η_m , together with variations in dynode responses and collection efficiencies.

The width η_I usually contributes little to η in comparison with η_p and η_m and little is known about its energy dependence. The energy dependence of η_m goes approximately as $E^{-\frac{1}{2}}$ while η_p is energy independent. However, the exact nature of the variation of these quantities with energy and their relative sizes have been shown to be dependent on the configuration of the detector employed (Birks 1964). Experimental calibration of the detector is therefore necessary and the calibration of $\eta(E)$ for each flight of the active telescope is shown in fig. 3.2. Linear fits to $\eta(E)$ as a function of E were found to be good approximations for the purposes of data analysis.

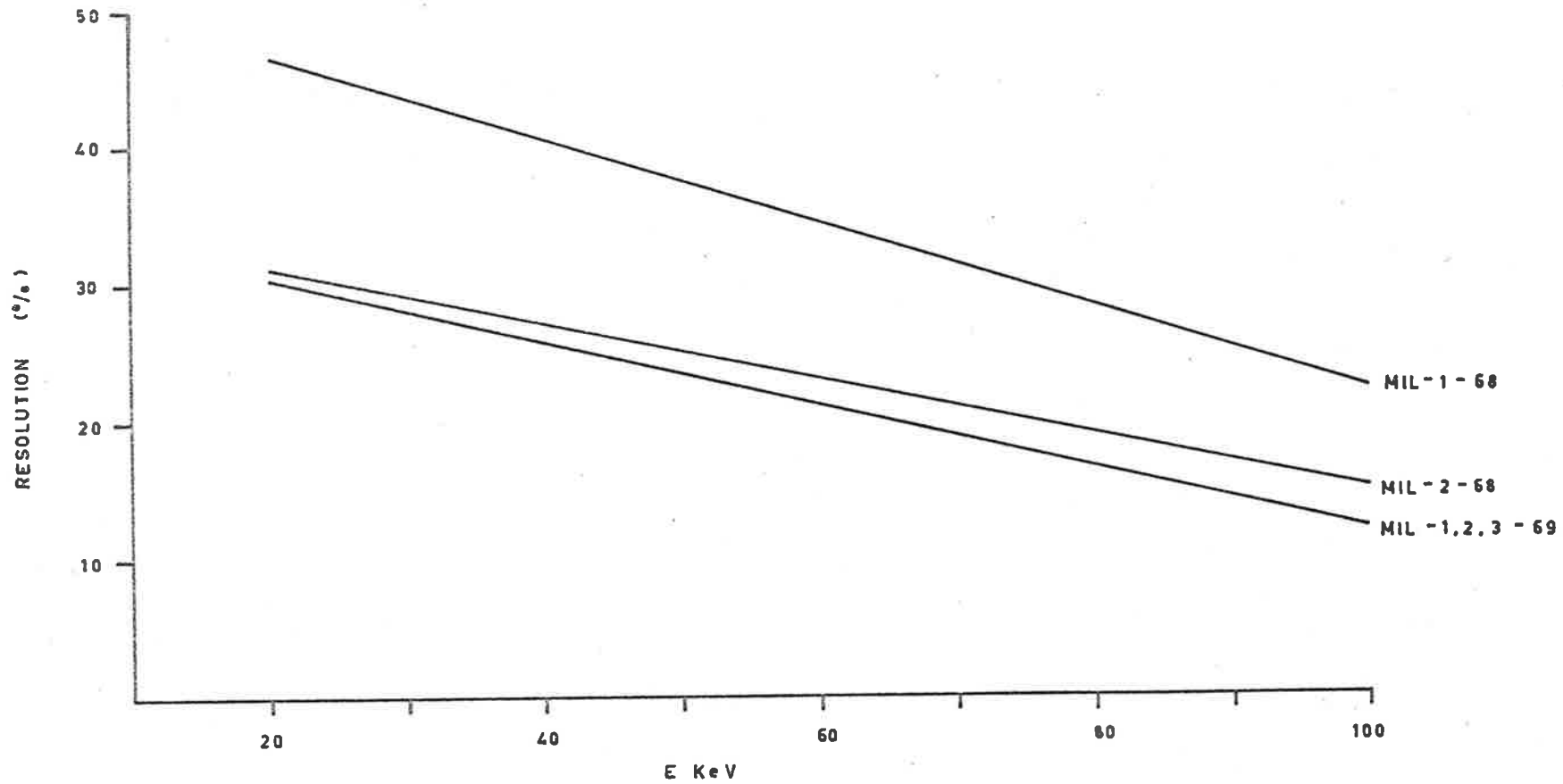


Fig: 3.2 Active telescope energy resolution $\eta(E)$ ($=\Delta E/E$) x 100% for different flights.

No attempt was made to fit the data with functions of the form

$\eta^2 = A + BE^{-1}$ (A, B constants) such as may be theoretically expected, since it was not warranted under the circumstances, but examination of fig. 3.2 indicates that comparable relative contributions from η_m and η_p are present.

3.2.5 Summary

The effects described above all determine the final form of the output pulse-height distribution $F(H)dH$ which results when a photon spectrum $N(E)dE$ is normally incident on the surface of a NaI(Tl) crystal. The number of output pulses in the height interval H to $H+dH$ (KeV) will be given by

$$F(H)dH = \int_0^{\infty} N'(E) \left\{ 1 - \exp(-\mu_c(E) \cdot C) \right\} \left[\frac{p(E)}{(2\pi)^{\frac{1}{2}} \sigma(E-29.2)} \exp\left(-\frac{(E-H-29.2)^2}{2\sigma^2(E-29.2)}\right) + \frac{1-p(E)}{(2\pi)^{\frac{1}{2}} \sigma(E)} \exp\left(-\frac{(E-H)^2}{2\sigma^2(E)}\right) \right] dE dH \quad 3.4,$$

where $\mu_c(E)$ is the mass absorption co-efficient ($\text{cm}^2 \text{ gm}^{-1}$) of the NaI(Tl) crystal of thickness $C \text{ gm. cm}^{-2}$; $p(E)$ is the K X-ray escape probability and the terms in square brackets describe the normal energy resolution of the escape and total absorption events respectively.

3.3 ANALYSIS OF COSMIC X-RAY SPECTRA

Equation 3.4 above describes the transformation into a pulse height distribution of a photon spectrum $N'(E)dE$ incident at the crystal surface. However, in X-ray astronomy applications, the spectrum $N'(E)dE$ is itself **derived from** a primary spectrum $N(E)dE$ which has interacted with the residual atmosphere above the balloon, with the payload thermal insulation lying in the telescope field of view and with the window materials protecting both the active collimator crystal and the main NaI(Tl) crystal.

At photon energies accessible to balloon experiments, interstellar absorption effects should be negligible and will not be considered in this analysis. Another point to consider before equation 3.4 can be applied to real data is that integration with respect to H must be performed over the finite FHA channel widths which are typically 10 KeV in size .

These matters are now discussed with respect to the unfolding of any cosmic X-ray source spectrum $N(E)dE$ from observed j^{th} channel count rates $R_j = \int_{H_j}^{H_{j+1}} F(H)dH$ ($\text{cm}^{-2} \text{sec}^{-1}$), $j = 0, \dots, 15$ where the H_j are the pulse height channel boundaries.

3.3.1 Atmospheric and payload absorption

If the depth of residual atmosphere above the payload is a gm. cm^{-2} , z is the telescope zenith angle, $\mu_a(E)$, $\mu_i(E)$ and $\mu_w(E)$ are the mass attenuation co-efficients of air, the payload insulating material and the telescope window material respectively, and i , w are the respective thicknesses, then the differential spectrum normally incident at the NaI(Tl) crystal surface is

$$N'(E)dE = N(E) \exp \left[-\mu_a(E) a \sec z + \mu_i(E) i + \mu_w(E) w \right] dE \quad \text{--- 3.5}$$

3.3.2 The final response function

All factors affecting the measured response $F(H)dH$ of an X-ray telescope to an axially incident primary cosmic X-ray spectrum have now been enumerated. Dead time effects on the central crystal counting rate due to pulse resolving times and random accidental anticoincidences are less than 4% and therefore need not be considered. The complete response function $F(H)dH$ can now be written by combining equations 3.4 and 3.5 thus:

$$F(H)dH = \int_0^{\infty} N(E) \exp \left[- \left(\mu_a(E) \frac{a}{\cos \bar{z}} + \mu_i(E) i + \mu_w(E) w \right) \right] \left[1 - \exp(-\mu_c(E)c) \right] \cdot \left[\frac{p(E)}{(2\pi)^{1/2} \sigma(E-29.2)} \exp\left(\frac{-(E-H-29.2)^2}{2\sigma^2(E-29.2)}\right) + \frac{1-p(E)}{(2\pi)^{1/2} \sigma(E)} \exp\left(\frac{-(E-H)^2}{\sigma^2(E).2}\right) \right] dE dH \quad 3.6$$

The counting rate (sec^{-1}) in the j^{th} channel with pulse height bounds H_j, H_{j+1} (KeV.) is then given by

$$R_j = A \cdot \int_{H_j}^{H_{j+1}} F(H)dH \quad 3.7$$

where $A(\text{cm}^2)$ is the effective area of crystal exposed by the collimator.

It should be noted that equations 3.4 to 3.7 have been derived for a spectrum from a point source on the telescope axis. The response for an off-axis source is modulated by the collimator angular response function as described in section 3.4.2.

When an isotropic flux is being measured, the above discussion remains valid with $F(H)dH$ and $N(E)dE$ in $\text{cm}^{-2} \text{sec}^{-1} \text{ster}^{-1}$ and with equation 3.7 replaced by $R_j^{\text{diff}} = G \int_{H_j}^{H_{j+1}} F(H)dH \quad 3.8$, where $G(\text{cm}^2 \text{ster})$ is the telescope geometric factor which we take to be energy independent and is defined in section 3.4.2.

Consideration of equations 3.6, 3.7, and 3.8 shows that it is impracticable to analytically unfold the primary spectrum $N(E)dE$ from the channel rates R_j . A method due to Gorenstein et al. (1968) and used by a number of workers, is to take trial spectra $N(E)dE$ numerically through the integral transformation process and to make a least squares (χ^2) comparison between the computed (R_j^c) and experimental (R_j^e) channel rates. The quantity $\chi^2 = \frac{(R_j^c - R_j^e)^2}{V(R_j^e)}$, where $V(R_j^e)$ is the statistical variance of R_j^e , is computed for different trial spectra.

The true primary spectrum is taken to be that which best fits the data, for which χ^2 is a minimum. This method is of course only valid as long as the statistical uncertainty exceeds systematic uncertainties due to calibration and background subtraction errors.

3.3.3. Spectral Correction Factors

We define the j^{th} channel correction factor F_j as

$$F_j = \frac{\int_{H_j}^{H_{j+1}} N(E) dE}{R_j}$$

This is the ratio of the count rate which would be observed by a perfect detector (i.e. no window absorption, 100% photon detection efficiency, no K-escape, energy resolution $\eta \rightarrow 0$) at the top of the atmosphere, to that observed by our detector. It is found that F_j is a function of the spectral shape of $N(E)dE$ as a result of the necessity to integrate energy-dependent corrections over the relatively broad energy channel widths (~ 10 KeV). Table 3.2 gives F_j values applicable to the flight MIL-1-68 (with $\frac{\sigma}{\rho} = 3.2 \text{ gm.cm}^{-2}$) for exponential spectra $N(E)dE = N_0 E^{-1} \exp\left(\frac{-E}{kT}\right)$ with different values of kT , and power law spectra $N(E)dE = N_0 E^{-(\lambda + 1)} dE$, with different values of λ (see section 1.4 for the physical justification of these spectral forms). These tabular values have been used in chapters 5 and 8 to deduce the form of X-ray spectra above the atmosphere for discrete sources and the isotropic background, respectively.

3.4 TELESCOPE CALIBRATION

Thorough preflight testing is essential to ensure correct operation of the detector and its anticoincidence system and to precisely determine the calibration characteristics necessary for the analysis

Table 3.2 Total correction factors F_j , MIL-1-68

Channel		Exponential, kT (KeV)				Power law, number exponent ($\lambda+1$)			
#	Bounds (KeV)	5	10	15	20	1.5	2.0	2.5	3.0
0	7- 17	1093	266.9	151.0	110.3	65.97	117.0	205.3	356.5
1	17-27	33.98	20.68	16.42	14.34	10.42	12.63	15.06	17.68
2	27-37	3.96	4.85	4.80	4.68	4.08	4.29	4.45	4.53
3	37-47	1.15	2.36	2.69	2.79	2.71	2.73	2.71	2.64
4	47-57	0.59	1.68	2.06	2.20	2.26	2.26	2.22	2.16
5	57-67	0.39	1.37	1.77	1.93	2.10	2.08	2.04	1.98
6	67-77	0.27	1.19	1.63	1.83	2.10	2.07	2.03	1.97
7	77-87	0.20	1.11	1.60	1.85	2.22	2.19	2.14	2.08
8	87-97	0.16	1.07	1.65	1.94	2.45	2.41	2.35	2.28
9-15	97-167	0.12	1.08	1.84	2.32	3.81	3.67	3.51	3.35

of data. The most important calibration measurement is that of the detector energy response which involves (a) determining the near linear relation between output pulse height and photon energy, and

(b) the energy resolution $\eta(E)$ of the detector. Also of great importance is the experimental determination of the collimator response function.

3.4.1 Background rejection.

Background rejection is achieved by active anticoincidence methods. Scintillators are employed to shield the central crystal from directly incident background radiation and in particular to minimize the secondary background which results from Compton scattering in the central crystal and guard scintillators themselves (see sections 2.3.2, 2.4 and 2.5).

Compton scattering in the central crystal will result in a considerable number of photons being scattered into the collimator. The collimator discriminator threshold should therefore be set at a sufficiently low value to recognise these events and inhibit their analysis by the 16 channel P.H.A. However, since we include an iodine K escape correction in our spectral analysis, no detection of K-escape photons (29.2 KeV) from the central crystal need be recorded. Consequently the collimator threshold was set at 40 KeV.

The background resulting from Compton scattering of photons from the collimator or well into the central detector is also minimized using the anticoincidence technique. Figure 3.1 shows that in NaI (Tl) the Compton effect is the dominant interaction for incident photon energies exceeding about 250 KeV. However, owing to multiple interactions which end in full photoabsorption, little contribution to the central detector rate from Compton collisions in the NaI (Tl) well is expected until incident photon energies of about 400 KeV are reached (at which the well thickness corresponds to unit attenuation length). Since recoil electrons corresponding to 400 KeV photons have a maximum energy of 240 KeV, the well threshold setting at 80 KeV ensured the detection of most of the Compton interactions in the well.

The background production from Compton interactions involving the plastic light pipe is minimized using the phoswich pulse shape discrimination technique (see section 2.4). Two factors must be considered when setting the phoswich discrimination threshold. Firstly, it should be sufficiently low to achieve its purpose of "picking-off" the negative backswing of the plastic pulses and so reducing the low energy Compton continuum. Secondly, it should also be sufficiently high to prevent the small negative backswing of genuine NaI(Tl) events of energy ≤ 180 KeV from contributing to the discriminator rate. Failure to meet this second condition will result in a high energy cut-off to the observed central detector spectral response.

In preflight tests, pulses from the 0.66 MeV line of Cs¹³⁷ were used to adjust the threshold level. Verification that the backswing of these pulses was insufficient to trigger the discriminator ensured that valid NaI(Tl) events between about 10 and 180 KeV certainly would not. The Compton continuum generated by scattering of the 0.66 MeV photons in the light pipe and central crystal, was employed to ensure that the threshold was not too high. Figure 3.3 shows the effect of correct phoswich operation on a spectrum accumulated from the central detector using a 400 channel analyser. Two sources, Cs¹³⁷ (to generate Compton background) and Am²⁴¹ (to provide a photopeak at ~ 60 KeV) were placed together in the telescope field of view. With no phoswich discrimination the Am²⁴¹ photopeak cannot be resolved. However use of the phoswich system results in reduction of the Compton continuum from energies below 10 KeV upward and enables the photopeak to be resolved.

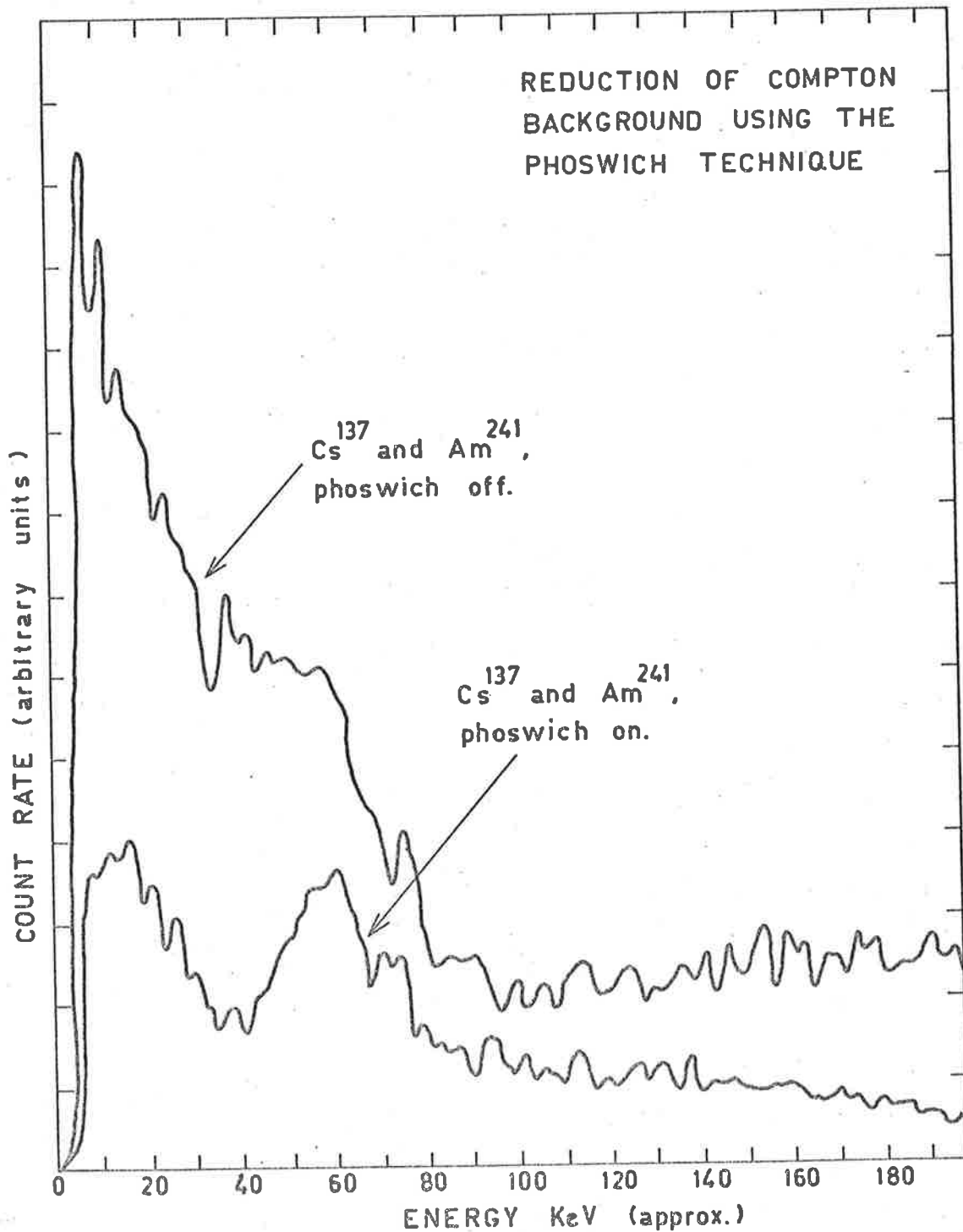


Fig: 3.3 Reduction of Compton background effected by the phoswich technique. The 60 KeV line of Am²⁴¹ can only be resolved from the continuum generated by Compton interactions of the 0.66 MeV line of Cs¹³⁷ when the phoswich is operating.

Laboratory measurements of the effects of various background reduction techniques are shown in fig. 3.4. The curves (1) apply to the unshielded flight crystal of 2mm. thickness and to a crystal of similar area but 25.4 mm. thick. The high energy discrepancy between the two curves is the result of the greater transparency with photon energy of the thin crystal. The curves (2) were obtained with each crystal passively shielded by the CsI(Na) collimator and the NaI(Tl) well. In addition to the expected background reduction in comparison with the unshielded crystals, there is also a low energy fluorescence peak as a result of iodine K-escape from the shield. Further background reduction is achieved (curves (3)) by using the guards actively, and the fluorescence peak is also removed. Another factor of 2 reduction for the thin crystal is obtained when the phoswich system is employed.

The net result of using active anticoincidence techniques is to achieve a background reduction in the laboratory of between 1 and 2 orders of magnitude compared with an unshielded crystal. Also a decrease of greater than an order of magnitude is obtained over the background rate of the graded shield detector, as is shown in fig. 3.4.

3.4.2. Energy calibration.

The energy response of the detector was measured by recording pulse height spectra of a number of monoenergetic γ -emitting radioactive nuclides placed on the telescope axis. These were located at distances as large as were allowed (≥ 10 ft.) by the respective source strengths, in order to minimize the effects of surface non-uniformities in the crystal response. Radioactive sources used for the purposes of calibration are listed in table 3.3. (details from Holt (1967)).

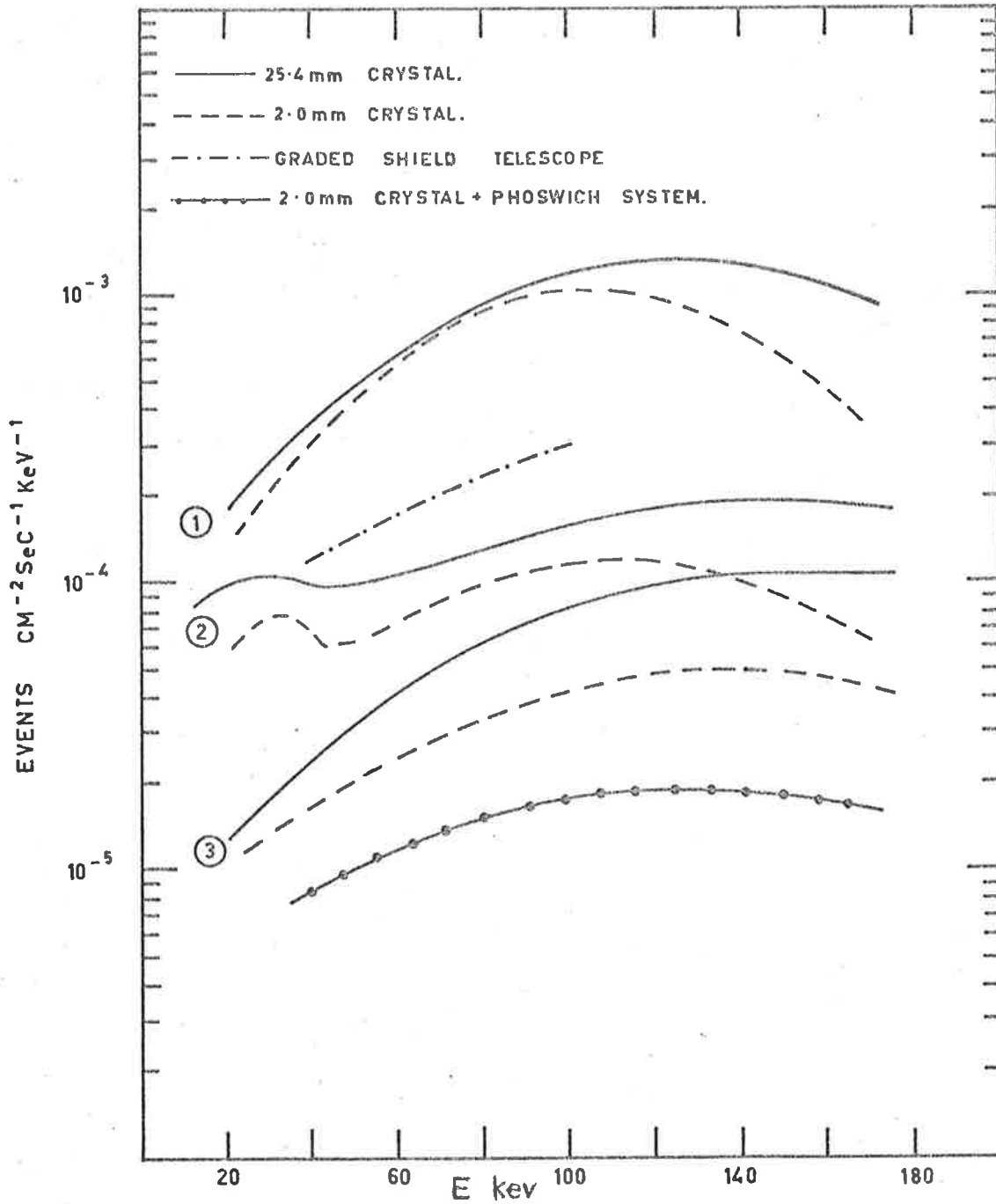


Fig: 3.4 Comparison of laboratory background rates for crystals 2.0mm and 25.4mm. thick. Curves (1) apply to completely unshielded crystals, (2) passive shielding and (3) active shielding. In addition the effect of using the phoswich is shown. Comparison with the graded shield telescope background is also made.

Table 3.3. Calibration X-ray sources.

Source	Half-life	Decay mode	Principal energies (KeV)
Co ⁵⁷	267d	E.C	121.9
Sr. 119	250d	I.C	24, 25.3
133 Ba	7.2y	E.C.	31, 81
Cs ¹³⁷	27y	β^-	32, 662
Gd ¹⁵³	236d	E.C	41, 100
Au ¹⁹⁵	192d	E.C	65.1, 66.8 , 75.7
Am ²⁴¹	460y	α	59.6

The calibrated energy response for all flights as measured by the laboratory 400-channel analyser was to a good approximation linear. The 400-channel calibration spectra were compared with the same spectra obtained through the 16-channel flight P.H.A. and in this way the channel boundaries of the latter were determined. Channel boundary uncertainties varied typically from about ± 1.0 KeV for the lowest energy channels to about ± 2.5 KeV at higher energies.

The detector energy resolution $\eta(E)$ was determined at this time also. The results are shown in figure 3.2 and discussed in section 3.2.4.

3.4.3 The Active Collimator Angular Response.

Aitken (1968b) has calculated the transmission function $T(\theta)$ for an active collimator consisting of a number of cylindrical holes axially parallel, drilled in material with a mass absorption coefficient which approaches infinity at all energies.

The result in this idealized, energy-independent case is:-

$$T(\phi) = \cos \phi \left\{ 1 - \frac{2}{\pi} \left(\frac{\tan \phi}{2 \tan \frac{\theta}{2}} \right) \sqrt{1 - \left(\frac{\tan \phi}{2 \tan \frac{\theta}{2}} \right)^2} - \frac{2}{\pi} \arcsin \left(\frac{\tan \phi}{2 \tan \frac{\theta}{2}} \right) \right\} \dots 3.9$$

where ϕ is the angle between the photon direction of arrival and the axial direction of the telescope, and $\frac{\theta}{2}$ is the collimator opening half-width. For $\frac{\theta}{2} \lesssim 10^\circ$, equation 3.9 is well approximated by

$$T(\phi) \sim 1 - \frac{2}{\pi} \cdot \frac{\phi}{\theta} \cdot \sqrt{1 - \frac{\phi^2}{\theta^2}} - \frac{2}{\pi} \arcsin \left(\frac{\phi}{\theta} \right) \dots 3.10$$

The theoretical response calculated from equation 3.10 for the active collimator ($\frac{\theta}{2} = 4^\circ 32'$) is shown in figure 3.5, along with the measured response and its triangular approximation;

$$T'(\phi) = 1 - \frac{\phi}{\phi_0} \dots \dots \dots 3.11 .$$

The experimental points were obtained by measuring the integrated count rate due to two radiation sources (Am^{241} and Sn^{119}) located 60.5 ft. in front of the telescope. The points thus represent an energy-averaged (over the approximate interval 15 to 75 KeV) angular response and no attempt has been made to determine the exact energy dependence. Clearly the triangular function with $\phi_0 = 8.9^\circ$ is a better fit to the data than the idealized function $T(\phi)$, presumably due to

- (a) imperfect geometry of the drilled cylindrical holes,
- (b) scattering off the collimator walls and,
- (c) energy dependence of the collimator transparency.

This experimentally determined transmission function has been used to obtain the results subsequently reported in this thesis.

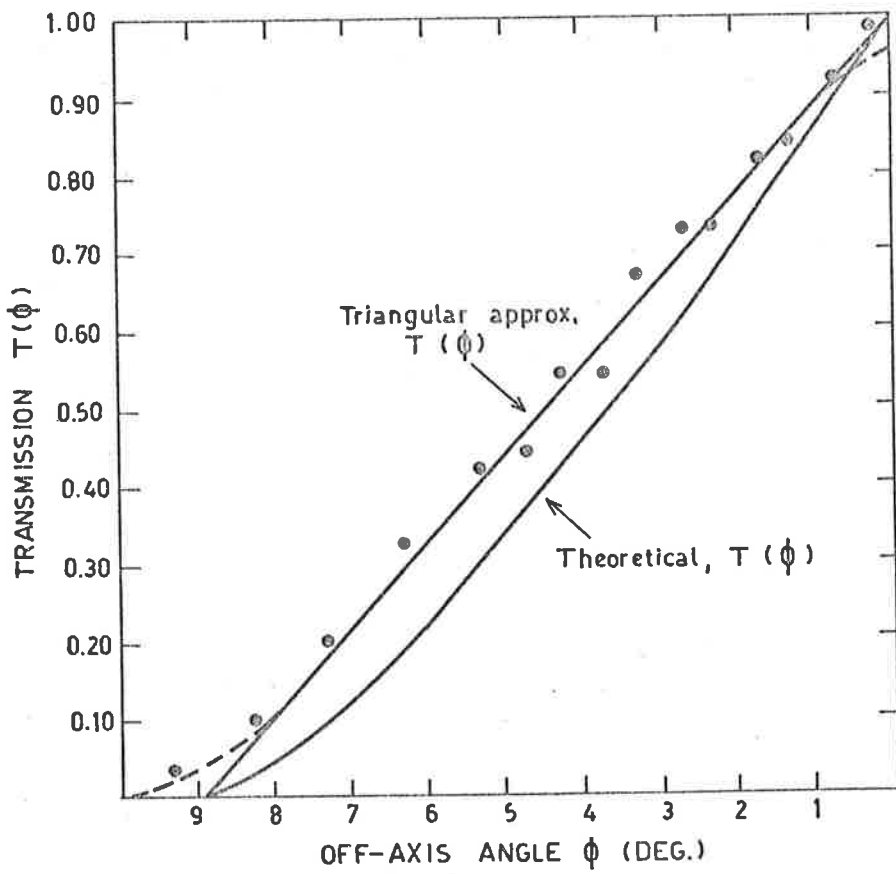


Fig: 3.5 Active collimator transmission $T(\phi)$ as a function of point source off-axis angle ϕ .

Note that the off-axis angle ϕ and hence $T'(\phi)$ can be calculated for azimuth sweeps across a source of known position (azimuth Az_s , zenith z_s) using

$\cos \phi = \sin z_s \sin z_t \cos (Az_t - Az_s) + \cos z_s \cos z_t$, where Az_t and z_t are the telescope azimuth and zenith angles.

3.4.4. Telescope geometric factor:

The collimator angular response function $T(\phi)$ finds direct use in the analysis of point source data as a function of telescope azimuth. Analysis of isotropic source data does not involve its direct use. Instead the telescope geometric factor $G(\text{cm}^2 \text{ ster.})$ is the important aperture characteristic and is given in the energy independent limit by $G = 2\pi A \int_0^{\phi_{co}} \sin \phi \cdot T(\phi) \cdot d\phi \dots \dots \dots 3.12$ where A is the exposed area of the NaI(Tl) crystal and ϕ_{co} is the cut-off angle ($= 8.9^\circ$) for which $T(\phi) = 0$. Substitution of equation 3.10 into 3.12 followed by integration gives $G = X - Y - Z$ where

$$X = A \phi_{co}^2$$

$$Y = \frac{4A}{\theta^2} \left\{ -\frac{\phi_{co}}{4} (\theta^2 - \phi_{co}^2)^{\frac{3}{2}} + \frac{\theta^2}{8} \left[\phi_{co} (\theta^2 - \phi_{co}^2)^{\frac{1}{2}} + \theta^2 \arcsin \left(\frac{\phi_{co}}{\theta} \right) \right] \right\}$$

$$Z = A\theta^2 \left\{ \left(2 \frac{\phi_{co}}{\theta^2} - 1 \right) \arcsin \left(\frac{\phi_{co}}{\theta} \right) + \frac{\phi_{co}}{\theta} \cdot \left(1 - \frac{\phi_{co}^2}{\theta^2} \right)^{\frac{1}{2}} \right\}$$

with the result, $G = 1.07 \text{ cm}^2 \text{ ster.}$

Using $T'(\phi)$ (equation 3.11) with $\phi_o = 8.9^\circ$ gives $G = 1.36 \text{ cm}^2 \text{ ster.}$ Thus a relatively small change in the form used for the point source transmission function $T(\phi)$, results in a variation of almost 30% in the value calculated for the geometric factor for an isotropic flux.

This emphasizes the necessity for an accurate experimental determination of the collimator response function. Work on diffuse fluxes reported in this thesis has employed the geometric factor value, $G = 1.36 \text{ cm}^2 \text{ sterad}$.

3.5 PREFLIGHT ENVIRONMENTAL TESTING.

A number of important laboratory tests were carried out on the payload to ensure its correct operation in the hostile environment at balloon altitudes. The most important of these was vacuum testing since this payload is not contained in a pressurized gondola. High voltage discharges in the photo-multiplier electronics normally appear in their mildest form as an anomalous increase in telescope counting rate and at worst will have a massive loading effect on the high tension supplies thus rendering the P.M. tubes inoperative.

The test was carried out by placing the telescopes and all systems connected with high voltage supplies inside the large vacuum chamber maintained by the Adelaide Space Physics Group. All PM tube output pulse shapes and rates were monitored by visual inspection on oscilloscope displays and by employment of a digital pulse counter. A continuous fault-free run of 12 hours' duration (to allow for any deep-seated outgassing effects) is required before the test is considered to have been successfully passed.

Another important test is to ensure that there is negligible interference to the payload electronics from radiofrequency (RF) fields radiated by the data telemetry transmitters and also by the Department of Supply command system. This test is difficult to control properly since the flight configuration of the antennas and the payload in free space can be only approximately duplicated on the ground. This payload has proven very prone to RF effects, especially in the very fast, high gain phoswich circuitry possibly owing to the unfortunate fact that the payload long dimension is almost exactly equal to one quarter of the telemetry carrier wavelength. The effects are eliminated by tedious trial-and-error procedures of re-routing antenna feeder cables and generally changing the payload-feeder-antenna geometric configuration. Care taken to ensure the spacing of feeders at least two inches from the aluminium structural members has always been found worthwhile.

In conclusion, the behaviour of the payload electronics to temperature changes was determined, although this is not as critical as the above tests due to the efficiency of the payload thermal insulation which has been found to keep temperatures stable to within about 5°C . The electronics packages, the magnetometers and telemetry transmitters have all undergone temperature tests however, and the correct operation of these units has been verified within the range $\pm 30^{\circ}\text{C}$.

CHAPTER 4THE MAGNETOMETERS

Since the direction of pointing of the X-ray telescopes is an essential experimental parameter, magnetometers have been used to determine telescope azimuth angles in those experiments which employed non-vertically-looking telescopes. The instruments and the basic theory of their use for azimuth measurement have been described in section 2.7. However, since no sun-sensor or other auxiliary azimuth-measuring instrument was employed to confirm the magnetometer measurements, it was considered necessary to investigate the reliability of the magnetometers and assess their accuracy under flight conditions. In addition, the adequacy of the ambient magnetic field at balloon altitudes in providing a stable azimuth reference frame was investigated.

The results of these studies are presented in this chapter, together with details of instrument calibration and in-flight performance. The performance of a rotating reference magnetometer, intended for use in an azimuth servo-controlled system, is also examined.

4.1 THE GEOMAGNETIC FIELD.

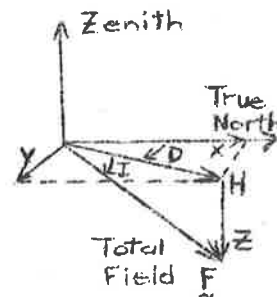
Variations in geomagnetic field properties during a flight which traverses 200 to 300 miles are significant and produce changes in the properties of the preflight calibration sinusoids (see equation 2.1). In particular the quantities D and H change. The former of these is directly relevant to the measurement of

azimuth ϕ and allowance must be made for its variation over a balloon flight path. The latter exerts no influence on the azimuth measurement (see equation 2.2) for precisely horizontal magnetometers. However, it is in principle possible to measure the horizontal intensity from a calculated value of ϕ and use it as a check on the valid operation of the magnetometers. It is then of interest to examine the predicted behaviour of H as it varies over a balloon flight path.

4.1.1. The geomagnetic elements.

In dealing with the geomagnetic field, the symbols and sign conventions usual to the discipline of geomagnetism will be used.

The diagram (right) illustrates how the generally recognised elements are defined. \underline{F} is the total field vector, H is its horizontal intensity and Z its vertical (downward) component.



H can be resolved into orthogonal components

X and Y in the directions of true north and east, respectively.

The declination or deviation D is the angle measured eastward between true and magnetic north, while the inclination or dip

I is the angle by which \underline{F} dips below the horizon.

In this work, Gaussian units are employed in which the permeability (μ_0) of free space is defined to be unity, with the result that in regions where the susceptibility $\chi_m = 0$, the magnetic field intensity is numerically equal to the magnetic induction, and will be quoted in units of gauss or gamma ($1 \gamma \equiv 10^{-5}$ gauss).

4.1.2. Variation of smoothed field near Mildura.

Hurwitz et al. (1966) have published a spherical harmonic model using internal and external coefficients to degree and order 12 which describes the smoothed surface field for epoch 1965.0. This model was used to compute variations in F, H D and I in the vicinity of Mildura, as functions of geographic latitude, longitude and altitude. No secular variation corrections were applied since changes rather than exact absolute values of parameters were important.

Results of these computations for a vertical ascent to 140 K ft. above Mildura (latitude -34.23° , longitude 142.05°) are shown in table 4.1.

Table 4.1: Geomagnetic elements as functions of altitude above Mildura:

Altitude (K ft.)	D (degrees)	I (degrees)	F (γ)	H (γ)
0	8.52	-65.52	59723	24744
40	8.52	-65.52	59356	24593
30	8.51	-65.52	58991	24443
120	8.50	-65.52	58629	24295
140	8.49	-65.52	58450	24221

A check on these computations for 1965.0 is provided by measurements at Mildura of the Geophysical Branch, Australian Bureau of Mineral Resources (B.M.R) which are listed in table 4.2, together with computed values for zero K ft. altitude and measured values of the secular variations.

Table 4.2: B.M.R. measurements at Mildura.

	D(degrees)	I(degrees)	H(γ)
Computed values (1965.0)	8.52	-65.52	24744
B.M.R. measurements (1965.0)	8.4	-65.6	24480
B.M.R. measured secular variations (1965.0)	+3.5' E	-0.7'	-25

Table 4.1 reveals a negligible altitude gradient in D and I but an H gradient of \sim minus 4 γ per 1,000 ft. upward, or \sim -500 γ per 140 K ft. This is about 4 times the minimum detectable field change for the instruments employed and will produce a change of about 4 counts in the amplitudes of the magnetometer sinusoids.

Table 4.3 shows the longitude variation at an altitude of 130 K ft. and a latitude of -34.2° , which amounts to $\sim 0.35^\circ$ per longitude degree, or per 60 miles eastward, for D. This is a significant variation with regard to the measurement of azimuth and must be compensated for over the balloon flight path.

Table 4.3: Geomagnetic elements vs. longitude.

Longitude (degrees)	D (degrees)	I (degrees)	F (γ)	H (γ)
140.0	7.75	-65.71	58709	24151
141.2	8.18	-65.57	58596	24234
142.4	8.61	-65.43	58476	24315
143.6	9.03	-65.29	58349	24394

The longitude gradient in H is about 1.1 γ per mile eastward or 250 γ per 220 miles which for a typical flight is a smaller

total change than that due to altitude alone.

The latitude variation is greater, about 600 γ per degree northward, but since the prevailing winds are usually easterlies or westerlies, this is rarely of any concern.

4.1.3 Geomagnetic Anomalies.

The mathematical field model of Hurwitz et al (1966) describes only the smoothed surface field. However, localized geomagnetic anomalies due to irregularities in geological structure are also superimposed on this smoothed field and it is desirable to investigate their possible effects at balloon altitudes.

A frequently encountered anomaly appears on aeromagnetic survey maps to have almost radially symmetric intensity contours. Such a form may be ascribed most simply to a nearly spherical magnetic body buried a short distance below the earth's surface. Jakosky (1950, page 205) gives a theoretical treatment of the magnetic effect expected for such a body. Applying these calculations to the maximum observed horizontal intensity anomaly of $\sim 1,000 \gamma$ (at 500 ft. altitude, within 250 miles of Mildura) shows that the resulting perturbation ΔH on the smoothed horizontal intensity is many orders of magnitude below the threshold sensitivity of the magnetometers employed.

The most outstanding feature on aeromagnetic maps of the area resembles a magnetic sheet anomaly extending some 100 miles in the north-south direction and about 50 miles east-west. This anomaly is coincident with the Mt. Lofty Ranges, about 200 miles west of Mildura. The maximum H anomaly at 500 ft. altitude within

this sheet is of the order of 1,000 γ . Boyd (1970) estimates that at balloon float altitudes, any effect attributable to this anomaly is an order of magnitude below the instrumental sensitivity.

It is therefore concluded that geomagnetic local anomalies have no significant effect upon the magnetometer measurements made by the Adelaide payload at float altitudes.

4.1.4 Time Variations.

Periodic time variations of the geomagnetic field, such as the quiet-day solar (Sq) variation with an amplitude of about 25 γ at Adelaide during solar-active periods, and the lunar (L) variation of about 1 γ amplitude, may be important for magnetometer measurements made at float altitudes since these, in comparison with measurements made at ground level, are closer to the ionospheric current system sources. This is even more strongly true for the irregular phenomena of geomagnetic storms.

Predicted effects at float altitudes depend on assumptions with respect to the physical nature and the height of the current systems which produce the field variations. If the currents flow at a well-defined height x km., $\Delta H(40)$ and $\Delta H(0)$ are the perturbations in H at float altitude (40Km) and ground level (0Km) respectively, then we can write

$$\Delta H(40) = \Delta H(0) \left(\frac{x}{x-40} \right)^n,$$

where the value of n depends on the model adopted for the current system. For a line current $n = 1$, and for an infinite current sheet, $n = 0$.

For the latter case, $\Delta H(40) = \Delta H(0)$ and only large and relatively infrequent geomagnetic storms with $\Delta H \geq 100 \gamma$ will be of significance. In the former case, and for $x = 120$ Km, (E region), we have $\Delta H(40) = \frac{3}{2} \Delta H(0)$, and the conclusions are little different from the case $n=0$. Thus Sq and L variations will not have a significant effect on the magnetometers at an altitude of 40 Km.

Only large geomagnetic storms, will produce significant effects. Variations can occur in all geomagnetic elements during such phenomena. In particular D variations can occur which will lead to absolute errors in the azimuth measurement. The size of any such D variations at 40 Km altitude would have to be inferred from ground-based observatory records, making azimuth corrections difficult. It is thus advantageous to be aware of the scale of magnetic activity during a flight, since this is relevant to the accuracy of X-ray source position determinations.

4.2 ORIENTATION OF THE CROSSED MAGNETOMETERS.

This section contains computations which describe the effect on the azimuth measurement of deviations from the nominally horizontal orientation of the two crossed magnetometers. Such deviations can be due to:-

- (a) Orientation errors in the mounting of the magnetometers within the payload and,
- (b) a non-vertical payload rotation axis resulting from an uneven distribution of mass within the payload.

4.2.1. Theory.

The coordinate system defined by the Cartesian axes having unit vectors $(\underline{I}, \underline{J}, \underline{K})$ where \underline{K} is directed vertically upwards and \underline{J} is the direction of the horizontal intensity is shown in fig. 4.1(a). Thus, $\underline{F} = \underline{J} H - \underline{K} Z = F (\underline{J} \cos I - \underline{K} \sin I)$ 4.1. where $|\underline{F}|^2 = H^2 + Z^2$.

The axes $(\underline{I}, \underline{J}, \underline{K})$ will be referred to as space axes. We also define the payload coordinate system by the unit vectors $(\underline{i}, \underline{j}, \underline{k})$ where \underline{k} is the payload rotation axis, directed approximately upward, and \underline{j} is the vertical projection of the telescope viewing axis in the plane normal to \underline{k} (see fig. 4.1 (b)). The right-handed convention is adopted for rotations. Then the matrix transformation from payload to space coordinates is:

$$\underline{x} = A B C \underline{X} \quad \dots\dots\dots 4.2$$

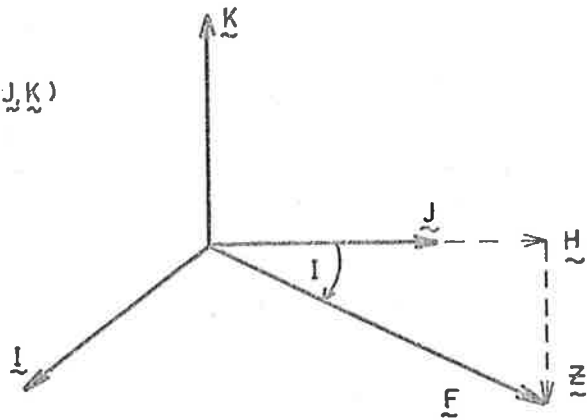
$$\text{where } \underline{x} = \begin{bmatrix} \underline{i} \\ \underline{j} \\ \underline{k} \end{bmatrix}, \underline{X} = \begin{bmatrix} \underline{I} \\ \underline{J} \\ \underline{K} \end{bmatrix}, C = \begin{bmatrix} \cos(\phi + \phi_0) & -\sin(\phi + \phi_0) & 0 \\ \sin(\phi + \phi_0) & \cos(\phi + \phi_0) & 0 \\ 0 & 0 & 1 \end{bmatrix},$$

$$B = \begin{bmatrix} 1 & 0 & 0 \\ 0 & \cos \theta & -\sin \theta \\ 0 & \sin \theta & \cos \theta \end{bmatrix}, A = \begin{bmatrix} \cos \eta_0 & \sin \eta_0 & 0 \\ -\sin \eta_0 & \cos \eta_0 & 0 \\ 0 & 0 & 1 \end{bmatrix}.$$

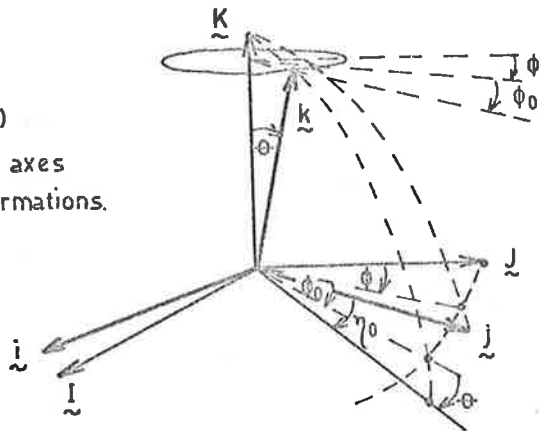
The angles ϕ , ϕ_0 , θ and η_0 are shown in figure 4.1 (b).

The angle ϕ is the telescope magnetic azimuth, θ the angle between \underline{K} and \underline{k} i.e. the off-vertical hanging angle of the payload, ϕ_0 gives the azimuthal direction of the $(\underline{k}, \underline{K})$ plane relative to the telescope azimuth, η_0 is the projection in the $(\underline{i}, \underline{j})$ plane of the angle ϕ_0 , and is given by the condition:

- (a) Space coordinate system $(\underline{i}, \underline{j}, \underline{k})$ defined such that the geomagnetic total field is given by $\underline{F} = H\underline{j} - Z\underline{k}$



- (b) Payload axes $(\underline{i}', \underline{j}', \underline{k}')$ derived from space axes by rotational transformations. Order of rotations is $\phi, \phi_0, \theta, \gamma_0$.



- (c) Magnetometer axes $(\underline{i}'', \underline{j}'', \underline{k}'')$ in terms of payload axes $(\underline{i}', \underline{j}', \underline{k}')$

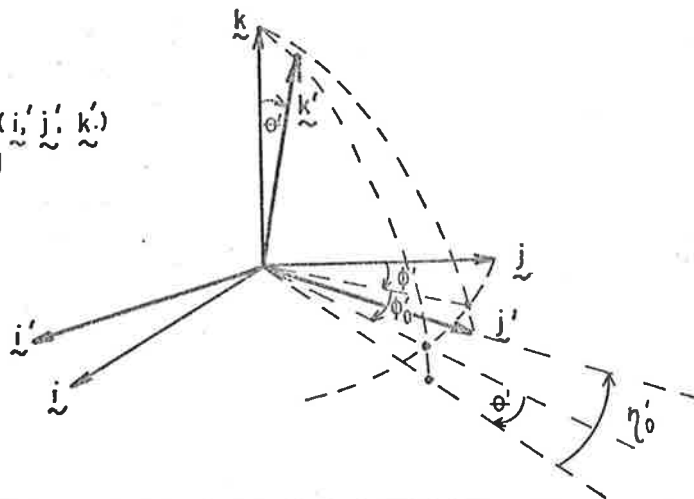


Fig: 4.1 Co-ordinate systems used in the derivation of equation 4.6 for the magnetometer response.

$$\sin \eta_0 \cos \phi_0 - \cos \eta_0 \cos \Theta \sin \phi_0 = 0 \quad \dots\dots\dots 4.3$$

To be noted is that if $\Theta \neq 0$, i.e. the payload is incorrectly balanced, the rotation axis \underline{k} will precess about the vertical \underline{K} as the payload rotates and ϕ varies. The precession cone will have half-angle Θ and the position of the \underline{k} vector on the cone will be given in azimuth by the angle $(\phi + \phi_0)$.

The transformation describing the orientation of a mounted magnetometer relative to the payload coordinate system is identical in form to equation 4.2 (see fig. 4.1 (c) compared with fig. 4.1. (b)). Consequently, analogous formalism is used, and we define the mounted magnetometer coordinate system $(\underline{i}', \underline{j}', \underline{k}')$ where \underline{j}' is the unit vector in the direction of the sensor axis, \underline{k}' is perpendicular to \underline{j}' and in the $(\underline{j}', \underline{k})$ plane and \underline{i}' is the normal to the $(\underline{j}', \underline{k}')$ plane. Thus the mounted magnetometer axes in terms of the payload axes are:-

$$\underline{x}' = A' B' C' \underline{x} \quad \dots\dots\dots 4.4$$

$$\text{where } \underline{x}' = \begin{bmatrix} \underline{i}' \\ \underline{j}' \\ \underline{k}' \end{bmatrix}, \quad A' = \begin{bmatrix} \cos \eta_0' & \sin \eta_0' & 0 \\ -\sin \eta_0' & \cos \eta_0' & 0 \\ 0 & 0 & 1 \end{bmatrix},$$

$$B' = \begin{bmatrix} 1 & 0 & 0 \\ 0 & \cos \Theta & -\sin \Theta \\ 0 & \sin \Theta & \cos \Theta \end{bmatrix}, \quad C' = \begin{bmatrix} \cos (\phi' + \phi_0') & -\sin (\phi' + \phi_0') & 0 \\ \sin (\phi' + \phi_0') & \cos (\phi' + \phi_0') & 0 \\ 0 & 0 & 1 \end{bmatrix}.$$

Combining equations 4.2. and 4.4. gives the most general expression for the orientation of a magnetometer in space:

$$\underline{x}' = A' B' C' \underline{x} \quad \dots\dots\dots 4.5$$

The response of the sensor to the geomagnetic field is given by the dot product $\underline{j}' \cdot \underline{F}$. Cartesian tensor notation is adopted in which summation is implied over repeated subscripts, thus:

$$\underline{j}' \cdot \underline{F} = A'_{2i} B'_{ij} C'_{jk} A_{kl} B_{lm} C_{mn} F_n \dots\dots\dots 4.6$$

where $F_1 = 0$, $F_2 = H = |\underline{F}| \cos I$, and $F_3 = -Z = H \tan I$.

The case of perfect alignment, which has $\phi_0 = \theta = \eta_0 = \phi' = \phi'_0 = \theta' = \eta'_0 = 0$, yields $\underline{j}' \cdot \underline{F} = H \cos \phi$, the correct result. Other simple cases are (a) that in which θ' is the only non-zero angle, for which $\underline{j}' \cdot \underline{F} = |\underline{F}| \cos (I - \theta)$ when $\phi = 0^\circ$, and (b) comparison of the results for the two cases (i) $\phi_0 = \phi' = \phi'_0 = \theta = 0$, $\theta \neq 0$, and (ii) $\phi_0 = \phi' = 0$, $\theta \neq 0$, $\phi'_0 = 90^\circ$, θ' arbitrary, which are identical to each other due to the axial symmetry of the sensor.

The result:-

$$\underline{j}' \cdot \underline{F} = |\underline{F}| (\cos I \cos \theta \cos \phi + \sin I \sin \theta) \dots\dots 4.7$$

is in fact given by equation 4.6 for each case.

It should be noted that equation 4.6 no longer has the sinusoidal form of equation 2.1. However for small deviations from ideal orientation, the response is almost sinusoidal.

4.2.2. Numerical computations.

Equation 4.6. has been computed as a function of azimuth for a model balloon trajectory under the following conditions:-

- (a) Balloon trajectory: Launch from Mildura (-34.23° , 142.05°), westward constant latitude ascent to 130 K ft. given by: altitude (≤ 130 K ft) = - 185 (longitude - 142.05°).

(b) Geomagnetic elements are computed along the trajectory from the model of Hurwitz et. al. (1966).

(c) One calculation is for zero altitude at Mildura and for a precisely levelled payload i.e. $\underline{k} = \underline{K}$ and hence $\Theta = \phi_0 = 0$. This simulates the preflight calibration which is performed by placing the payload upon an accurately horizontal platform which is rotated through all azimuth angles. The magnetometer mounting parameters $(\phi', \phi'_0, \Theta')$ have values listed in (e) below.

(d) Other calculations along the balloon flight path are performed for a poorly levelled payload i.e. $\underline{k} \neq \underline{K}$. The payload suspension parameters (Θ, ϕ_0) used are $\Theta = 1^\circ$, $\phi_0 = 45^\circ$.

(e) Magnetometer mounting parameters, defining the orientation of the sensors within the payload, are for magnetometer #1:

$\phi' = 2^\circ$, $\phi'_0 = 120^\circ$, $\Theta' = 1^\circ$; and for #2 : $\phi' = 94^\circ$, $\phi'_0 = 210^\circ$,

$\Theta' = 1^\circ$. These values are the same for both calculation (c) and (d) above

(f) The final computed values of \underline{j}' . \underline{F} as a function of azimuth are biased by a constant field of $30,000 \gamma$, corresponding to the bias level V_B (see equation 2.6), and the peak and trough values of \underline{j}' . \underline{F} are used to determine the mean levels and the amplitudes of the respective sinusoid approximations.

The results are presented in table 4.4. and show that sinusoid mean levels are determined mainly by the orientational parameters $(\Theta, \phi_0, \phi', \phi'_0, \Theta')$, and the amplitudes by the horizontal intensity (see also equation 4.7). An important consequence is that for both flight and preflight azimuth calibration, the condition $\underline{k} = \underline{K}$ should be met if irregularities in the azimuth measurement

due to shifting mean values are to be minimized. The effective sinusoid phase angles $\phi_{i,0}$ ($i = 1,2$, see equation 2.1) are found to remain constant to within 0.1° of their expected values for all parameter combinations tried.

Table 4.4: Changes in sinusoid characteristics for a model flight.

Long (degrees)	Altitude (K ft)	H (γ)	MAG.#1 (γ)		MAG.#2 (γ)	
			MEAN	AMP	MEAN	AMP
MILDURA	FREEFLIGHT	24744	30465	24735	30830	24743
142.0	10	24703	29780	24710	30200	24720
141.8	46	24554	29780	24560	30200	24570
141.5	102	24324	29780	24325	30200	24340
141.0	130	24186	29785	24195	30195	24205
140.0	130	24117	29783	24123	30195	24135
139.0	130	24045	29780	24050	30200	24060

The precision of the azimuth measurement under the above conditions was investigated by treating computed pairs of magnetometer outputs, \tilde{j}_i ($i = 1,2$) to exactly the same analysis as is used with the flight output pairs. The appropriate approximations to sinusoids as given in table 4.4. were employed as calibrations, and a computed azimuth angle ϕ_c was obtained using equation 2.2.. The value ϕ_c was then compared with the true azimuth angle ϕ used in the original \tilde{j}_i calculation and the size of the azimuth discrepancy, $|\phi_c - \phi| = |\epsilon(\phi)|$, was obtained. The maximum value of the discrepancy in the azimuth range $0^\circ \leq \phi \leq 360^\circ$ was then determined.

The following parameter values were used in the calculations:

payload suspension $\phi_0 = 0^\circ$, $0 \leq \theta \leq 5^\circ$; magnetometer #1 :
 $\theta' = 1^\circ$, $\phi' = 2^\circ$; magnetometer #2: $\theta' = 1^\circ$, $\phi' = 94^\circ$, $\phi_0' = 0^\circ$; geomagnetic
 field: $H = 24744 \gamma$, $I = -65.52^\circ$.

It was found that $\text{MAX}|\epsilon(\phi)| \leq 0.5^\circ$ ($0^\circ \leq \phi \leq 360^\circ$, $0^\circ \leq \theta \leq 5^\circ$),
 a figure comparable to the azimuth resolution of $\sim 0.3^\circ$ (equation 2.3).

4.2.3 Summary

- (a) Small deviations ($\leq 5^\circ$) from precisely horizontal payload and magnetometer orientation result in small deviations from the ideally sinusoidal form of the magnetometer output as a function of azimuth.
- (b) The outputs may be approximated by sinusoids and the azimuths so determined will agree with the true azimuth to $\leq \frac{1}{2}^\circ$.
- (c) The sinusoid approximations for small deviations, have mean levels which are determined by the sensor's spatial orientation, and amplitudes which are functions of the horizontal intensity.
- (d) The azimuth dependence of the error $\epsilon(\phi)$ implies that if a celestial X-ray source of known position is to be used to provide an in-flight calibration for the azimuth measurement, any correction thus derived may only be safely applied to azimuths in the vicinity of the source.

4.3 CALIBRATION OF THE MAGNETOMETERS

Preflight calibration on the ground is used in order to determine magnetometer sensitivity K_i and the sinusoid phase angle $\phi_{i,0}$ (see equations 2.1, 2.2).

However uncertainties concerning the final payload hanging angle Θ during flight, and the dependence on Θ of the sinusoid calibration means $M_{i,0}$, make necessary an in-flight calibration of the values of $M_{i,0}$ ($i = 1,2$).

4.3.1 Preflight experimental procedure.

The payload is placed upon an accurately levelled rotating platform, well removed from any magnetic materials. A relative azimuth scale is provided by graduations in units of one degree around the table perimeter, and magnetometer output pairs are obtained at 10° intervals around the azimuth circle. The true azimuth scale is determined from the relative azimuth measurement by using the active telescope to determine the relative azimuth of a distant (~ 30 ft.) X-ray emitting isotope. Theodolite measurements of the direction of this isotope relative to astronomical objects at accurately determined times yield its true azimuth and hence the angular displacement between the true and relative scales.

Thus magnetometer calibration sinusoids are obtained as functions of true azimuth angle and it is not necessary to know the absolute value of the magnetic declination D at Mildura. Its vector gradient in the vicinity of Mildura must be known in order to make flight path corrections, and this can be obtained from aeromagnetic maps or can be computed (Hurwitz et al 1966).

4.3.2 Reduction of preflight calibration data.

The measured amplitudes of the calibration sinusoids were used together with B.M.R. horizontal intensity measurements (24,480γ at 1965.C, secular variation = - 25γ per year) to determine the sensitivities K_i in gammas per A-D converter output count.

The phase angles $(\phi_{i,0} - D)$ were determined by obtaining a first approximation calibration by careful visual inspection of the sinusoid. If $D + \delta_i$ is the exact phase angle, the correction δ_i is found by using equation 2.1 and forming the residual

$R_{i,j} = M_i (\phi_j, D + \delta_i) - M_i (\phi_j, D)$, for the j^{th} datum point as follows:-

$$R_{i,j} = \frac{H}{K_i} \left[\cos (\phi_j + \phi_{i,0} - D - \delta_i) - \cos (\phi_j + \phi_{i,0} - D) \right] \dots\dots 4.8$$

Simplifying, assuming $\cos \delta_i \approx 1$, squaring and summing over all calibration points, yields:

$$\sin^2 \delta_i = \left(\frac{K_i}{H}\right)^2 \frac{\sum_j R_{i,j}^2}{\sum_j \sin^2(\phi_j + \phi_{i,0} - D)} \dots\dots\dots 4.9$$

This may be regarded as giving the second approximation to $(\phi_{i,0} - D)$ and is usually accurate to within about $10'$, making further iterations unnecessary. The invariance of both the K_i and $\phi_{i,0}$ ($i = 1,2$) over a balloon flight path is assumed.

4.3.3. In-flight calibration.

Only the $M_{i,0}$ now require to be determined and this is performed using flight data since the addition of Department of Supply flight support equipment makes it very difficult to control the condition $k = K$ for the payload rotation axis. The flight $M_{i,0}$ values invariably show a discrepancy relative to the pre-flight calibration values, owing to their dependence on orientational parameters.

The $M_{i,0}$ are determined by taking a trial calibration and computing H as a function of ϕ , as outlined in section 2.7.3. For a sufficiently small traverse of the balloon flight path and for the correct calibration, the function $H(\phi)$ should be constant. However, if incorrect values of $M_{i,0}$ are used, $H(\phi)$ will display a sinusoidal modulation.

If $M_{i,0}^a$ is the approximation employed to calculate values of the function $H^a(\phi)$, if $M_{i,0}^e$ and H^e are the corresponding exact values to be found and if the approximation $\phi^a \sim \phi^e$ is made, then

$$H^a(\phi) = H^e + K_i (M_{i,0}^e - M_{i,0}^a) \cos(\phi + \phi_{i,0} - D). \dots\dots\dots 4.10$$

Thus the amplitude and phase of equation 4.10 give the necessary corrections to the $M_{i,0}$, $i = 1, 2$. Figure 4.2 shows plots of $H(\phi)$ for different choices of $M_{1,0}$ and $M_{2,0}$ during the flight MIL -2-69, from 1002 to 1136 hr. E.A.S.T. (Eastern Australian Standard Time).

4.3.4. Final Values of Calibration Parameters.

Full calibration details for all flights which employed magnetometers are listed in table 4.5.

Fig. 4.2 Determination of magnetometer calibration sinusoid
means by plotting flight data in the form $H(\phi)$.

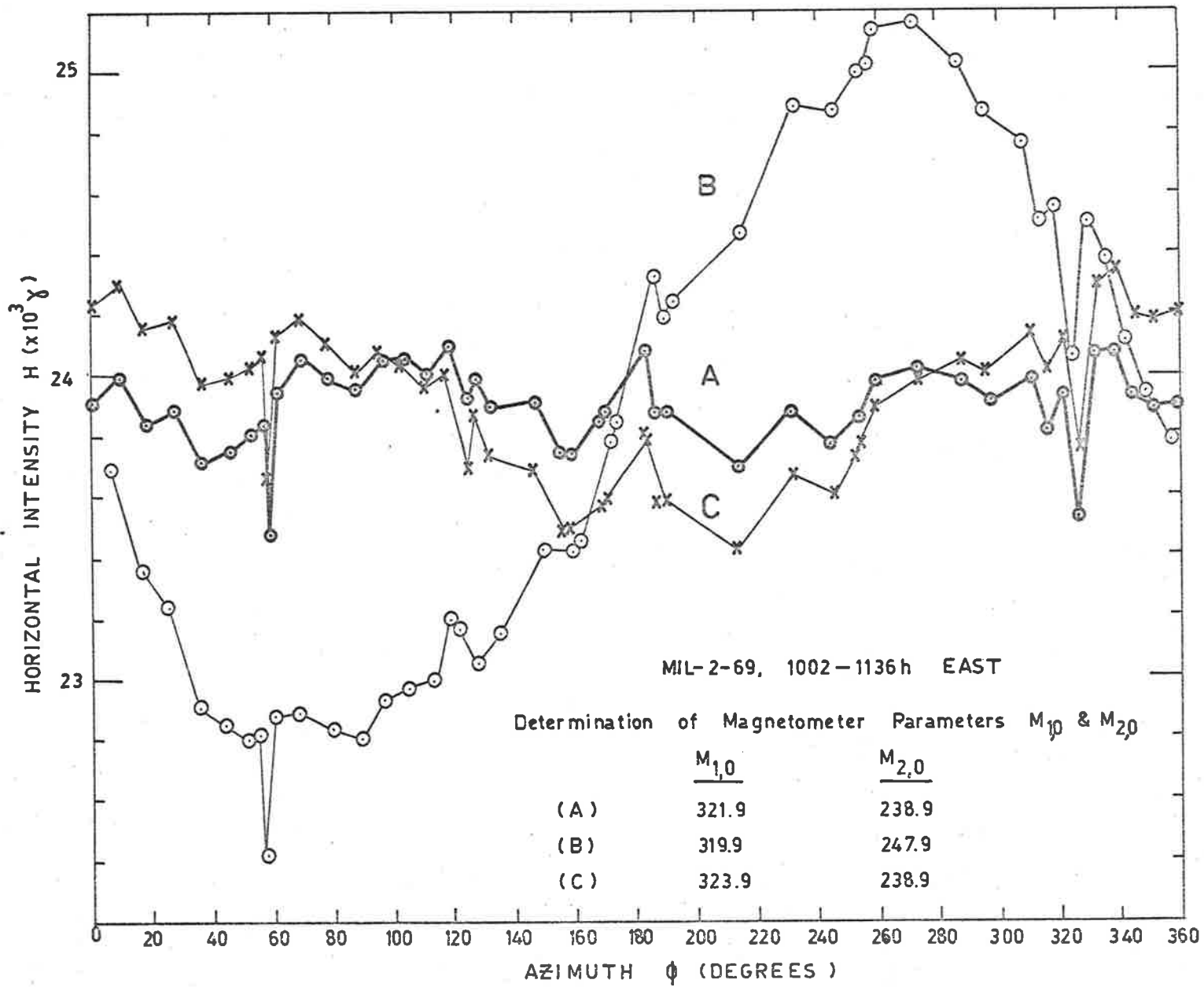


Table 4.5: Magnetometer calibration data, all flights.

Flight No.	K1	K2	$\phi_{1,o} - D$	$\phi_{2,o} - D$	PRE-FLIGHT		FLIGHT	
					$M_{1,o}$	$M_{2,o}$	$M_{1,o}$	$M_{2,o}$
MIL-1-68	136	121	-183°	-100°	318	227	313	233
MIL-2-68	151	124	-188°	-100°	312	244	308	245
MIL-1-69	150	123	-188°	-100°	312	234	306	229
MIL-2-69	150	123	-188°	-100°	309	247	*322 324	239 246

* On MIL-2-69 both $M_{1,o}$ and $M_{2,o}$ were observed to change during flight, having the respective values of 322 and 239 counts from 0900 to 1232 E.A.S.T. and 324 and 246 counts from 1232 to 1718 hours E.A.S.T. This change was attributed to a small slip of the payload rigging under tension.

4.4. FLIGHT PERFORMANCE OF THE MAGNETOMETERS.

In this section, an anomalous effect in the measurement of H is discussed, and the possible error in a final azimuth determination is estimated.

4.4.1. Anomalous H measurement.

It has been mentioned (Section 2.7.3) that the determination of horizontal intensity using a measured azimuth value can in principle be used to check the correct operation of the magnetometers. Figure 4.3 shows H as a function of time during the flight MIL-2-69 and reveals apparent variations of up to 2000 γ in quite short intervals. These variations are recorded by both magnetometers and there are no correlations with azimuth or telescope zenith angle.

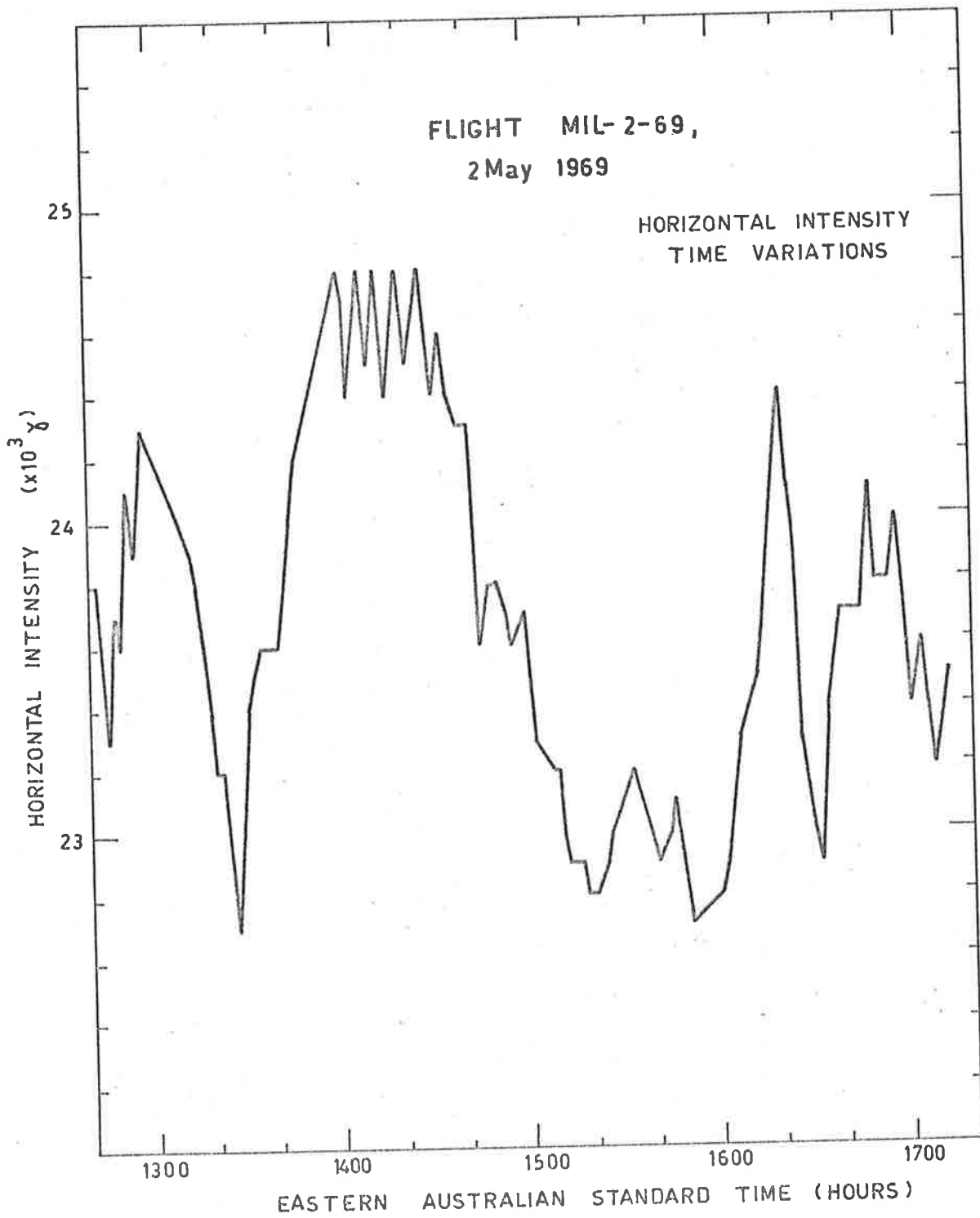


Fig: 4.3 Horizontal intensity measurement as a function of time for the flight MIL-2-69.

The H variations pose difficult problems with regard to their interpretation. Section 2.7.5 indicates that instrumental effects are unlikely since the stabilized 6.3 volt supply was observed to be well-behaved for the duration of the flight, as were the calibration numbers $M_{i,cal}$ and the payload temperatures. The finite digitization time effect does not produce effects of the observed magnitude (see section 2.7.4)

A real geomagnetic field variation does not seem possible either since there is no correlation with known surface anomalies and in any case the variation is too large. Geomagnetic storm activity is ruled out by the records (fig. 4.4.) of the ground-based B.M.R. magnetic observatories at Gnangara (W.A.) and Toolangi (Vic). These magnetograms reveal no H excursions of the order of $10^3 \gamma$, as section 4.1.4 has shown would be necessary to explain the balloon observations. Records of the 3-hourly K_p index (Solar Geophysical Data Reports 1969) confirm the absence of large scale magnetic activity at this time. There is also no correlation in time with any ballast drop from the payload.

There is no explanation at present for the observations in fig. 4.3. However, since the effect is a real horizontal intensity change or is at least equivalent to one, the azimuth measurement should not be affected (see equation 2.2). However, the advantage of having an independent check on the azimuth angle using say a sun-sensor or star-camera is apparent. A sun-sensor has been designed in our laboratory and is expected to be used in the near future (Clancy 1971).

B.M.R. HORIZONTAL INTENSITY MAGNETOGRAMS DURING MIL-2-69

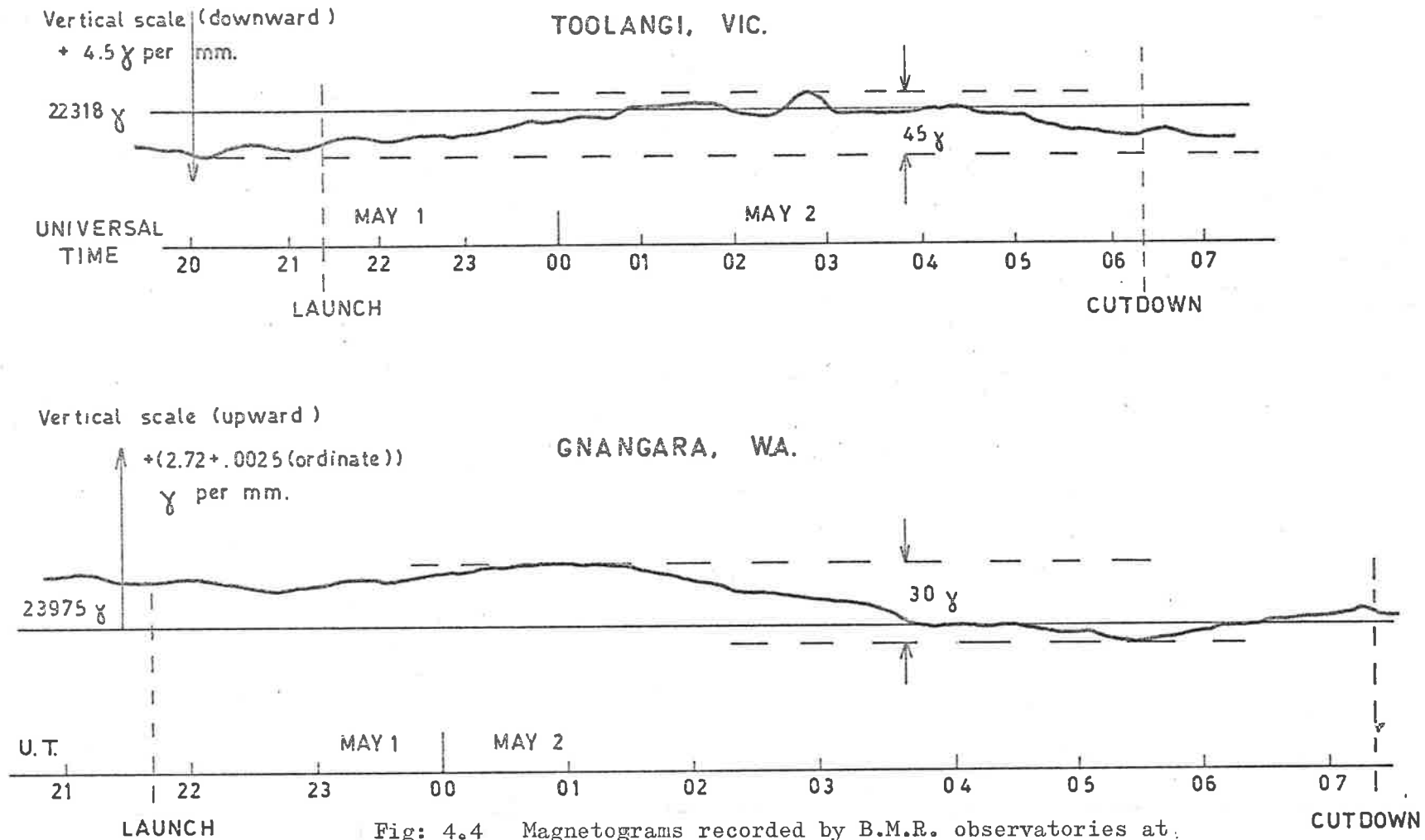


Fig: 4.4 Magnetograms recorded by B.M.R. observatories at Gnangara (W.A.) and Toolangi (Vic) during the flight MIL-2-69.

4.4.2 Accuracy of the Azimuth Measurement.

The following effects contribute to the uncertainty in the final azimuth measurement at any given time:

(a) digitization of the magnetometer signal, $\leq 0.3^\circ$ (section 2.7.4).

(b) misorientation of the payload and/or magnetometers, $\leq 0.5^\circ$ (section 4.2.2).

(c) possible error in calibrated phase angle $\phi_{i,0}$, $\leq 0.1^\circ$ (section 4.3.2).

(d) possible error in interpolating to a given time between successive azimuth readouts for a payload rotation rate of $\sim 1^\circ$ per second, $\leq 0.5^\circ$ (section 2.7.2).

Hence the telescope azimuth at any given time should never be in error by more than 1.4° .

These figures apply to ~~instrumental~~ errors only and do not include the statistical uncertainty associated with the detection of an X-ray source. This will be discussed in chapter 5.

4.5 A ROTATING REFERENCE MAGNETOMETER.

Up to this point, this chapter has described the azimuth measurement by a pair of crossed magnetometers mounted upon a payload which is unstabilized in azimuth. A single magnetometer, mounted horizontally and able to be driven about a vertical rotation axis, can be used to stabilize the payload within a narrow azimuth range by aligning itself in the magnetic east-west direction, thereby acting as an azimuth reference relative to which the payload may

be rotated by the desired amount.

The azimuthal angle between the telescope viewing axis and the magnetometer sensor axis must be known in order that the telescope may be directed by command towards a source of known position. This angle is obtained from a shaft encoder mounted on the magnetometer rotation axis and whose output, which is a telemetered 9 bit Gray Code, has been calibrated as a function of telescope azimuth. Its resolution is about 0.7 degrees per bit. The calibration curves prepared for MIL-1-69 and MIL-2-69 are shown in figure 4.5 although neither was used owing to malfunctions of the orientation system, and no inflight results can be quoted. Evident in each curve is a considerable "wobble" about the theoretical straight line, with the suggestion of a sinusoidal component of period 180° in azimuth.

The unknown origin of this perturbation has led to a theoretical analysis of orientation effects analogous to that for the crossed magnetometers in section 4.2.

4.5.1 Theory

The matrix formulation here differs from that of section 4.2 only in that the magnetometer mounting rotates. A co-ordinate system $(\underline{i}^R, \underline{j}^R, \underline{k}^R)$ is thus constructed to describe the rotating mount relative to the payload axes $(\underline{i}, \underline{j}, \underline{k})$. The parameters used are analogous to those of section 4.2 and fig. 4.6 illustrates the geometry. Note that ϕ is magnetic azimuth, and the angle measured by the shaft encoder is the angle ψ^R , generated by a rotation about the axis \underline{k}^R , beginning from the vertical $(\underline{j}, \underline{k})$ plane which contains the telescope axis.

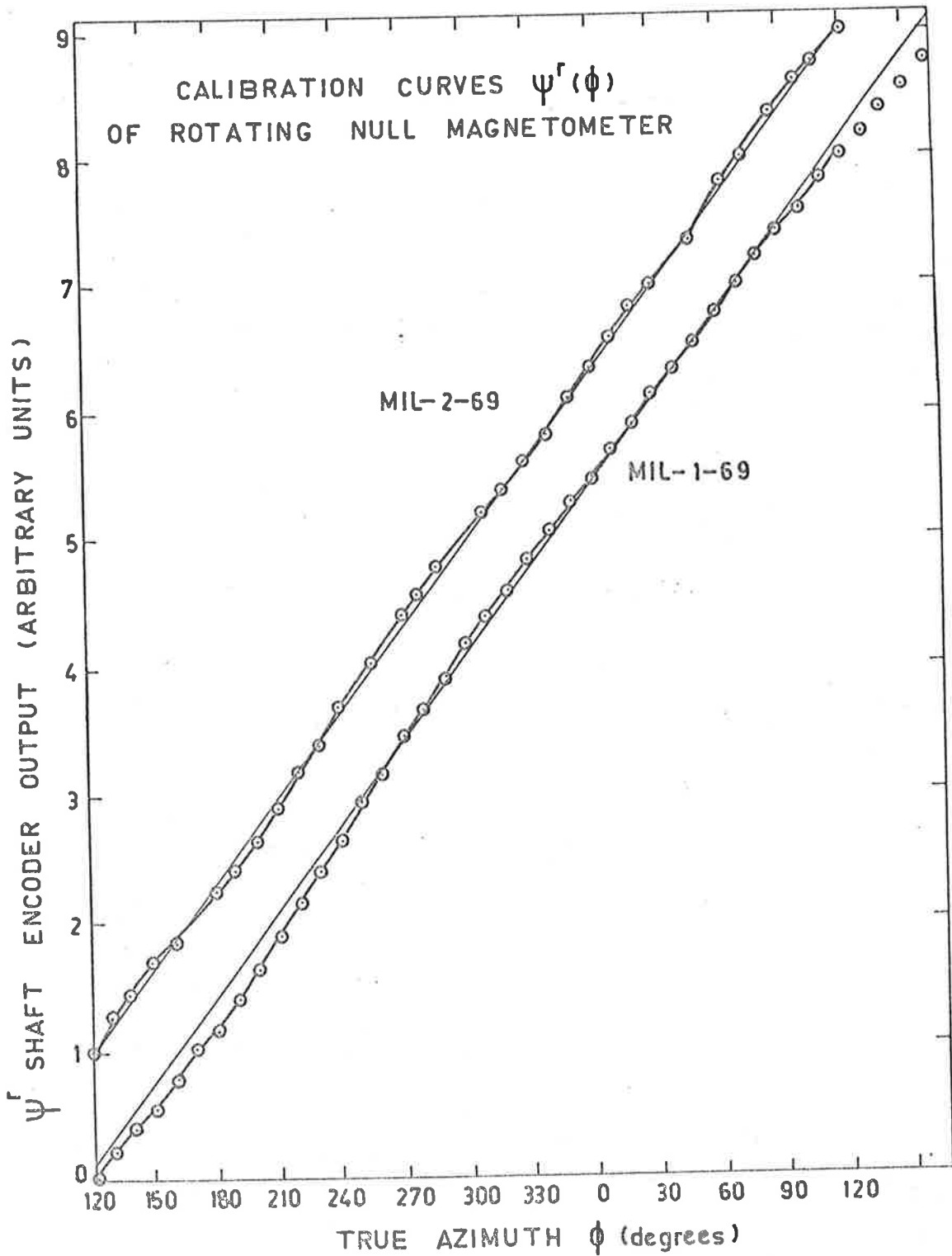
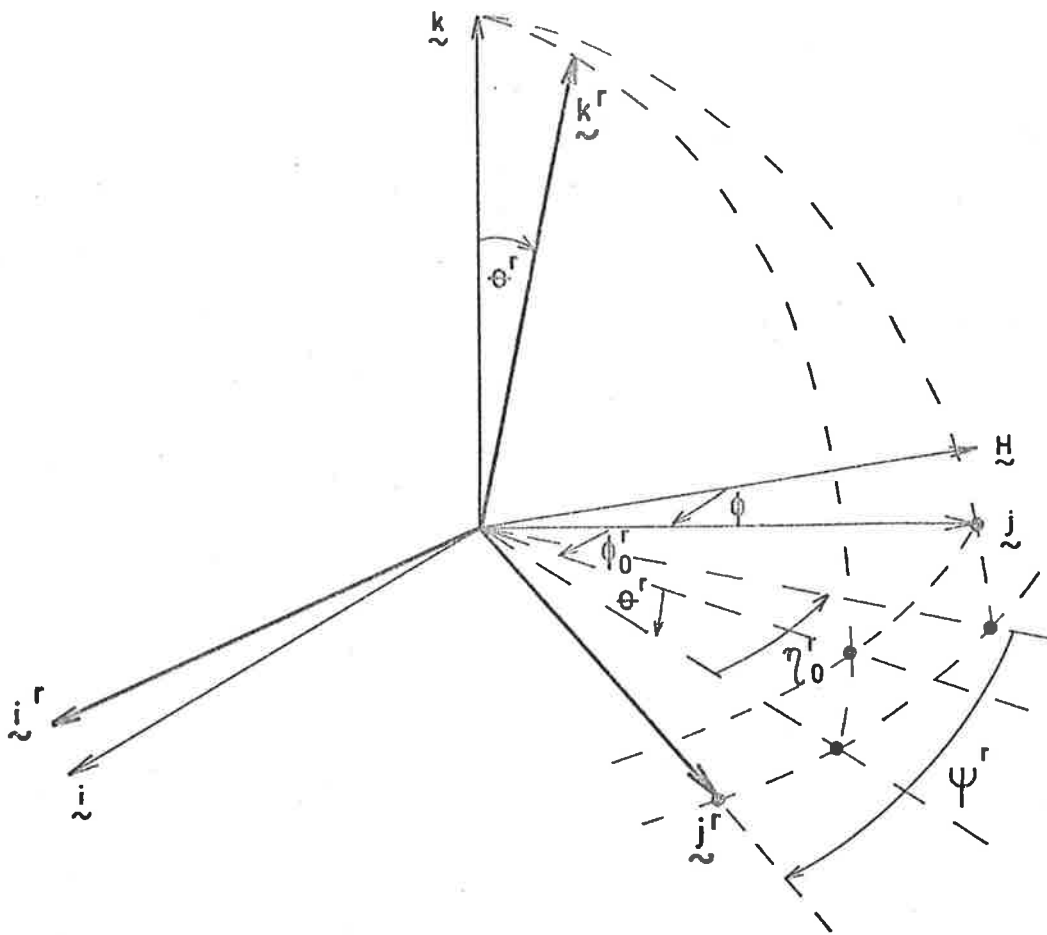


Fig: 4.5 Calibration curves of the rotating reference magnetometer for flights MIL-1-69 and MIL-2-69.



Transformation between rotating magnetometer axes ($\underline{i}_r, \underline{j}_r, \underline{k}_r$) and payload axes ($\underline{i}, \underline{j}, \underline{k}$).

Fig: 4.6.

If the sensor axis is given by \tilde{j}^r and orientation is perfect, the null magnetometer calibration curve $\psi^r(\phi)$ is given by:

$$\psi^r(\phi) = 90^\circ - \phi \dots\dots\dots 4.11$$

which is a straight line of unit slope. Misorientation is now introduced and the resulting perturbations on equation 4.11 are examined.

The mounting coordinates in terms of payload axes are given by:

$$\tilde{x}^r = B^r C^r D^r E^r \tilde{x} \dots\dots\dots 4.12$$

where $\tilde{x}^r = \begin{bmatrix} \tilde{i}^r \\ \tilde{j}^r \\ \tilde{k}^r \end{bmatrix}$, $\tilde{x} = \begin{bmatrix} i \\ j \\ k \end{bmatrix}$,

$$B^r = \begin{bmatrix} \cos \psi^r & -\sin \psi^r & 0 \\ \sin \psi^r & \cos \psi^r & 0 \\ 0 & 0 & 1 \end{bmatrix}, \quad C^r = \begin{bmatrix} \cos \eta_0^r & \sin \eta_0^r & 0 \\ -\sin \eta_0^r & \cos \eta_0^r & 0 \\ 0 & 0 & 1 \end{bmatrix},$$

$$D^r = \begin{bmatrix} 1 & 0 & 0 \\ 0 & \cos \theta^r & -\sin \theta^r \\ 0 & \sin \theta^r & \cos \theta^r \end{bmatrix}, \quad E^r = \begin{bmatrix} \cos \phi_0^r & -\sin \phi_0^r & 0 \\ \sin \phi_0^r & \cos \phi_0^r & 0 \\ 0 & 0 & 1 \end{bmatrix}.$$

To describe the orientation of the sensor in completely general terms it is necessary only to produce a rotation by an angle $-\tau$ about \tilde{i}^r i.e. make the probe axis non-perpendicular to the mount rotation axis. Rotation about \tilde{j}^r is trivial due to symmetry and about \tilde{k}^r is unnecessary since it adds only a constant to the angle ψ^r already defined. Hence we rotate about \tilde{i}^r by an angle $-\tau$ to define the magnetometer coordinates $(\tilde{i}', \tilde{j}', \tilde{k}')$ where \tilde{j}' is the direction of the sensor axis:

where $\tilde{x}^i = \begin{bmatrix} i \\ j \\ k \end{bmatrix}$, $A^r = \begin{bmatrix} 1 & 0 & 0 \\ 0 & \cos \tau^r & -\sin \tau^r \\ 0 & \sin \tau^r & \cos \tau^r \end{bmatrix}$ 4.13

To find the magnetometer orientation \tilde{x}^i in terms of space axes X , we combine equations 4.2, 4.12 and 4.13 to obtain

$$\tilde{x}^i = A^r B^r C^r D^r E^r ABC \tilde{x} \quad \dots\dots\dots 4.14$$

The response of the sensor axis \tilde{j}^i to the field \tilde{F} is by analogy with equation 4.6:-

$$\tilde{j}^i \cdot \tilde{F} = A_{zi}^r B_{ij}^r C_{jk}^r D_{kl}^r E_{lm}^r A_{mn} B_{np} C_{pq} F_q \dots\dots\dots 4.15$$

The necessary null constraint, $\tilde{j}^i \cdot \tilde{F} = 0$ is now applied and values of the function $\psi^r(\phi)$ computed for different sets of orientation parameters in order to examine any perturbations introduced into equation 4.11

4.5.2 Computations.

Results are plotted in fig. 4.7 in the form of the error in ϕ , $\epsilon^r(\phi)$, which results from incorrectly assuming equation 4.11 to be valid. That is, $\epsilon^r(\phi) = 90^\circ - (\psi^r + \phi)$. The curves are labelled with numbers corresponding to the parameter list given in table 4.6 which also tabulates the maximum of each $\epsilon^r(\phi)$.

Table 4.6 Parameter lists for the curves of figure 4.7

Curve #	θ	ϕ_0	θ^r	ϕ_0^r	τ^r	$\max \epsilon^r(\phi) $
3	1	0	1	0	1	4.4°
4	1	45	1	0	1	4.0°
10	1	135	1	0	1	1.7°
12	1	225	1	0	1	1.7°
14	1	315	1	0	1	4.0°
15	3	90	1	45	1	8.3°
16	1	90	1	45	3	4.0°
19	1	0	3	0	1	8.7°

Figure 4.7 shows sinusoidal forms for all $\epsilon^r(\phi)$, of period 360° . Other configurations (not shown here) were also computed but no 180° period component could be produced by manipulation of orientational parameters. However, table 4.6 does show that substantial errors in pointing azimuth can be expected if insufficient care is taken in the orientation of the magnetometer, its rotating mount, and the balancing of the payload.

4.6 EFFECTS OF CONTAMINANT MAGNETIC FIELDS.

Materials which may produce undesirable magnetic effects are kept to a minimum during payload construction. However, small amounts are inevitably present and can produce both permanent and induced fields which contaminate the geomagnetic field. Such materials exist in the Nicad batteries, in Dept. of Supply flight support equipment, in the payload ballast

ROTATING NULL MAGNETOMETER
 AZIMUTH ERROR $\epsilon^r(\phi)$ DUE TO MISORIENTATION

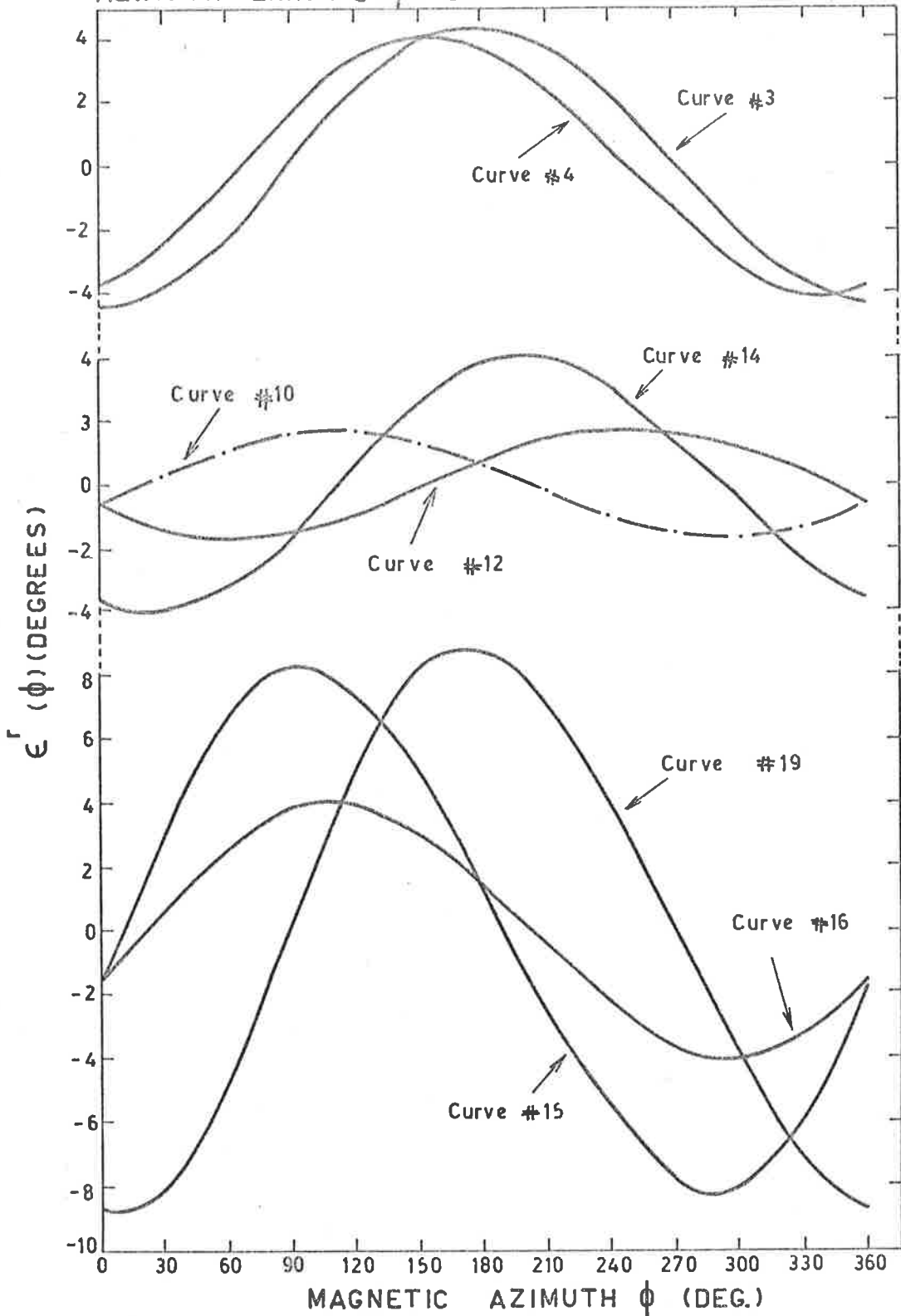


Fig: 4.7 Misorientation errors in the azimuth measured by a null magnetometer, for orientational parameters listed in table 4.6.

(iron dust), and in the graded shield telescope which contains a cylindrical, high permeability, conetic shield intended to minimize magnetic effects in the 7.5 inch P.M. tube. These materials and their fields may have significant effects upon both the crossed magnetometers and the null magnetometer.

4.6.1 Permanent fields.

Each of the crossed magnetometers will sense a constant component of any permanent field. Consequently, the only effect will be to change the mean level of each sinusoid by an amount independent of the azimuth angle.

However a rotating reference magnetometer will be differently affected, since it senses zero resultant magnetic field, and unless the payload field is fortuitously in the vertical direction, the direction of zero resultant field will differ from that of zero geomagnetic field as the payload rotates in azimuth. A quick analysis shows that the difference δ between the directions is a sinusoidal function of azimuth, with period 360° . The maximum value δ_{\max} exceeds 1° for a permanent field having a horizontal component in excess of about 400γ at the magnetometer. Hence although permanent fields may affect the null magnetometer calibration, the perturbation so produced does not by itself explain the discrepancies in figure 4.5.

4.6.2 Induced fields.

A highly permeable body with a two-fold vertical axis of symmetry will generate an induced magnetization field of 180° symmetry, as it rotates about this vertical axis. An example is a hollow right cylinder, e.g. of conetic shielding material, with its long axis in the horizontal plane. If the symmetry axis is gradually inclined to the vertical direction, the 180° periodic effect will be progressively destroyed. A simple case is that in which the inclination to the vertical is by the angle I , the geomagnetic dip angle. Qualitative considerations lead us to expect that the maximum perturbation as a function of azimuth should occur with the cylinder long axis parallel to F . The azimuth angle 180° from this position may produce a minor magnetization field enhancement, thereby introducing a small 180° component in the perturbation field.

It is thus possible that the conetic shielding may have had the observed effect on the reference magnetometer (fig. 4.5). Similar effects upon the crossed magnetometers were investigated by plotting the residuals $R_{i,j}$ ($i = 1,2$) as a function of azimuth ϕ_j (equation 4.8), using the correct phase angle $(\phi_{j,0} - D)$. Any irregularities or periodic components in the magnetometer calibration data with periods other than 360° should reveal themselves in such an analysis.

Figure 4.8 shows the two residuals R_1 and R_2 for the MIL-1-69 preflight calibration. The form of R_1 is consistent with the suggested hypothesis and contains an appreciable component of period 180° . R_2 has an essentially random scatter about the mean and reveals no obvious periodic behaviour. However, this magnetometer may not have been advantageously oriented to observe the effect.

It is thus suggested that the perturbations evident in the calibration curves of both the crossed magnetometers and the rotating reference magnetometer, may have their origins in the permanent and induced magnetic fields which arise from the presence in the payload of small amounts of magnetic materials.

MIL-1-69 : Crossed magnetometer calibration residuals

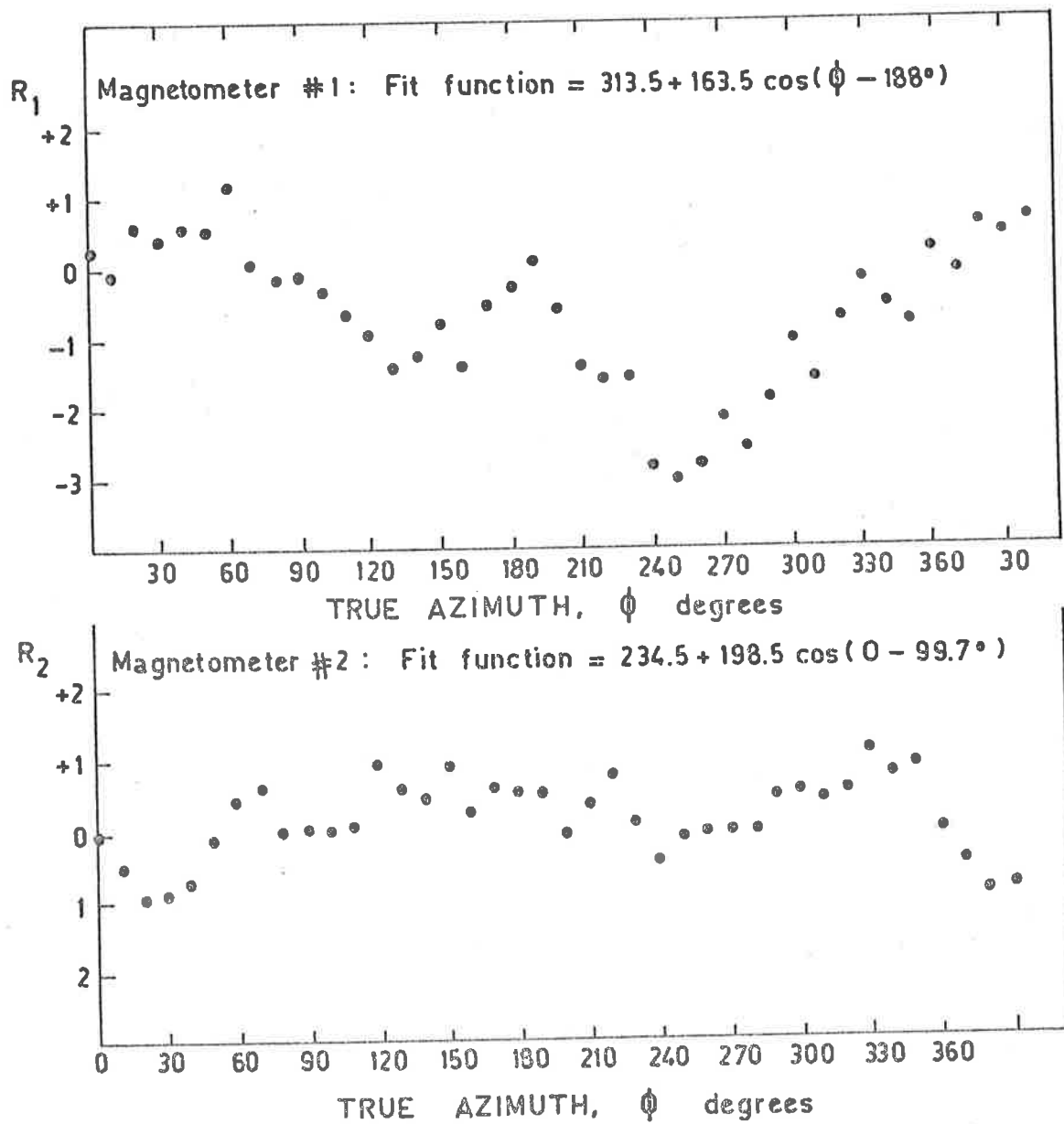


Fig: 4.8 Crossed magnetometer calibration residuals as a function of azimuth for the flight MIL-1-69.

DISCRETE SOURCE RESULTS, $320^\circ < l^{II} < 350^\circ$ 5.1 INTRODUCTION

In this chapter I present a report of a search for weak X-ray sources in the range of galactic longitudes $320^\circ < l^{II} < 350^\circ$, conducted during the flight MIL-1-68 (see tables 1.4 (a) and (b)). These sources previously have had limited exposure to observation because of their southern celestial locations, and some of the results are the first reported for photon energies in excess of 15 KeV. A brief preliminary report has already been published (Thomas 1968a). The strong discrete sources GX 3+1, Sco XR-1 and GX 354-5 were also observed during this flight and these results have been published elsewhere (Buselli et al. 1968, Buselli 1968, Clancy 1968, Davison 1968).

The instrumentation has been described in chapter 2. The results were obtained with the active telescope which was set at a constant zenith angle of 32° . In order to adequately survey the sky region of interest, it was driven back and forth in azimuth by means of radio commands. Source positions given by the NRL group (Friedman et al. 1967, this thesis section 1.1.1) were the nominal objects of interest and the region of sky scanned during the whole flight is shown in fig. 5.1. The source positions plotted are those of NRL, the Lockheed group (LL, Fisher et al. 1966) and the University of Adelaide (Cen X-2 Harries et al. 1967; GX 3+1 and GX 354-5, Buselli et al. 1968). A more detailed diagram of source positions as of August 1970, for the galactic disc between longitudes 320° and 350° , is presented in figure 5.5 and will be discussed in section 5.5.

UAX-032

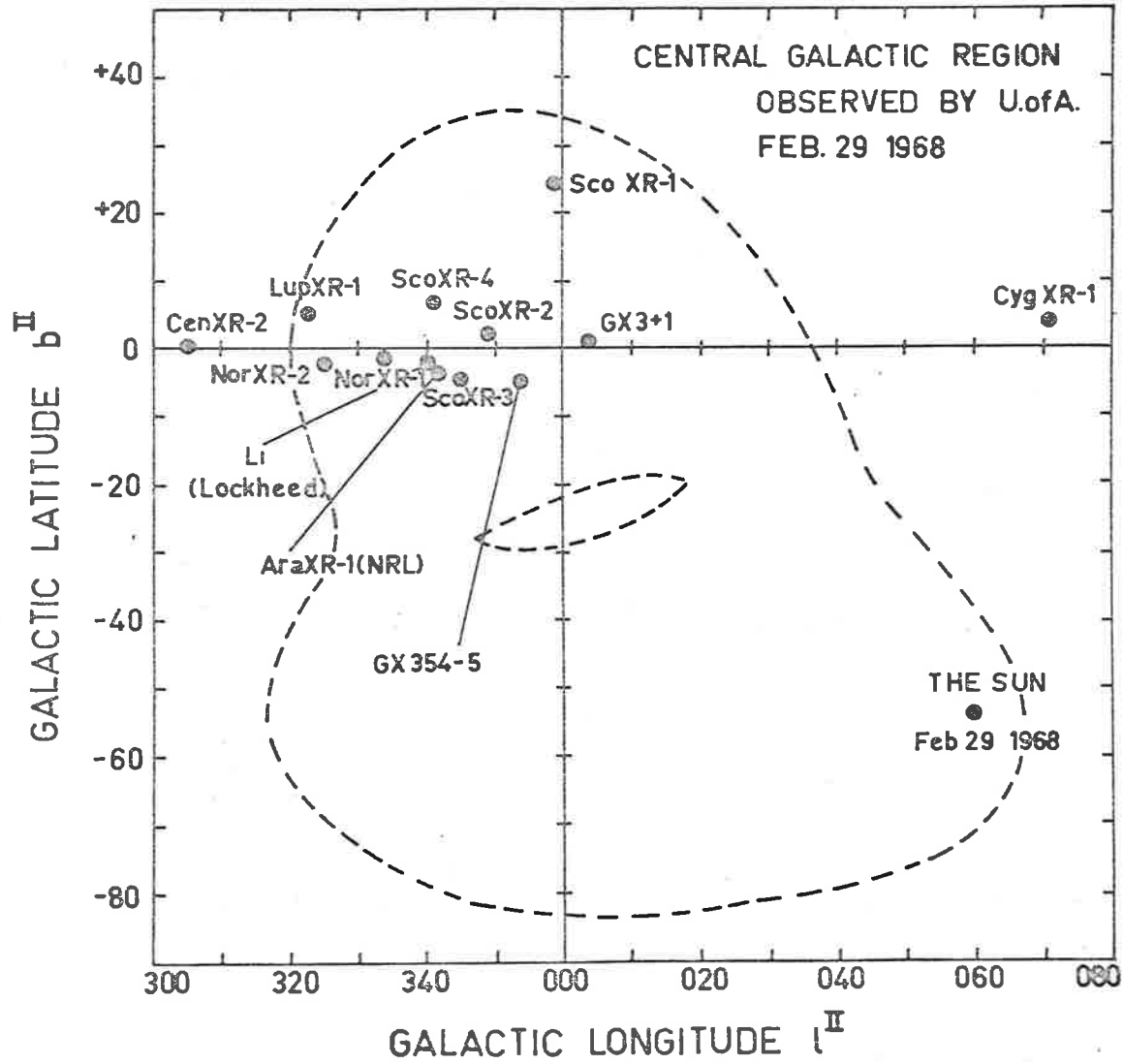


Fig: 5.1 Region of sky scanned in the experiment MIL-1-68.

3.2 DATA ANALYSIS

The count rate data for each energy channel were analysed by generating count rate versus azimuth profiles for each 10 minute interval of observing time. Azimuth bins of width 5° were used. By this means a strong source can be detected and the azimuth and time of maximum telescope response found. The accurate source position and raw count rate spectrum then easily follow by performing a least squares fit of the known telescope response function to the count rate data with background subtracted.

No strong sources were detected in the $320^\circ < l^{\text{II}} < 350^\circ$ survey however, and the approach adopted was to single out suspected source positions, as given by the NRL group, and improve the statistical precision of the observations by superposing the data of successive 10 minute intervals, making due allowance for the approximate azimuthal motion of each suspected source. The summing of two or more energy channels was sometimes necessary also. Data intervals were used only in which the mean source zenith angle \bar{z} was such that $|\bar{z} - 32^\circ| \leq 4^\circ$ in order that the gain in statistical weight was not offset by degradation of any source count rate peak due to collimator shadowing at large off-axis angles.

The superposition of up to an hour of data in this way resulted necessarily in the use of mean values for a number of quantities essential to the analysis. For example the response triangle azimuthal width varies significantly for azimuthal scans at different off-axis zenith angles.

The mean width \bar{W} taken over n ten minute intervals of which the i^{th} ($1 \leq i \leq n$) contained N_i telemetry frames of data was taken to be

$$\bar{W} = \frac{\sum_{i=1}^n W_i(z_i) N_i}{\sum_{i=1}^n N_i} \quad \text{5.1}$$

where $W_i(z_i)$ is the width for the mean source zenith angle z_i during the i^{th} data interval. Note that in addition to the effect on W_i of the telescope aperture, W_i if in units of degrees of azimuth is further modulated by z_i and is related to the angular FWHM (see section 3.4.3) of the telescope through

$$W_i(z_i) = 2 (\text{FWHM}) \operatorname{cosec} z_i (z_i \neq 0).$$

For $z_i = |z - 32^\circ| \neq 0$, the response function departs more from the assumed triangular shape. However, for these weak sources, and for simplicity in the least squares fit procedure, the assumed triangular shape was considered adequate.

A simple least squares fit method was used. First, the background was estimated (by averaging over "off-source" times) and subtracted from the observed mean counting rate for each 5° bin. The resulting counting rate, $n(\phi_i)$ at azimuth ϕ_i was then fitted by a function $f(\phi) = A, g(\phi - \phi_0)$, where g is the triangular response centred on azimuth ϕ_0 and given by

$$g(\phi - \phi_0) = \begin{cases} 1 - \frac{2|\phi - \phi_0|}{\bar{W}}, & |\phi - \phi_0| \leq \frac{1}{2} \bar{W} \\ 0, & \therefore |\phi - \phi_0| > \frac{1}{2} \bar{W} \end{cases} \quad \text{5.2.}$$

Minimization with respect to A of the error function $E = \frac{\sum_i (n(\phi_i) - f(\phi_i))^2}{\sum_i V(n(\phi_i))}$

where $V(n(\phi_i))$ is the variance of the datum point $n(\phi_i)$, gives the best value of the amplitude of the response as:

$$A = \frac{\sum_i \frac{g(\phi_i - \phi_0) n(\phi_i)}{V(n(\phi_i))}}{\sum_i \frac{g^2(\phi_i - \phi_0)}{V(n(\phi_i))}}$$

with a standard deviation

$$\sigma(A) = \left[\sum_i \frac{g^2(\phi_i - \phi_0)}{V(n(\phi_i))} \right]^{-\frac{1}{2}} \quad \text{--- 5.3}$$

For this ϕ_0 then, the minimum value of E , $E_{\min}(\phi_0)$, is consequently calculated. Variation of the parameter ϕ_0 then determines the azimuth for which $E_{\min}(\phi_0)$ is itself a minimum. The error in this "best" azimuth is given by (Giacconi et al. 1968)

$$\sigma(\phi_0) = \frac{\bar{W}}{2\sqrt{3}} \cdot \frac{\sigma(A)}{A} \quad \text{--- 5.4}$$

It should be noted that not everybody uses equation 5.4 to compute $\sigma(\phi_0)$. For example, Lewin of MIT uses as a "rule of thumb" the telescope FWHM divided by half of $A/\sigma(A)$.

Having found the best fit count rate $A \pm \sigma(A)$ for each channel, a mean off-axis shadowing correction must be applied. Its calculation is analogous to the mean triangle width calculation and is given by

$$\bar{C}_s = \frac{\sum_{i=1}^n C_s^i(\bar{z}'_i) N_i}{\sum_{i=1}^n N_i}$$

where $C_s^i(\bar{z}'_i)$ is the correction applicable to the mean off-axis angle \bar{z}'_i during the i^{th} data interval. Finally corrections are applied for atmospheric and telescope window attenuation, NaI(Tl) crystal transparency, energy resolution and iodine K-escape in order to obtain a final, corrected source spectrum (see chapter 3).

5.3 NORMA XR-1 AND ARA XR-1

The method of analysis described above was applied to the galactic disc region between longitudes 320° and 350° . Since no significant background variations were observed as a function of azimuth in "off-source" directions, these data were combined during the time interval of source observation in order to obtain a background of high statistical precision.

The completion of the analysis resulted in the observation of significant hard fluxes from two sources and upper limits for a number of others. These two sources were observed respectively at azimuths within 0.7° and 1.0° of the NRL positions nominated for Nor XR-1 and Ara XR-1.

5.3.1 The Spectrum of Norma XR-1

In the energy range 27 to 57 KeV, Nor XR-1 was observed to have an intensity equal to 3.5 standard deviations above the background counting rate. This is the only balloon-borne observation of this source reported to date. Figure 5.2 shows the spectral results for Nor XR-1. Also plotted are the measurements due to NRL and to the Leicester group (Cooke and Pounds, 1970). Two sets of Adelaide points are displayed, corresponding to the use of two different assumed spectra for the calculation of energy-dependent corrections. These spectra are respectively a power law with exponent $\lambda = 1.5$, and an exponential with $kT = 13$ KeV (see Section 1.1.4). The NRL measurement is inconsistent with all other data and will not be discussed further.

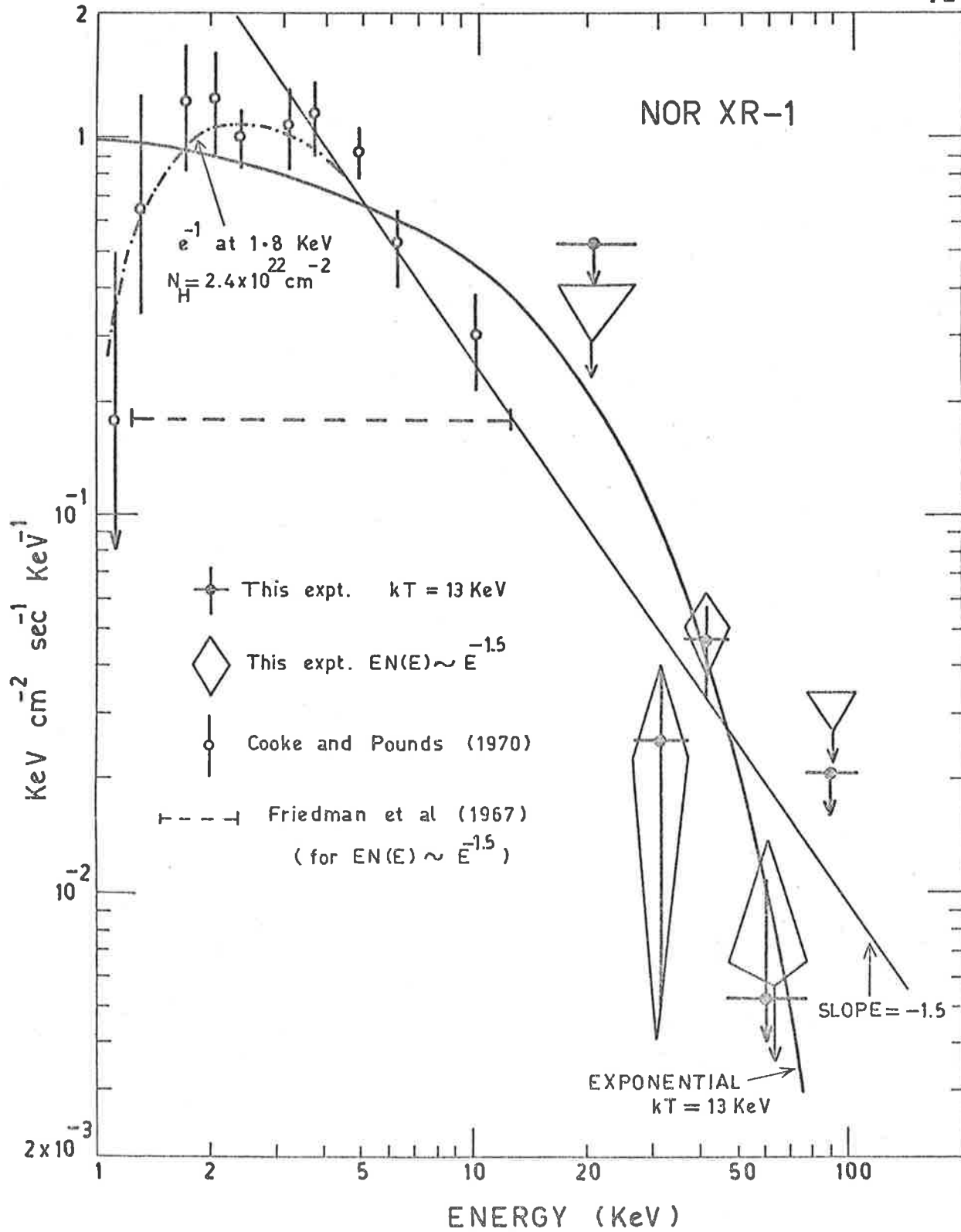


Fig: 5.2 Spectral results for Nor XR-1.

Cooke and Pounds found that their data alone were best fitted by an exponential spectrum with $kT = 5$ KeV, attenuated by interstellar matter having a column density of $\sim 4 \times 10^{21}$ H atoms cm^{-2} . This column density was calculated using the total X-ray absorption cross-section per H atom for normal cosmic abundances given by Brown and Gould (1970). However, their data and ours combined are best fitted by the power law with $\lambda = 1.5$, with interstellar attenuation corresponding to a column density of $\sim 2.4 \times 10^{22}$ H atoms cm^{-2} rather greater than the Leicester value. The exponential fit to the combined data is not as good and also yields a value for the column density $\ll 10^{21}$ H atoms cm^{-2} .

With regard to the power law fit, it may be significant that a supernova remnant P 1613-50 lies very close to the source position (Cooke and Pounds 1970). The Crab Nebula is of course a supernova remnant and has a power law X-ray spectrum. The measured column density of 2.4×10^{22} H atoms cm^{-2} may be compared with results of Rappaport et al. (1969 a, b) who find $\sim 2 \times 10^{22}$ cm^{-2} for the nearby Scorpius-Sagittarius region.

Thus the revision of the spectrum of Nor XR-1 which has resulted from the present high energy measurements, has produced a column density in much better agreement with that from other nearby sources than was obtained by Cooke and Pounds using low energy data only. This result is consistent with the proposition that all these sources lie in the same galactic spiral arm (see section 1.1.1).

5.3.2 The Spectrum of Ara XR-1

Ara XR-1 was observed to be 3.2 standard deviations above the background count rate in the energy range 27 to 57 KeV. The derived spectrum is presented in figure 5.3. The points have been corrected for atmospheric absorption, etc. by assuming an exponential spectrum with $kT = 11$ KeV. For comparison, the fit function $EN(E)dE = 1.4 \exp\left(\frac{-E}{11}\right)dE$ is shown, together with low energy attenuation corresponding to a column density of 2×10^{22} H atom cm^{-2} in the line of sight as for Nor XR-1. Also shown are data points due to (a) Lewin et al. (1969) for their source M2, (b) Fisher et al. (1968) for their source L3, (c) Bunner et al (1969) for GX 340-2, and (d) the NRL measurement of Ara XR-1. The points (c) and (d) extend over a broad energy interval and have been adjusted to correspond to an 11 KeV spectrum.

The fit function provides a very good fit to the data over the complete observed energy range. At present it is not certain that all points apply to the same source, but figure 5.5 shows that all the sources listed above do have error boxes which overlap, sharing a small region of sky centred at about $RA = 17^{\text{h}} 8^{\text{m}}$, $Dec. = -45.0^{\circ}$. The complex of sources observed in the Ara region will be further discussed in section 5.5.

If the points shown on fig. 5.3 do originate at a single source, the excellent spectral fit indicates that any time variations between the dates of the observations have been small. The low energy turnover incorporated in the fit by assuming a Hydrogen column density of 2×10^{22} atoms cm^{-2} is hypothetical and it can be seen that there are at present insufficient low energy data (≤ 5 KeV) to determine whether the amount of interstellar absorption (if any) is comparable with that in the direction of Nor XR-1.

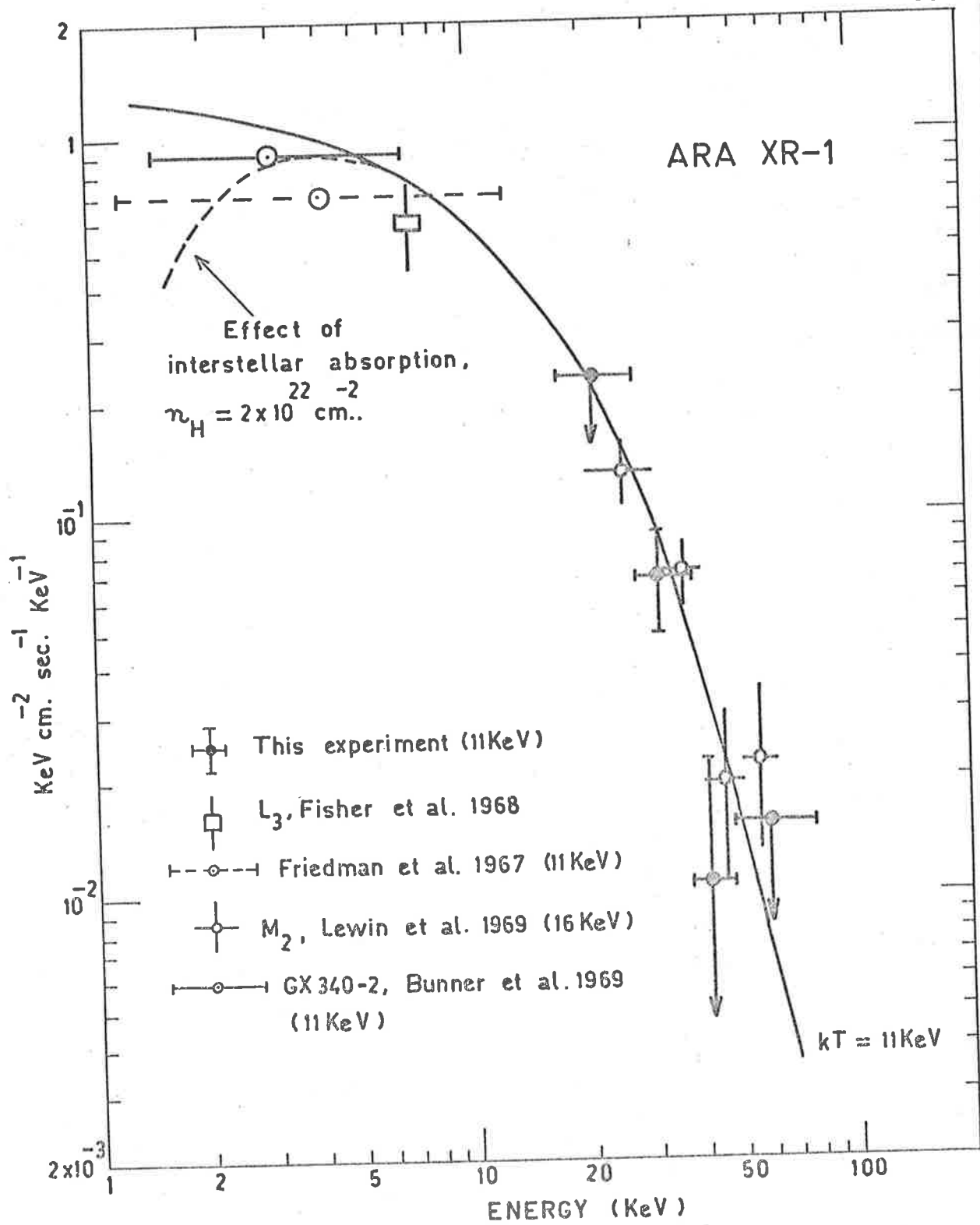


Fig: 5.3 Spectral results for Ara XR-1.

The spectral results obtained for both sources, Nor XR-1 and Ara XR-1, are presented in tabular form in table 5.1.

5.4 UPPER LIMITS

Other NRL sources for which searches were made were Lup XR-1 (see also Chodil et al. 1967), Nor XR-2 (also Lewin et al. 1968a, Cooke and Pounds 1970), Sco XR-2 and Sco XR-3 (Fisher et al. 1966), and Sco XR-4. Upper limits only could be assigned to these sources.

The results to date for Nor XR-2 are shown in fig. 5.4. The Adelaide upper limits correspond to 3 standard deviations above background and contain spectral corrections based on the assumption of an 11.4 KeV exponential spectrum. These upper limits are consistent with the other results plotted, both at low and high energies. The wide-band NRL result has been plotted by assuming an exponential spectrum with $kT = 11.4$ KeV and is more than a factor of two below the measurements of Cooke and Pounds (1970). It is interesting to note that the low energy data show no evidence of interstellar absorption, in contrast to Nor XR-1, indicating that the hydrogen atom column density in the line of sight to Nor XR-2 is considerably less than 10^{22} atoms cm^{-2} .

The Sun was in the field of view for a short time and no hard X-rays were detected. Satellite observations have established that the Sun emits hard X-rays in association with flares and radio bursts (Cline et al. 1968, Hudson et al. 1969). However, there was no abnormal solar activity during MIL-1-68 and no flare greater than importance 1 occurred (ESSA Solar Geophysical Reports, 1968).

Upper limits (at the 3 sigma level) for the intensities of the sources mentioned above were determined by calculating equation 5.3, using the value of ϕ_0 corresponding to the NRL source position. These upper limits, along with the Nor XR-1 and Ara XR-1 results, are tabulated in table 5.1. The spectral form assumed for each source in order to make count rate corrections is also tabulated.

Table 5.1: Discrete source intensities $320^\circ < l^{II} < 350^\circ$

	Energy Interval (KeV.)	Flux (*) or 3 σ Upper Limit (photons cm sec KeV.)	Number Spectrum Assumed	Remarks
Nor XR-1	17-27	1.95×10^{-2}	Power law	Position (this experiment) $(\alpha, \delta) = (16.5_h^\circ, -51.5^\circ)$ with uncertainty as shown in fig.5.5
	27-37	$*(7.46^{+6.00}) \times 10^{-4}$	$N(E)dE \sim E^{-2.5} dE$	
	37-47	$*(1.24^{+0.34}) \times 10^{-3}$		
	47-77	$*(1.09^{+1.18}) \times 10^{-4}$		
	77-107	3.77×10^{-4}		
Ara XR-1	17-27	1.10×10^{-2}	Exponential	Position (this experiment) $(\alpha, \delta) = (17.1_h^\circ, -45.4^\circ)$ with uncertainty as shown in fig.5.5
	27-37	$*(2.19^{+0.65}) \times 10^{-3}$		
	37-47	$*(2.58^{+2.91}) \times 10^{-4}$	$N(E)dE \sim E^{-1} \exp\left(\frac{-E}{11}\right) dE$	
	47-67	2.72×10^{-4}		
Lup XR-1	27-77	5.25×10^{-4}	Power Law	Upper limits have been computed for NRL source positions
Nor XR-2	27-77	3.25×10^{-4}	$N(E)dE \sim E^{-2.0} dE$	
Sco XR-4	27-77	3.14×10^{-4}		
Sco XR-2	27-77	$\sim 3 \times 10^{-4}$		
Sco XR-3	27-77	$\sim 3 \times 10^{-4}$		
The Sun	27-67	6.58×10^{-4}		

5.5 SOURCE LOCATIONS

Also listed in table 5.1 are the least squares fit positions obtained for Nor XR-1 and Ara XR-1, which are also shown on fig.5.5. The error boxes correspond to uncertainties of $\pm 4^\circ$ in both zenith and azimuth angles.

The azimuth uncertainty has two components, (a) the statistical uncertainty, given by equation 5.4 which is 2.5° for Nor XR-1 and 2.7° for Ara XR-1, and (b) the systematic uncertainty of the azimuth measurement, $\pm 1.4^\circ$ (see chapter 4). The zenith uncertainty of $\pm 4^\circ$ corresponds to the expected variation of zenith angle, during the period of observation of approximately 1 hour, of a source in this region of the sky.

Results obtained from this part of the sky by other workers are also shown in fig.5.5. It should be noted that the date listed beside each group of workers is the date of publication rather than observation. Figure 5.5 presents a very confusing appearance and the poor angular resolution of the measurements is immediately apparent. However, there is broad agreement between observations.

Of particular interest is the source complex at the vicinity of Ara which can be taken to include Sco XR-3 and Sco XR-4, and which requires a survey of far better angular resolution than has so far been performed. The results of Fisher et al. (1968) and Bunner et al. (1969) appear to be the most precise to date and show reasonable but not perfect agreement with each other.

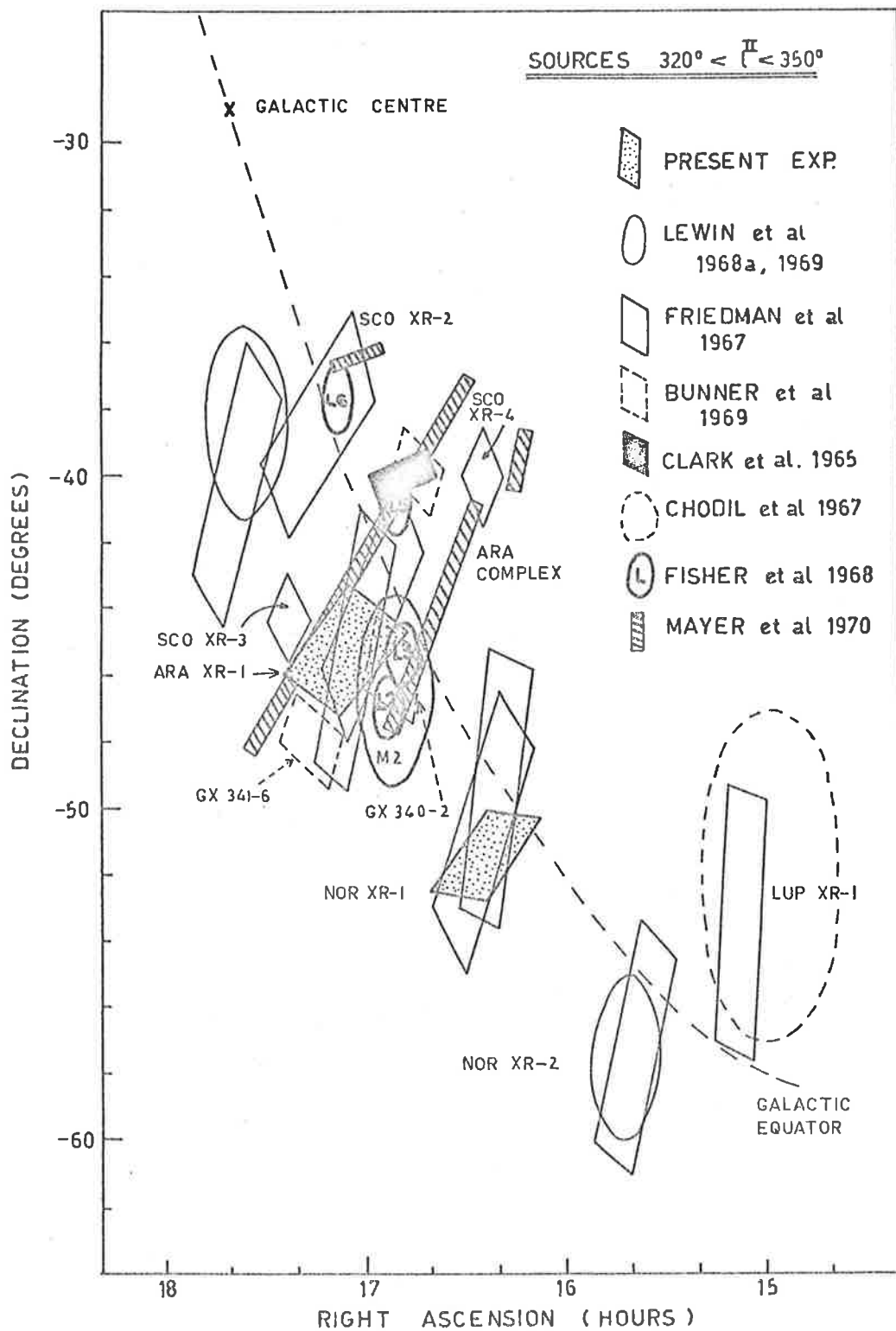


Fig: 5.5 Positional data for sources $320^\circ < l < 350^\circ$.

These results indicate that poor-resolution studies such as our experiment, and those experiments of Lewin et al. (1969) and Friedman et al. (1967) would experience difficulty in resolving separate sources in the Ara complex. The problem is especially difficult for balloon-borne experiments because of the low intensity of the high energy radiation.

Inconsistencies between different observations also exist within the Sco XR-2 complex which at the present time consists of the Lockheed group's source L6 (Fisher et al. 1968), a source designated M4 by Lewin et al. (1969) and one GX 349+2 by Mayer et al. (1970). Also associated with these sources is GX 354-5 ($\alpha = 17^{\text{h}}47^{\text{m}}$, $\delta = -36^{\circ}$, uncertainty $\sim 2^{\circ}$) observed by Buselli et al. (1968) and identified with GX-5.6 (Gursky et al. 1967). This is reported in detail by Clancy (1971).

The sources Nor XR-1, Nor XR-2 and Lup XR-1 have had little observational exposure and demand closer examination. Variability has been mentioned to account for inconsistencies which have appeared in the limited number of observations of Nor XR-2 and Lup XR-1 (McGregor et al. 1969, Lewin et al. 1968a, Cooke and Pounds 1970). The limited data available for Nor XR-1 indicates that it has suffered little variation in intensity between observations (Cooke and Pounds 1970). The inability of Lewin et al (1968a, 1969) to detect a significant flux from Nor XR-1 during the experiment in which they observed Nor XR-2, may suggest variability in either (or both) sources of high energies since both regions of sky received comparable exposure times from them and comparison of figures 5.2 and 5.4 show that Nor XR-1 was the stronger of the two at the time of our experiment.

The galactic disc region $320^\circ < l^{\text{II}} < 350^\circ$ requires further intensive study. It has been shown to be rich in X-ray sources, as is the case for the adjoining Centaurus region also (Cooke and Pounds 1970). From our work it is clear that to be successful, future experiments directed towards this part of the sky should possess angular resolutions better than about a tenth of a degree (rocket-borne). A large area proportional counter plus rotating modulation collimator experiment similar to that carried out by Schnopper et al. (1970) in Sagittarius, would give resolutions of the order of **one minute of arc**, and would be a significant contribution. Intensity thresholds for such an experiment should be of the order of 0.1 and $0.05 \text{ KeV cm.}^{-2} \text{ sec.}^{-1} \text{ KeV}^{-1}$ at energies of 1 and 10 KeV respectively. For balloon-borne experiments with an intensity threshold of about $0.01 \text{ KeV cm.}^{-2} \text{ sec.}^{-1} \text{ KeV}^{-1}$ and with an accurate telescope pointing system, an angular resolution of $\sim 1^\circ$ seems a reasonable goal for which to aim.

CHAPTER 6ATMOSPHERIC X-RAYS, I6.1 INTRODUCTION:

Observations of cosmic X-rays at balloon altitudes are hampered by the presence of a large background produced by the interactions of cosmic rays with the atmosphere and telescope surroundings. Reduction of this background is essential if X-ray astronomy studies are to be effectively pursued, and consequently an understanding of the processes by which the background is produced is desirable.

6.1.1. The Telescope Background:

Three distinct sources contribute to the total background count rate (B_{tot}) of the telescope.

(a) A diffuse flux (B_{atm}) of photons which enters through the telescope aperture and which is produced by cosmic ray interactions with atmospheric nuclei; the count rate B_{atm} is proportional to the telescope geometric factor G cm.² ster. (see chapter 3), and is a function of (i) photon energy E (KeV), (ii) the depth of residual atmosphere p (gm.cm⁻²), (iii) the geomagnetic cut-off rigidity (since this determines the incident primary cosmic ray spectrum), (iv) the prevailing cosmic ray flux at the time of the experiment, and perhaps (v) the telescope zenith angle Z . Charged particles entering through the forward aperture have been found to contribute $\approx 2\%$ to B_{atm} (Bleeker and Deerenberg 1969).

(b) A cosmic ray induced leakage background (B_1) which is a result of the detector's characteristics and of the atmospheric radiation environment. It is caused by high energy gamma rays which pass through the guard scintillator without interaction and which subsequently Compton scatter in the central crystal, and by the high energy daughter products of interactions occurring in and around the telescope which also evade the anticoincidence system. B_1 is a function of (i) E , (ii) p , (iii) cut-off rigidity, (iv) time, and (v) the physical and geometrical configuration of the detector and its guard system which leads to variations in the magnitude and properties of B_1 from detector to detector. B_1 is independent of G and can only be separated from B_{atm} by employing a variable opening solid angle. Recently an experiment was flown in which the active telescope aperture was periodically screened by another scintillator in anticoincidence with the telescope central detector; however, no data regarding B_1 and B_{atm} were obtained, as there was a major malfunction of the observatory. Hence, in the work done to this date, the separate components B_{atm} and B_1 cannot be distinguished and will be collectively referred to as the local background B_{loc} , as opposed to the count rate produced by the diffuse background of cosmic origin, B_{cos} . That is, $B_{loc} = B_{atm} + B_1$.

(c) The third component is the cosmic diffuse X-ray background, B_{cos} (see chapter 3) which enters the collimator opening angle after attenuation by the residual atmosphere. It is a function of (i) E , (ii) $p \sec Z$, and (iii) G .

It is independent of cut-off rigidity and suffers no known observable time variations. It contributes significantly to the total background rate at pressures $p \lesssim 10 \text{ gm. cm}^{-2}$, increasing with decreasing p , as opposed to B_{loc} which decreases.

The uncertainty of the relative contributions of B_{atm} and B_1 and the dependence of B_1 on detector configuration will lead to difficulties in the intercomparison of the results of different workers on the cosmic ray production of X-rays in the atmosphere. For these reasons conversion of measured background rates to absolute atmospheric X-ray fluxes is a rather speculative venture. However it is believed that B_1 has been reduced most effectively in the active telescope described in previous pages as a result of background rejection techniques **which** are generally superior to those of other detectors for which atmospheric photon results have been reported in detail. This fact together with the small effective solid angle of $\sim 2 \times 10^{-2}$ ster means that the results presented in this chapter apply to unidirectional atmospheric X-ray fluxes more accurately than any others published to date.

It should be emphasized that since different detectors may be measuring fluxes of substantially different origins owing to the B_1 ambiguity, intercomparisons must be made with care. For the same reason, corrections of count rates to absolute atmospheric X-ray fluxes is uncertain and in this chapter conclusions will be mostly drawn using raw, uncorrected count rates only.

6.1.2. The atmospheric radiation environment.

The cosmic radiation within the atmosphere consists of a number of components which can be classified in a number of ways and the following is a very brief précis of the currently accepted facts (Hayakawa, 1969a). Penetrability of matter is one classification criterion which allows the division into two components, a hard component which penetrates $\gtrsim 10$ cm. of lead and a non-penetrating soft component.

The production of a shower of secondary particles by interactions of primaries with matter provides another means of classification. One type of shower is generated in small thicknesses of matter and its secondaries emerge at large angles and are rapidly absorbed. This electronic or E-component is associated with the soft component and is accounted for by the theory of the cascade shower initiated by electrons and photons, and sustained by pair production, bremsstrahlung and Compton scattering. The other type of shower is generated with large mean free paths and its secondaries are very penetrating with little angular spread. This is associated with the hard component and nucleons and charged pions are its primary and secondary particles. The shower is produced by a combination of multiple meson production and a cascade process and is denoted as the nuclear -active or N-component of cosmic rays. At high energies both E-andN-showers occur together, the E-showers being initiated by the decay of neutral pions.

At sea-level most cosmic rays are neither E nor N-particles but form the penetrating component consisting of hard muons.

The manner in which this total radiation environment interacts with the active telescope is then responsible for the observed local background. The altitude dependence or transition curve, of the total background rate in the energy range 37 to 47 KeV for the flight MIL-1-68 is plotted in figure 6.1 as a function of slant atmospheric depth ($= p \sec Z \text{ gm.cm.}^{-2}$, $Z=32^\circ$). The count rate increase as the balloon reaches float depth, for $p \sec Z \leq 10 \text{ gm.cm.}^{-2}$, is due to the contribution B_{cos} of the cosmic diffuse background which becomes progressively less attenuated by the decreasing thickness of the overlying air. At slant depths exceeding 10 gm.cm.^{-2} , the count rate increases, reaches a maximum at about 100 gm.cm.^{-2} , and then decreases.

The shape of the transition curve at depths greater than 10 gm.cm.^{-2} , is broadly understood from N- and E-cascade shower theory and is characteristic of secondary cosmic radiation (Hayakawa 1969a). For example, a 1 GeV cosmic ray proton interacting with atmospheric nuclei will lead to the multiple production of charged and neutral pions which initiate E- cascades of electrons, positrons and photons. There is a rapid increase in the number of particles in the shower until the average particle energy is degraded below that necessary for further secondary production, and the number of particles reaches a maximum (the Pfofzer maximum at an atmospheric pressure of about 100 gm.cm.^{-2}).

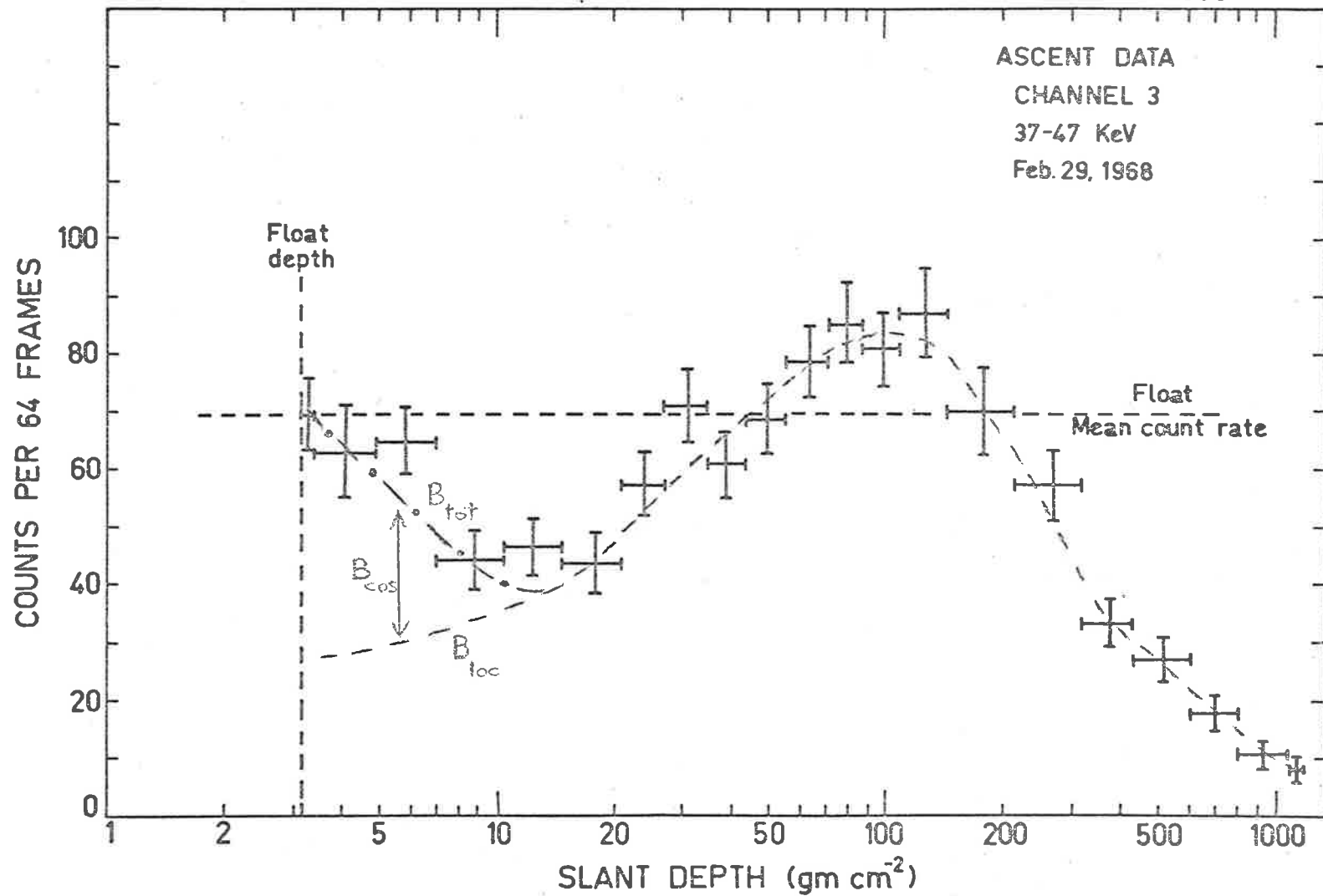


Fig: 6.1 The active telescope transition curve (37 - 47 KeV) as a function of slant atmospheric depth (= vertical depth/cos(zenith angle)) for MIL-1-68. The background components B_{loc} and B_{cos} (see text) are shown.

It then decreases due to atmospheric attenuation with a constant e-folding attenuation length ($L \text{ gm.cm}^{-2}$) between about 200 and 700 gm.cm^{-2} . The rate of decrease then slows down due to (a) the increasing contribution of hard muons relative to the severely attenuated soft component, and (b) crustal radioactivity.

Thus it would seem that the broad features of figure 6.1 are understood. However, detailed analysis reveals some anomalous features which may be due to phenomena in the secondary cosmic radiation which have not been observed before because of inadequate techniques of background rejection. A study of the atmospheric background is then of value for this reason and also for the necessity of understanding the background production processes in the detector.

6.2. TRANSITION CURVES, $200 \leq P \leq 700 \text{ GM.CM}^{-2}$

The attenuation length L of the exponential portion of the count rate transition curve has been determined as a function of photon energy for four flights and for both the active and graded shield telescopes. Differences are observed between different flights, and between the two telescopes. Further, values of L obtained for the active telescope guard rates differ from those of the energy channel count rates.

6.2.1. Results.

Fig. 6.2 shows a comparison of three count rates plotted against pressure for the flight MIL-1-69:

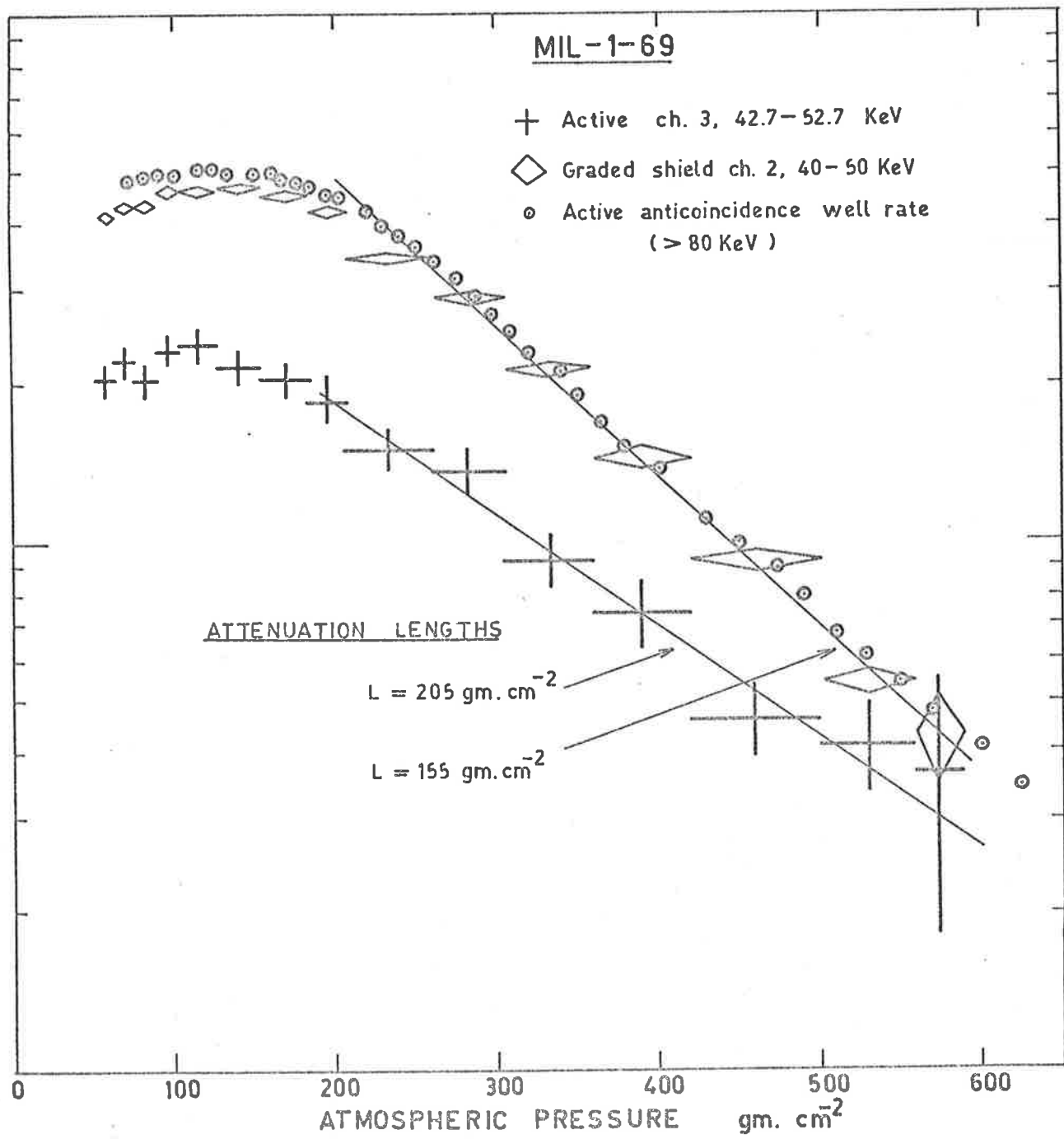


Fig: 6.2 Comparison of attenuation lengths for count rates measured during the ascent of MIL-1-69.

- (a) the active telescope channel 3 (42.7-52.7 KeV);
- (b) the active telescope NaI(Tl) anticoincidence well ($>80\text{KeV}$);
- (c) the graded shield (G.S.) telescope channel 2 (40-50 KeV).

These plots are typical examples of the three types of count rate as they have been obtained on all flights. A striking discrepancy is observed between the attenuation lengths of the count rates in the active telescope channel 3 and the G.S. telescope channel 2, which cover approximately the same photon energy range. This serves to emphasize that caution should be exercised in the comparison of the results obtained using different instruments. Also notable is the close agreement between the attenuation lengths for the G.S. telescope channel 2 and the active well rate.

The guard rates of the active telescope i.e. the well ($>80\text{KeV}$), the collimator ($>40\text{KeV}$), the lower level discriminator ($\geq 10\text{KeV}$), and the upper level discriminator ($\geq 180\text{KeV}$), are all in excellent agreement with each other for a given flight. These values and their average (L_0) are tabulated for the different flights in table 6.1. Values and uncertainties of individual rates were determined graphically.

Table 6.1: Attenuation lengths (gm.cm^{-2}) of active guard rates.

Flight	Well	Collimator	Lower disc	Upper Disc	Average L_0
MIL-1-68	175 ± 5	168 ± 10	172 ± 8	170 ± 10	171 ± 8
MIL-1-69	155 ± 7	150 ± 8	150 ± 8	145 ± 8	150 ± 8
MIL-2-69	170 ± 7	165 ± 3	163 ± 8	160 ± 8	165 ± 7
MIL-3-69	166 ± 5	164 ± 4	160 ± 6	158 ± 6	163 ± 5

The values of $L(E)$ obtained for the different active and G.S. telescope energy channels are plotted against photon energy E in figs. 6.3 and 6.4. Error bars correspond to one standard deviation and the telescope zenith angle for each set of observations is indicated. These results were obtained by performing a least square fit to the background data of each energy channel as a function of pressure . The data were fitted by the exponential function

$$B_{loc}(E, p) = B_{loc}(E, 0) \exp\left(-\frac{p}{L(E)}\right)$$

and the method of least squares given by Wolberg (1967) was employed to determine the best fit values of $B_{loc}(E, 0)$ and $L(E)$. Chi-squared tests indicated that in all cases this function was a satisfactory fit. Also shown are points due to Haymes et al (1969) which accentuate the problem of detector-dependence in the results obtained.

Table 6.2 lists for each flight the three types of attenuation length

- (a) L_a , the average over all energy channels of the active telescope (except the lowest channel whose attenuation length was always much greater than the others due to its susceptibility to noise and the large number of spurious low energy background events);
- (b) L_0 , the average of the active telescope guard count rates (see table 6.1); and
- (c) L_{GS} , the average over all energy channels (except the lowest) of the attenuation lengths for the G S telescope i.e. energy channels 2 to 5 (40 to 125 KeV).

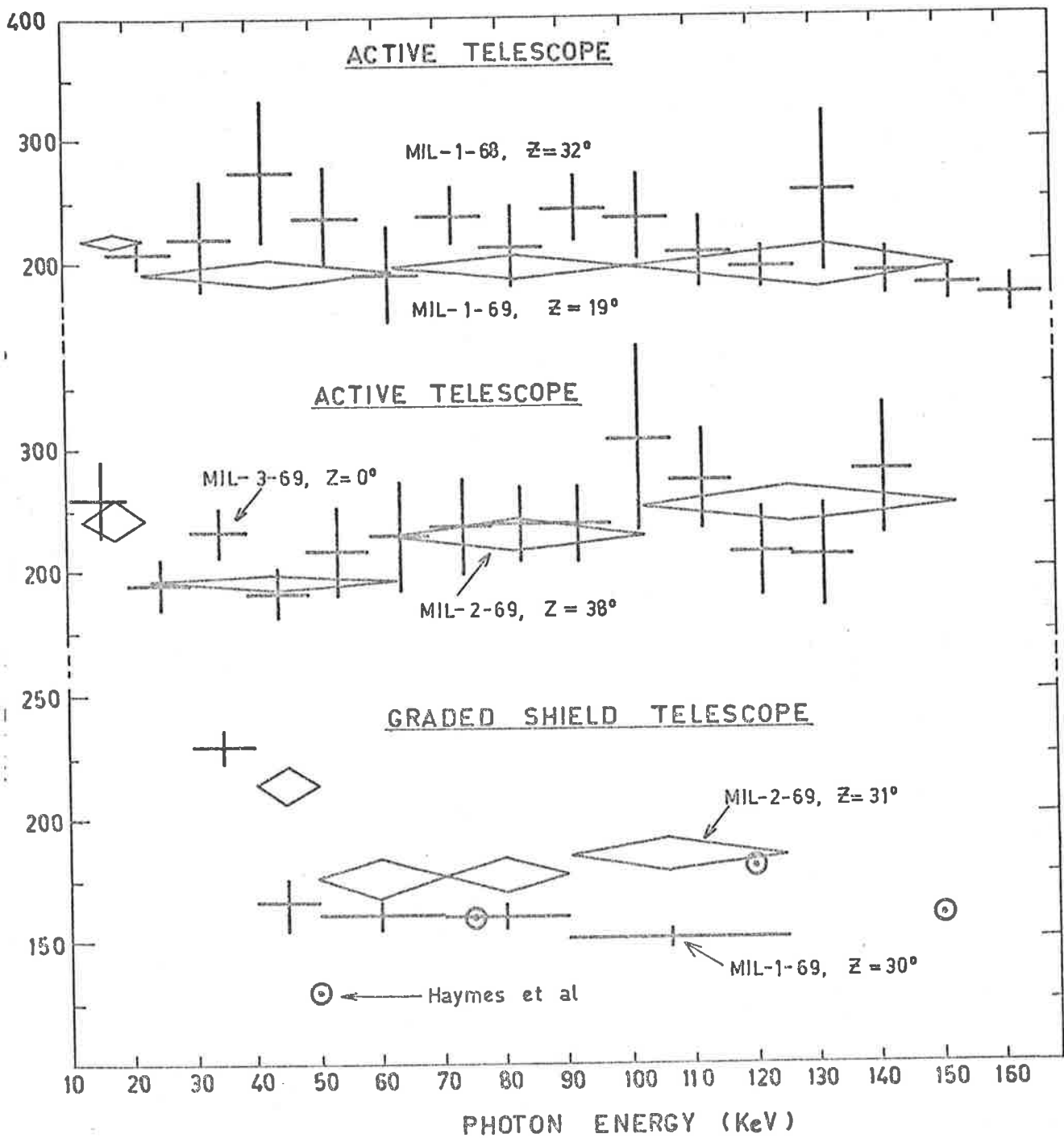


Fig: 6.3 Attenuation length as a function of energy for different flights of both telescopes. Data for Haymes et al. (1969) are shown for comparison.

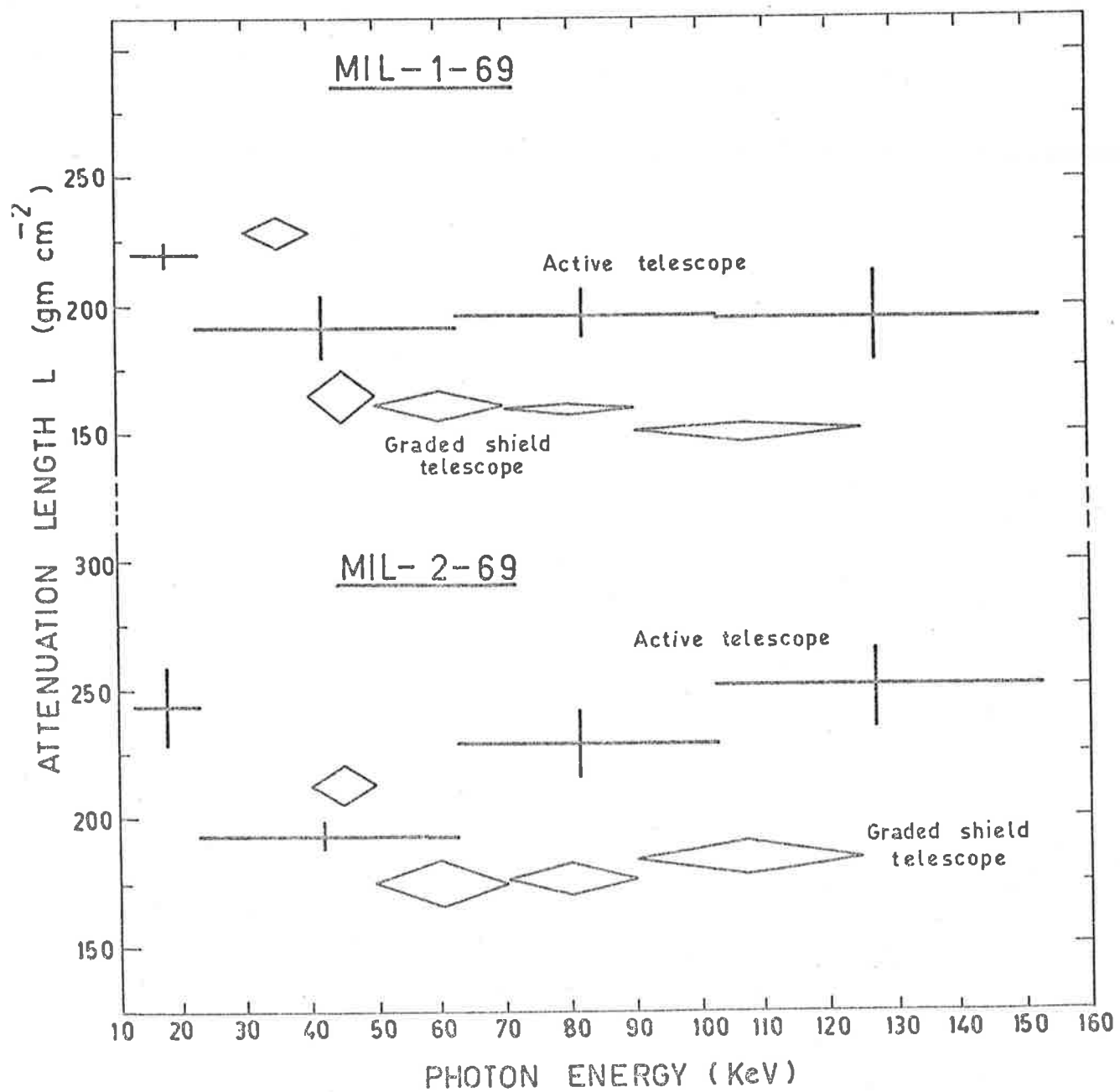


Fig: 6.4 The differences between flights MIL-1-69 and MIL-2-69 for both telescopes.

Also tabulated are the active telescope zenith angle z for each flight, the corresponding value of $L=L_a/\cos z$, and the ratios L/L_o and L_{GS}/L_o , which will be seen to have relevance in section 6.2.4.

Table 6.2 Comparison of Attenuation Lengths.

Flight	Active telescope					GS telescope	
	z	L_a	$L_a/\cos z$	L_o	L/L_o	L_{GS}	L_{GS}/L_o
MIL-1-68	32°	217 ± 31	256 ± 37	171 ± 8	1.50 ± 0.28	—	—
MIL-1-69	19°	195 ± 18	206 ± 19	150 ± 8	1.37 ± 0.20	159 ± 5	$1.06\pm .08$
MIL-2-69	38°	224 ± 15	284 ± 19	165 ± 7	1.72 ± 0.19	187 ± 7	$1.13\pm .09$
MIL-3-69	0°	234 ± 37	234 ± 37	163 ± 5	1.44 ± 0.27	—	—

6.2.2. Flight-to-flight variations of attenuation length.

Fig. 6.3 and tables 6.1 and 6.2 show variations between flights in each of L_a , L_o , and L_{GS} . Possible reasons for these variations include instrumental effects, differences in the local times of the ascents, differences in local geomagnetic cut-off rigidities for the different flights and differences in telescope zenith angles. The fact that variations show correlation between flights indicates that instrumental effects are unlikely. Fig. 6.4 compares the two telescopes and shows that in MIL-2-69 compared with MIL-1-69, both instruments independently recorded an increase in $L(E)$ for $E \geq 70$ KeV, although the increase was relatively more pronounced for the active than for the G.S. telescope. There has been no reason to doubt the correct operation of either telescope on any of the flights concerned here.

It therefore appears that real physical variations have been observed. The geomagnetic latitudes during the ascent phases of the different flights differed by less than $\frac{1}{2}^{\circ}$ and are not expected to result in significant effects (see section 7.5). For example, Soberman (1956) has noted a geomagnetic latitude effect in slow-neutron attenuation lengths of about minus 2 gm.cm^{-2} , per degree increase in geomagnetic latitude. While it is not suggested that photon attenuation lengths behave in the same manner as those of slow-neutrons, it nevertheless appears that a geomagnetic latitude variation of less than $\frac{1}{2}^{\circ}$ is insufficient to provide an explanation for the data reported here.

Differences in the local times of the respective ascents also do not provide an adequate explanation. Table 1.4(a) shows that the ascents of MIL-1-68 and MIL-1-69 took place at night, while those of MIL-2-69 and MIL-3-69 were in daylight. Examination of table 6.2 reveals a slight suggestion of a day/night effect in the values of L_a , which are marginally smaller for the night flights. The values of L_o do not support this suggestion but this may be due to the fact that the guard count rates are "contaminated" by cosmic ray interactions and are not due entirely to photons, as is very nearly the case for the channel rates.

Another flight parameter which may be of importance is the telescope zenith angle. Table 6.2 shows no obvious zenith angle correlations. However there are other good reasons to believe that zenith angle effects do exist, and this topic will be further discussed in section 6.2.4.

6.2.3 Differences between the two telescopes.

The discrepancy between the attenuation lengths measured by the two telescopes has been mentioned. One possible explanation may lie in the different shielding characteristics of the two telescopes which lead to differences in the relative contributions of B_1 and B_{atm} . The G.S. telescope count rate doubtless possesses a greater amount of B_1 contamination than does the active telescope and this may lead to the shorter observed attenuation length. The value $L \sim 120 \text{ gm.cm}^{-2}$ for very energetic primary cosmic ray protons (see table 6.4, section 6.2.6) which may contribute to the generation of B_1 in the graded shield material, may support this idea.

Also the active anticoincidence rates i.e. the collimator, the well, the low energy ($\geq 10 \text{ KeV}$), and high energy ($\geq 180 \text{ KeV}$) central detector discriminator rates, which reflect the total cosmic ray background rather than genuine X-rays, all display comparable attenuation lengths.

An alternative explanation to account for the discrepancies between L_a , L_o and L_{GS} is achieved by means of the Gross Transformation and is now described.

6.2.4. The Gross Transformation.

The time correlation between $L_a(E)$ and $L_{GS}(E)$ for $E \geq 70 \text{ KeV}$ observed in the two flights MIL-1-69 and MIL-2-69, 5 days apart, has been remarked upon. The larger change noted for the active telescope data relative to the graded shield telescope, and the fact that the active zenith angle changed from 19° to 38° while that of the G.S. telescope varied only from 30° to 31° leads to the consideration of zenith angle effects.

In fact if there are zenith angle effects, the attenuation length discrepancies may receive a self-consistent explanation by means of the Gross Transformation (Gross 1933, Janossy 1950, Rossi 1952, Hayakawa 1969a). This can be used to relate the counting rate due to a unidirectional pressure- and zenith-dependent intensity $J(p,z)$ (as is approximately measured by the active telescope central detector) to the rate of the omnidirectional intensity $J'(p)$ measured by a detector whose response is integrated over all zenith angles (for example the active telescope guard rates). It is derived by assuming that the direction of primary and secondary particles is conserved in all interactions, that spontaneous decay phenomena are neglected and that the radiation responsible for the count rate is isotropic at the top of the atmosphere.

It is acknowledged that there are serious doubts with regard to the application of the Gross Transformation to atmospheric photons, since if they belong to the secondary electron-photon cosmic ray component, multiple Compton scattering would be expected to invalidate the first assumption above. However, no a priori assumptions will be made concerning the origin of atmospheric photons in this section. The only additional assumption made with respect to the application of the Gross Transformation to these results is that the telescope PHA channel rates and guard rates are due predominantly to photons.

If the unidirectional intensity $J(p,z)$ is exponentially absorbed by the total air thickness along its path i.e

$$J(p,z) = J_0 \exp\left(\frac{-p}{L \cos z}\right) = J_0 \exp(-y/L) \dots \dots \dots 6.1$$

then the omnidirectional intensity integrated over all angles of incidence in the upper hemisphere is

$$J'(p) = 2\pi \int_0^{\pi/2} J(p,z) \sin z \, dz = 2\pi J_0 \mathcal{E}_1(p/L) \dots \dots 6.2$$

where $\mathcal{E}_1(p/L)$ is the Gold integral, given by

$$\mathcal{E}_1(p/L) = p \int_p^\infty y^{-2} \exp(-y/L) \, dy.$$

Figure 6.5 compares the altitude dependence of the vertical intensity $J(p,0) \propto \exp(-p/L)$ with the omnidirectional intensity $J'(p) \propto \mathcal{E}_1(p/L)$. The deviation of $\mathcal{E}_1(p/L)$ from an exponential shape is small for $1 \lesssim p/L \lesssim 4$ and its form can be seen to be approximated by $\exp(-p/0.77L)$. Thus the apparent omnidirectional attenuation length i.e. the attenuation length of the active guard rates is given by

$$L_0 \sim 0.77L, \text{ and so } L/L_0 \sim 1.30.$$

Also shown is the theoretical behaviour of the graded shield telescope, which is obtained by integrating over the telescope aperture solid angle thus:

$$J_{GS}'(p) = \int J(p,z) R(z) \, d\Omega \dots \dots \dots 6.3,$$

where $R(z)$ is the collimator response function in zenith, and $d\Omega$ is the solid angle element, which can be written as $d\Omega = \text{constant} \cdot dz$, since the collimator FWHM in azimuth is very narrow (5° for MIL-1-69 and MIL-2-69). The telescope axis is assumed to be at a zenith angle of 34° and the integration is carried out from $z = 0^\circ$ to $z = 68^\circ$, since the collimator FWHM in zenith is 34° .

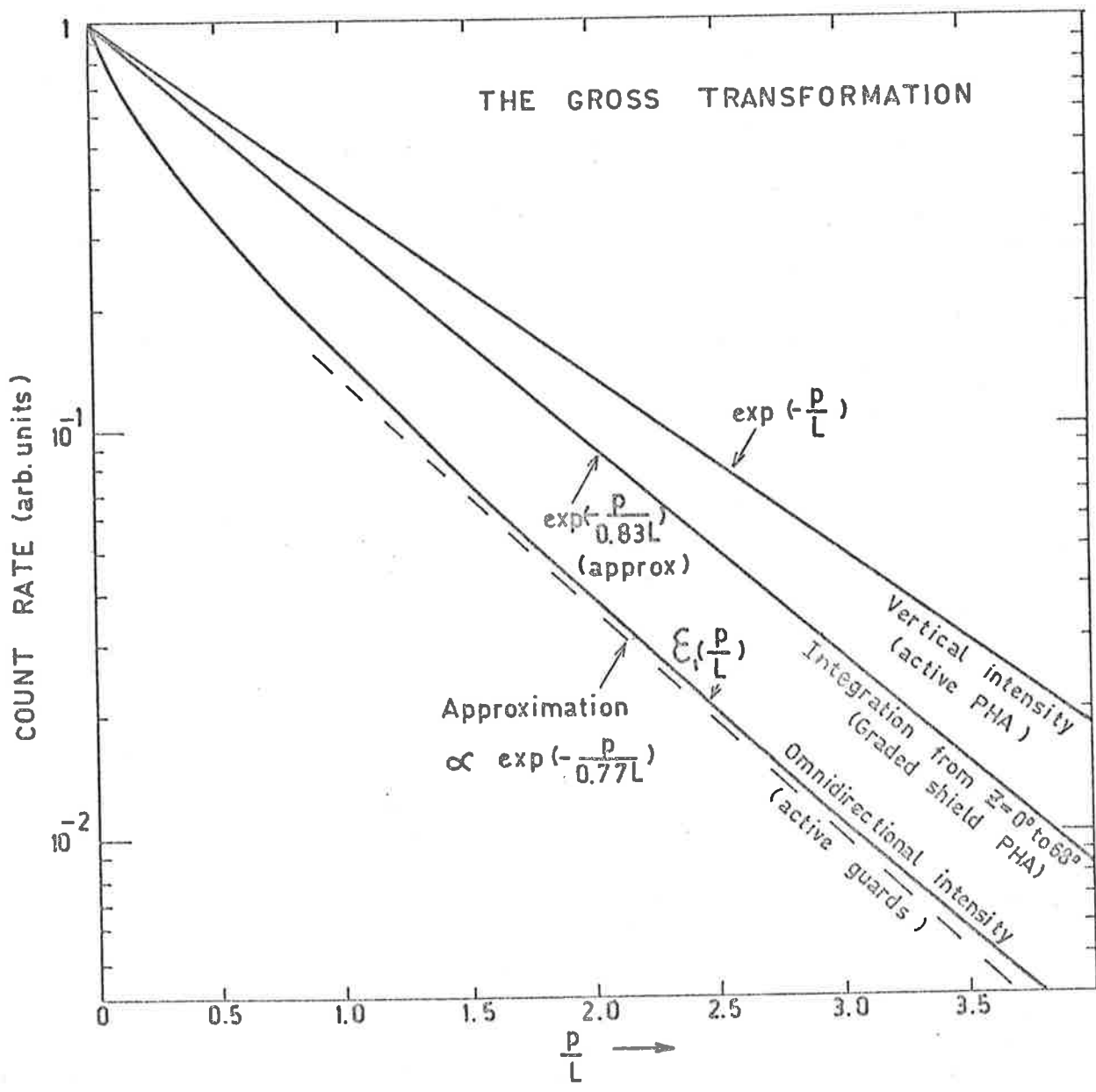


Fig: 6.5 Predicted attenuation lengths under the Gross Transformation for the active and graded shield telescope PHA channel rates and the active guard rates.

The values calculated using equation 6.3, are plotted in figure 6.5, and it can be seen that the effective graded shield attenuation length is given by $L_{GS}/L_0 \sim 1.08$.

Comparison of the theoretical ratios $L/L_0 \sim 1.30$ and $L_{GS}/L_0 \sim 1.08$, with the experimental values tabulated in table 6.2 reveals good agreement. Both the active and graded shield telescope results therefore support the Gross Transformation hypothesis and this implies a zenith angle dependence of the background attenuation length. A consequence of this hypothesis is that the vertical attenuation length $L = L_a / \cos z$, for a given energy interval, should be invariant during any given flight, and invariant from flight to flight in the absence of real time variations. No experiment employing a variable zenith angle has been flown to test the first suggestion, although other results have been reported which imply near isotropy for the atmospheric X-ray flux (Brini et al. 1965). Table 6.2 shows that the suggestion of flight-to-flight invariance only roughly holds, but this may be indicative of the occurrence of real time variations. Certainly significant differences are observed between MIL-1-69 and MIL-2-69 for both telescopes.

In view of the currently accepted belief that atmospheric X-ray photons are part of the soft E-component of secondary cosmic radiation and as such have probably undergone multiple large angle scattering, application of the Gross Transformation to the results reported here would appear to be theoretically questionable. But since photons of these energies are almost completely absorbed in $\lesssim 10\text{gm.cm}^{-2}$ of air, the observed altitude

dependence of photon count rates in reality reflects the photon production rate rather than the properties of X-ray photon propagation in the atmosphere. Consequently, the value obtained for L is determined by the altitude dependence of the photon-producing interactions and hence of the parent radiations. Therefore the apparent validity of the Gross Transformation may simply reflect a zenith angle dependence in the photon-producing radiation. However theoretical difficulties still exist if, as is believed, the photons are produced by interactions of electrons of the soft component which themselves have probably undergone multiple large angle scattering.

Nevertheless other experimenters have been tempted to use the Gross Transformation in recent years to explain observational discrepancies in the altitude of the transition maximum (Peterson 1963, Vette 1962) but have not committed themselves because of the theoretical objection. I shall make no further attempts here to theoretically justify its use and shall simply point out that these results and certain results obtained by other workers indicate that its use does have some observational justification.

6.2.5. Comparison with other experiments:

Comparatively few investigations of atmospheric X-ray photons in the pressure range $200 \lesssim p \lesssim 700 \text{ gm.cm}^{-2}$ have been published in the literature (Jones 1961, Anderson 1961, Vette 1962, Peterson 1963, Rocchia et al 1965, Brini et al 1965, 1967, Haymes et al 1969, Frost et al. 1966). These measurements were made with a variety of experimental techniques; at different energies, using different zenith angles, from different opening solid angles,

various shielding configurations, from many geomagnetic latitudes and at different times in the solar cycle. As a result care must be exercised when making comparisons.

Table 6.3 lists experimental attenuation lengths obtained by different workers under this multiplicity of conditions. No attempt has been made to correct measurements to vertical attenuation lengths but the opening solid angle is tabulated to indicate the type of measurement. In the column (Sh) describing the type of shielding, the letter P denotes the active rejection of charged particles with or without a phoswich system, U represents a completely unshielded detector, L denotes lead collimation and A actively collimated and shielded. The height of the transition curve maximum is also tabulated (see section 6.3). An omnidirectional detector is denoted by a 4π steradian solid angle.

Table 6.3: Experimental photon attenuation lengths.

Reference	Geom. lat. (deg)	z (deg)	Solid angle (ster)	Sh	Energy Range (KeV)	Att. length (gm.cm ⁻²)	Depth of Trans. max. (gm.cm ⁻²)
Jones (1961)	41°N	0°	~0.5	P,L	250-10 ⁶	163	60-70
Vette (1962)	40.5°N	-	4 π	U	25-1060	163	70
"	"	-	"	"	>1060	163	55
Peterson (1963)	55°N	-	4 π	P	37-75	~170	90
"	"	-	"	"	511	185	90
Rocchia et al (1965)	47°N	-	4 π	U	511	180	95
"	"	-	"	U	100-1500	170	100

Table 6.3. (cont)

Reference	Geom. lat(deg)	Z(deg)	Solid Angle (ster)	Sh.	Energy Range (KeV)	Att. length (gm. cm. ⁻²)	Depth of Trans. Max (gmcm. ⁻²)
Frost et al (1966)	55°N	0°	~1	A	>300KeV	170	50
"	"	-	4π	U	>50KeV	180	30
"	"	-	4π	U	>3.5MeV	165	100
Brini et al(1967)	45°N	0°	0.46	P, L	20-200	165	100
Haymes (1964)	41°N	-	4π	P	470-3.5MeV	186±5	90
Cline(1961)	55°N	-	4π		~50MeV	180	180
Duthie et al(1963)	40°N	0°	Vert	(Spark Chamb)	~100MeV	180	180
Okudaira et al (1968)	26°N	-	4π	P	>1.2 MeV	195	100
Kondo et al (1968)	~20°N	-	4π	P	1-30MeV	190	100
Haymes et al (1969)	41°N	~45°(?)	*~0.15	A	~50*	130	58-92 ind of energy
			~0.15		~75	160	
*Approx. values are read off graphs.			~0.15		~120	180	
			~0.2		~150	160	
			~0.2		~180	135	
			~0.2		~220	135	
			~0.3		~300	110	
			~0.6		~400	115	
			~1.0		~500	140	

The wide divergence of individual results is obvious.

In particular, the L values of Haymes et al. will be systematically ~10% smaller than other comparable values owing to the fit to their data of an exponential-plus-background function (i.e. $A+B \exp(-\frac{P}{L})$) rather than a pure exponential function ($A \exp(-\frac{P}{L})$) as is usually done by workers in this field. The remaining discrepancy between their values and those obtained from the Adelaide active telescope is perhaps the most serious in table 6.3 since of all the instruments tabulated, theirs should be comparable most directly with ours. Their only zenith angle information is that it is "often but not always $\sim 45^\circ$ ". If $Z = 45^\circ$ is taken and the correction is made to a vertical attenuation length, their table 6.3 values are raised by ~40% and come close to the active telescope L values.

Little more than this can be said since owing to the impossible complexity of normalizing each result to a standard set of experimental circumstances, direct comparison cannot be validly made,

6.2.6 Other radiations:

In attempting to find the origin of the atmospheric X-ray spectrum, previous workers have compared their measured L values with the attenuation lengths of various other cosmic ray components at the same geomagnetic latitude, some of which are listed in table 6.4. Vertical (V) or omnidirectional (O) values are indicated.

Table 6.4: Attenuation lengths for cosmic ray components.

Component	Geomag. lat.	V ₀	Att. length (gm.cm ⁻²)	Reference.
Total cosmic rad.	45°	V	200	Hayakawa (1969a)
"	≥45°	V	190	Rossi (1948)
"	0°	V	220	Rossi (1948)
Soft component	45°	V	160	Hayakawa (1969a)
"	45°	V	123	Puppi et al (1952)
"	≥45°	V	150	Rossi (1948)
"	0°	V	160	Rossi (1948)
"	55°	O	160	Peterson(1963)
Components of soft:				
electrons from π ⁰ 's	45°	V	130	Hayakawa (1969a)
electrons from Knock-on and decay processes of muons	45°	V	280	"
soft muons	45°	V	210	"
soft protons	45°	V	110	"
electrons ≤10 GeV	50°	V	150	"
low energy muons	50°	V	300	Hayakawa (1969a)
gammas, 0.3-10TeV	?	V	110	"
slow mesons	45°	V	230	Rossi (1948)
Hard component	45°	V	300	Hayakawa (1969a)
"	45°	V	340	Rossi (1948)
"	0°	V	400	Rossi (1948)

Table 6.4. (cont).

Component	Geomag lat	V,0	Atten length gm.cm ⁻²	Reference
Nucleonic comp:				
Relativistic nucleons	45°	V	120	Hayakawa (1969)
low energy nuclearactive	>45°	0	138	Rossi (1948)
Fast neutrons, 1-14 MeV	41°	0	169±13	Haymes (1964)
Slow neutrons, <500KeV	0°	0	212	Simpson (1951)
"	10.1°	0	212	Soberman (1956)
"	19°	0	206	Simpson (1951)
"	30.4°	0	196	Staker (1950)
"	40°	0	181	Simpson (1951)
"	51°	0	156	Yuan (1951)
"	55.1°	0	164	Soberman (1956)
"	69°	0	162	Staker et al (1951)
"	88.6°	0	164	Soberman (1956)
Penetrating showers	53°	V	118	Tinlot (1948)
"	38°	V	123	Fretter (1949)

It is interesting to note the conclusions of others with respect to their photon results when faced with the bewildering array in table 6.4. For example, Jones (1961) concluded that the atmospheric photon component was directly produced by the nucleonic component since his L value was more in line with slow neutron values than with the soft component results of Puppi et al (1952), 123 gm.cm⁻².

However, other soft component measurements show values of 150 to 160 gm. cm^{-2} , very close to Jones' results. Had he used these results for comparison, he would have found the choice between slow neutrons and the soft component very difficult to make. As another example, Peterson (1963) obtained about 180 gm.cm^{-2} , compared it with the value of $\sim 160 \text{ gm.cm}^{-2}$ for an omnidirectional GM counter measuring the soft component, and concluded that photons are associated with the electronic component. On the basis of attenuation lengths alone it is of course equally valid to conclude that photons are associated with the low energy nucleonic component.

Haymes (1964) obtained $186 \pm 5 \text{ gm.cm}^{-2}$ for low energy gammas, barely greater statistically than the value $169 \pm 13 \text{ gm.cm}^{-2}$ obtained in the same experiment for fast neutrons, and concluded that the two components probably were not associated. He then proceeded to connect the gammas with the soft component, when by the same reasoning its attenuation length of 123 gm.cm^{-2} or even 160 gm.cm^{-2} , makes this even less likely than the association with fast neutrons. Haymes et al (1969) found a large variation of photon attenuation length with energy ranging from 110 to 180 gm.cm^{-2} between 30 and 570 KeV. Upon averaging these, they obtained a value closer to the soft component's 123 gm.cm^{-2} of Puppi et al than to the fast neutron value of 169 gm.cm^{-2} . The conclusion was then reached that the photons most likely have an electronic origin rather than nucleonic, even though (i) three of the sixteen plotted $I(E)$ points were closer to 169 gm.cm^{-2} than to 123 gm.cm^{-2} (no error bars were given on these points);

(ii) they used an exponential-plus-background fit function to determine L , which gives a value about 10% smaller than does the pure exponential which has been used by all other workers for all other radiation components; and (iii) other soft component measurements give $L \sim 150 \text{ gm.cm}^{-2}$.

It therefore seems that spurious arguments have occasionally been used with regard to using attenuation lengths to associate atmospheric X-ray photons with the electronic component. Also in only a few cases have there been simultaneous measurements of the attenuation lengths of photons and other radiation species. It is therefore concluded that there is in fact little observational evidence to connect photons with the electronic component. From the theoretical viewpoints of production mechanisms and total cosmic ray energy balance considerations (Puppi 1956, Vette 1962) it does seem the most likely hypothesis. However it is clear that radiation attenuation length comparisons are not of major importance in the support of this hypothesis.

6.3. The Transition curve maximum ($p \sim 100 \text{ gm.cm}^{-2}$).

Another property of the atmospheric photon intensity which may be of help in determining its origin is the depth ($p_{\text{max}} \text{ gm.cm}^{-2}$) at which the Pfozter maximum occurs in the transition curve. As in the case of L measurements, the experimental configuration is again important, since if the Gross Transformation is valid, an omnidirectional measurement will yield a maximum at a smaller depth than will a vertical flux measurement. When this is considered, comparison of photon results with those of other radiation components will hopefully give a clue to the photon source.

However, this method experiences the same difficulties as do L comparisons and the results too are somewhat inconclusive.

6.3.1. Results:

The values of p_{\max} , without any corrections to $Z=0^\circ$, obtained on each flight are listed in table 6.5. Uncertainties are typically about $\pm 20 \text{ gm.cm}^{-2}$.

Table 6.5: Transition maximum altitudes (gm.cm^{-2}).

Flight	Active Energy Range (KeV)	p_{\max} (PHA)	p_{\max} (Guard avg)	G.S telescope (40-125 KeV) p_{\max}
MIL-1-68	27-167	110	90	-
MIL-1-69	12.7-142.7	130	110	140
MIL-2-69	12.7-142.7	100	80	100
MIL-3-69	20-90	140	100	-
	90-150	110		

These results are in general agreement with those of other workers (table 6.3). However significant differences are apparent, especially between MIL-1-69 and MIL-2-69, as was noted for the L value determinations. Also the energy dependence of p_{\max} obtained for MIL-3-69 is not apparent in the other flights. In addition p_{\max} for the averaged guard rates is consistently smaller than for the nearly unidirectional active PHA rates as would be expected from absorption varying as $\exp(-p/L \cos z)$. The G.S telescope results however tend not to agree with this expectation since they group with the active PHA values rather than those of the active guards. This apparent disagreement, if indeed it is a disagreement since statistics are poor, cannot be explained within the framework

of the Gross Transformation hypothesis.

6.3.2. Discussion:

Values of p_{\max} obtained for other cosmic ray components appear in table 6.6.

Table 6.6. Transition maxima for cosmic ray components.

Component	Geomag lat	θ, V	p_{\max} (gm.cm^{-2})	Reference.
Soft	45°	V	200	Puppi et al (1952)
Soft	55°	0	50	Peterson (1963)
Soft	Midlat	0	70	Millikan et al(1944)
Electrons	69°	V	150-200	Meyer and Vogt(1962)
Charged particles	40°	V	130	Duthie et al(1963)
Fast neutrons, 1-14MeV	41°	0	95	Haymes (1964)
Slow neutrons (< 500KeV)	10.1°	0	120	Soberman (1956)
"	30.4°	0	110	Staker (1950)
"	55.1°	0	100	Soberman (1956)
"	69°	0	90	Staker et al (1951)
"	88.9°	0	75	Soberman (1956)

The variations evident in table 6.5, together with the variety of results in table 6.6. enable photons to be associated with practically any cosmic ray component if only p_{\max} comparisons are made.

Values of p_{\max} , as are those of L , are thus unreliable indicators of the generic relation of atmospheric X-ray photons to cosmic rays and any conclusions reached by such means cannot be taken too seriously.

6.4. SUMMARY:

The results presented show differences between flights of the order of 15% in X-ray attenuation lengths L in the atmospheric depth interval $200 \leq p \leq 700 \text{ gm.cm}^{-2}$. There is only a small energy dependence in L for energies $10 < E < 180 \text{ KeV}$.

Good evidence exists that at these depths either the photon intensity itself or the photon-producing radiation possesses a zenith angle dependence. This is so because of the empirical fact that the Gross Transformation is found to provide a good explanation of the observed numerical relationships between L values for the active telescope energy channels, for the active guard rates and for the graded shield telescope energy channels. However the theoretical validity of the Gross Transformation when applied to secondary photons or electrons at such large atmospheric depths is questionable.

Comparison of photon attenuation lengths obtained here with those of other workers should be made with care since L has been shown to be a function of energy, the detector configuration, zenith angle and detector acceptance solid angle and possibly of time. Since the active telescope of this experiment is believed to possess superior background rejection characteristics and has a small collimator opening angle, it is believed to give the most

comprehensive results to date on directional X-ray fluxes in the atmosphere.

Comparison of photon attenuation lengths and Pfofzer maximum heights with the corresponding values of other atmospheric radiations does not appear to be a reliable method of determining the generic relationship of photons to the secondary cosmic radiation.

CHAPTER 7: ATMOSPHERIC X-RAYS, II7.1 INTRODUCTION

This chapter is basically a continuation of chapter 6.

The atmospheric transition curve will be examined for $p < 100 \text{ gm.cm}^{-2}$, an important region for the determination of the diffuse cosmic X-ray spectrum. The spectral form of atmospheric X-rays will be examined as a function of depth, time variations in background characteristics will be further pursued and mention will be made of geomagnetic latitude variations.

7.2 THE HIGHEST ALTITUDES ($p < 100 \text{ GM.CM}^{-2}$).

The channel 3 transition curve obtained during the ascent of the flight MIL-1-68 has been shown in fig. 6.1. The corresponding curves for other channels are given for comparison in figures 7.1 to 7.5. In fig. 6.1 the approximate background contributions B_{loc} ($= B_{\text{atm}} + B_1$) and B_{cos} are indicated where B_{loc} is the local background due to X-rays of atmospheric origin (B_{atm}) and to the leakage background (B_1) which enters undetected through the telescope shielding. These components are described more fully in chapter 6.

The evaluation of the cosmic background component B_{cos} at depths less than about 10 gm.cm^{-2} is dependent upon its effective separation from the local background. For channel 3 this separation would not appear to be difficult. However in the other channels the relative contributions of B_{cos} are considerably smaller owing to the form of the diffuse background spectrum and the spectral response of the telescope, and it is important to make the best estimation possible of the local background.

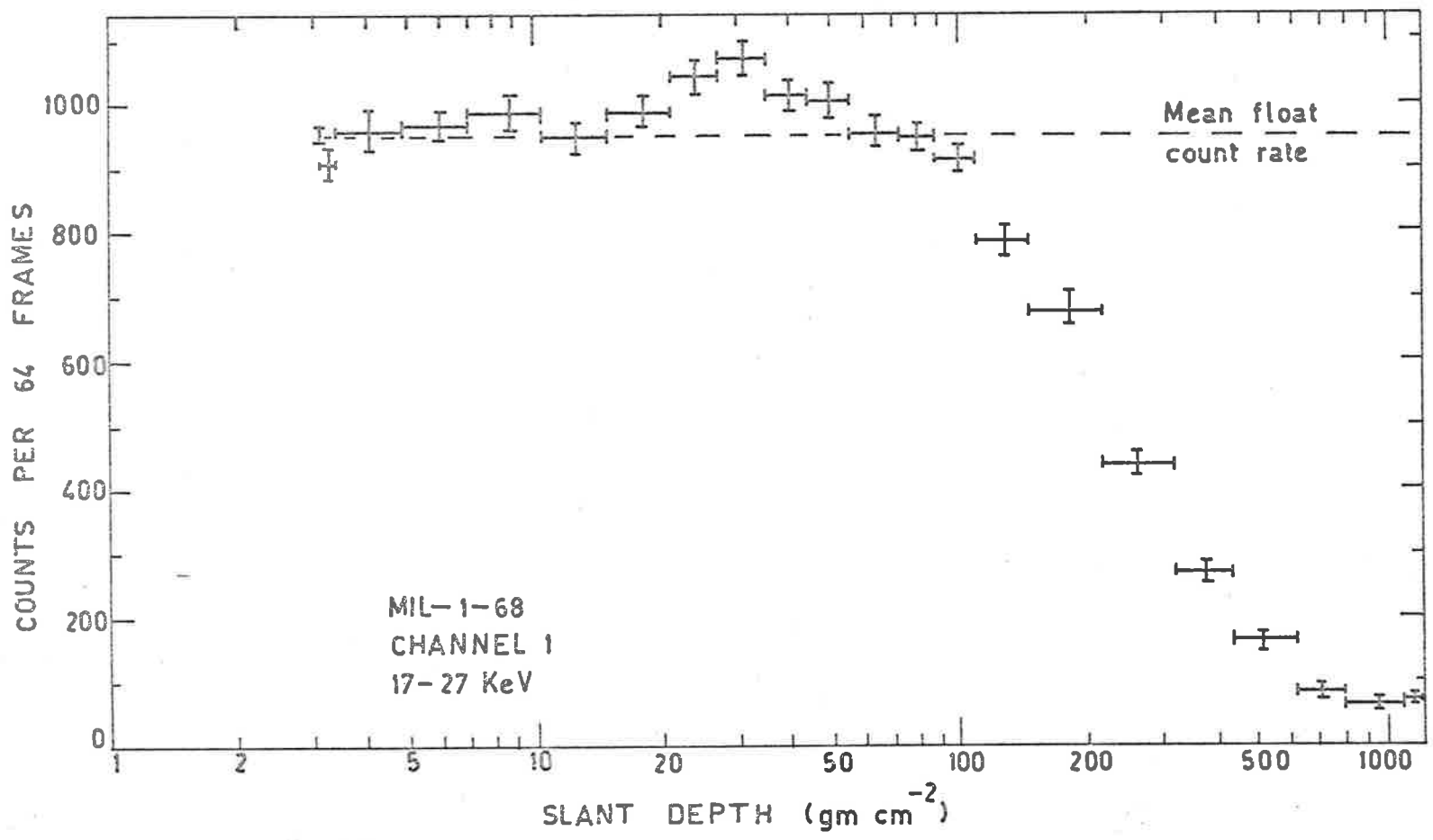


Fig. 7.1 Transition curve for channel 1, MIL-1-68

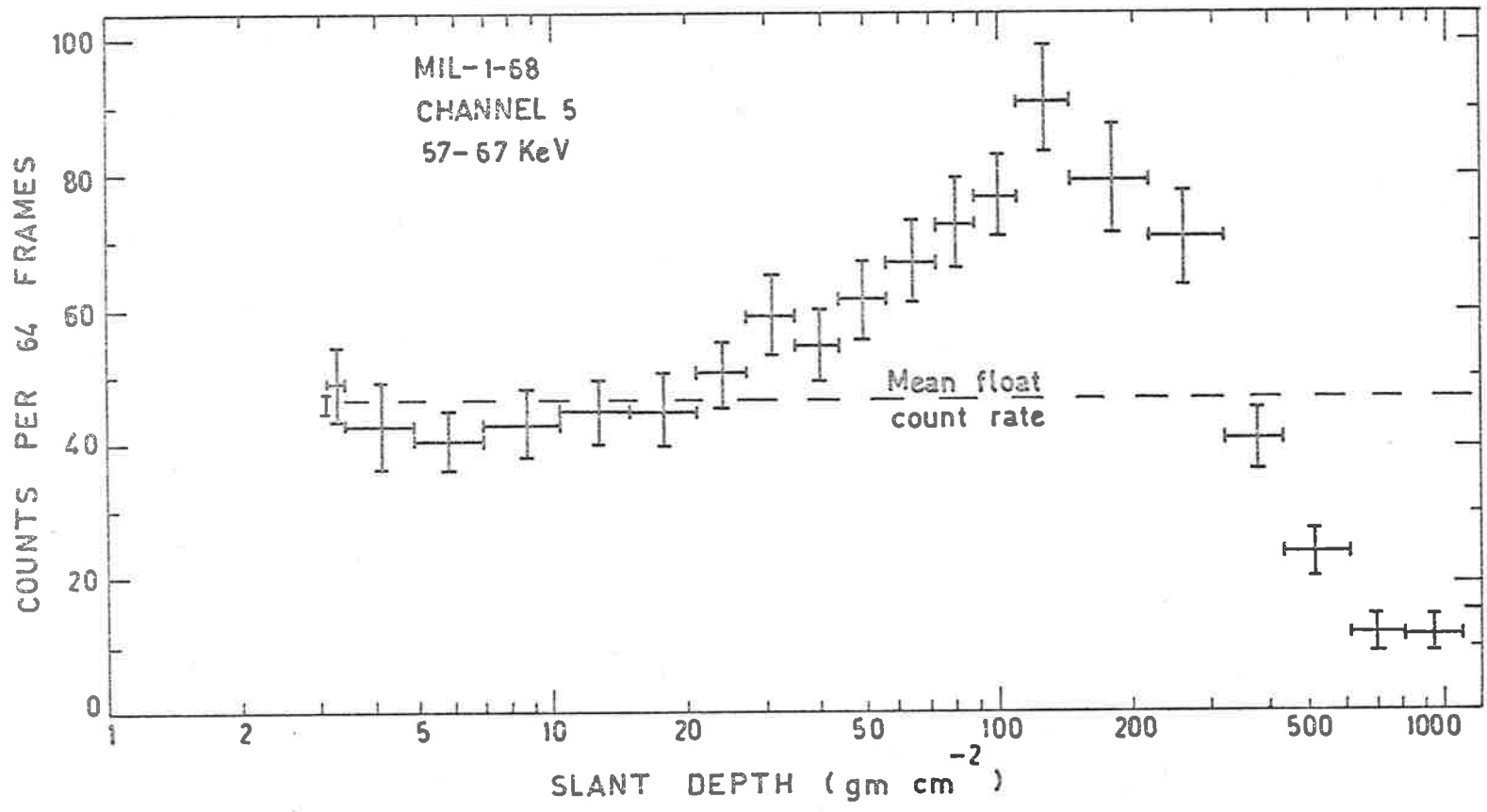


Fig. 7.2 Transition curve for channel 5, MIL-1-68

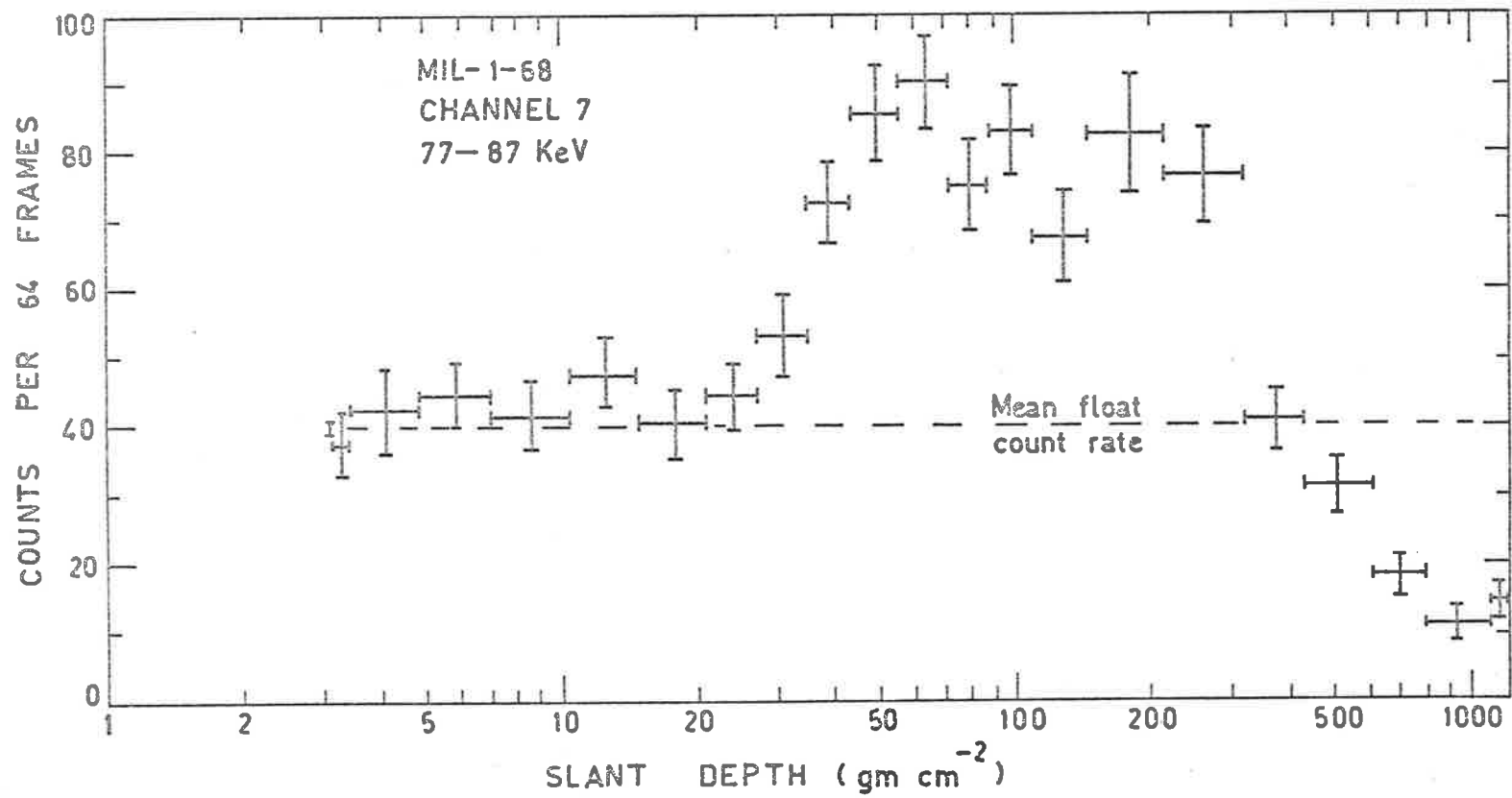


Fig. 7.3 Transition curve for channel 7, MIL-1-68

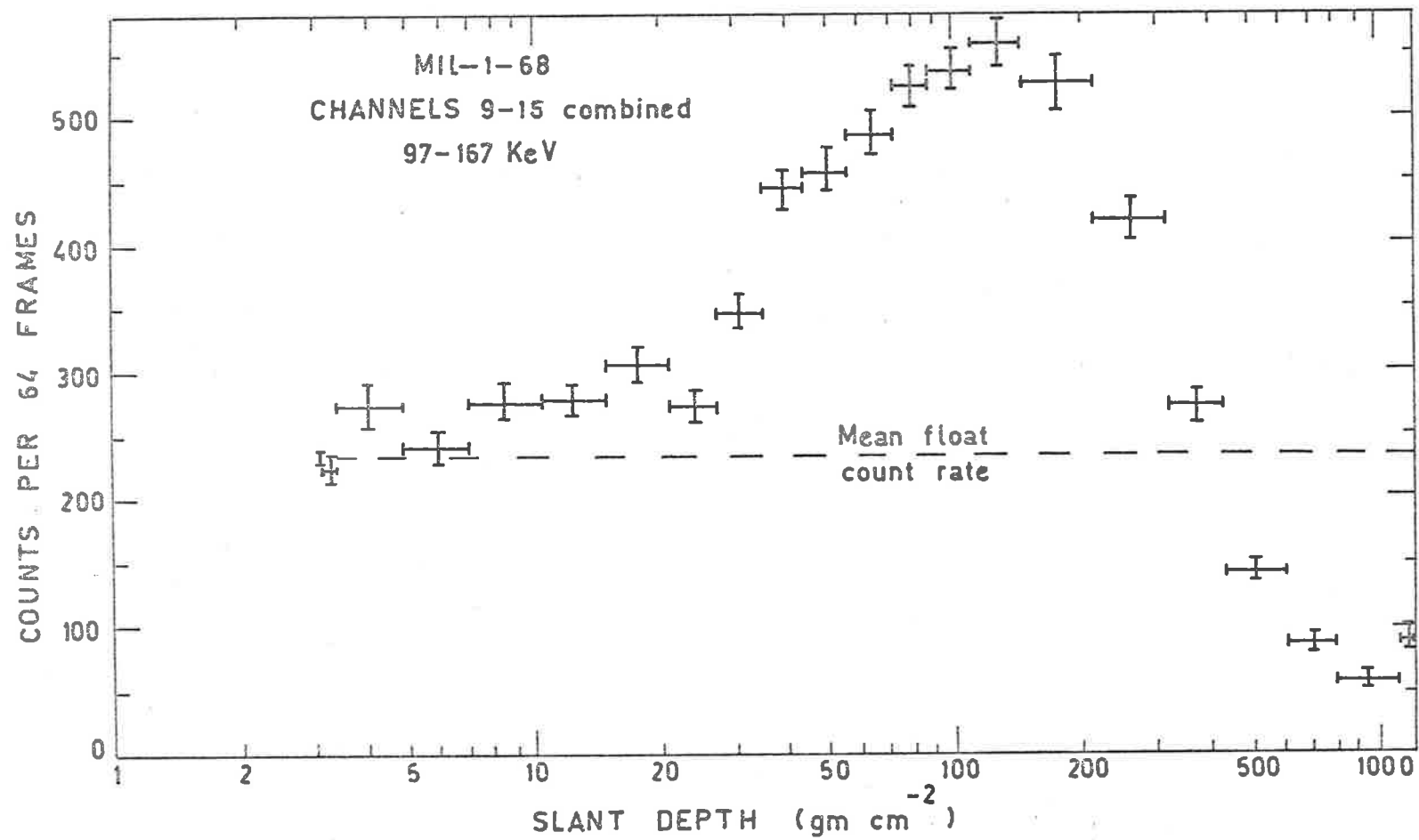


Fig. 7.4 Transition curve for channels 9 to 15 combined, MIL-1-68

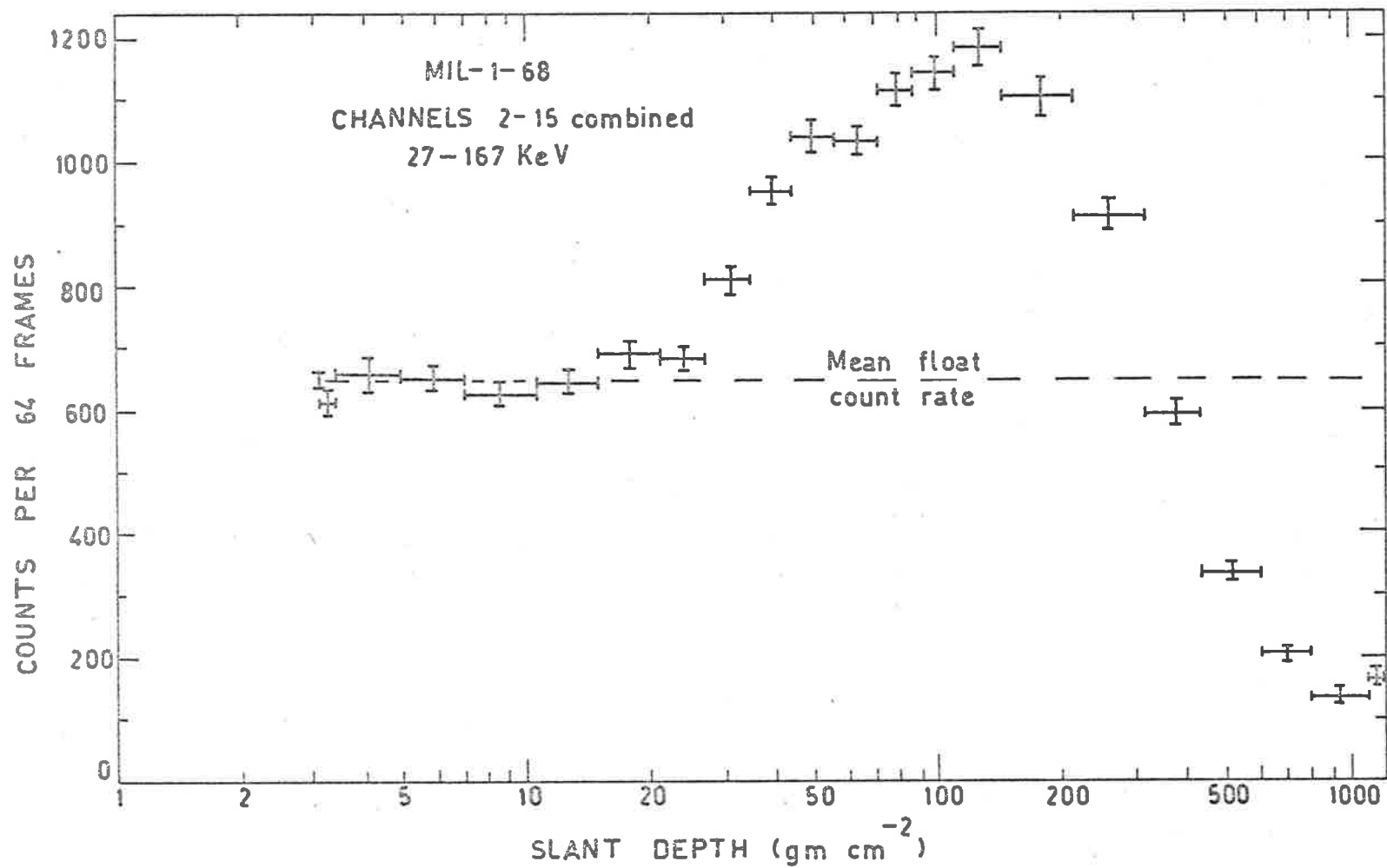


Fig. 7.5 Transition curve for channels 2 to 15 combined, MIL-1-68

This has been accomplished by the least-squares fitting of an appropriate function to the total background data points (B_{tot}) in the depth interval $10 \lesssim p \lesssim 70 \text{ gm.cm.}^{-2}$, where $B_{tot} = B_{loc} + B_{cos} \sim B_{loc}$. This least squares fit function is then extrapolated to balloon float depth to give a value there for B_{loc} . Upon subtraction of B_{loc} from the total background rate, the cosmic component is obtained. This analysis procedure has been followed using the data from the flights MIL-1-68 and MIL-3-69.

7.2.1 Transition curve, $10 < p < 70 \text{ gm.c m}^{-2}$.

Three different functional forms $F_j(p, E)$ have been fitted to data from MIL-1-68 and MIL-3-69. These have been respectively linear, ($j=1$, see equation 7.3) power law ($j=2$) and logarithmic ($j=3$) count rate functions of pressure (see equation 7.3). The linear least squares method described by Wolberg (1967) was used in all three cases and the computations were done on the CDC 6400 computer at the University of Adelaide. The goodness of each type of fit was evaluated for each energy channel by computing

$$\chi_j^2 = \sum_{i=1}^N \frac{(R(p_i) - F_j(p_i))^2}{V(R(p_i))} \dots\dots\dots 7.1$$

where $R(p_i)$ is the count rate at pressure p_i , $V(R(p_i))$ is its statistical variance, $F_j(p_i)$ is the fit function value at p_i and N is the number of data points. In the case of MIL-1-68 data points for $10 < p < 70 \text{ gm.cm.}^{-2}$ were used.

For MIL-3-69 the float depth was greater (4.5 gm.cm^{-2} as compared to 2.7 gm.cm^{-2} for MIL-1-68, see table 1.4a). As a result the local background was considerably larger (see fig. 7.9) and a rather less reliable cosmic background determination could be made. Consequently it was resolved to use this data to examine in detail the B_{loc} extrapolation-to-float procedure and in particular, determine which form of count rate vs depth function was most appropriate.

To do this the estimated cosmic background, B_{cos} , was subtracted from the total background data points B_{tot} in the interval $4.5 \leq p \leq 10 \text{ gm.cm}^{-2}$. The difference data were simply values of B_{loc} which provided additional points for the least squares fit procedure. By using data from the depth interval $4.5 \leq p \leq 70 \text{ gm.cm}^{-2}$ it was hoped to obtain a better determination of the fit function than could be obtained using the smaller number of points from the interval $10 < p < 70 \text{ gm.cm}^{-2}$.

The cosmic background spectrum used to calculate B_{cos} followed the results of Seward et al. (1967) who obtained a power law with spectral index ~ 1.6 between 4 and 40 KeV, and the results of Bleeker et al. (1970a) who found an index of ~ 2.5 between 20 and 220 KeV. The exact magnitude and location in energy of the index break is still the subject of speculation, but for the present purpose it is assumed to be at 38.1 KeV, almost at the boundary of channels 2 and 3 for MIL-3-69. Normalization at 38.1 KeV led to the adoption of the following spectrum (photons $\text{cm}^{-2} \text{sec}^{-1} \text{ster}^{-1}$):

$$N(E) dE = \begin{cases} 9 E^{-1.6} dE, & E \leq 38.1 \text{ KeV.} \\ 244 E^{-2.5} dE, & E > 38.1 \text{ KeV.} \end{cases} \dots\dots\dots 7.2$$

The telescope response to this spectrum was calculated for $4.5 \leq p < 10 \text{ gm.cm.}^{-2}$ using equations 3.6 and 3.8, the results for channel 2 (29.4 to 39.1 KeV) being presented in fig. 7.6. The inadequacy of using MIL-3-69 for a cosmic background spectral calculation can be seen from the fact that $B_{\text{cos}} \ll B_{\text{tot}}$, even in channel 2 for which the expected response is greatest (see fig 7.9). The computed telescope response was then subtracted from the total background in each energy channel and the least squares fits applied to the data in the depth interval $4.5 \leq p < 70 \text{ gm.cm.}^{-2}$. For comparison, least squares fits were also made to the data $10 < p < 70 \text{ gm.cm.}^{-2}$, since extrapolation to float of these fits is the usual method of determining B_{cos} experimentally.

Linear, power law, and logarithmic functions were used as trial fits to the data. The functional forms were

$$\begin{aligned} F_1(p, E) &= A(E)p + B(E) \\ F_2(p, E) &= A(E)p^{B(E)} \dots\dots\dots 7.3 \\ F_3(p, E) &= A(E) \log_{10} \left(\frac{p}{B(E)} \right) \end{aligned}$$

where the parameters $A(E)$ and $B(E)$ were determined by the method of least squares for each channel (Wolberg 1967).

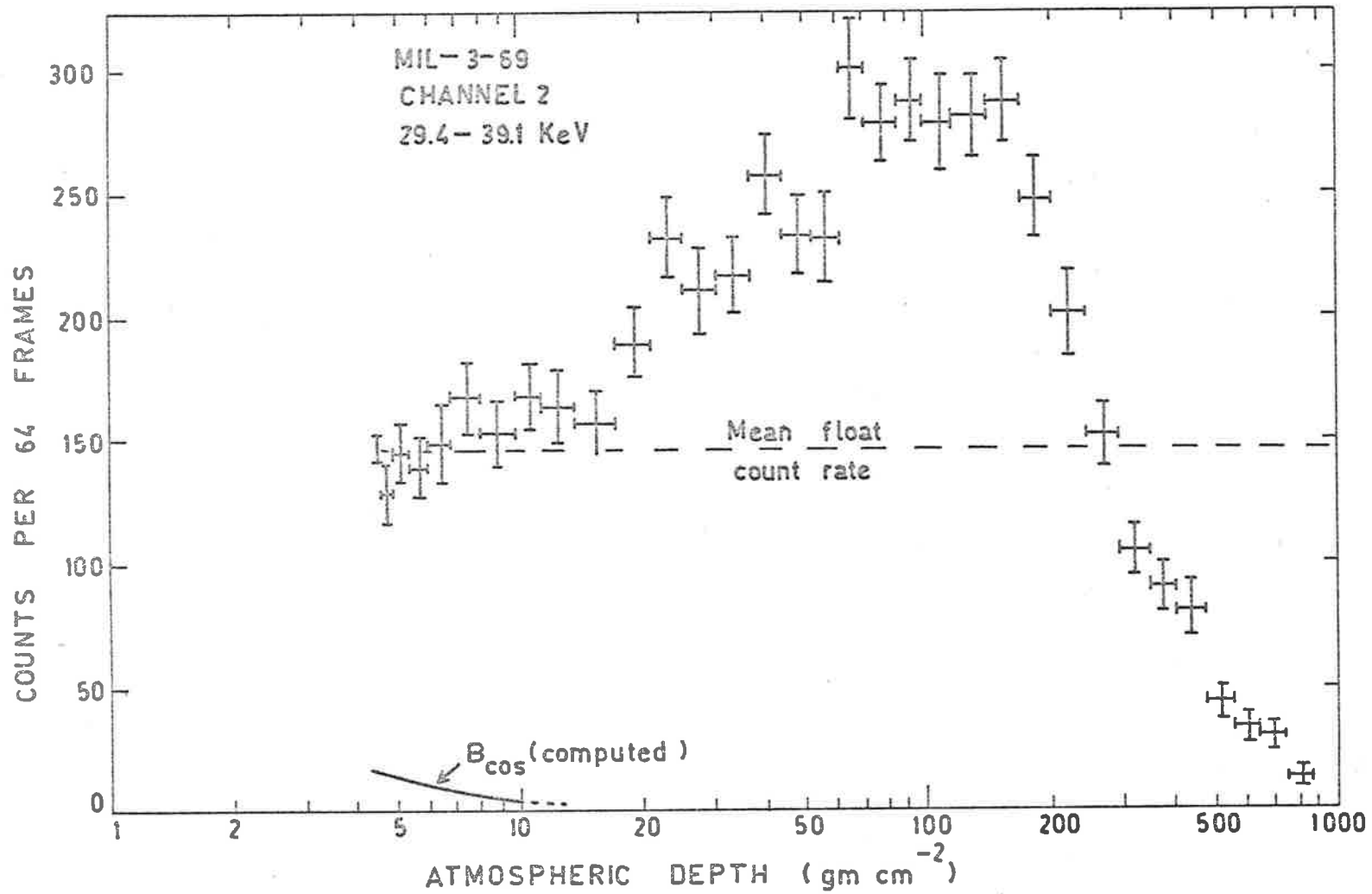


Fig. 7.6 Transition curve for channel 2 (29.4 to 39.1 KeV), MIL-3-69, with the computed contribution of B_{\cos} .

The goodness of fit of each of these functions in each energy channel can be examined by reference to table 7.1(a) in which best fit values of χ_j^2 ($j = 1, 2, 3$, see equation 7.1) are compared. Fits to both the $4.5 \leq p < 70 \text{ gm.cm}^{-2}$ data and the $10 < p < 70 \text{ gm.cm}^{-2}$ data are considered.

Table 7.1(a): Fit functions, $p < 70 \text{ gm.cm}^{-2}$, MIL-3-69

Ch. i	Energy Range (KeV)	$4.5 \leq p < 70 \text{ gm.cm}^{-2}$			$10 < p < 70 \text{ gm.cm}^{-2}$				
		No. Degrees Freedom	χ_1^2	χ_2^2	χ_3^2	No Deg Freed	χ_1^2	χ_2^2	χ_3^2
0	10.8-19.7	10	14.03	8.17	7.83	3	0.43	0.30	0.30
1	19.7-29.4	10	15.44	13.02	16.17	3	1.68	1.32	1.05
2	29.4-39.1	16	29.53	16.02	16.38	7	15.23	11.90	10.24
3	39.1-48.8	16	34.25	26.47	30.27	7	17.55	15.70	13.59
4	48.8-58.5	16	21.87	11.60	15.30	7	4.79	2.58	2.02
5	58.5-68.2	16	18.34	11.86	14.66	7	4.64	5.54	6.59
6	68.2-77.9	16	35.04	17.49	11.79	7	9.69	8.29	7.97
7	77.9-87.6	16	27.09	17.44	13.98	7	2.82	2.11	1.93
8	87.6-97.3	16	16.39	18.91	22.34	7	11.94	12.08	11.99
9	97.3-107.0	16	18.66	19.08	19.36	7	8.86	9.62	8.97
10	107.0-116.7	16	9.43	6.41	7.38	7	5.60	4.32	4.00
11	116.7-126.4	16	15.21	13.43	14.33	7	7.41	8.21	8.08
12	126.4-136.1	16	16.21	14.48	21.44	7	5.59	6.34	8.27
13	136.1-145.8	16	19.50	11.60	11.31	7	3.70	4.88	4.67

In table 7.1(b) the data are grouped into 3 lots of channel sums: (a) channels 0 and 1, (b) channels 2 to 8, and (c) channels 9 to 13. The average value of χ_j^2 per channel in each group is computed and the corresponding χ^2 probability is tabulated.

Concerning tables 7.1(a) and (b):

(i) All three functional forms can be made to provide reasonable fits to both sets of data,

Table 7.1(b) Lumped channel averages of X^2 values.

Channel group Avg. X^2 & Probability	$4.5 \leq p < 70$			$10 < p < 70$				
	No deg free- dom	X_1^2	X_2^2	X_3^2	No deg. free- dom	X_1^2	X_2^2	X_3^2
Average, 0-1 Probability	10	14.73 0.15	10.9 0.38	12.0 0.29	3	1.05 0.75	0.81 0.85	0.67 0.90
Average 2-8 Probability	16	26.07 0.06	17.11 0.38	17.81 0.35	7	9.52 0.20	8.31 0.30	7.76 0.35
Average, 9-13 Probability	16	15.92 0.48	13.00 0.68	14.76 0.55	7	6.23 0.50	6.67 0.45	6.80 0.47

since the probabilities corresponding to the average values of X^2 per channel lie within the range $0.05 \leq P \leq 0.95$.

(ii) The power law provides the best fit to the $4.5 \leq p < 70$ gm.cm⁻² data, with the logarithmic function only a little poorer. The linear function gives a fit whose quality shows rapid improvement in the high energy channels.

(iii) As would be expected there is less difference between the probabilities of the three different fits to the data $10 < p < 70$ gm.cm⁻², since there are fewer experimental points to define a fit. Once again the improvement of the linear fit in the high energy channels is apparent.

7.2.2. Extrapolation to balloon float depth.

In view of the uncertainty involved in the choice of fit function, it is of interest to see with how much reliability the different functions extrapolate to float depth. Since in what follows in chapter 8, the fit to the data in the depth range $10 < p < 70 \text{ gm.cm.}^{-2}$ will be extrapolated to float, we wish to examine the agreement, especially at float pressure, between:

- (1) the curve of best fit for $10 < p < 70 \text{ gm.cm.}^{-2}$, and
- (2) the curve of best fit for $4.5 \leq p < 70 \text{ gm.cm.}^{-2}$,

using the MIL-3-69 channel 2 data from fig. 7.6. These two curves, a logarithmic function for (1) and a power law for (2) (see table 7.1(a)) are compared in fig. 7.7. Also plotted is the power law fit, curve (3), to the $10 < p < 70 \text{ gm.cm.}^{-2}$ data.

It can be seen that the logarithmic function gives a progressively poorer extrapolation as float is approached, compared with the actual variation of B_{loc} , which is closely described by curve (2). The logarithmic function therefore is rather unsatisfactory for the purpose of predicting the float value of B_{loc} . The power law fit (3) to the $10 < p < 70 \text{ gm.cm.}^{-2}$ data has only a marginally smaller χ^2 probability and is seen to result in an extrapolation-to-float value which is in much better agreement with the calculated form of B_{loc} .

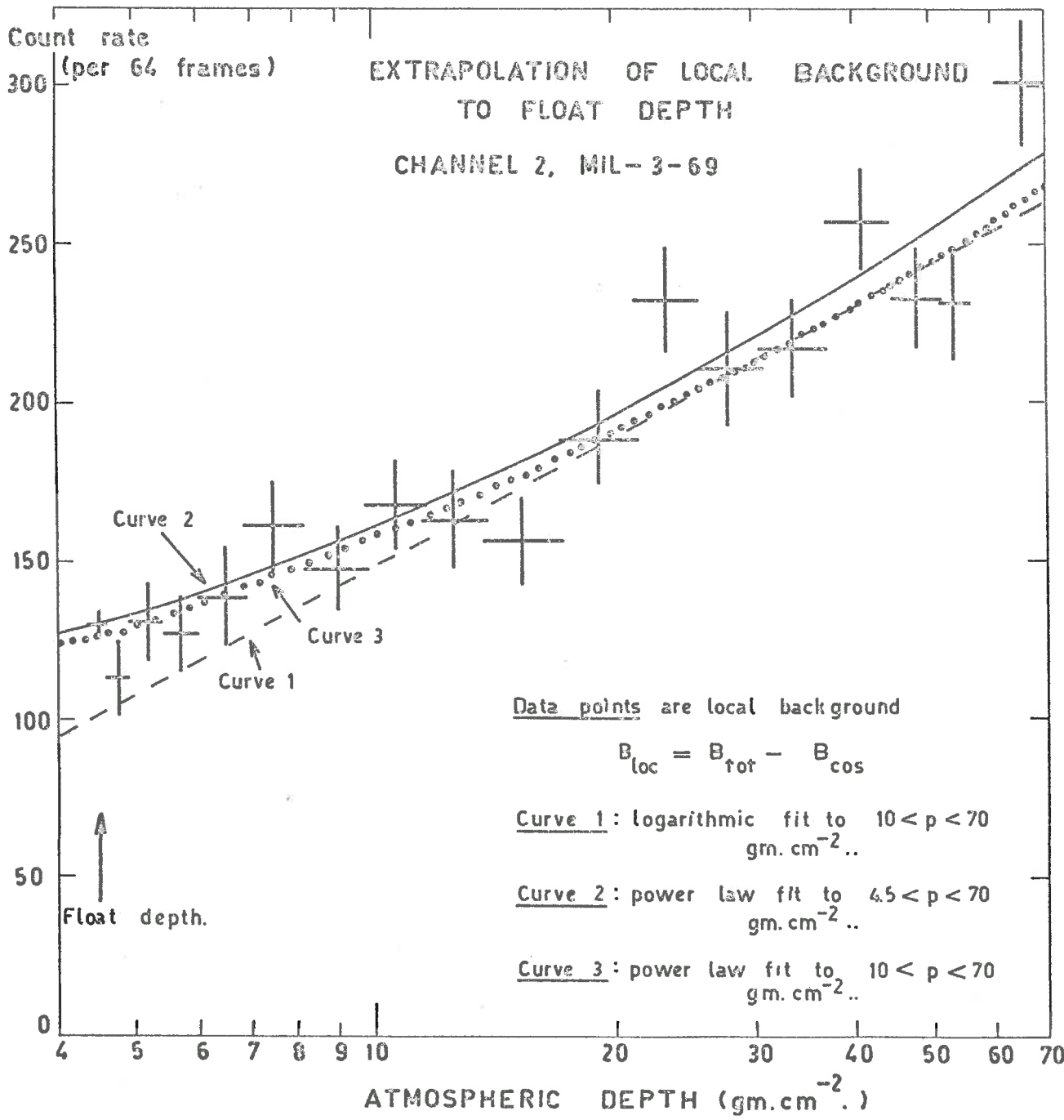


Fig. 7.7 Comparison of fit functions for channel 2, MIL-3-69

The float extrapolation value B_{1oc} (extrap.) for each type of best fit function ($10 < p < 70 \text{ gm.cm}^{-2}$) is compared with the calculated float value of B_{1oc} ($= B_{tot} - B_{cos}$) as a function of energy in fig. 7.8. The residual

$$R_j = (B_{tot} - B_{cos}) - (B_{1oc}(\text{extrap}))_j, \quad j = 1, 2, 3,$$

is plotted against energy for each fit F_j ($j=1, 2, 3$).

Examination of fig. 7.8 shows that although the errors on each R_j are large the residuals R_2 corresponding to the power law fit provide the closest agreement with the calculated value of B_{1oc} over the complete range of energies from 10.8 to 145.8 KeV, and positive and negative values appear with almost equal frequency. In contrast, the logarithmic fit generally has residuals R_3 of larger magnitude and mostly of positive sign, indicating that F_3 gives less reliable results and further that extrapolated values thus obtained may be systematically smaller than the actual values of B_{1oc} .

The linear fit F_1 behaves in the opposite fashion, yielding a majority of negative residuals R_1 which indicate a systematic overestimate of the float value of B_{1oc} . However it is to be noted that for channel 8 and above, the residuals R_1 become very close to zero, and that

$$\sum_{i=8}^{13} [R_1(\Delta E_i)]^2 \sim \sum_{i=8}^{13} [(R_2(\Delta E_i))]^2$$

where ΔE_i denotes the i^{th} energy channel.

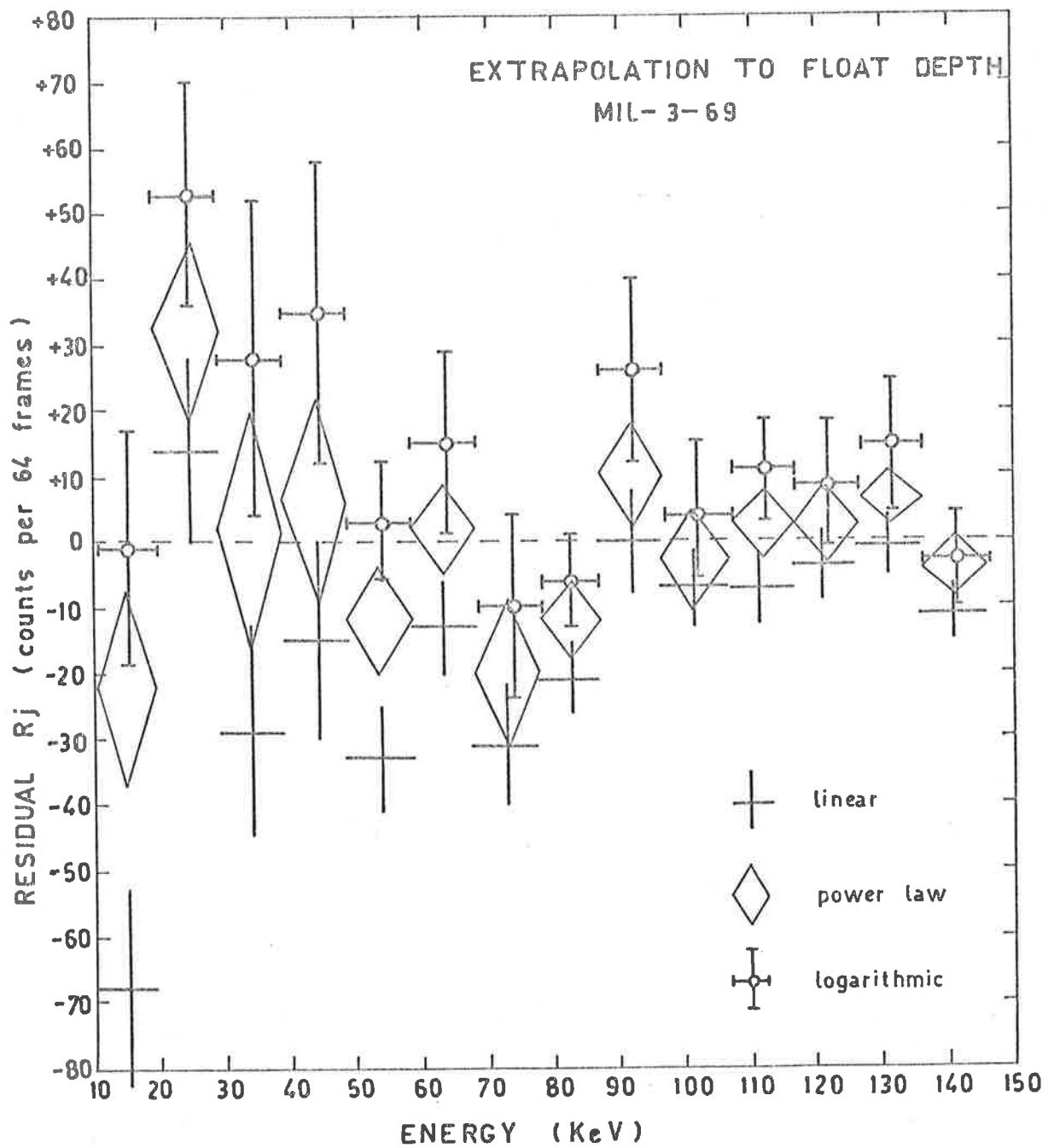


Fig. 7.8 Comparison of the residuals R_j between extrapolated and calculated values of B_{loc} for the different fit functions F_j .

The linear fit therefore rivals the power law at higher energies in giving an extrapolation-to-float in close agreement with B_{loc} . However at the lower energies, the power law is clearly the better choice.

Further observational evidence in support of this apparent energy dependence of the type of fit function, will be presented in chapter 8 using the data from the flight MIL-1-68.

7.2.3 Discussion:

It is thus concluded that from about 10 to 150 KeV, the power law probably provides the best fit to the count rates as a function of residual pressure for $p < 70 \text{ gm.cm.}^{-2}$, while the linear fit is also satisfactory at the higher energies. Although the logarithmic fit has a comparable χ^2 probability in the interval $10 < p < 70 \text{ gm.cm.}^{-2}$, it gives an extrapolation into the region $p < 10 \text{ gm.cm.}^{-2}$ which lies considerably below the expected variation of B_{loc} with pressure.

Bleeker et al. (1966, 1968, 1970a) and Kasturi Rangan et al. (1969) found that power law fits to their data provided the best extrapolations to float depth. Bleeker et al. (1970a) found their power law exponent to lie between 0.30 and 0.40 and to be independent of energy and geomagnetic latitude. Nothing can be said of the latitude dependence from our results but the exponent value of MIL-3-69 is approximately energy independent with an average value over all energy channels of 0.32 for both sets of data (a) $10 < p < 70 \text{ gm.cm.}^{-2}$ and (b) $4.5 \leq p < 70 \text{ gm.cm.}^{-2}$. The MIL -1-68 data also yield an average exponent of 0.32.

A power law is also consistent with the data of Riegler (1969) although this author preferred to use the function

$$F(p) = A \exp\left(-\frac{p}{a}\right) - B \exp\left(-\frac{p}{b}\right).$$

It is not consistent with the data of Brini et al (1965) who used $F(p) = A - B \exp(-bp)$, or of Peterson (1967) who used $F(p) = Ap + B$. It is also at variance with the theory of electronic cascade showers resulting from π^0 decay, which predicts a linear variation (Hayakawa 1969a).

7.3 ENERGY LOSS SPECTRA.

The uncertainties involved in applying corrections to individual channel rates to derive an absolute atmospheric X-ray spectrum have been mentioned. Hence the spectral results presented in this section refer to active telescope pulse height distributions (or NaI(Tl) energy loss spectra) rather than to absolute photon intensities. Conclusions can however still be drawn.

7.3.1. Pulse Height Distributions:

Fig 7.9 shows energy loss spectra observed during MIL-1-68 and MIL-3-69 at different atmospheric depths (slant depths for MIL-1-68). The ordinate is counts per 64 frames (64 frames \equiv 256 sec) per energy channel. There is reasonable agreement between the two flights at low altitudes but with increasing height a dramatic intensity difference becomes apparent in the energy range $20 < E < 80$ KeV.

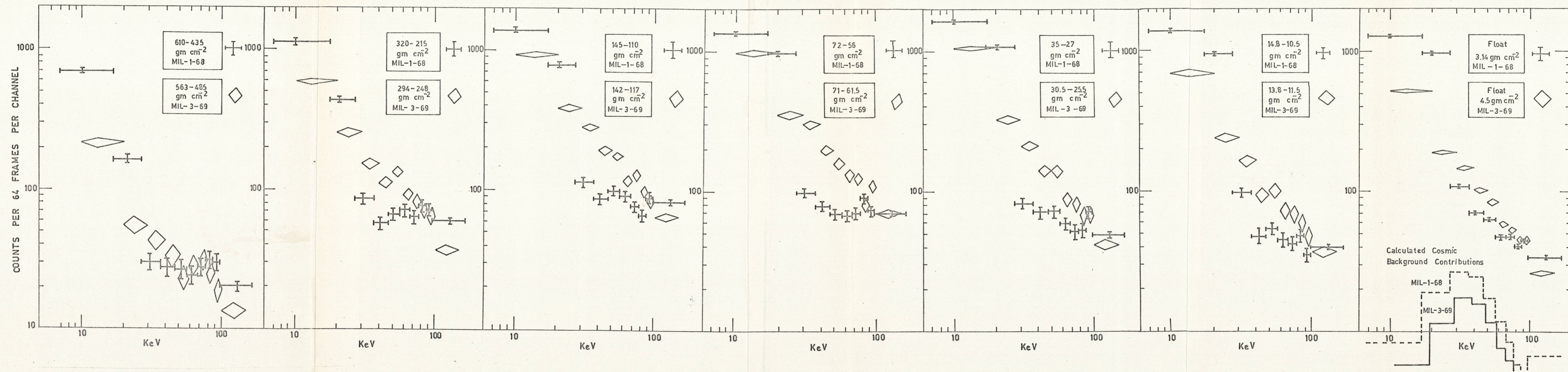


Fig. 7.9 Energy loss spectra for MIL-1-68 and MIL-3-69 at different atmospheric depths (slant depths for MIL-1-68).

Since the two results come from the same detector whose spectral response function (equation 3.6) was essentially the same for both flights and whose correct operation on both occasions has been verified, it is apparent that a real time variation occurred in the radiation environment from which the telescope background originates. Spectra from MIL-1-69 and MIL-2-69 are in close agreement with the MIL-3-69 results. Comparison of G.S. telescope backgrounds between the flights MIL-1-68 on one hand and MIL-1-69 and MIL-2-69 on the other, is difficult since the detector opening solid angle and also the shielding efficiency were different.

Environmental conditions during each flight are tabulated in table 1.1.(b) and the 3-hourly K_p indices do reveal a greater geomagnetic disturbance for MIL-1-68 than for the other flights. However a local geomagnetic rigidity change of even exceptionally great size should be quite unable to produce the observed difference in background intensity of about a factor of 5. Comparison of the active well rates for the two flights reveals little difference (fig. 7.10), a fact which is difficult to reconcile with any hypothesis of real time variations of atmospheric radiation. The presence of radioactive debris as fall-out from nuclear weapon tests is such a hypothesis. The intensity difference observed in fig. 7.9 thus has not yet been satisfactorily explained.

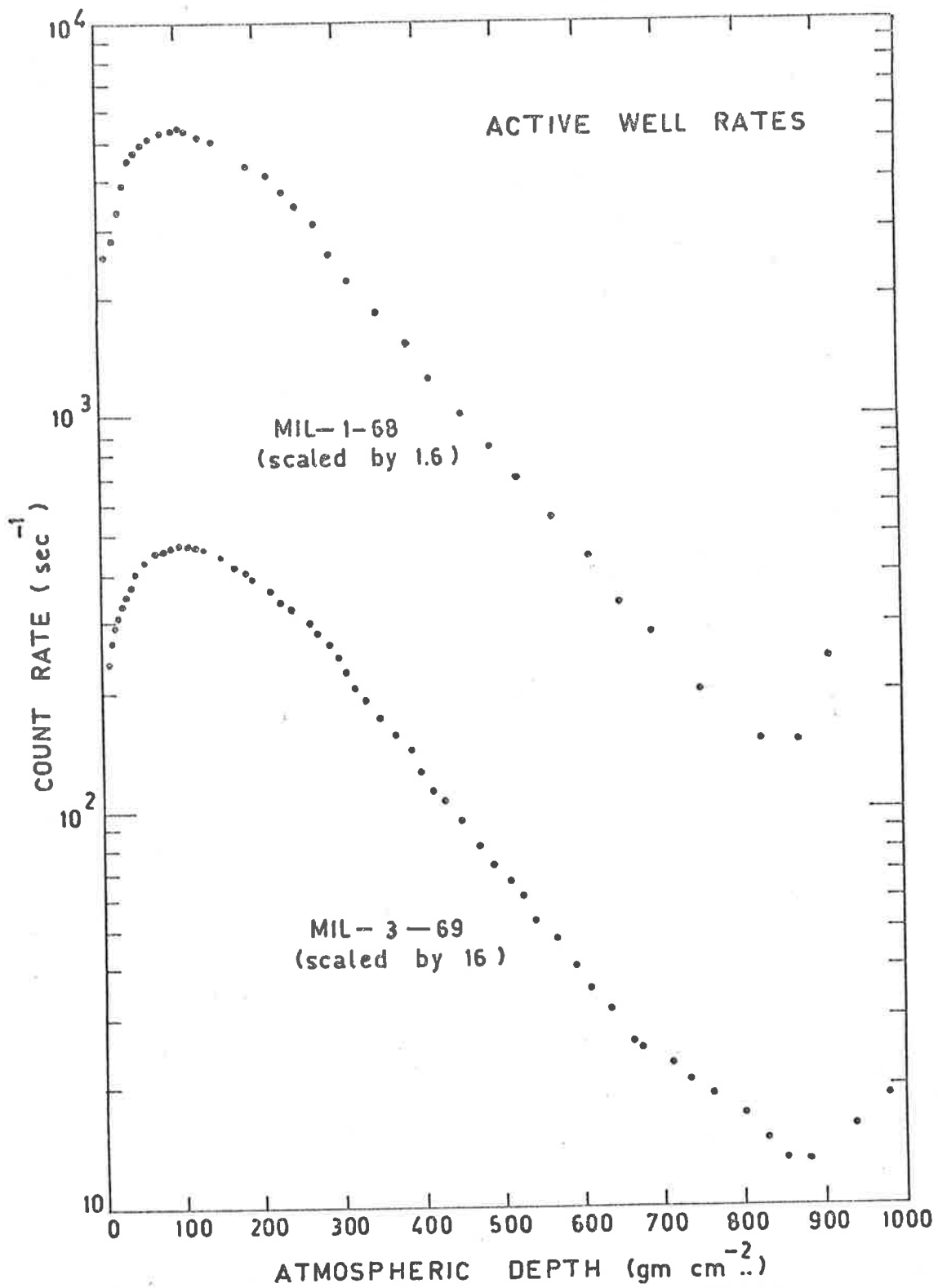


Fig. 7.10 Active well rates for the flights MIL-1-68 and MIL-3-69 as a function of vertical atmospheric depth.

For $E \lesssim 20$ KeV and $E \gtrsim 100$ KeV the intensity agrees well between flights but at intermediate energies and at pressures between 300 and 10 gm.cm.^{-2} , the MIL-1-68 pulse height distribution is almost flat, while that of MIL-3-69 closely follows a power law dependence of the approximate form E^{-n} where $n \sim 1.1$ for $100 \lesssim p \lesssim 300 \text{ gm.cm.}^{-2}$, and $n \sim 1.3$ for $4.5 \lesssim p \lesssim 100 \text{ gm.cm.}^{-2}$, implying a softening of the atmospheric X-ray spectrum at the highest altitudes.

The low MIL-1-68 background, coupled with the small residual pressure at ceiling altitude (2.7 gm.cm.^{-2}) made MIL-1-68 an ideal flight from which to examine the cosmic diffuse background, and this will be described in the following chapter. At float altitude the intensities on the two flights show closer agreement, presumably due to the greater contribution of the cosmic diffuse background B_{cos} to the MIL-1-68 counting rates. The relative contributions at float altitude of B_{cos} in MIL-1-68 and MIL-3-69 are shown in fig 7.9.

7.3.2. Spectral colour indices:

The apparent background spectral softening at depths $\lesssim 100 \text{ gm.cm.}^{-2}$ remarked upon above, is seen to better advantage by defining colour indices (Haymes et al. 1969).

We define the following indices:

$$\text{MIL-1-68} \left\{ \begin{array}{l} \alpha(p) = \frac{\sum_{i=2}^4 R_i(p)}{\sum_{i=9}^{15} R_i(p)} \\ \beta(p) = \frac{\sum_{i=5}^8 R_i(p)}{\sum_{i=9}^{15} R_i(p)} \\ \gamma(p) = \frac{\sum_{i=2}^4 R_i(p)}{\sum_{i=5}^8 R_i(p)} \end{array} \right.$$

$$\text{MIL-3-69} \left\{ \begin{array}{l} \alpha_0(p) = R_0(p) / \sum_{i=9}^{13} R_i(p) \\ \alpha(p) = \sum_{i=1}^4 R_i(p) / \sum_{i=9}^{13} R_i(p) \\ \beta(p) = \sum_{i=5}^8 R_i(p) / \sum_{i=9}^{13} R_i(p) \end{array} \right.$$

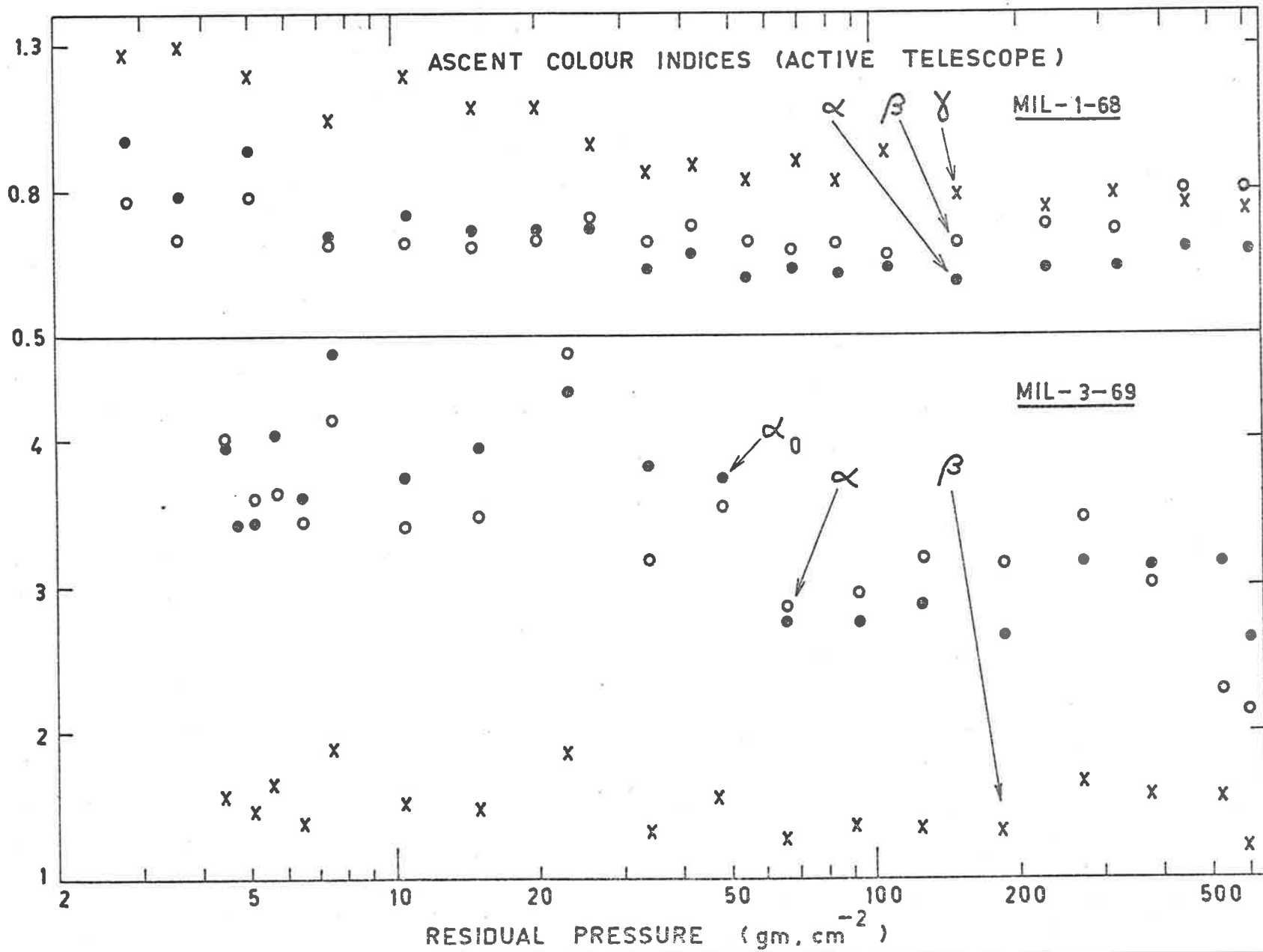
where $R_i(p)$ is the count rate in the i^{th} energy channel at residual pressure p gm.cm.⁻²

The pressure variation of these indices is plotted in fig. 7.11. The spectral softening at high altitudes is evident in both flights and is supported by results obtained in the other flights for both the active and graded shield telescopes. The degree of softening is almost independent of the cosmic diffuse background contribution and for MIL-3-69 the effect has been estimated to be less than 6%. The observed spectral softening is in agreement with the results of Vette (1962) and Haymes et al. (1969).

7.3.3. Spectral structure.

Very little structure is seen to be superposed upon the spectral continuum of fig. 7.9. The most distinctive feature appears at the lowest altitudes at about 80 KeV and has not received an explanation. There is also a suggestion of an enhancement above the continuum level between about 50 and 60 KeV but this is not statistically significant. If it is real, a possibility is that it results from the inelastic scattering of fast (1 to 10 MeV) secondary neutrons by I¹²⁷ nuclei in the NaI(Tl) crystal, since a deexcitation gamma ray has been observed at about 60 KeV in laboratory scattering experiments (Van Loef and Lind 1956).

Fig. 7.11 Pressure variation of spectral colour indices.



No other I^{127} deexcitation lines would be observed in fig. 7.9 as they lie at energies greater than the energy interval analysed.

There has been speculation as to whether these higher energy lines have been observed by other balloon experiments (Chupp et al 1967, 1968, 1970, Haymes et al. 1969) but no satisfactory conclusions could be reached. Theoretical calculations argue against a significant effect of this type, as is the case for thermal neutron capture effects also (Vette 1962). Neutron interactions with air molecules e.g. (n, γ) capture reactions and inelastic scattering are also thought to be insignificant (Peterson 1963).

There are other possible origins for the existence of atmospheric gamma ray lines. For example, Frost et al (1966) have reported observing at high altitude a line at 660 KeV and attribute it to the contamination of Cs^{137} in nuclear fallout debris. Chupp et al (1967) have also been led to believe that such fission products are instrumental in producing line sources of gamma rays at balloon altitudes. There is also the possibility that lines may result from interactions of cosmic rays with the detector shielding masses.

The uncertainty evident in these spectral measurements can only be resolved by performing experiments with much improved energy resolution using, say, Ge(Li) detectors (Womack and Overbeck 1968).

7.4 TIME VARIATIONS:

Flight-to-flight variations of certain characteristics of the atmospheric radiation environment have been described already. Examples have been attenuation lengths for $200 < p < 700 \text{ gm.cm.}^{-2}$, altitudes of transition maxima, and background pulse height distributions. One peculiarity which has not yet been discussed and which has appeared during the flights MIL-1-68 and MIL-3-69 only, has been a count rate increase in the low energy channels at depths of $28 \pm 5 \text{ gm.cm.}^{-2}$, corresponding to a time interval of ~ 10 minutes. In MIL-1-68, channel 0 was subject to register overflow problems which led to some ambiguity in the determination of the transition curve. However, the data for the channel 1 are to be seen in fig. 7.1. The channel 0 count rate for MIL-3-69 was not great enough to cause overflow problems and the results for it and channel 1 are shown in fig. 7.12. Some of the higher energy transition curves for both flights also suggest this feature but at a statistically insignificant level (see figure 6.1). There was no significant effect in the active guard rates (fig. 7.10). The possibility that the variations resulted from corona discharge in the central detector PM tubes can be rejected since vacuum testing performed prior to each flight failed to find any such malfunction.

The only radiation for which a transition maximum has been observed at about 30 gm.cm.^{-2} , is the secondary neutron flux resulting from the interactions with the atmosphere of energetic ($\geq 100 \text{ MeV}$) solar flare protons (Smith et al 1962, Lingenfelter

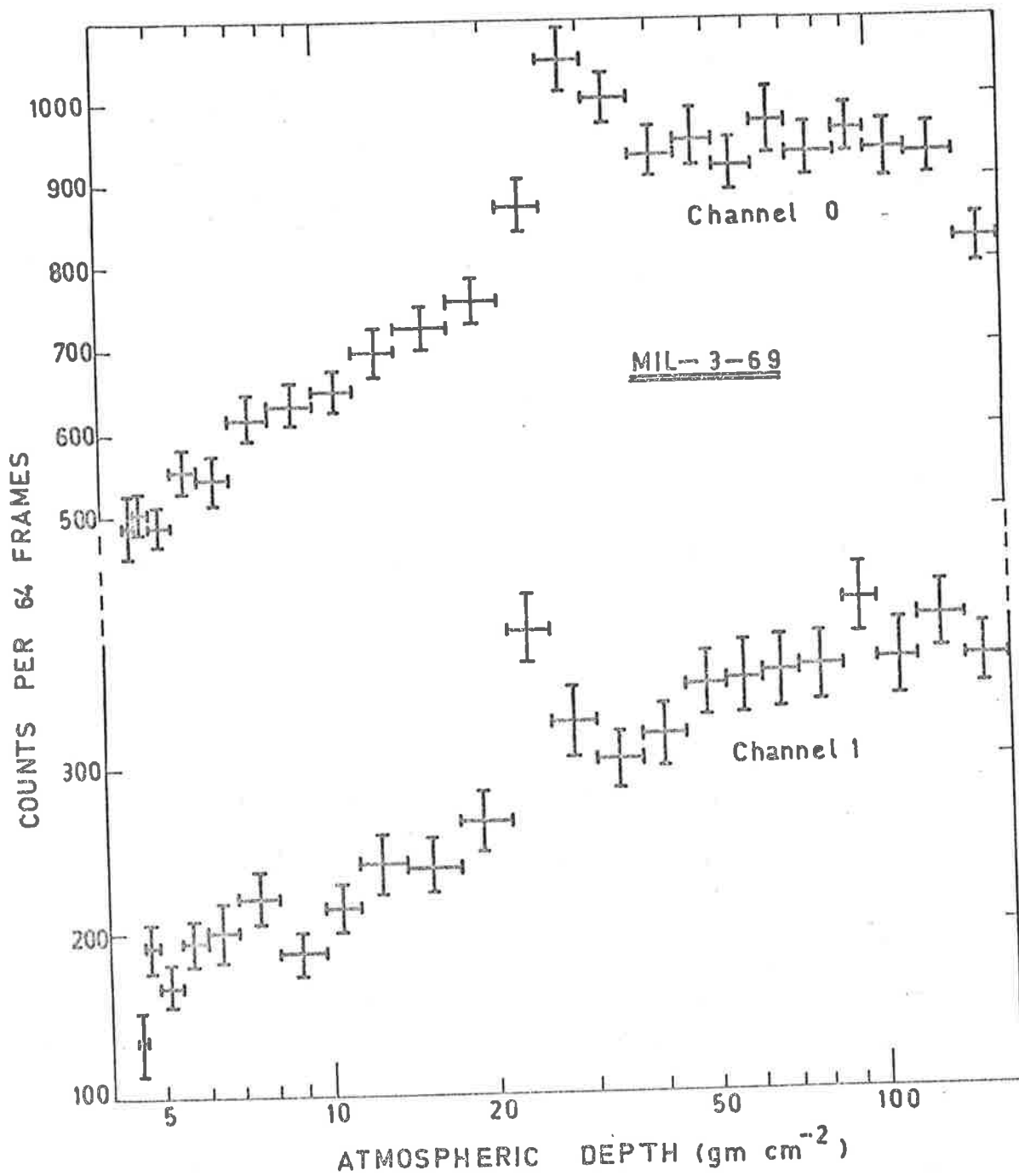


Fig. 7.12 Count rate enhancement at $28^{+5} \text{ gm.cm.}^{-2}$ for channels 0 and 1, MIL-3-69.

and Flamm 1964, Greenhill et al. 1970). This effect is only observed during solar proton events.

Haymes (1964) observed sharp time-correlated intensity increases for both fast neutrons and gamma rays (gammas 0.47 to 3.5 MeV) while at a ceiling altitude of 4.7 gm.cm.^{-2} . No good explanation could be found for these variations since no solar flares of greater than importance 1 were reported and the geomagnetic field was quiet. Haymes et al (1969) also remarked that events as small as subflares may produce sufficient hard radiation to cause secondary photon intensity variations at balloon altitudes.

There was little solar activity and no solar proton events which correlated with MIL-1-68 or MIL-3-69. Consequently if the time variations are solar-controlled, they must be associated with small events such as subflares, as suggested by Haymes et al (1969). Further since the above-mentioned neutron data were taken during the solar proton events, there are no grounds for identifying the observed X-ray time variations with neutron effects. No significant background time variations were observed while the balloon floated at ceiling altitude during either flight.

7.5 GEOMAGNETIC LATITUDE VARIATIONS:

Since the prevailing winds at $\sim 4 \text{ gm.cm}^{-2}$ above Mildura are either easterlies or westerlies, little variation in geomagnetic latitude occurs for the balloon during a typical flight. For example, Mildura has a geomagnetic latitude of 44.0°S , with a rate of change of 0.1° per degree of geographic longitude (Finch and Leaton 1967).

Hence a traverse of 240 miles or 4° of longitude to the east or west results in a geomagnetic latitude change of $\sim 0.5^\circ$ implying a change in cut-off rigidity of ~ 0.5 Gv. In view of this small variation, no attempt has been made to determine the dependence of atmospheric X-ray intensity upon geomagnetic latitude. Other results have been given by Bleeker and Deerenberg (1970a).

7.6 CONCLUSIONS:

It has been shown in this chapter that:

- (1) Linear, power law and logarithmic functions of pressure are all good approximations to the atmospheric background (B_{loc}) transition curves in the pressure interval $10 < p < 70 \text{ gm.cm}^{-2}$. However for $p < 10 \text{ gm.cm}^{-2}$ the logarithmic fit appears to extrapolate to values which are too small. With respect to extrapolation the power law is the most satisfactory over the complete energy range and there is evidence to believe that the linear fit is acceptable at the higher energies. However its low energy performance is not as good as the power law.
- (2) There was a significant difference in the intensity of B_{loc} observed in February 1968 and April, May and August 1969. This difference was about a factor of 5 in the pressure interval $10 < p < 300 \text{ gm.cm}^{-2}$ and the energy interval $20 < E < 80 \text{ KeV}$. No such difference was observed in the anticoincidence well rate for the different flights. The pulse height distribution in February 1968 was almost flat

while a power law was a good approximation to the 1969 data.

- (3) There is a spectral softening at pressures $p < 100 \text{ gm.cm}^{-2}$, and,
- (4) An intensity enhancement of uncertain origin at a depth of $28 \pm 5 \text{ gm.cm}^{-2}$ and at energies less than about 20 KeV was observed on MIL-1-68 and MIL-3-69 but not on the other flights. No effect was observed in the anticoincidence guard rates.

CHAPTER 8THE DIFFUSE X-RAY BACKGROUND, 20-170 KeV8.1 INTRODUCTION

The following chapter presents results from the actively collimated and shielded telescope concerning the spectrum and angular distribution of the diffuse X-ray background in the approximate energy range, 20 to 170KeV.

Observations of the diffuse background perhaps have a greater significance for astrophysics than do discrete source observations. Whereas discrete sources are predominantly galactic phenomena, the diffuse background appears to be extragalactic in origin. This is so in the 1 to 200 KeV region at least, since this radiation has been observed to be isotropic with respect to the galactic plane to within about 10% (see section 8,3). As a result there may be important consequences for cosmology, galaxy evolution, the intergalactic medium and cosmic ray physics (Wilson 1968, Sciama 1969, Brecher and Burbidge 1970), as has been outlined in section 1.3.

8.2 THE DIFFUSE BACKGROUND SPECTRUM

In addition to the constraint of isotropy to within 10%, suggested theoretical models of the origin of the diffuse background must also account for the spectral shape. The observed break in spectral index somewhere between 10 and 100 KeV has been discussed in section 1.3 and more definitive measurements of its magnitude and the energy range over which it occurs are essential. An attempt at such a measurement is now described.

The method used to determine the diffuse background intensity as a function of photon energy, in which the total telescope background obtained in the pressure range $10 \lesssim p \lesssim 70 \text{ gm. cm.}^{-2}$ is extrapolated to balloon float depth and subtracted from the measured background, has been described in Chapter 7. Three types of fit to the transition curve data were considered in order to perform the extrapolation. These were linear, power law and logarithmic functions of pressure. Comparison of minimum χ^2 values does not decisively determine which of the 3 fits is the most appropriate for a given channel since the low background rates make counting statistics poor.

For the flight MIL-1-68, the logarithmic function was found to give extrapolations to float depth which were far too small, two channels actually extrapolating to negative counting rates for the total background. Cosmic diffuse fluxes resulted which were between 2 and 5 times higher than those expected. Consequently although the logarithmic function was a good fit for $p \gtrsim 10 \text{ gm. cm.}^{-2}$, it was not seriously considered to provide a good extrapolation to lower pressures and was not used in the diffuse background determination.

In view of the indecision as to whether to use the linear or the power law extrapolation, it has been decided to present three sets of spectral results, obtained using (a) linear extrapolation for all channels, (b) power law extrapolation for all channels, and (c) a linear or power law extrapolation depending on which fit has minimum χ^2 for the energy channel concerned. The total observed float background from which the extrapolated background was subtracted, was obtained during the entire float period except when resolved discrete sources were in the telescope field of view.

There were no significant azimuthal effects in the background for the energy channels used, nor were there any significant time variations. The three spectra thus obtained, fully corrected (see Chapter 3) except for atmospheric Compton scattering effects (Makino 1970), are shown in fig. 8.1, 8.2 and 8.3. A number spectrum of exponent 2.4 has been assumed and the points are plotted alongside data of other groups, as presented by Kasturi Rangan et al. (1969). The data are also tabulated in table 8.1, together with the number of degrees of freedom (= number of data points minus number of unknown parameters) used in the least squares fit.

Table 8.1 shows that using the χ^2 criterion the lower energy transition curves (channels 2 to 6) are in general better fitted by the power law, while for channels 7 and above the linear fit is better. This energy dependence was also marginally apparent in the MIL-3-69 data (see Chapter 7). That it is a real effect is supported by comparison of the plotted spectra (figs. 8.1, 8.2, 8.3) in which it is clear that the diffuse background results of this experiment agree best with other experiments in the low energy region for a power law extrapolation (fig.8.2) and at higher energies for the linear extrapolation (fig. 8.1). Over the full energy range, best agreement is obtained if the minimum χ^2 criterion is applied to determine whether the power law or linear fit should be used for a given energy channel (fig. 8.3). It is strikingly evident that although there are really no significant differences between the two fits using the χ^2 criterion, the final spectral results are strongly dependent on the type of fit used.

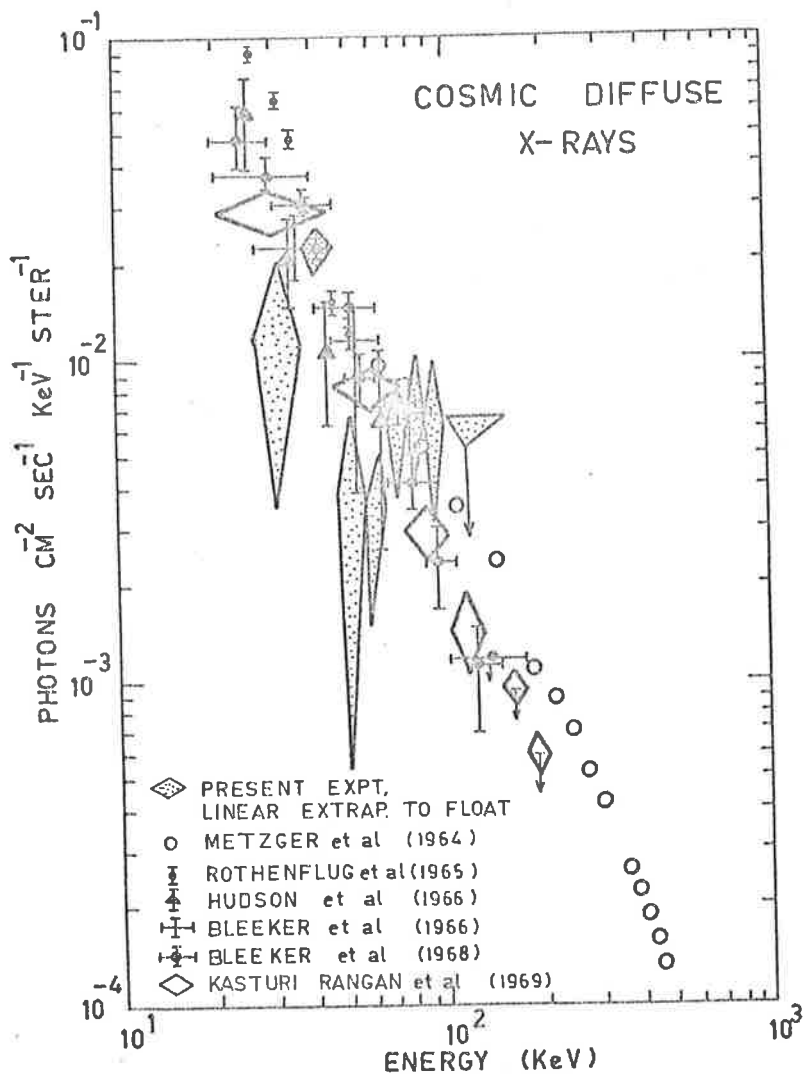


Fig: 8.1 Diffuse background spectrum obtained by extrapolating to float depth using a linear transition curve for each energy channel.

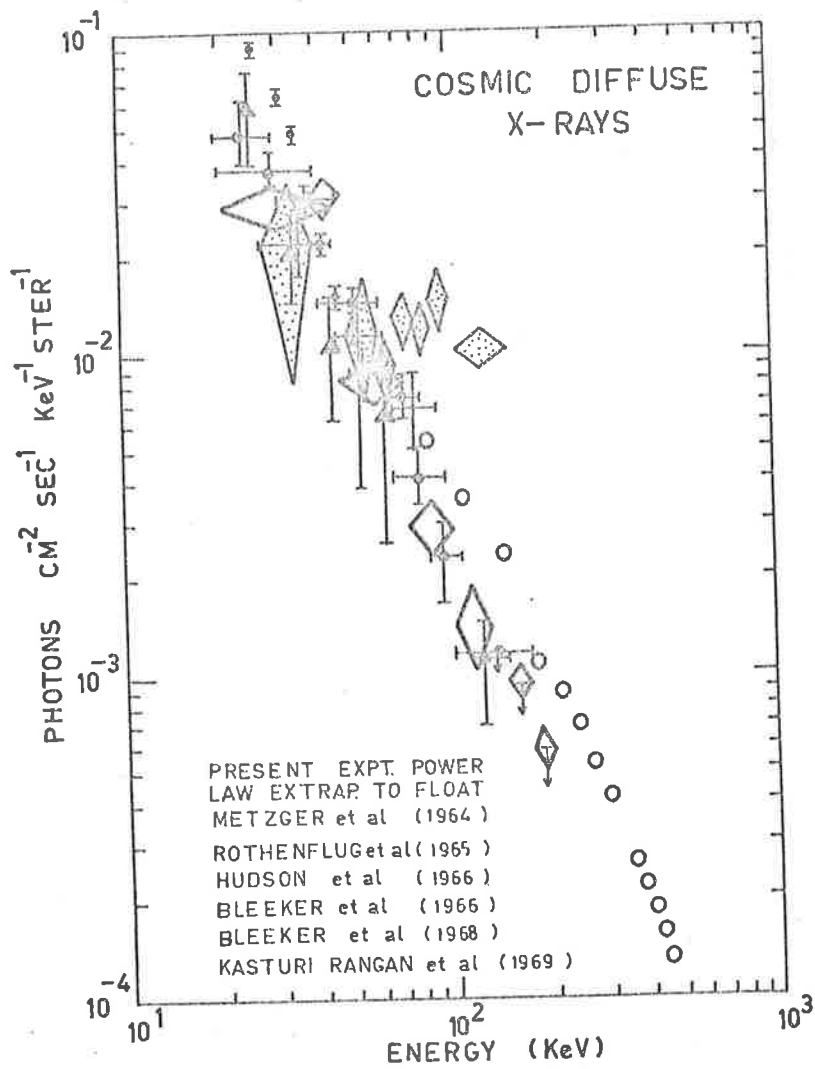


Fig: 8.2 Diffuse background spectrum obtained by extrapolating to float depth using a power law transition curve for each energy channel.

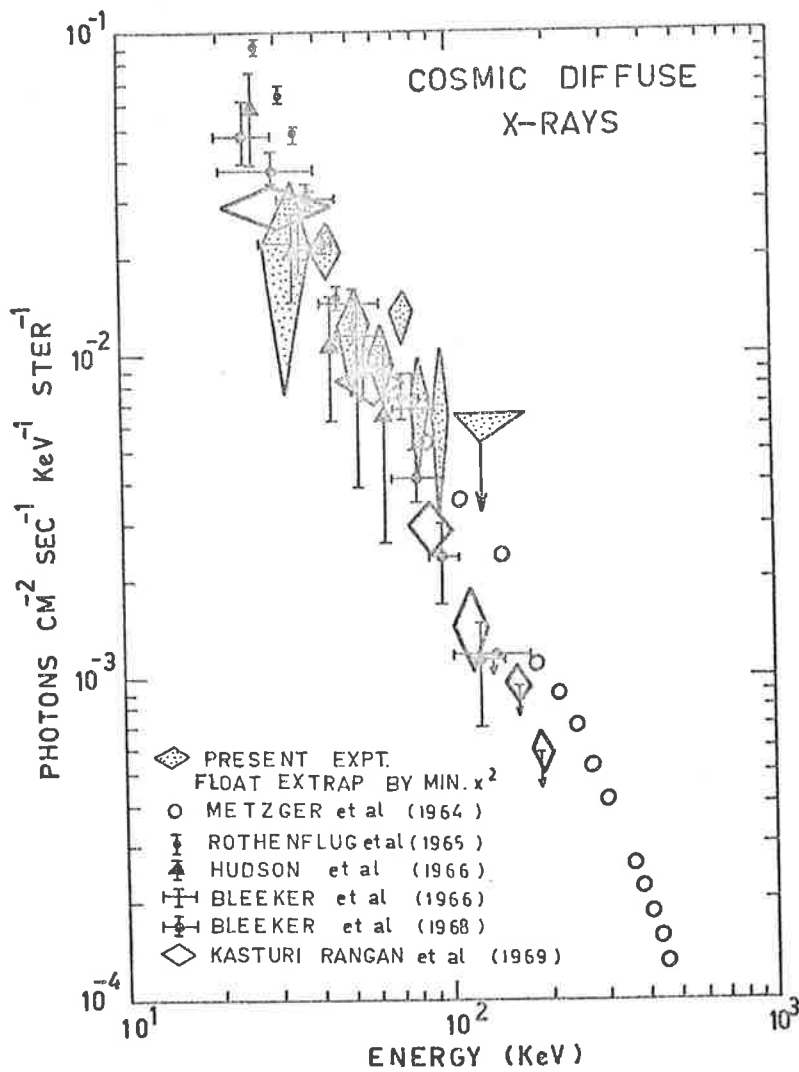


Fig: 8.3 Diffuse background spectrum, obtained by using the minimum χ^2 criterion to decide between the linear and power law extrapolation-to-float functions.

Table 8.1: Spectra from two different transition curve fits

Ch No i	Energy KeV.	No. degrees of freedom	Best linear fit		Best power law fit	
			χ^2	Diffuse background ₂ photons cm. ⁻² sec ⁻¹ KeV ⁻¹ ster ⁻¹	χ^2	Diffuse background ₂ photons cm. ⁻² sec ⁻¹ KeV ⁻¹ ster ⁻¹
2	27-37	12	16.44	$(1.18^{+0.84}) \times 10^{-2}$	15.94	$(2.18^{+1.45}) \times 10^{-2}$
3	37-47	12	12.50	$(2.08^{+0.34}) \times 10^{-2}$	14.59	$(3.01^{+0.41}) \times 10^{-2}$
4	47-57	12	14.86	$(3.65^{+3.14}) \times 10^{-3}$	13.91	$(1.19^{+0.44}) \times 10^{-2}$
5	57-67	12	7.62	$(3.65^{+1.89}) \times 10^{-3}$	6.41	$(9.39^{+2.39}) \times 10^{-2}$
6	67-77	12	14.93	$(6.27^{+2.64}) \times 10^{-3}$	12.04	$(1.40^{+0.26}) \times 10^{-2}$
7	77-87	12	16.80	$(7.10^{+3.02}) \times 10^{-3}$	20.24	$(1.25^{+0.26}) \times 10^{-2}$
8	87-97	12	25.21	$(6.44^{+4.00}) \times 10^{-3}$	26.83	$(1.59^{+0.35}) \times 10^{-2}$
9-15	97-167	12	26.56	$*6.69 \times 10^{-3}$	32.30	$(1.15^{+0.23}) \times 10^{-2}$
χ^2 sums : $\sum_{i=2}^6 \chi_i^2$			66.35		62.89	
$(\sum_{i=7}^8 \chi_i^2) + \chi_{9-15}^2$			68.57		79.37	
$(\sum_{i=2}^8 \chi_i^2) + \chi_{9-15}^2$			134.92		142.26	

*Upper limit at 3 sigma level

8.2.2. Spectral results

It is therefore concluded that fig. 8.3 gives the best determination from this experiment of the diffuse cosmic X-ray background. It is statistically consistent with the other measurements plotted on the same graph. However, the large error bars reflect the disadvantage of using the active telescope for diffuse background work which results from the small geometric factor of $\sim 1.4 \text{ cm}^2 \text{ ster.}$ which is between 5 and 10 times less than is usually employed in this work. In particular, it is not possible for conclusions to be drawn with respect to any change of spectral index within the observed energy range.

Note should be made that a small correction must be made to the results of this experiment and also to the other data points on figs. 8.1, 8.2 and 8.3 which were obtained from balloon experiments (i.e. all except Matzger et al. 1964). Makino (1970) has very recently pointed out that failure of balloon experimenters to allow for the contribution of atmospheric Compton scattering to the detector count rate has resulted in intensity over-estimates of about 20% to 40% in all results published to date. The necessary correction factor is almost energy independent and varies from about 0.85 for a float depth of $\sim 3 \text{ gm. cm.}^{-2}$, to about 0.65 at 10 gm. cm.^{-2} .

8.3. GALACTIC DIFFUSE X-RAYS

The question of the existence of a high energy X-ray anisotropy in the direction of the galactic plane has been investigated. At energies $\gtrsim 5 \text{ KeV}$, the galaxy is transparent to X-rays and no anisotropy is expected for a background flux of entirely extragalactic origin. However, the concentration of matter and photons in the galactic disc may lead to enhanced X-ray emission at low galactic latitudes. Maraschi et al (1967)

have shown that this is possible as a result of interactions of galactic cosmic ray electrons with matter (bremsstrahlung) or with the 3°K. and starlight photons (inverse Compton effect). They predict a galactic plane anisotropy, $\alpha = \frac{I_{\max} - I_{\min}}{I_{\max}}$, of between 1 and 10% depending on the form of the demodulated galactic electron spectrum. Also the recent discovery of intense diffuse galactic infra-red radiation (Shivanandan et al. (1968), Houck and Harwit (1969), Ipavich and Lenchek (1970)) has provided another possible source of low energy photons for the Compton production of galactic X-rays.

It is thus of interest to determine observationally whether there is an anisotropy in the diffuse X-ray background, oriented relative to the galactic plane.

8.3.1 Galactic plane anisotropy

A galactic latitude survey was carried out for MIL-1-68 in the longitude range $320^\circ < l^{\text{II}} < 40^\circ$ and for energies 27 to 67 KeV. Regions of the sky containing resolved discrete sources were excluded from the analysis. The sky was divided into two parts for the purpose of accumulating counts. One of these, the galactic plane region, included all telescope axis directions for which the galactic latitude b^{II} satisfied the requirement $|b^{\text{II}}| < 10^\circ$. The other was for directions $|b^{\text{II}}| > 10^\circ$, out of the galactic plane. Counts in each region were added together without subtracting the non-cosmic telescope background (B_{loc}) to obtain an average total count rate (B_{tot}). The two total background rates (counts per frame of 4 sec. duration) between 27 and 67 KeV were

$$B_{\text{tot}} (|b^{\text{II}}| < 10^\circ) = 4.461 \pm 0.092$$

$$B_{\text{tot}} (|b^{\text{II}}| > 10^\circ) = 4.179 \pm 0.059$$

The uncorrected X-ray emission from the galactic plane is therefore

$\Delta = 0.282 \pm 0.109$ counts per 4 seconds, since the atmospheric X-ray and telescope leakage backgrounds are independent of b^{II} . This difference is 2.6 standard deviations above that expected for an isotropic flux and is significant at about the 99% confidence level. The anisotropy factor is given by $\alpha = \frac{\Delta}{B \cos \left(\int b^{\text{II}} < 10^\circ \right)}$, which gives $\alpha = (17.5 \pm 9.5)\%$.

If instead of using $\left\{ b^{\text{II}} \right\} = 10^\circ$ as the criterion for sorting counts, $\left\{ b^{\text{II}} \right\} = 15^\circ$ is used, the difference Δ becomes 0.07 ± 0.09 counts per 4 seconds, and the 2.60 σ anisotropy has become a null result. This fact, together with the serious problem of unresolved discrete sources in the analysis interval $320^\circ < l^{\text{II}} < 40^\circ$ (containing the galactic centre) suggests that the observed anisotropy is not the result of a diffuse flux.

The contribution from unresolved discrete sources can be estimated by assuming that they number about 10, have spectra similar to that of Sco X-1, and intensities of about 1 photon $\text{cm}^{-2} \text{sec}^{-1}$ between 1 and 8 KeV. (Mayer et al. 1970, Gursky et al. 1967). Each source is estimated to have been within 4° of the telescope axis for about 300 seconds during the flight. Extrapolation to the energy interval 27 to 67 KeV predicts a contribution of ~ 100 counts to the total accumulated count from the directions $\left\{ b^{\text{II}} \right\} < 10^\circ$ during the flight. This is in good agreement with observation since the observed disc contribution of 0.28 ± 0.11 counts per 4 seconds from ~ 2000 seconds of data, corresponds to a total accumulation of 140 ± 55 counts.

Also the University of Leicester group has recently withdrawn an apparent anisotropy in the range $220^\circ < l^{\text{II}} < 320^\circ$ of $\sim 50\%$ (Cooke et al. 1969) and have replaced it with an upper limit corresponding to a line flux

<10% of that originally claimed, owing to the resolution of the region concerned into a number of discrete sources (Cooke and Pounds 1970).

Consequently it is preferable to interpret the above results in terms of an upper limit for α , which at the 30' level is given by

$$\alpha \lesssim 30\%.$$

This result is almost independent of the functional form used in extrapolating background rates to float.

It is of interest to compare this result with those obtained by other workers who have attempted to find an X-ray anisotropy with respect to the galactic plane. Seward et al. (1967) examined the interval $85^\circ < l^{II} < 130^\circ$ at photon energies between 4 and 40 KeV and were unable to detect any anisotropy greater than the uncertainty due to their counting statistics which were determined to about 10% (one standard deviation). On this basis they reported the cosmic background to be isotropic to within 10% and this is essentially a one sigma result. Gorenstein et al. (1969) examined $190^\circ < l^{II} < 150^\circ$ between 1 and 13 KeV and determined that the background was isotropic to within 8% in the same manner as Seward et al. had done. Rothenflug et al. (1968) observed $1.60^{+0.35}$ photons $\text{cm}^{-2} \text{sec}^{-1} \text{ster}^{-1}$ between 20 and 80 KeV from the Cygnus region of the galactic plane, and $1.72^{+0.16}$ photons $\text{cm}^{-2} \text{sec}^{-1} \text{ster}^{-1}$ from the galactic pole and noted that there was no difference within the errors of the counting statistics. They concluded in the same way as had Seward et al. and Gorenstein et al. that the diffuse flux was isotropic to within 20%, another one sigma result.

In order to make a fair comparison with these other results, the result of this experiment should be quoted at the one sigma level also.

Hence it is concluded that for energies $27 \leq E \leq 67$ KeV and for galactic longitudes $320^\circ < l^{\text{II}} < 40^\circ$, the diffuse background is isotropic with respect to the galactic plane to within 10%. This result is comparable with those obtained above by other groups. The regions of sky from which the various measurements were taken are shown in figure 8.4.

8.3.2. Galactic lineflux

Other workers have preferred to present their results in terms of a derived line flux in the galactic plane, rather than as a value for the degree of anisotropy, \propto . In this experiment the active telescope response factor for a line source passing through the centre of the field of view is $8.44 \text{ cm}^2 \text{ rad}$. Using this the upper limit (3 σ) for the intensity of a line source in the galactic plane is $7.26 \times 10^{-4} \text{ photons cm}^{-2} \text{ sec}^{-1} \text{ KeV}^{-1} \text{ rad}^{-1}$ between 27 and 67 KeV and for longitudes $320^\circ < l^{\text{II}} < 40^\circ$. This upper limit assumes a thermal spectrum with temperature 10 KeV, after Bleeker and Deerenberg (1970b).

It is plotted in fig. 8.5 along with the results of Bleeker and Deerenberg (1970b) for $130^\circ < l^{\text{II}} < 160^\circ$, $20 < E < 80$ KeV, and of Schwartz (1969) for $130^\circ < l^{\text{II}} < 160^\circ$, $220^\circ < l^{\text{II}} < 240^\circ$, $7.7 \leq E \leq 110$ KeV. The upper limit shown for the Leicester results is an estimate based on their report (Cooke and Pounds 1970) that discrete sources can account for more than 90% of the previously reported (Cooke et al. 1969) diffuse flux between 1.4 and 18 KeV at $220^\circ < l^{\text{II}} < 320^\circ$. The results of Schwartz (1969) have only reached the author second-hand but it is interesting to note that the significant point between 7.7 and 12.5 KeV shown in fig. 8.5 has been interpreted by many others (e.g. Vette et al. 1970) as an upper limit, presumably due to the uncertainty of the unresolved discrete source contribution.

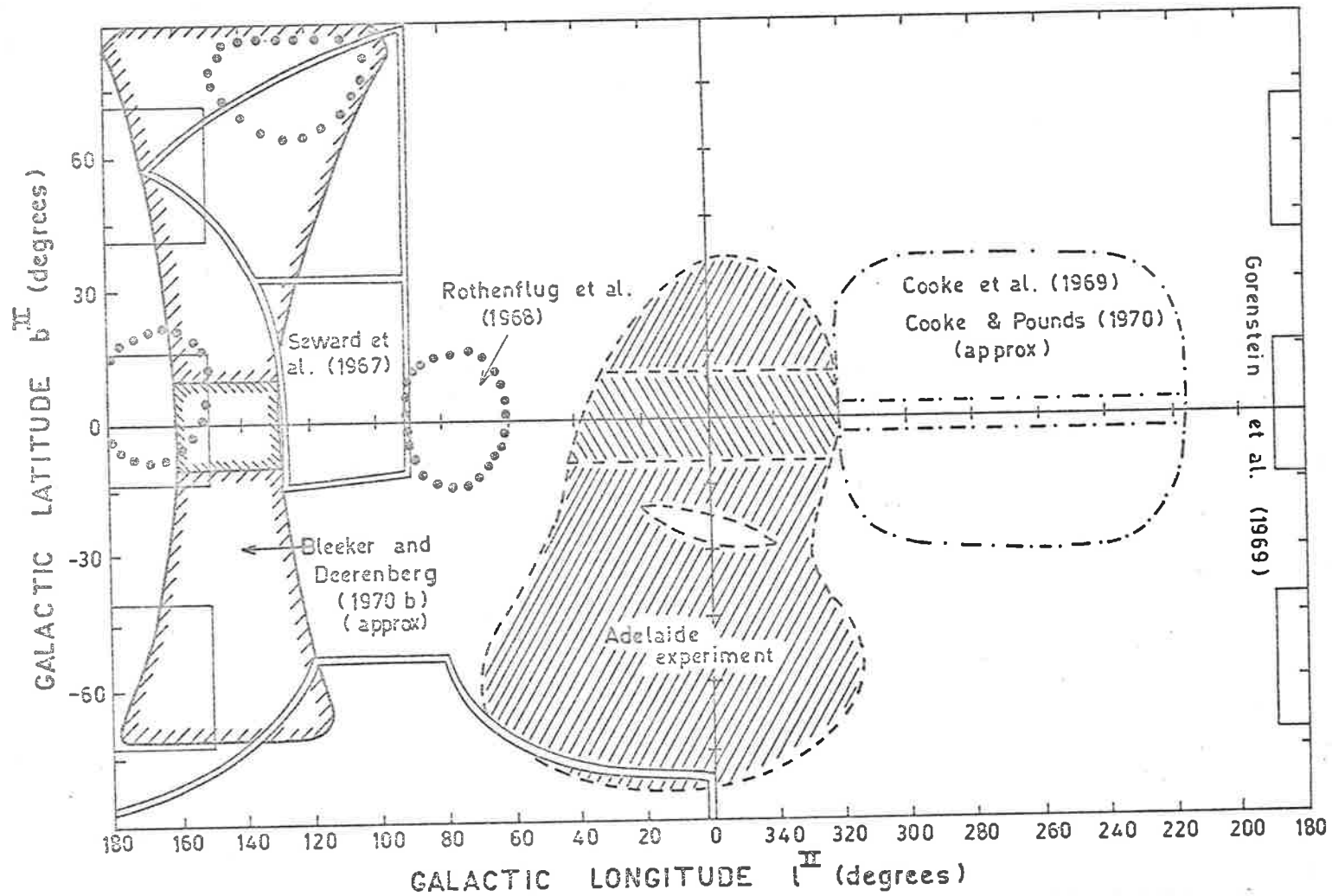


Fig: 8.4 The directions in the sky from which anisotropy measurements of the diffuse background have been made. The boundaries used in the respective experiments for latitude discrimination are shown.

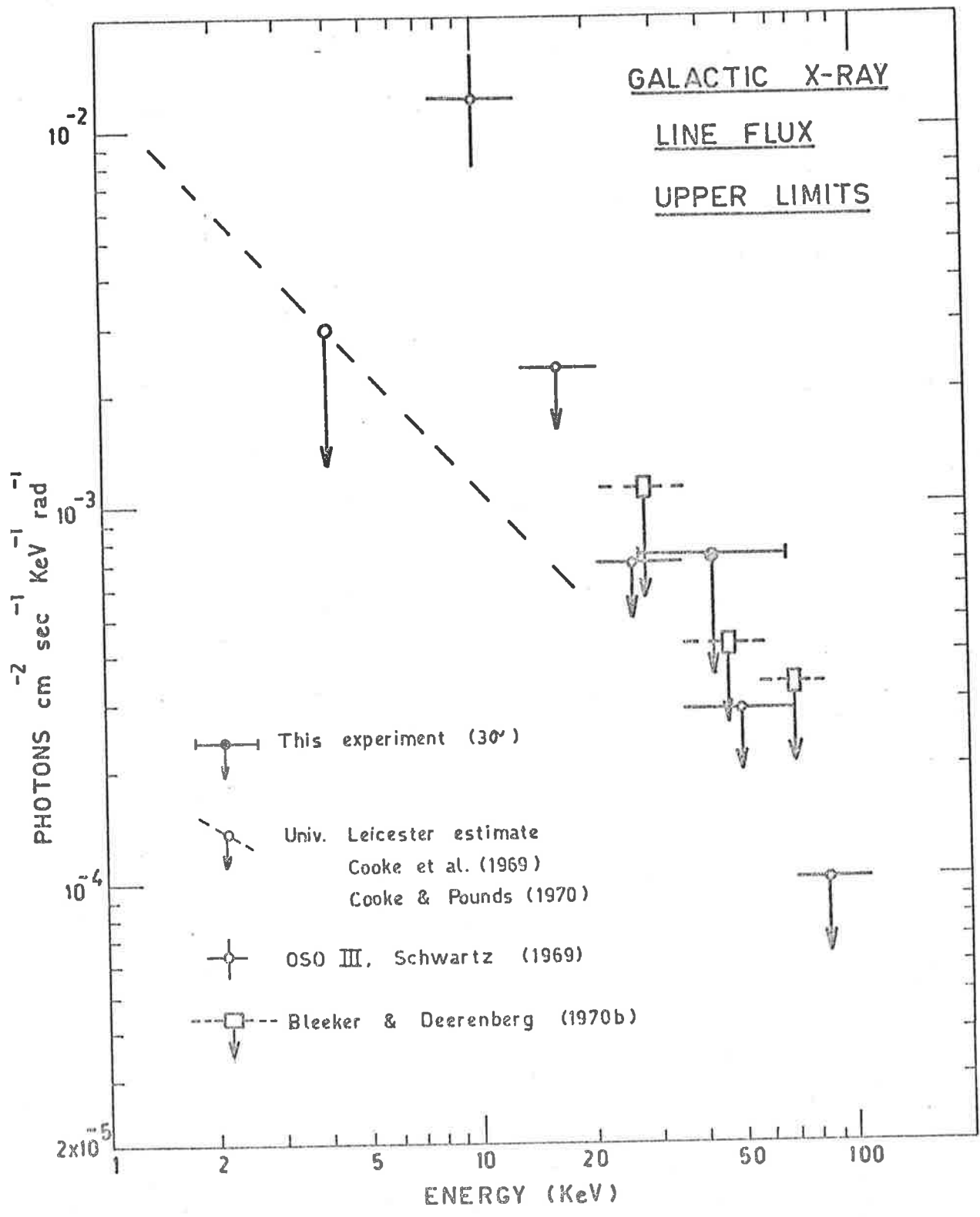


Fig: 8.5 Galactic X-ray line flux measurements.

Thus no detection of a significant galactic X-ray line flux has yet been made in the energy range $1 \lesssim E \lesssim 80$ KeV. This result does not conflict with any theoretical predictions (Maraschi et al. 1967, Ipavich and Lenchek 1970), and greater instrumental sensitivity is needed to push the observed upper limits to smaller values. The observed galactic line flux at 100 KeV (Clark et al. 1968, 1969, Garmire 1970, Kniffen and Fichtel 1970) can be explained by either pion decay resulting from interstellar p-p interactions, or Compton scattering of galactic electrons on the submillimetre far-infra-red radiation (Ipavich and Lenchek 1970, Stecher and Stecker 1970, Longair and Sunyaev 1969b). However, neither of these mechanisms is expected to contribute a flux at X-ray energies which is observable with present instrumentation.

APPENDIXPublications:

- Thomas R.M., "The detection of high energy X-rays from Ara XR-1 and Nor XR-1," Proc. Astron. Soc. Aust., 1, 4, 165, 1968a.
- Thomas R.M., "A measurement of the diffuse cosmic X-ray background from 17 to 167 KeV," Proc. Astron. Soc. Aust., 1, 4, 171, 1968b.
- Buselli G., Clancy M.C., Davison P.J.N., Edwards P.J., McCracken K.G., Thomas R.M., "Spectral properties of the X-ray objects GX3+1, GX354-5, and Sco XR-1", Nature, 219, 1124, 1968; erratum Nature 220, 940, 1968.
- Thomas R.M., Buselli G., Clancy M.C., Davison P.J.N., "Balloon observations of a new-born X-ray source", Ap. J., 158, L151, 1969; erratum Ap. J., 161, L155, 1970.
- Thomas R.M., Buselli G., Clancy M.C., Davison P.J.N., "Balloon observations of a new-born X-ray source", Proc. Astron. Soc. Aust., 1, 7, 345, 1970.

BIBLIOGRAPHY

- Ables J.G., Ap. J., 155, L27, 1969.
- Acton L.W., Catura R.C., Culhane J.L., Fisher P.C., Ap J., 161;
L175, 1970.
- Aitken D.W., Beron B.L., Yenicay G., Zulliger H.R., I.E.E.E. Trans.
Nuc. Sci., NS-14, 468, 1967.
- Aitken D.W., I.E.E.E. Trans Nuc. Sci., NS-15, 10, 1968a.
- Aitken D.W., I.E.E.E. Trans. Nuc. Sci., NS-15, 214, 1968b.
- Allen C.W., "Astrophysical Quantities," Athlone Press, 1963.
- Anderson K.A., Phys. Rev., 123, 1435, 1961.
- Andrew B.H., Purton C.R., Nature, 218, 855, 1968.
- Angel J.R.P., Novick R., Vanden Bout P., Wolff R.S., Phys. Rev.
Letters, 22, 861, 1969.
- Apparao M., "Pulsars and the Universal X-ray Background", preprint,
Tata Inst. of Fund. Res., Bombay, 1969.
- Axel P., Rev. Sci. Inst., 25, 391, 1954.
- Barnden L.R., Francey R.J., Proc. Astron. Soc. Aust, 1, 236, 1969.
- Baxter A.J., Wilson B.G., Green D.W., Ap. J., 155, L145, 1969.
- Bergamini R., Londrillo P., Setti G., Nuovo. Cim., 52B, 495, 1967.
- Birks J.B. "The Theory and Practice of Scintillation Counting"
Pergamon Press, 1964.
- Blanco V., Kunkel W., Hiltner W.A., Lynga G., Bradt H., Clark G.W.,
Naranan S., Rappaport S., Spada G., Ap. J., 152, 1015,
1968.
- Bleeker J.A.M., Burger J.J., Scheepmaker A., Swanenburg B.N.,
Tanaka Y., Phys. Lett., 21, 301, 1966.
- Bleeker J.A.M., Burger J.J., Deerenberg, A.J.M. Scheepmaker A.,
Swanenburg B.N., Tanaka Y., Hayakawa S., Makino F.,
Ogawa H., Can. J. Phys., 46, S461, 1968.

- Bleeker J.A.M., Deerenberg A.J.M., Ap. J., 159, 215, 1970a.
- Bleeker J.A.M., Deerenberg A.J.M., Nature 227, 470, 1970b.
- Boldt E., McDonald F.B., Riegler G., Serlemitsos P., Phys. Rev. Letters, 17, 447, 1966.
- Boldt E.A. Desai U.D., Holt S.S., Ap. J., 156, 427, 1968.
- Boldt E.A., Desai U.D., Holt S.S., Serlemitsos P., Proc. I.A.U. Symp. No.37, Rome, 1969.
- Boldt E., Serlemitsos P., Ap. J., 157, 557, 1969a.
- Bowyer C.S. Byram E.T., Chubb T.A., Friedman H., Science, 146, 912, 1964.
- Bowyer C.S., Field G.B., Mack J.E., Nature, 217, 32, 1968.
- Boyd D.M., private communication, 1970.
- Bradt H., Mayer W., Naranan S., Rappaport S., Spada G., Ap. J., 150, L199, 1967.
- Bradt H., Rappaport S., Mayer W., Nather R.E., Warner B., MacFarlane M., Kristian J., Nature, 222, 728, 1969.
- Brecher K., Morrison P., Ap. J., 150, L61, 1967.
- Brecher K., Morrison P., Phys. Rev. Lett., 23, 802, 1969.
- Brecher K., Burbidge G., Comments on Astrophysics and Space Physics, 2, 75, 1970.
- Brini D., Ciriegi U., Fuligni F., Ric. Sci., 6, 565, 1964.
- Brini D., Ciriegi U., Fuligni F., Gandolfi A., Moretti E., J.G.R., 70, 5460, 1965.
- Brini D., Ciriegi U., Fuligni F., Moretti E., J.G.R., 72, 903, 1967.
- Brown R.L., Gould R.J., Phys. Rev. D, 1, 2252, 1970.
- Bunner A.N., Coleman P.C., Kraushaar W.L., McCammon D., Palmieri T.M., Shilepsky A., Ulmer M., Nature, 223, 1222, 1969.
- Bunner A.N., Palmieri T.M., Ap. J., 158, L35, 1969.
- Burbidge G., Proc. Royal Soc. London, Series A, 313, 331, 1969.

- Buselli G., Proc. Astron Soc., Aust., 1, 168, 1968.
- Buselli G., Clancy M.C., Davison P.J.N., Edwards P.J., McCracken K.G., Thomas R.M., Nature, 219, 1124, 1968; Erratum Nature, 220, 940, 1968.
- Buselli G., Ph. D. thesis, 1971.
- Chiu H.Y., Pub. Astron. Soc. Pac., 82, 487, 1970.
- Chodil G., Mark H., Rodrigues R., Seward F., Swift C.D., Phys. Rev. Letters, 19, 681, 1967.
- Chodil G., Mark H., Rodrigues R., Swift C.D., Ap. J., 152, L45, 1968.
- Chupp E.L., Sarkady A.A., Gilman H.P., Plan. Sp. Sci., 15, 881, 1967.
- Chupp E.L., Forrest D.J., Lavakare P.J., Sarkady A.A., Bull. Amer. Phys. Soc., 13, 1399, 1968.
- Chupp E.L., Forrest D.J., J.G.R., 75, 871, 1970.
- Clark G.W., Garmire G., Oda M., Wada M., Giacconi R., Gursky H., Waters J., Nature, 207, 584, 1965.
- Clark G.W., Garmire G.P., Kraushaar W.L., Ap. J., 153, L203, 1968.
- Clark G.W., Garmire G.P., Kraushaar W.L., Proc. I.A.U. Symp. No. 37., Rome, 1969.
- Clancy M.C., Proc. Astron. Soc. Aust., 1, 166, 1968.
- Clancy M.C., Ph. D. thesis, 1971.
- Cline T.L., Phys. Rev. Lett., 7, 109, 1961.
- Cline T.L., Holt S.S., Honer E.W., J.G.R., 73, 434, 1968.
- Cocke W.J., Disney M.J., Taylor D.J., Nature, 221, 525, 1969.
- Conner J.P., Evans W.P., Belian R.D., Ap. J., 152, L45, 1969.
- Cooke B.A., Pounds K.A., Stewardson E.A., Adams D.J., Ap. J., 150, L189, 1967.
- Cooke B.A., Griffiths R.E., Pounds K.A., Nature, 224, 134, 1969.
- Cooke B.A., Pounds K.A., Univ. Leicester preprint, 1970.
- Cunningham C., Groves D., Price, R., Rodrigues R., Swift C., Ap. J., 160, 1177, 1970.

- Davison P.J.N., Proc. Astron. Soc. Aust., 1, 169, 1968.
- Demoulin M.H., Burbidge G.R., Ap. J., 154, 3, 1968.
- Dolan J.F., Astron. J., 75, 223, 1970a.
- Dolan J.F., Sp. Sci. Rev., 10, 830, 1970b.
- Ducros G., Ducros R., Rocchia R., Tarrius A., Saclay preprint, 1969.
- Duthie J.G., Haffner E.M., Kaplon M.F., Fazio G.G., Phys. Rev. Lett. 10, 364, 1963.
- Edwards P.J., Burt G.J., Knox F., Nature, 222, 1053, 1969.
- Eggen O.J., Freeman K.C., Sandage A.R., Ap. J., 154, L27, 1968.
- Eggen O.J., Rodgers A.W., Ap. J., 158, L111, 1969.
- Evans R.D., Methods of Experimental Physics, 5B, 761, 1963.
- Evans W.D., Belian R.D., Conner J.P., Ap. J., 159, L57, 1970a.
- Evans W.D., Belian R.D., Conner J.P., Strong I.B., Hiltner W.A., Kunkel W.E., "X-ray and optical variations of Sco X-1", Univ. of Calif., Los Alamos, preprint no. LA-DC-11877, 1970b.
- Felten J.E., Morrison P., Phys. Rev. Letters, 10, 453, 1963.
- Felten J.E., Morrison P., Ap. J., 146, 686, 1966.
- Felten J.E., Rees M.J., Nature, 221, 924, 1969.
- Finch H.F., Leaton B.R., Month. Not. Roy. Astron. Soc. Geophys. Supp., 7, 314, 1967.
- Fisher P.C., Jordan W.C., Meyerott A.J., Acton L.W., Roethig D.T., Nature, 211, 920, 1966.
- Fisher P.C., Jordan W.C., Meyerott A.J., Acton L.W., Roethig D.T., Ap. J., 151, 1, 1968.
- Fishman A.J., Harnden F.R. jr., Haymes R.C., Ap. J., 156, L107, 1969.
- Floyd F.W., Glass I.S., Schnopper H.W., Nature, 224, 50, 1969.

- Francey R.J., Fenton A.G., Harries J.R., McCracken K.G., *Nature*, 216, 773, 1967.
- Freeman K.C., Rodgers A.W., Lynga G., *Nature*, 219, 251, 1968.
- Fretter W.B., *Phys. Rev.*, 76, 511, 1949.
- Friedman H., Byram E.T., Chubb T.A., *Science*, 156, 374, 1967.
- Friedman H., Byram E.T., *Science*, 158, 257, 1967a.
- Friedman H., Fritz G., Henry R.C., Hollinger J.P., Meekins J.F., Sadeh D., *Nature* 221, 345, 1969.
- Fritz G., Henry R.C., Meekins J.F., Chubb T.A., Friedman H., *Science*, 164, 709, 1969.
- Frost K.J., Rothe E.D., Peterson L.E., *J.G.R.*, 71, 4079, 1966.
- Garmire G.P., *Bull Am. Phys. Soc.*, 15, 564, 1970.
- Giacconi R., Gursky H., Paolini F.R., Rossi B.B., *Phys. Rev. Letters*, 9, 439, 1962.
- Giacconi R., Gorenstein P., Gursky H., Usher P.D., Waters J.R., Sandage A., Osmer P., Peach J.V., *Ap. J.*, 148, L129, 1967.
- Giacconi R., Gursky H., Van Speybroeck L.P., *Ann. Rev. Astron. Astp. 6*, 373, 1968.
- Goldreich P., *Proc. Astron. Soc. Aust.* 1, 227, 1969.
- Gorenstein P., Gursky H., Garmire G., *Ap. J.*, 153, 885, 1968.
- Gorenstein P., Kellogg E.M., Gursky H., *Ap. J.*, 156, 315, 1969.
- Gorenstein P., Kellogg E.M., Gursky H., *Ap. J.*, 160, 199, 1970.
- Gould R.J., Burbidge G.R., *Ap. J.*, 138, 969, 1963.
- Gould R.J., *Ann Rev. Astron. and Astropcs.*, 6, 195, 1968.
- Grader R.J., Hill R.W., Seward F.D., Toor A., *Science*, 152, 1499, 1966.
- Grader R.J., Hill R.W., Stoering J.P., *Ap. J.*, 161, L45, 1970.
- Greenhill J.G., Fenton K.B., Fenton A.G., White K.S., *J.G.R.*, 75, 4595, 1970.

- Gross B., Z. Phys., 83, 214, 1933.
- Gunn J.E., Ostriker J.P., Preprint, Princeton Univ. Observatory, 1969.
- Gursky H., Giacconi R., Gorenstein P., Waters J.R., Oda M., Bradt H., Garmire G., Sreekantan B.V., Ap. J., 146, 310, 1966.
- Gursky H., Gorenstein P., Giacconi R., Ap. J., 150, L75, 1967.
- Harries J.R., McCracken K.G., Francey R.J., Fenton A.G., Nature, 215, 38, 1967.
- Hayakawa S., Matsuoka M., Sugimoto D., Sp. Sci. Rev., 5, 109, 1966.
- Hayakawa S. "Cosmic Ray Physics", Wiley-Interscience, 1969a.
- Hayakawa S., Proc. I.A.U. Symp. No.37 Rome, 1969b.
- Haymes R.C., J.G.R., 69, 841, 1964,
- Haymes R.C., Ellis D.V., Fishman G.J., Glenn S.W., Kurfess J.D., Ap. J., 151, L131, 1968.
- Haymes R.C., Glenn S.W., Fishman G.J., Harnden F.R., J.G.R., 74, 5792, 1969.
- Henry R.C., Fritz G., Meekins J.F., Friedman H., Byram E.J., Ap. J., 153, L11, 1968.
- Hill R.W., Grader R.J., Seward F.D., Ap., J., 154, 655, 1968.
- Holt S.S. "Calibration standards for photon spectroscopy between 20-200KeV", NASA - Goddard preprint X-611-67-433, Sept. 1967.
- Holt S.S., Boldt E.A., Serlemitsos P.J., NASA - Goddard preprint X-611-69-456, 1969.
- Houck J.R., Harwit M., Ap. J., 157, L45, 1969.
- Houck J.R., Bull. Am. Phys. Soc., 15, 564, 1970.
- Howard R.L., Nelson S.W., Winckler J.R., Rev. Sci. Inst., 39, 1013, 1968.
- Hudson H.S., Primbsch J.H., Anderson K.A., 71, 5665, 1966.

- Hudson H.S., Peterson L.E., Schwartz D.A., Solar Physics, 6, 205
1969.
- Hurwitz L., Knapp D.G., Nelson J.H., Watson D.E., J.G.R., 71,
2373, 1966.
- Ipavich F.M., Lenchek A.M., Phys. Rev. D., 2, 266, 1970.
- Jakosky J.J., "Exploration Geophysics," 2nd ed., Trija Pub. Co.
Los Angeles, 1950.
- Janossy L., "Cosmic Rays", Oxford U.P., 1950.
- Johnson H.M., Golson J.C., Ap. J., 154, L77, 1968.
- Jones F.C., J.G.R., 66, 2029, 1961.
- Kasturi Rangan K., Bhavsar P.D., Nerurkar N.W., J.G.R., 74, 5139,
1969.
- Kellermann K.I., Ap. J., 146, 621, 1966.
- Kitamura T., Matsuoka M., Miyamoto S., Nakagawa M., Oda M.,
Ogawara Y., Takagishi K., Nature, 224, 784, 1969.
- Kniffen D.A., Fichtel C.E., Ap. J., 161, L157, 1970.
- Kondo I., Nagase F., Nagoya Univ. Preprint, June 1968.
- Kraft R.P., Demoulin M.H., Ap. J., 150, L183, 1967.
- Kunkel W., Osmer P., Smith M., Hoag A., Schroeder D., Hiltner W.A.,
Bradt H., Rappaport S., Schnopper H.W., Ap. J., 161,
L169, 1970.
- Lewin W.H.G., Clark G.W., Smith W.B., Ap. J., 152, L49, 1968a.
- Lewin W.H.G., Clark G.W., Smith W.B., Ap. J., 152, L55, 1968b.
- Lewin W.H.G., Clark G.W., Smith W.B., Nature, 219, 1235, 1968c.
- Lewin W.H.G., Clark G.W., Gerassimenko M., Smith W.B., Nature, 223
1142, 1969.
- Lewin W.H.G., McClintock J.E., Smith W.B., Ap. J., 159, L193, 1970a.
- Lewin W.H.G., McClintock J.E., Ryckman S.G., Glass I.S., Smith W.B.,
Ap. J., 162, L109, 1970b.

- Lingenfelter, R.E., Flamm E.J., J.G.R., 69, 2199, 1964.
- Longair M.S., Sunyaev R.A., *Astrophys. Lett.*, 4, 65, 1969a.
- Longair M.S., Sunyaev R.A., *Astrophys. Lett.*, 4, 191, 1969b.
- Makino F., *Astrophys. and Sp. Sci.*, 8, 251, 1970.
- Manley O., *Ap. J.*, 144, 1253, 1966.
- Manley O.P., *Astrophys. Lett.* 5, 43, 1970.
- Maraschi L., Perola G.C., Schwarz S., preprint GRUPPO GIFCO del CNR, Milano, 1967.
- Mark H., Price R., Rodrigues R., Seward F.D., Swift C.D., *Ap. J.*, 155, L143, 1969.
- Matsuoka M., Oda M., Ogawara Y., Hayakawa S., Kato T., *Can. J. Phys.*, 46, S466, 1968.
- Mayer W., Bradt H.V., Rappaport S., *Ap. J.*, 159, L115, 1970.
- McGregor A., Seward F., Turiel I., U.C.R.L. preprint no.72031, Dec. 17, 1969.
- Metzger A.E., Anderson E.C., Van Dilla M.A., Arnold J.R., *Nature*, 204, 766, 1964.
- Meyer P., Vogt R.E., *Phys. Rev. Letters*, 8, 387, 1962.
- Millikan R.A., Neher H.V., Pickering W.H., *Phys. Rev.*, 66, 295, 1944.
- Morrison P., *Ann. Rev. Astron. and Astrophys.*, 5, 325, 1967.
- Mott W.E., Sutton R.B., *Handbuch der Physik*, Vol XLV, 86, 1958.
- Oda M., *J. App. Opt.*, 4, 143, 1965.
- Okudaira K., Hirasima Y., *Can. J. Phys.*, 46, S494, 1968.
- Overbeck J.W., Tananbaum H.D., *Ap. J.*, 153, 899, 1968.
- Patla N., Kiss A.E., *Brit. J. App. Phys.*, 16, 1871, 1965.
- Peterson L.E., Winckler J.R., J.G.R., 64, 697, 1959.

- Peterson L.E., Nitardy J.H., Rev. Sci. Inst., 12, 1390, 1961.
- Peterson L.E., J.G.R., 68, 979, 1963.
- Peterson L.E., Jerde R.L., Jacobson A.S., A.I.A.A. Journal, 5, 1921, 1967.
- Peterson L.E., Jacobson A.S., Pelling R.M., Schwartz D.A., Can. J. Phys., 46, S437, 1968.
- Price W.J., "Nuclear Radiation Detection," 2nd edition, McGraw Hill, 1964.
- Puppi G., Dallaporta N., Prog. Cos. Ray Phys., 1, 315, 1952.
- Puppi G., Prog. Cos. Ray Phys., 3, 339, Interscience, N.Y., 1956.
- Radhakrishnan V., Proc. Astron. Soc. Aust., 1, 254, 1969.
- Rao U.R., Chitnis E.V., Prakasa Rao A.S., Jayanthi U.B., Proc. Ind. Acad. Sci., Vol. LXX, No.6, Sec. A., 257, 1969.
- Rappaport S., Bradt H.V., Naranan S., Spada G., Nature, 221, 428, 1969a.
- Rappaport S., Bradt H.V., Mayer W., Ap. J., 157, L21, 1969b.
- Rees M.J., Setti G., Nature, 219, 127, 1968.
- Richards D., I.A.U. Circ. No.2114, 1968.
- Riegler G.R., Boldt E., Serlemitsos P., Ap. J., 153, L95, 1968.
- Riegler G.R., Ph.D. thesis, Univ. of Maryland, and NASA - Goddard report X-611-69-1, 1969.
- Rocchia R., Labeyrie J., Ducros G., Boclet D., Proc. Intern. Conf. Cosmic Rays, London, 423, 1965.
- Rocchia R., Rothenflug R., Boclet D., Ducros G., Labeyrie J., "Space Research" Vol. VIII, 1327, North Holland Pub. Co., Amsterdam, 1967.
- Rossi B., Rev. Mod. Phys., 20, 537, 1948
- Rossi B., "High Energy Particles", Prentice-Hall, N.Y., 1952.
- Rothenflug R., Rocchia R., Koch L., Proc. Intern. Conf. Cosmic Rays, London, 1, 446, 1965.

- Rothenflug R., Rocchia R., Boclet D., Durouchoux P., "Space Research".
Vol. VIII, 423, North Holland Pub. Co., Amsterdam, 1968.
- Sandage A.R., Osmer P., Giacconi R., Gorenstein P., Gursky H,
Waters J., Bradt H., Garmire G., Sreekantan B.V., Oda M.,
Osawa K., Jugaku J., Ap. J., 146, 316, 1966.
- Sartori L., Morrison P., Ap. J., 150, 385, 1967.
- Schklovsky I.S., "Supernovae", (New York Wiley Interscience) 1968.
- Schnopper H.W., Bradt H.V., Rappaport S., Bougham E., Burnett B.,
Doxsey R., Mayer W., Watt S., Ap. J., 161, L161, 1970.
- Schwartz D., Ph. D. thesis (unpub.) Univ. Calif., San Diego, 1969.
- Sciama D.W., Proc. Roy. Soc. Lond. A, 313, 349, 1969.
- Seward F., Chodil G., Mark H., Swift C., Toor A., Ap. J., 150, 845
1967.
- Sharpless S., "Galactic Structure", ed. A. Blaauw and M. Schmidt
(Chicago: Univ. of Chicago Press) 1965.
- Shivanandan K., Houck J.R., Harwit M., Phys. Rev. Lett., 21, 1460,
1968.
- Shukla P.G., Wilson B.G., Nature, 228, 1077, 1970.
- Silk J., Ap. J., 151, L19, 1968.
- Silk J., McCray R., Astrophys. Lett., 3, 59, 1969.
- Simpson, J.A. Phys. Rev., 83, 1175, 1951.
- Smith R.V., Chase L.F., Imhof W.L., Reagan J.B., Walt M., "Radiation
measurements with balloons", ARL-TDR-62-2, 6571 st,
Aeromedical Res. Lab., Holloman A.F.B., New Mexico, 1962.
- Soberman R.K., Phys. Rev., 102, 1399, 1956.
- Staelin D.H., Reifenstein III, E.C., I.A.U., Circ. No. 2110, 1968.
- Staker W.P., Phys. Rev., 80, 52, 1950.
- Staker W.P., Pavalow M., Korff, S.A., Phys. Rev., 81, 889, 1951.
- Stecher T.P., Stecker F.W., Nature, 226, 1234, 1970.
- Stecker F.W., Ap. J., 157, 507, 1969a

- Stecker F.W., Nature 224, 870, 1969b.
- Stein J.A., Lewin W.H.G., J.G.R., 72, 383, 1967.
- Stein W.A., Ney E.P., J.G.R., 68, 65, 1963.
- Thomas R.M., Proc. Astron. Soc. Aust., 1, 165, 1968a.
- Thomas R.M., Proc. Astron. Soc. Aust., 1, 171, 1968b.
- Thomas R.M., Buselli G., Clancy M.C., Davison P.J.N., Ap. J., 158
L151, 1969; erratum, Ap. J., 161, L155, 1970.
- Thomas R.M., Buselli G., Clancy M.C., Davison P.J.N., Proc. Astron.
Soc. Aust., 1, 345, 1970.
- Tinlot J.H., Phys. Rev., 74, 1197, 1948.
- Tucker W.H., Gould R.J., Ap. J., 144, 244, 1966.
- Tucker W.H., Ap. J., 161, 1161, 1970.
- Van Loef J.J., Lind D.A., Phys. Rev., 101, 103, 1956.
- Vette J.I., J.G.R., 67, 1731, 1962.
- Vette J.I., Gruber D., Matteson J.L., Peterson L.E., Ap. J., 160,
L161, 1970.
- Victoreen J.A., J. App. Phys., 14, 95, 1943.
- Webber W.R., Proc. Astron. Soc. Aust. 1, 160, 1968.
- Westphal J.A., Sandage A., Kristian J., Ap. J., 154, 139, 1968.
- Wilson B.G., Inst. Space and Aeronaut. Sci., Univ. Tokyo, Report
No.428, 1968.
- Wolberg J.R., "Prediction Analysis", Van Nostrand, 1967.
- Wolff R.S., Angel J.R.P., Novick E., Vanden Bout P., Ap. J., 160,
L21, 1970.
- Woltjer L., Ap. J., 152, L179, 1968.
- Womack E., Overbeck J., Bull. Amer. Phys. Soc., 13, 1398, 1968.
- Yuan L.C.L., Phys. Rev., 81, 175, 1951.
- Zerby C.D., Meyer A., Murray R.B., Nuc. Inst. Meth., 12, 115, 1961.